Reliability of Doped SnAgCu Solder Alloys with Various Surface Finishes Under Realistic Service Conditions

by

Sinan Su

A dissertation submitted to the Graduate Faculty of
Auburn University
in partial fulfillment of the
requirements for the Degree of
Doctor of Philosophy

Auburn, Alabama
May 4, 2019

Keywords: Lead-free solder, Fatigue, Shear, Reliability

Approved by

Sa’s Hamasha, Chair, Assistant Professor of Industrial and Systems Engineering

John Evans, Charles D. Miller Endowed Chair Professor of Industrial and Systems Engineering

Sean Gallagher, Hal N. and Peggy S. Pennington Associate Professor of Industrial and Systems Engineering

Gregory Harris, Associate Professor of Industrial and Systems Engineering

Abstract

The electronic packaging industry has moved from eutectic Sn-Pb solder materials to near-eutectic SnAgCu (SAC) solder materials in the past decade because of the increasing awareness of health and safety concerns associated with the use of Lead (Pb). The reliability performances for SAC solder materials under thermal and isothermal aging conditions have been extensively studied and results show aging is universally detrimental to the solder joints reliability, which leads to a large degradation of mechanical properties including tensile strength, shear strength and fatigue behaviors. Moreover, solder joint in realistic applications are typically exposed to cyclic loading, either through thermal cycling or mechanical cycling. Numerous solutions have been proposed to mitigate the aging-induced or cyclic-induced mechanical properties degradation. One of the possible solutions is to develop “next generation” solder alloys with additional elements mixed with SAC solder alloys. This process is called solder doping. Common solder dopants include nickel (Ni), bismuth (Bi), antimony (Sb), and indium (In). Solder doping was observed to have substantial influence on mechanical properties of solder joints, such as an increase of solder ultimate tensile strength and shear strength. However, as bulk sample has been used in decades in testing the mechanical properties of solder materials, studies have revealed that mechanical properties exacted from bulk sample may not be the real reflection of solder joints implemented in the realistic application, since the solder joint was proved to demonstrate a much more complex structure than bulk sample. Therefore, in this study, solder joints assembled on the PCB were used directly as test specimens, where several important factors that may have critical impacts on solder joint reliability can be tested, for example, intermetallic compound (IMC) and surface plating (surface finish). The purpose of this dissertation is to study several impact factors (aging, surface finish, solder doping, IMC) on the reliability of solder joints under realistic applications.

In this study, 5 commercially available doped solder alloys including SAC305 (Sn-3.0%Ag-0.5%Cu) and SAC105 (Sn-1.0%Ag-0.5%Cu) solder alloys were used as test samples. Three types of surface finishes were applied on the test vehicles, which were Organic Solderability Preservative (OSP), Immersion Silver (ImAg), and Electroless Nickle Immersion Gold (ENIG).

The first part of the research investigates the effect of long-term room temperature aging on the fatigue behaviors of SAC305, SAC105 and various doped solder joints. Prior to assessment, all the specimens are exposed to room temperature (25°C) for 4 years. Test specimens were then subjected to cyclic stress-strain loading under these two aging conditions, 0 aging and 4 years of aging. Failure data is carefully collected and analyzed using a Weibull distribution to study the effect of room temperature aging on the reliability of solder alloys. Results show that 4 years' room temperature aging leads to a significant degradation on the fatigue properties (fatigue life and energy dissipation per cycle) and solder alloy doped with Bi exhibit better fatigue resistance than SAC solder alloys.

In the second part of this research, different surface finishes and solder doping alternatives are studied under shear testing to examine their impacts on the shear properties of solder joints under realistic applications. The solder joint under each condition is tested using an innovative test schematic (cyclic shear testing) and ultimate shear strength and shear energy (area under the shear curve) are recorded within each condition. Results demonstrate that solder joint with higher Bi and Ag content demonstrates larger shear strength compared to SAC305 solder joint. The OSP surface finish demonstrates the largest shear strength, followed by ImAg, with ENIG demonstrating the least shear strength, regardless of solder alloy types. Ductile failure is the most prevalent failure mechanism during the shear testing, however, brittle failure is detected as well where the fracture occurred at the interfacial area between the Ni layer and bulk solder.

Finally, the effects of surface finish and doped solder alloy are investigated under cyclic shear testing to study the interaction effects of both impact factors on the reliability of solder joint under realistic applications. Results reveal that solder alloys with high Ag and Bi content demonstrate higher strength, therefore, the fatigue resistance under cyclic shear testing is improved. However, the same doping option also increases the brittleness of the solder alloy, where increases the risk of brittle failure, especially when combing with ENIG surface finish.

Acknowledgments

I would like to express my deepest appreciation to my advisor Dr. Sa'd M Hamasha. I am extremely thankful for his timely help and support at my tough times. I am indebted to him for all the work, advice, encouragement and friendship he extended to me. Without his support and encouragement, this dissertation would not have been possible.

I would also like to extend my sincere gratitude and appreciation to my committee members: Dr. John Evens, Dr. Sean Gallagher, Dr. Gregory Harris for their valuable insights and precious time in the course of this research. Specially thanks Dr. Bozack for his SEM training and useful discussions.

In addition, I would like to thank all my lab-mates, coworkers and friends: Dr. Nianjun Fu, Dr. Cong Zhao, Dr. Thomas Sanders, Francy John Akkara, Anto Raj, Minghong Jian, Xin Wei, Seth Gordon, Abdullah Fahim, Mohammed Abueed, Raed Alathamneh, Nicholas Smith, Tianqi Smith and Wong Bin.

Thank you to my parents Guoqing Su and Shuhong Wang who provided me the opportunity and financial assistance to study abroad. This day would not be possible without their deeply love, support and education. I would also like to thank you my aunt Lili Su and her husband Ji Li for the selfless assistance and making me feel like home whenever I went to their house.

Finally, I would like to save the best for my wife, Dr. Wang, a way more brilliant lady who I want to spend the rest of my life with.

Endless love to Auburn University and land of Alabama for hosting me for 6 years. War Eagle!

Table of Contents

List of Tables

List of Figures

List of Abbreviations

BGA	Ball Grid array
IMC	Intermetallic Compounds
OSP	Organic Solderability Preservation
ImAg	Immersion Silver
ENIG	Electroless Nickle Immersion Gold
SAC	Tin-Silver-Copper
PCB	Printed Circuit Board
THMT	Through-Hole Mount Technology
SMT	Surface Mount Technology

Chapter 1 General Introduction

1.1 Electronic Packaging

Electronic packaging is defined as "the science and art of establishing interconnections and a suitable operating environment for predominantly electrical circuits to process or store information"[1]. Basically, electronic packaging provides housing and interconnection of integrated circuits to perform designed functions. The electronic packaging system has four major functions [1]:

1. Signal distribution, involving mainly topological and electromagnetic considerations;

2. Power distribution, involving electromagnetic, structural, and materials aspects;

3. Heat dissipation (cooling), involving structural and materials considerations;

4. Protection (mechanical, chemical, and electromagnetic) of components and interconnections;

Moreover, Four levels of electrical interconnections exist in an electronic packaging system (level zero, one, two, and three).[2]:

Level zero is gate-to-gate interconnections on a chip. A silicon "die", which is diced from a single-crystal silicon wafer, contains many solid-state electronic devices (e.g. transistors, resistors, capacitors etc.) that have been defined and connected to form functional electrical circuitry [2]. Level 1 is chip-to-module connections. In this level, the chip is mechanically affixed to a lead frame or interposer layer inside a chip carrier through use of either wire bonding or flip chip bumping technology. A variety of chip carriers have been produced including dual-in-line package, quad flat pack, and Ball Grid Array (BGA). Each chip carrier has its positives and negatives depending on various factors such as type of attachment to the substrate, internal structure, materials, or lead pitch. The packaged device is then attached to a Printed Circuit Board (PCB), which is defined as the second level. The PCB, typically, is a rigid laminated board constructed with layers of fiberglass-epoxy composites on which components can be soldered. A PCB can be one-sided or two-sided, and it provides mechanical supports and electronic connections between components using tracks, pads, and other features etched from copper sheets. Level three of interconnections consists of substrate to substrate, such as mounting a daughter card to a motherboard. When designing and manufacturing the electronic packaging, the common practice of industry is to focus on the first and second level of interconnections.

Technically, there are two types of component mounting technologies [3]. The first is Through-Hole Mount Technology (THMT), and the other is Surface Mount Technology (SMT). THMT secures component on a PCB through the leads of through-hole components. The leads are inserted throughout the board via through holes. The through holes are then filled with solder to affix through-hole components to the PCB. This helps to create a stronger bond between the components and board causing board level reliability to be higher accordingly. However, the additional drilling does generate higher cost, take more space on the PCB, and can only be used on one side of the PCB. In contrast, surface mount technology secures the component to the PCB with solder. SMT is much faster and more cost effective as opposed to THMT. The size of surface mount components is relatively smaller, which allows for more surface mount components to be attached to the surface of PCB. However, since less solder is used to attach component on the PCB, the connections are weaker, which can cause reliability concerns.

1.2 Reliability of Electronic Packaging

Reliability of electronic packaging is the probability electronic packages will not fail under operational conditions in a service before the end of its expected life. The key factors in the definition are how the packages will be used and for what length of time. Due to the variations in the manufacturing processes and operational conditions, reliability is founded based on the theory of probability. The probability of failure normally increases with time. Failure data from reliability life testing (accelerated life testing) is used to generate failure distributions accordance to time. Nonparametric (empirical distributions) or parametric methods are applied to fit a suitable probability distribution to the failure data, and reliability can then be predicted based on the failure distribution. An accurate description of packaging failure distribution is one of the vital steps in analyzing the reliability of electronic packaging.

Based on the various demands on service duration and reliability, three major classes of electronic products are defined:

Class I: Consumer products. The service life for this class is usually less than 5 years and the reliability demand is relatively low;

Class II: Dedicated/Industrial products. The service life for this class is longer than class I, and the reliability demand is higher;

Class III: Critical products. Service life is more than 20 years and the reliability demand is the highest. A failure can be life threatening.

Unreliable products may result in either financial losses or tarnishing the goodwill of a manufacture, or the combination of both, depending on the degree of seriousness. Financial losses include warranty claims costs and potential compensation.

1.3 Electronic Packages in Realistic Applications

Electronic packages utilize a diverse mix of materials including metal, ceramic, and polymers. Each material has its own thermal and mechanical properties, which together will influence the failure mechanisms and reliability of the entire electronic assembly. Interconnections in this system serve as mechanical support and electrical conduction between components and substrates in an electronic packaging system are commonly subjected to relatively high plastic strain. The cause of the plastic strain is the mismatch of Coefficient of Thermal Expansion (CTE) between component and substrate under a thermal cycling environment.

Extensive research has been conducted to investigate the behaviors of interconnections under thermal cycling tests, and a number of models have been developed to predict the reliability of interconnections under thermal cycling environment. The interconnections may also be exposed to an isothermal cycling condition for a long period of time such as vibration. Unfortunately, a significant amounts of research focused on the isothermal cycling behaviors of solder materials has not been performed especially for an extended length of time under room-temperature deposition.

To better assess the reliability of any electronic assembly, Accelerated Life Tests (ALT) are commonly conducted. By applying ALT, we are expecting to uncover faults and potential modes of failures in a shorter amount of time by introducing “accelerated factors” to accelerate the reliability test process without introducing any unrealistic failure mechanisms. One basic assumption of an ALT is a system that performs better in a ALT would perform similar in real life applications [4]. However, this assumption is not always correct. For example, we artificially simplify the fatigue properties of lead-free solder joints in a realistic service condition by interpreting the fatigue results from a “bulk” sample. Incorrect use of ALT can lead to serious bias in the reliability prediction.

1.4 Problem Statement

Solder joints in real service conditions are often exposed to temperature changing environments. Cyclic changing temperature leads to a cyclic alternating stresses and strains within the solder joints, which leads to the fatigue failure. However, most of the fatigue properties of solder joints are tested in bulk material samples, typically in a “dumbbell” type. The cross-section of bulk samples is either rectangular or circular, and the samples are machined, cast or prepared from tubes, wire or rod [5]. However, bulk samples are different from actual solder joints soldered on a BGA package, based on the following reasons: 1). Solder joints on a BGA package are generally smaller in size compared to their bulk sample contemporaries; 2). Intermetallic Compound (IMC) layer that formed during the process of reflow between solder joints and copper pads, will result to a negative effect on the fatigue life during reliability testing, thus, influence the fracture mechanics of realistic solder joints [6]; 3). The reliability of solder joints in real service can be further enhanced by different surface finishes; 4). The distribution of precipitate in a bulk sample is found to be very different from that in a realistic solder joint [7]; 5). Energy accumulation modes and crack propagation modes are also found varies from realistic solder joint to bulk sample [6]. In summary, the structure of realistic solder joints is more complex compared to that of bulk sample. By testing bulk sample, we pre-simplify several crucial factors disregarding those factors may be critical and have negative affects to the fatigue behaviors. Therefore, the mechanical properties from bulk samples give a reasonable picture on how solder joints will react in real service condition are questionable. The first gap is thus identified as the absence of decent data in publication on mechanical properties of solder joints in real service condition.

Other than the shape of testing samples, the focus of fatigue testing is the fatigue behaviors of solder materials under elevated temperature. A limited amount of research has been performed to study the effect of room-temperature aging on the solder material mechanical behaviors, and none of the research has focused on the effect of long-term room-temperature aging (e.g. more than 4 years of room-temperature aging) on different solder materials. Solder materials are found to lose substantial strength during room-temperature storage, defined as the “aging-softening” effect, as a result of the room-temperature recrystallization of solder material microstructure [8]. The “aging-softening” effect will continue until the fatigue failure of the solder material, which may lead to a larger drop in the solder material’s mechanical properties. The maximum duration of room temperature aging found in literature is 180 days of aging [9], which introduces the second gap: The absence of long-term room temperature aging effect on the cyclic fatigue behaviors of solder joints in the literature.

Thirdly, surface finishes are known to increase the reliability of solder joints. Moreover, strain rates are proven to also have effects on the reliability of solder joints. The interaction effects between surface finish and strain rate on the reliability of solder joints is still unknown, given no studies have ever done this. Therefore, the third gap is the absence of experimental results regarding the effect of different surface finishes with various strain rates in the literature.

1.5 Research Objectives

The motivation of this research is to systematically study the reliability of doped solder joints under realistic service conditions. From this, we hope to find possible solutions to enhance solder joints reliability and expand the current database on mechanical properties of various solder joints. The following objectives will be achieved in this research:

1) Develop appropriate specimen test procedures to conduct various reliability tests (fatigue, shear etc.) on individual solder joints;
2) Examine mechanical properties of various kinds of SnAgCu (SAC) solder alloys with doping effects under realistic service conditions;
3) Study the effect of long-time room temperature aging on the fatigue properties of SnAgCu solder alloys with doping effects under realistic service conditions;
4) Investigate the effects of different surface finishes on the mechanical properties of doped SnAgCu solder alloys with various strain rates;
5) Develop reliability models for predicting the fatigue life of solder alloys under realistic service conditions.

1.6 Proposed Dissertation Organization

This dissertation consists of eight chapters. Chapter I provides introduction to the proposed research with problem statement and detailed research objectives. Chapter II describes the most relevant concepts and methods about electronic packaging and reliability testing that will be used in this research. Chapter III covers literatures on isothermal aging effect on the SnAgCu solder joints, doping effects on the reliability of solder alloys and constitutive models about predicting the fatigue life of solder alloys. Chapter IV includes experimental procedures, preparation of test vehicles, experiment design, and proposed studies that will be conducted in this research. Chapter V addresses the effect of long-term room-temperature aging on the fatigue properties of SnAgCu solder alloys. Chapter VI studies the effect of different surface finishes on the shear properties of doped solder alloys with different shear strain rates. Chapter VII explores the effect of surface finishes on the reliability of SnAgCu solder alloys with doping effects. Chapter VIII summarizes the results and provides conclusions.

Chapter 2 Electronic Packaging and Reliability Testing

2.1 Electronic Components

Technically, there are two types of component mounting technologies. One is Through-Hole Mount Technology (THMT), another is Surface Mount Technology (SMT).

2.1.1 Through-hole Mount Technology (THMT)

Through-hole mount technology first appeared during the 1950s, and then was gradually replaced by Surface Mount Technology (SMT) in the late 1980s.

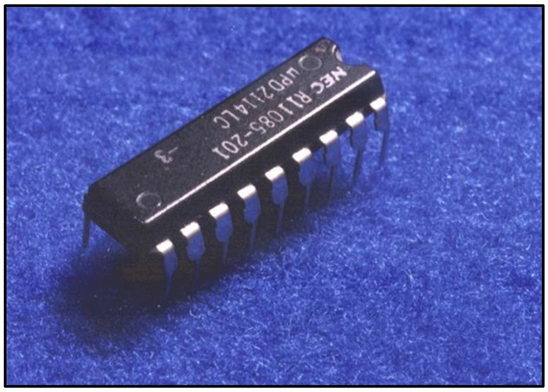

Figure 2.1 A dual inline package (DIP)

Figure 2.1 shows a typical example of through-hole component. One of the most important advantages for THMT is the excellent reliability of solder interconnections. Leads of through-hole components are inserted throughout the board via through hole, which give them the ability to withstand the stress placed on the components. That is basically where the strong bond between the components and board, and higher reliability comes from. THMT is also applied when manual adjustment or replacement is required.

However, the disadvantages for THMT are obvious. The additional drilling makes the boards more expensive to manufacture, let alone through hole components taking more space and can only be used on one side of the PCB. It also restricts the development of multi-layers board and signal traces based on the leads needing to pass through the board. Based on the disadvantages, even with better reliability, the through-hole components are gradually being replaced by smaller, more convenient Surface Mount Technology (SMT) components.

2.1.2 Surface Mount Technology (SMT)

Surface Mount Technology (SMT) started to become widely used in the 1980s. Essentially, the innovative technology where components are placed directly onto the surface of the PCB is defined as Surface Mount Technology (SMT). Figure 2.2 shows an example of surface mount components. Several advantages bring surface mount components to popularity in the market compared to through hole components [10]. The first advantage is size. Since today's electronics are expected to be more compact, there is a large push to decrease the size of all the units in the electronic system. Surface mount components are generally smaller than their through hole contemporaries. Also, with less volume, the surface mount components have more connections per each component, known as input/output (I/O) [3]. Moreover, surface mount components can be mounted on both sides of the PCB, and I/O connections can be placed around all four sides of the components. The number of advantages make the surface mount components more advanced and efficient than the counterpart.

Figure 2.2 Typical surface mount components on a PCB

Furthermore, manufacturing process can be performed much easier than through hole components as well. Fewer holes need to be drilled into the boards, which leads to a significant drop for the initial set up time and cost. With the development of automated assembly process, manufacturing time is further decreased. Besides this, the cost of many surface mount components and parts is less than the through hole components [10].

Unfortunately, there is no perfect technology to fit all the needs of the manufacturing process. SMT has its own drawbacks. SMT does not fit for large size, high voltage parts, so it has to be combined with THMT for better results. Moreover, because of the smaller size and finer pitch I/Os, less solder is used to attach the components onto the PCB, which causes a weaker connection. Therefore, the reliability for surface mount components becomes a big concern.

2.1.3 Ball Grid Array (BGA) component

As the requirements for I/O increases for more advanced components, packages with finer pitch I/Os are needed. However, finer pitch I/O often brings some reliability issues including: coplanarity problems (given finer pitch are easier to bend); wicking (solder climbing up the lead, leaving no solder on the PCB pad); shorting or bridging (unwanted solder connection during reflow process); place and print accuracy [11]. All these factors make finer pitches more costly and often inappropriate and not cost-efficient. Therefore, BGA design was developed to try to solve the issues stated above.

A Ball Grid Array (BGA) component is one form of surface mount technology. Instead of using leads around 4 sides of packages as connections, a BGA utilizes an array of metal spheres (solder joints) for electronic interconnection. Figure 2.3 shows the front and back side of a BGA package. By utilizing this design, space on a PCB is more efficiently used, connections are not limited to the periphery of the component, and it provides more connections for the SMT component.

Figure 2.3 A ball grid array (BGA) package

The development of the grid array design provides many benefits to Integrated Circuit (IC) as well as the electronic packaging industry. Some of the advantages of BGAs include [12]:

1. BGA dramatically increases I/O capabilities without decreasing the lead pitch. In other words, by applying ball grid array design, components can be smaller in size with the same connections than other package designs;

2. BGA improves yield and manufacturability as the solder balls are more robust than fine pitch leads. Also, it provides a better level of solderability with wider spaces between connections;

3. BGA improves electrical performance given the interconnections are shorter;

4. BGA is more firm and easier to handle during hand-assembly;

However, some reliability concerns come up while further investigating the properties of BGA components. BGA components tend to fail easily when exposed to thermal or mechanical harsh environment given the mismatch of Coefficient of Thermal Expansion (CTE) between the PCB pad and the BGA component. Also, inspection of the BGA can be very difficult because the BGA has been soldered onto the PCB with solder joints underneath.

Several types of BGA components exist in the market, which can be roughly organized into four basic families based on the material or technology that applied on fabricating them [13]:

1). Plastic BGA (PBGA): can be either 2 or 4 layers of FR-4 substrates, with organic materials, with a variety of BGA pitch sizes and components body sizes.

2). Ceramic BGA (CBGA): uses a multi-layer ceramic as substrate. Given the CTE of ceramic is close to the that of the silicon used for the micro-processor, this design improves the reliability on component level since the mismatch of CTE often leads to stress.

3). Tape BGA (TBGA): based on a flexible polyimide film (tape) with copper metallization on both sides. The back of the chip is designed to directly attach to a thermal conductive adhesive to provide an effective transport of heat to the metal cover or heatsink. This design allows a higher degree of power dissipation than plastic package.

4). Super BGA (SBGA): similar to TBGA, a metal heatsink is attach to the back side of the chip to dissipate extra heat.

2.1.4 Next generation of BGA

As Wolter et.al stated in 2012 [14], as the portable electronic market grows, the need for low cost, small size and low power has driven the development of thin and small plastic packages, chip on board and direct chip attach technologies as well as fine-line substrates. Advanced technologies like system on chip (SoC) and system in package (SiP) are likely to achieve more functionality with smaller size and less power consumption. Figure 2.4 demonstrates a schematic design of system-in-package (SiP).

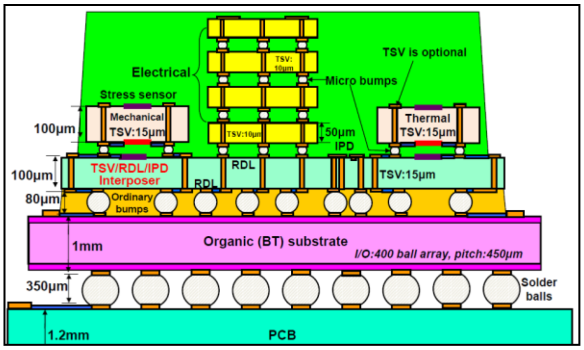

Figure 2.4 Cross-section view of system-in-package (SiP) using through silicon via (TSV)

Moreover, as stated by Elshabini et. al, “In the near future, electronic packaging will be involved into medical implantable devices to address certain human physical needs, enhance bodily functions and enable remote diagnostics” [15]. Micro or nanoscale packaging will replace most of the current packaging due to the complicity of the device functions and operating environment.

2.2 Printed Circuit Board for Electronic Packaging

Generally, a PCB mainly consists of two parts: laminate substrate and metal traces. Substrate serves as the foundation upon which electronic components are deposited, while the built-in metal traces provide the electrical interconnections between those components. PCBs can be single-sided, double-sided or multi-layers. Electrical components on each side are connected through vias. Vias are drilled holes through the substrates at appropriate locations where conductive material are plated inside the hole. Components on a PCB are electrically connected to the circuits by either through hole mount technology (THMT) or surface mount technology (SMT).

2.2.1 Substrate

Substrates play a vital role in ensuring the electrical, thermal, and mechanical reliability of electronic assemblies. It not only provides mechanical support for component, but also offers electrical insulation between conductive units. The most important material properties are the PCB’s linear Coefficient of Thermal Expansion (CTE) when selecting substrate materials. Basically, the CTE of substrate should be similar to the CTE of component, to minimize the stress between each other (reason will be discussed in section 2.4.2: Shear). Other important factors to be considered include, cost, temperature resistance, thermal conductivity. etc.

Substrates can be roughly classified into 6 major types, each working for specific applications [3, 16]:

1). Glass epoxy fiber substrate: consists of epoxy (resin) and glass fiber (base), and it is the most convenient option for both commercial and military use. Its advantages include: price, stronger in strength and more resistant to crack. FR-4 laminate is the market’s favorite [16].

2). Ceramic substrate: has a high thermal conductivity and a low CTE. The applications of ceramic substrates are limited by the demand of rigid, high-temperature or high-frequency situations due to its relatively higher price compares to glass epoxy material. The unique properties of ceramic give designer more options to create products that can’t be fabricated using conventional organic laminate technologies.

Other substrates options include porcelainized steel substrates, constraining core substrates, low CTE metal core substrate, graphite epoxy constraining core substrate, and compliant layer substrate.

2.2.2 Solder Mask

Solder mask is a thin layer of polymer that is applied to the copper traces of a PCB to prevent the PCB from being oxidized and protect the formation of “bridging” from closely spaced solder pads. There are two solder mask design methods: solder mask defined (SMD) and non-solder mask defined (NSMD). Figure 2.5 shows differences between NSMD versus SMD.

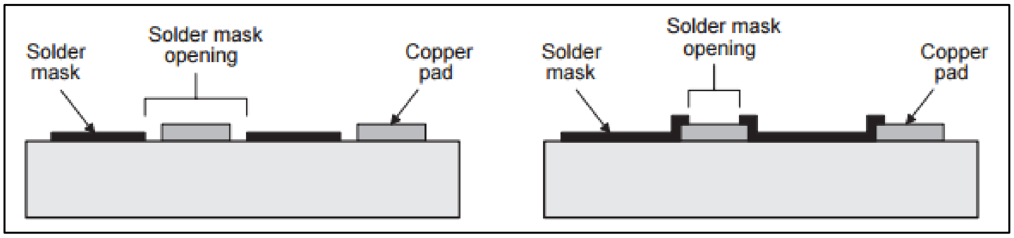

Figure 2.5 Cross-section view of NSMD vs. SMD

For the SMD pads, the solder mask opening is smaller than the copper pad, which shrinks the size of copper pad that components are soldered on. As shown on the right side of figure 2.5, a portion of copper pad is covered underneath, which protects the pads from lifting off during thermal or mechanical stress. For non-solder mask defined (NSMD) pads, the solder mask is printed carefully around the pad, intentionally leaving a gap between solder mask and copper pad as shown in the left side of Figure 2.5. In this way, given the entire pad is bare, solder can connect to the entire pad instead of partly covered by solder mask, which is believed to have higher resistance to thermal-mechanical fatigue based on the stronger bond of the interconnections, but opens up the potential for pads lifting off during thermal or mechanical stress.

2.2.3 Surface Finish

Since solder mask can only cover most of the copper traces, copper pads on PCB are still exposed in the air unprotected, which may also lead to a reliability issue. Therefore, surface finish is applied to protect the remaining copper pads, temporarily preventing the copper pads from further corrosion and oxidation prior to assembly. Moreover, surface finishes also serve as a foundation of connection to electronic devices, enhancing the assembly process and promoting more reliable solder joints for long-term performance.

There are a variety of surface finishes available in the market, with each having its own unique characteristics and processing challenges including:

- Hot Air Solder Level (HASL): the process consists of immersing the circuit boards into a molten pot of tin/lead (SnPb) solution and then removing the excessive solder by blowing hot air across the surface of the board, leaving only a layer of coating on the copper pad surface. HASL was the predominate surface finish type in the industry because of its relatively lower cost and better solderability. However, uneven surface and lead content are its biggest disadvantages.
- Organic Solderability Preservative (OSP): is organic-based coating with a thin carbon-based layer that selectively ties to copper and protects the copper pad from oxidation and corrosion. Unlike the other surface finishes, OSP is the only one that is not metal-based and environment friendly. It provides a lead-free and coplanar surface. However, it is less robust compared to HASL and can be sensitive while being handled.

- Immersion Silver (ImAg): is a stable surface finish with a moderate shelf-life, excellent solderability and relatively easier process control. However, it is sensitive to contaminators and needs to be packaged as soon as possible once finished.
- Electroless Nickel and Immersion Gold (ENIG): ENIG is a two-layer metallic coating with gold layer over nickel layer. Nickel serves as both a barrier to the copper and a surface to where soldering occurs, while the gold layer is covered on top of nickel to protect nickel from oxidation during storage. ENIG provides excellent solderability, wettability and flat surface. The downside of ENIG is its expensive cost and the "black pad syndrome", which refers to an accumulation of phosphorus between gold and nickel layers that results to a fracture surfaces and faulty connection.

2.3 Lead-free Solder Alloys

From the 1960s to the early 1990s, eutectic 63Sn-37Pb was the most widely used solder alloy in the electronic industry. The use of Sn-Pb solder is due to its relatively low melting point, good wetting behavior, good electrical conductivity, low cost, and is widely available. However, Environmental Protection Agency (EPA) has concluded lead (Pb) as one of the top 17 chemicals posing the greatest threat to human life and environment. Lead, as a heavy metal toxin, can damage the kidney, blood, and central nervous system of human body. International laws have been proposed to expand control laws to limit or ban the use of Pb in manufactured electronics products. The most aggressive and well-known efforts are the European Union's Waste in Electrical and Electronic Equipment (WEEE) and Restriction of Hazardous Substances (RoHS). Being considered and debated for years together, they announced that as of 1 July, 2006, lead must be replaced in electronic equipment. Over the years, industry has tried to find a suitable replacement material for SnPb solder materials. The suitable material must satisfy most of the important properties for a suitable candidate like mechanical load, melting temperature and other important characteristics like cost, toxicity and availability etc.

Researchers have developed more than 70 types of lead-free solder alloy compositions to attempt to replace the SnPb solder alloy. Many of them are ternaries or quaternaries [17] instead of binary. However, no new alloy has been found which could be a “drop in” replacement for the eutectic SnPb alloy. Most of the lead-free solder alloys are tin (Sn) -based, as shown in Figure 2.6, given tin has shown some outstanding properties including: 1. Relatively lower melting point compared to the other candidates like copper (Cu) or silver (Ag); 2. Excellent wettability that can be soldered on any substrate easily. 3. Relatively lower cost and better availability. However, pure tin also has potential reliability issues, for example, tin pest and tin whisker. Tin pest, which refers to the autocatalytic transformation of element of tin at low temperature, can cause of the deterioration of service life of tin products. Longer tin whiskers may cause electrical shorts in PCBs. Therefore, other elements like Cu, Ag, In, Sb, etc. are added into tin to strengthen the properties of new solder alloys.

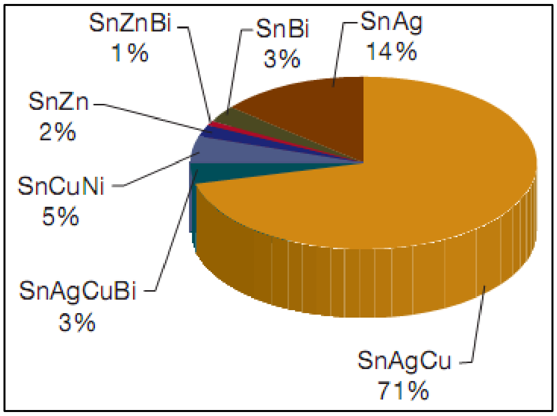

Figure 2.6 Lead-free solder market share about reflow solder

2.3.1 SnAgCu Solder Alloys

Among many types of lead-free solder alloys, Sn-Ag-Cu (SAC) solder alloys are the most prevailing and popular lead-free solder materials and are regarded as the best alternatives to eutectic Sn-Pb solder alloys. Silver and copper are selected based that neither is oxidation or corrosion sensitive. Also, the addition of silver and copper to tin is shown to increase several mechanical properties of this alloy. SAC family solder alloys are very popular because they are near eutectic, with relatively lower melting temperature, adequate thermal fatigue resistance, solderability, strength and wettability. The most widely accepted SAC solder alloys have the composition in the eutectic region, generally with 3-4 % Ag, 0.5-1 % Cu, and the remaining content is Sn. A variety of SAC alloys have been presented by solder companies and research groups including: SAC305 (96.5Sn-3.0Ag-0.5Cu); SAC105 (98.5Sn-1.0Ag-0.5Cu); SAC387 (95.5Sn-3.8Ag-0.7Cu); SAC396 (95.5Sn-5.5Ag-0.6Cu) etc., with each having used for different applications.

Despite the fact the SAC solder alloy family has shown some outstanding properties, they are still questionable in some areas compared to Sn-Pb solder alloys including melting temperature, unit cost, and some reliability concerns (e.g. Sn-Pb components shows better board level reliability in drop test than SAC305).

2.3.2 Doping Solder Alloys

Because of the disadvantages shown in the SAC family compared to Sn-Pb solder alloys, research is focusing on developing the next generation of solder alloys: doped solder alloys. Solder doping refers to as adding minor dopants (generally rare earth element such as Ni, Bi, In, Mg, Co etc. [18]) to the traditional eutectic or non-eutectic solder alloy to form another new solder alloy. The attraction of solder doping is having smaller volume of elements (normally less than 1%) that can have a large impact on enhancing the properties of solder alloy, with fewer drawbacks. Recent studies have shown that solder alloys with minor dopants can refine the microstructure, boost strength and ductility, change failure mode, improve creep behavior, and lower melting temperature [19]. Solder doping will be further discussed in section 3.3.

2.4 Mechanical Properties of Solder Materials

The strength of a material is its ability to withstand an applied load without failure or plastic deformation. When applying an external load on a material, it will induce internal forces within the material when the load expresses on a unit base, which causes stress. When stresses act on the material, deformation of the material results in various manners. The deformation of the material on a unit basis is called strain. With a complete description of loadings and geometry of the material, the state of stresses and strains can be calculated. The material’s strength, deformation, and stability are determined based on the stress and strain behaviors. Therefore, to calculate the mechanical properties of a material, stresses and strains that developed within the material must be studied first.

Stress is expressed by the force (F in N) divided by an area (A in m^2) that it acts on, the relation is shown in Equation 2.1:

$$\sigma = \frac{F}{A} \tag{2.1}$$

Strain is expressed as the ratio of total deformation to the initial dimension of the material body that forces are acting on. Strain formula is shown in Equation 2.2:

$$\varepsilon = \frac{l-L}{L} \tag{2.2}$$

where L is the original length and l is the final length after deformation.

Solder joints inside an electronic device are subjected to mechanical stresses and strains when the device is under operation. To select an ideal solder material, wettability or chemical properties and mechanical properties of solder joints must be tested to make sure the strength of this solder material is enough to provide adequate mechanical support and connection under various realistic operational conditions.

Mechanical properties of solder materials include tensile strength, shear strength, creep strength, and fatigue strength.

2.4.1 Tensile Property

Tensile property (strength) is the capacity of the material to withstand loads without deformation or break. The tensile property of a material is determined by the tensile test, where results are plotted in a form of a stress-strain diagram, shown in Figure 2.7. Although solder joints are barely under pure tensile loadings in realistic operational condition, tensile properties still are essential parts of indicators for design purpose.

The engineering stress and engineering strain in a tensile test can be expressed as:

$$\sigma_e = \frac{F}{A_0} \tag{2.3}$$

$$\varepsilon_e = \frac{L_f - L_0}{L_0} \tag{2.4}$$

Where F the load applied, A_0 is the original cross-sectional area, L_f is the final length (elongated length) and L_0 is the original length.

For ductile material, it will first display linear elastic behavior under tensile stress, up to point 3 in Figure 2.7. Within the elastic region, the engineering strain obeying Hooke’s law [20]:

$$\sigma = E * \varepsilon \tag{2.5}$$

where E is defined as the effective elastic modulus (Young's modulus) and can be calculated as the slope of the elastic part of stress-strain curve.

As more stress is applied, the elastic behavior of this material will turn into a non-linear region, up to point 2 (yield strength). By point 2, deformation from tensile stress can still be completely recoverable, meaning, when withdrawing load, all the elongating part will return to its original point. However, beyond the elastic region, for ductile material, strain hardening goes on and plastic deformation is taking over, which means material cannot completely return to its original form when unloaded. Specimens subjected to plastic deformation will simultaneously elongate and decrease in diameter until crack (point 4) happens. The ultimate tensile stress (UTS) (point 1) is defined as the maximum load divided by the initial cross-sectional area of the specimen. It indicates the maximal stress a material can withhold before failure.

In the tensile tests, material properties such as effective elastic modulus (Young's modulus), yield strength and UTS are normally characterized.

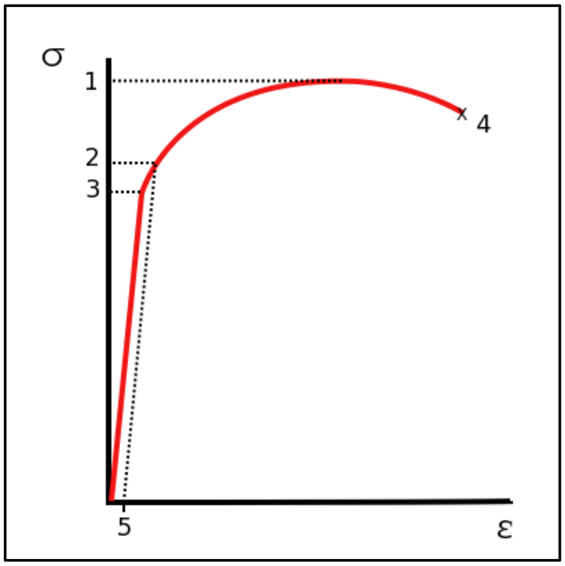

Figure 2.7 Typical tensile stress-strain response for ductile material

2.4.2 Shear Property

Given the mismatch of CTE between component and substrate, when under elevated temperature, the substrate (with relatively higher CTE) expands more than the component (with relatively lower CTE), resulting the solder joints being subjected to shear strain, as shown in Figure 2.8.

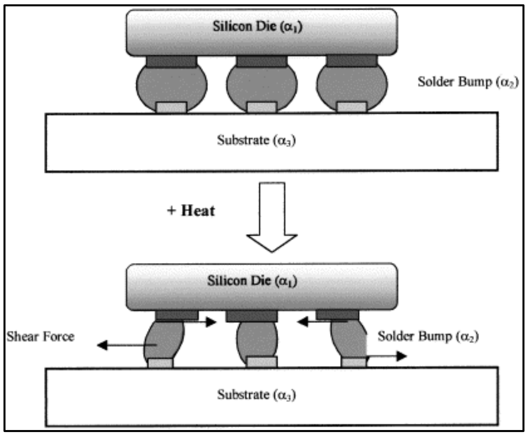

Figure 2.8 Solder Joints subjected to shear strain due to CTE mismatch

Stress-strain curve under shear stress is shown in Figure 2.9. When material is subjected to shear loading, it will first behave in a linear-elastic manner until one point (τ_{ys}), then strain hardening is taking over to the ultimate shear stress τ_{uts} where shear stress reaches its maximum. Then the shear strength will start to decline until the material fails at γ_f.

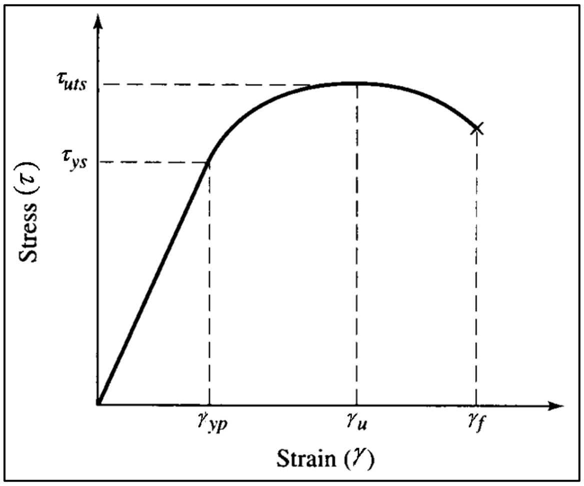

Figure 2.9 Typical shear stress-strain response for ductile materials

Shear stress τ and strain γ can be obtained by:

$$\tau = \frac{F}{A_0} \tag{2.6}$$

$$\gamma = \frac{\Delta x}{h} \tag{2.7}$$

where F is the applied shear force, A_0 is the cross-sectional area, Δx is the transverse displacement and h is the initial length.

$$\mathrm{T} = \mathrm{G} * \gamma \tag{2.8}$$

Shear strain is determined by shear modulus G (calculated in equation 2.8), measured as the slope of the linear portion on the shear stress-strain response. G can also be calculated with elastic modulus E and Poisson's ratio ν if no experimental data are available, as shown in equation 2.9:

$$\mathrm{G} = \frac{E}{2(1+\nu)} \tag{2.9}$$

2.4.3 Creep Property

Creep refers to the time-dependent permanent deformation when a material has to support a load for a long period of time under constant temperature. Since solder joints are often used under the environment where stress levels are below the solder yield strength, plastic strain sometimes doesn't play a critical role on the solder joint fatigue. However, under hours of loading, solder joints experience modest levels of strain due to creep effect in response to applied elastic forces from strain relief elements [21]. Therefore, creep is often viewed as one of the major failure modes of solder joints in the microelectronic packaging field, especially under an elevated temperature environment [11]. Stress level and temperature normally plays critical role in the development of creep.

For most of the materials, creep typically develops within the material in three stages includes primary creep, steady state creep, and tertiary creep with time. A creep curve under consistent stress level and temperature is shown in Figure 2.10.

The creep response starts with an instantaneous strain by the time when constant load is applied. This is the beginning of creep deformation. Following this, the initial strain begins to rise rapidly in a short period of time which is defined as the primary creep. The increase rate tends to be gently due to the strain hardening, where the creep development enters the second stages. In the second stage (steady-state creep), the creep strain rate is relatively stable because of the dynamic balance between strain hardening and recovery. The relatively constant creep strain rate is defined as the steady state creep rate, which is the linear slope of steady-state creep curve. Steady state creep rate is calculated as: $\dot{\varepsilon} = d\varepsilon/dt$ which has been used as one of the key mechanical properties to predict the material reliability. In the last stage, creep rate increases rapidly again given the metallurgical instabilities of the material, and finally, leads to the rupture.

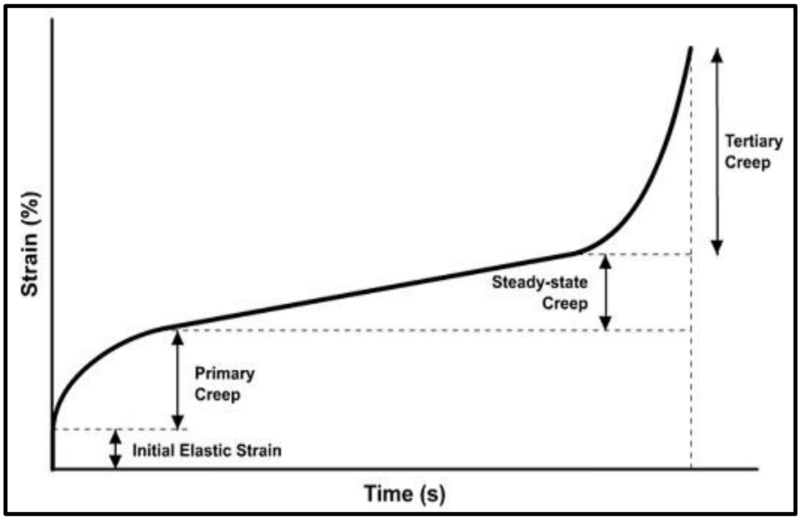

Figure 2.10 Creep curve under constant stress and temperature

2.4.4 Fatigue Property

Solder fatigue refers to as the mechanical degradation of solder material because of the deformation under cyclic loading condition. Fatigue damage can be extremely dangerous given the fact that, when fatigue failure happens, the design strength of solder material is not met yet. With small indiscernible internal cracks, it makes the fatigue failure very hard to identify and predict. Fatigue is responsible for a large percentage of failure of engineering materials.

Fatigue failure of solder joint results from 1) Initiation of small micro-cracks, accumulation of micro-cracks and initiation of major crack; 2) Propagation of the major crack; and 3) Ultimate failure, where cracks eventually reach critical dimension and propagates very quickly, finally, leading to the fatigue failure of the solder joints. Defects and irregularities in the microstructure normally will accelerate this process given those may serve as the crack initiation site.

Fatigue can be categorized as high cycle fatigue and low cycle fatigue based on the levels of stress amplitudes that cause the solder fatigue. Fatigue that caused by low stress, as it occurs at relatively large cycle numbers ($N_f > 10^5$), is defined as high cycle fatigue; for fatigue that caused by relatively higher stress, which leads to a lower cycle numbers ($N_f < 10^3$), is defined as low cycle fatigue.

Fatigue life (N_f) of solder joints is defined as the numbers of cycles that leads to the fatigue failure of solder materials at specific stress level. It is dependent on several factors such as aging temperature, aging length, load amplitude, geometry and size of specimen, and surface finish for the PCB, etc.

For low cycle fatigue, tests normally are represented in a S-N diagram [22], shown in Figure 2.11. Number of cycles to failure (N) is plotted versus the stress amplitude (S) so that several parameters related to this material can be found in this curve, such as endurance limit or fatigue strength level. Several modules have been developed to predict the number of cycles to failure for solder joints under different testing conditions. In those modules, fatigue life is correlated to various parameters, such as stress and strain level, or hysteresis loop (work dissipation). Some of them are very famous and widely applied, for example the Coffin-Manson model, or Morrow's energy model. Detail reviews of models that predict solder joint fatigue life will be shown in chapter 3.

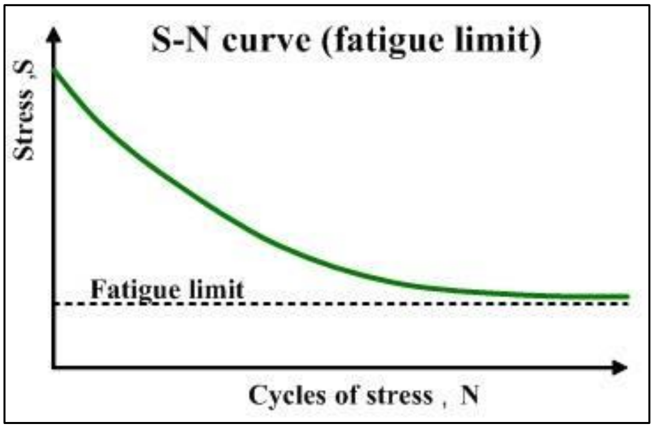

Figure 2.11 S-N curve

Fatigue test can be categorized into mechanical fatigue test and thermomechanical fatigue test:

2.4.4.1 Mechanical Fatigue Test

Mechanical fatigue test is accomplished by applying a sinusoidal stress of constant amplitude to the specimen until the fatigue failure of the specimen.

2.4.4.2 Thermomechanical Fatigue (TMF)

Thermomechanical fatigue (TMF) test is designed to simulate real-world service conditions of electronic components with power generation. Basically, TMF is the combination of both a cyclic mechanical loading, which leads to the fatigue of a material, with a fluctuating temperature to predict the complex effects of simultaneous thermal and mechanical strains. Many researchers prefer TMF test over mechanical fatigue test based on that fact that TMF can be more damaging when subjected to heat. Structure develop thermal gradients as they expanded and expansion of stress is often constrained by the nearby cooler materials. In this way, thermal strain is converted into mechanical strain which aggravates the fatigue damage in the structure. With the absence of thermal effect in the dynamic of fatigue, we cannot compensate for this missing effect without knowing how strain and temperature interacts [23].

Normally, TMF loading is described to be in-phase (IP) or out-of-phase (OP) [24]. Figure 2.12 shows a schematic illustration of the stress-strain interaction under two loading conditions. In IP, the maximal temperature and strain occurs at the same time. However, for OP, the material experiences compression at the highest temperature and tension at the lower temperature. It turns out OP is more likely to cause oxidation damage.

TMF can be used to better evaluate the life of materials and engineering components that are used in safety critical, higher temperature applications.

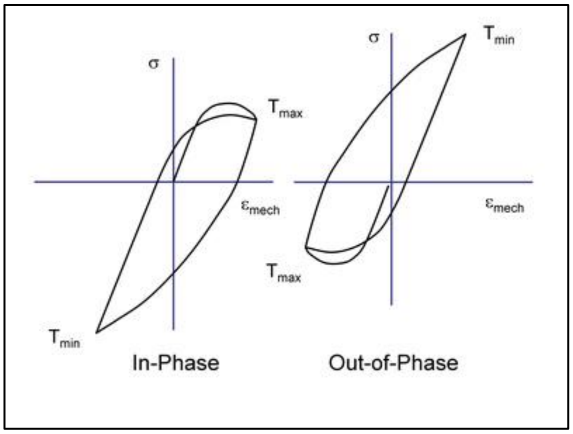

Figure 2.12 Loading and temperature phases

2.5 Reliability Testing for Electronic Packaging

Reliability tests are conducted to predict the reliability or quality of a product during the normal operational conditions. The aim of the test is to select stress factors that are heavily correlated with the design operation conditions, find out potential design errors, and assess product reliability issues in a shorter period of time.

Accelerated Life Testing (ALT) is often applied on a product to "accelerate" the exposure of potential reliability issues [25]. ALT is the process of testing a product in a condition (stress, temperature, strain, vibration etc.) more than its normal operating condition in order to generate potential failures in a shorter period of time without introducing unrealistic failure mechanisms. Engineers can then make reasonable predictions based on the results of accelerated testing about the reliability of the product.

Various types of reliability tests have been developed to be used on electronic components:

2.5.1 Thermal Cycling Test

Thermal cycling testing is the process of cycling products through two temperature extremes, especially between 2 relatively high rates of changes. This test is used to simulate the effect of product that are exposed to an environment with variable temperatures because of the repeatedly tuned on and off, or the results of cyclic environment changes. When being exposed to repeated temperature changes, electronic products will experience cyclic strain, thermal fatigue and finally lead to fatigue failure. To accelerate the thermal cycling process, products normally are cycled in high and low temperature that exceed its normal operational temperatures. Standards such as JEDEC/IPC are normally used for compliance testing since thermally cycling tests generates highly repeatable test results. JEDEC is the acronym of Joint Electron Device Engineering Council, which is the global leader in developing open standards and publications for the microelectronic industry. For example, JESD22-A104E standard provides a standardized testing method for determining solder state devices capability to withstand extreme temperature cycling. Similar to JEDEC, IPC, the Association Connecting Electronics Industries, is a trade association that aims bring all the players in the electronics manufacturing industry together: designers, board manufactures, assembly companies, and original equipment manufacturers. IPC standards are used by the electronics manufacturing industry, standard such as IPC-A-610, acceptability of electronic assemblies, is used worldwide by electronic manufacturing companies to train their employees.

Figure 2.13 is an example of thermal cycling profile. During the thermal cycling test, the product will cycle through ramp up, upper dwell, ramp down, and lower dwell stages in one chamber cell. Parameters like dwell temperature, dwell time and ramp rates are found to have larger influence on the product.

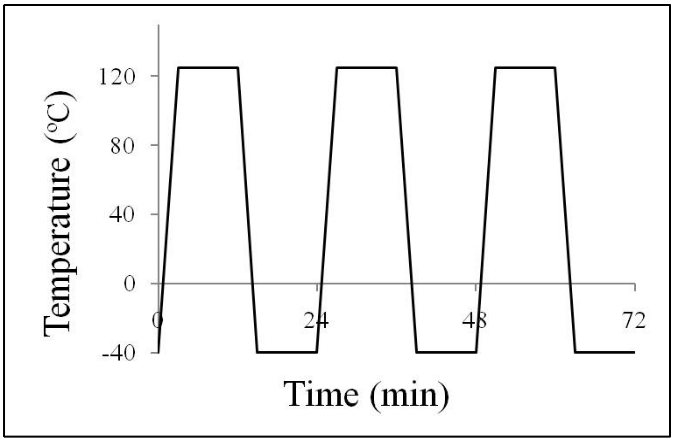

Figure 2.13 Thermal cycling profile example

2.5.2 Air-to-air Thermal Shock Test

Air-to-air thermal shock test evaluates the reliability of test samples by repeatedly applying alternating high and low temperatures to them. Variable temperatures cause expansion and contraction, and the mismatch of CTE of parts made of different bounded materials generates stress between each part. Applying these stresses repeatedly will lead to cracks, fatigue failure of materials and further, rupture at lower strength then the static strength.

Figure 2.14 shows an example of air-to-air thermal shock chamber. For a two-chamber design, one chamber is kept hot, and another is kept cold. A carriage is used to move testing samples between 2 chambers within few seconds.

Figure 2.14 Example of air-to-air thermal shock chamber

2.5.3 Liquid-to-liquid Thermal Shock Test

Liquid-to-liquid shock test, however, applies thermal shocks to testing samples by alternately immersing them in a high- and low- temperature liquid medium. Since liquid is used as medium, this type of test will perform a sharper temperature variation rate than air-to-air thermal shocking test. The liquid medium used in the test is an inert liquid that is highly electrical resistance and low surface tension that are specifically developed for thermal shock test.

Figure 2.15 displays the schematic design for the liquid-to-liquid shock testing. A high-temperature and low-temperature chamber are placed beside each other. An elevated mechanism places the specimen basket in each chamber alternatively, exposing it to thermal shock.

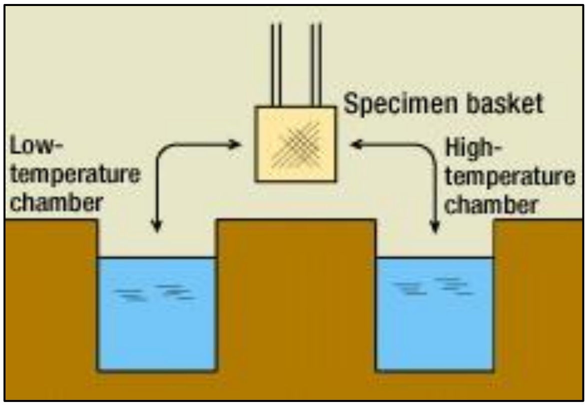

Figure 2.15 Schematic design of liquid-to-liquid shocking equipment

2.5.4 Low Cycle Fatigue (LCF) Test

Low Cycle Fatigue (LCF) testing refers to as cycling the specimen under strain control with the load as a dependent variable. LCF is characterized by high amplitude, low frequency plastic strains as shown in Figure 2.16. It is designed to replicate the high-strain condition normally develops in a region of a local discontinuity in a component where fatigue damage concentrated. LCF failure is shown as the predominant failure mode when components are under elevated temperature environment. Plastic strain, induces by the CTE mismatch of component and substrate, was used as a chief fatigue parameter to predict the fatigue life of a component in a LCF test.

The typical results of low cycle fatigue test include fatigue life and hysteresis loop. Fatigue life is defined as the number of cycles until the fatigue failure of components. Hysteresis loop shown in Figure 2.17 is the stress-strain curve during cyclic fatigue test. A hysteresis loop is used to represent the stable or steady-state cyclic stress-strain behavior of the material. In Figure 2.17, the area enclose in the loop represents the overall energy dissipated in one cycle. $\Delta\sigma$ represents true stress range, $\Delta\varepsilon_p$ represents true plastic strain range.

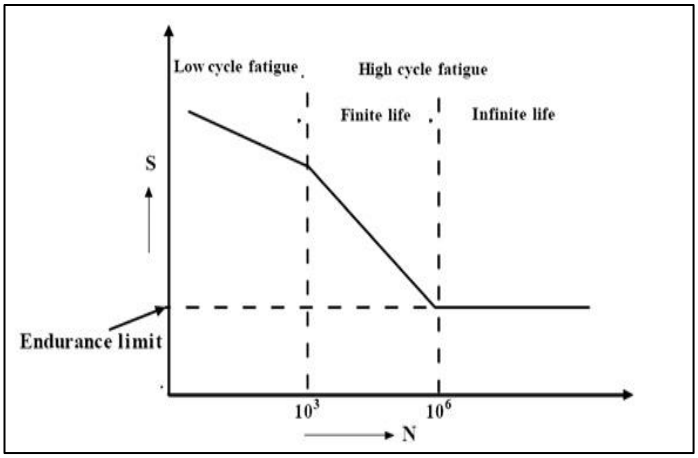

Figure 2.16 Low and high cycle fatigue

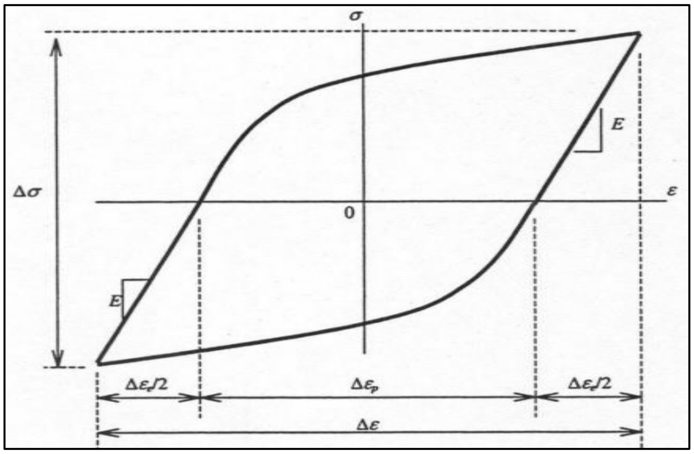

Figure 2.17 Cyclic stress-strain behavior in a fatigue test

2.5.5 Vibration Test

Under the normal operating conditions, electronic device can be subjected to various forms of vibrations over wide frequency ranges and acceleration levels. Vibrations induce displacement and usually displacement between electronic parts cause stresses. Vibration-induced stresses can then lead to the fatigue failure of electronic assemblies. The vibration testing is accomplished by introducing a forcing function into the Device Under Test (DUT) to examine the responses of this device to a defined vibration condition, and further estimate the reliability of this device under this given vibration condition. The most common types of vibration testing under laboratory condition are Sinusoidal wave and random wave vibration testing. For Sinusoidal wave testing, vibration can be applied with a constant frequency, or varied frequencies with upper and lower frequencies set. However, random wave testing is the simultaneously application of multiple sets of vibrations of specified frequency ranges. Random wave vibration is viewed as more closely simulation of a real-world environment.

Vibration testing systems most often are servo-hydraulic shakers, depending on the frequency range and displacement required. Servo-hydraulic shakers normally used for relatively low frequencies, while electrodynamic used for higher frequencies.

2.5.6 Drop Test

Drop test can be vitally important given most of the portable electronic devices such as mobile devices and personal laptops are prone to be dropped. Impacts of drops need to be carefully examined before further improving the drop resistance characteristics.

A drop test is used to assess the fragility of a product and simulate the shocks the product may encounter when subjected to repeatable drops. Two drop procedures are commonly used: 1) Free fall drop test, which means dropping the product in various conditions (heights, orientations etc.) based on its own weight; 2) Impact test, which involves the use of a steel striking element dropped vertically or by pendulum motion onto the unit.

2.6 Statistical Reliability Models

Generally, the reliability of a system is defined as the probability that a system will perform the designed function for a specific performance period under a given set of operating conditions. The performance time can be a function of cycles, distance or time [26].

2.6.1 Reliability Functions

To express the relationship between system reliability R and performance time t mathematically, we defined the continuous random variable (T) to be the time to failure of the system. The system reliability can be expressed as

$$\mathrm{R(t)} = \Pr\{T \geq t\} \tag{2.10}$$

For a given value of t, R(t) is the probability that the time to failure is greater than or equal to t.

$$\mathrm{F(t)} = 1 - \mathrm{R(t)} = Pr\{T < t\} \tag{2.11}$$

F(t) is the probability that a failure occurs before t.

$$f(t) = dF(t)/dt = -\,dR(t)/dt \tag{2.12}$$

Then, we define R(t) as the reliability function, and F(t) as the cumulative distribution function (CDF) of the failure distribution. $f(t)$ is the probability density function (PDF) of the failure distribution, which describes the shape of the failure distribution.

Another characterization of the system reliability can be expressed as hazard rate function, or instantaneous rate of occurrence of the event, defined as:

$$\lambda(\mathrm{t}) = \lim_{dt \to o} Pr\{t \leq T < t + dt | T \geq t\}/dt \tag{2.13}$$

The conditional probability of the hazard function can be written as the ratio of the joint probability that T is in the interval $t \leq T < t + dt$ and $T \geq t$ to the probability of the condition $T \geq t$. The former is $f(t)$ for small dt, and the latter is R(t). Therefore, the hazard rate function can also be expressed as:

$$\lambda(\mathrm{t}) = f(t)/R(t) \tag{2.14}$$

The hazard rate function λ(t) provides an alternative way of describing failure distribution, where failure rates can be further categorized as increasing failure rate (IFR), decreasing failure rate (DFR), and constant failure rate (CFR). A hazard rate function can uniquely determine a reliability function.

An important form of hazard rate is shown in Figure 2.18. It is commonly referring to as bathtub curve because of its shape [27]. The left-hand side of Figure 2.18 is a high but decreasing failure rates, which refers to as an early failure or infant mortality. It is primarily induced by the defects or weakness of a product and it can be reduced by several reliability tests such as burn-in test or screening test. The middle part of the curve is a nearly constant failure rate representing the useful life. The right-hand side of the curve is an increasing failure rate because of the wear-out of the product.

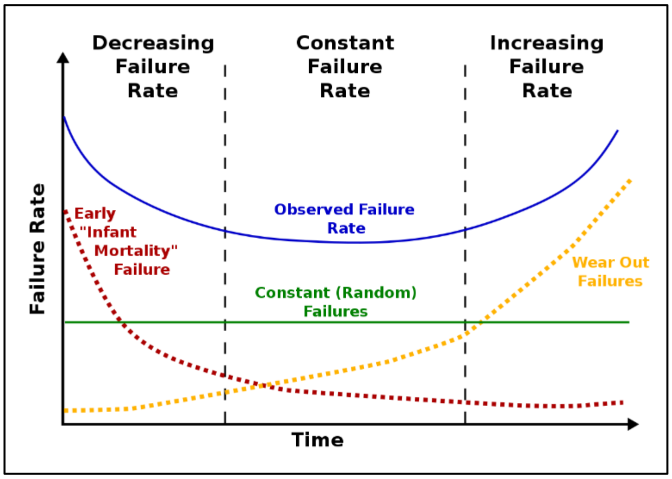

Figure 2.18 A bathtub curve of failure rate

2.6.2 Reliability Distribution

Various reliability life distributions are available to describe the failure rates over time, each has its own application scope. The exponential distribution is one of the easiest distributions to analyze. Failures due to complete randomness will follow this distribution. A Weibull distribution is the most extensively used distribution given its ability to model varieties of failure rates. The normal distribution is implemented to model increasing failure rate. The lognormal distribution fits well with the failure distribution when the failure is the result multiplicative degradation, such as crack propagation. For specific cases, a gamma or Poisson distribution can also be applied [26].

2.6.2.1 Weibull Distribution

The Weibull distribution analysis is widely used to evaluate the experimental data from accelerated life testing. The primary advantage of the Weibull analysis is the ability to assume the characteristics of many types of distributions, which makes it flexible enough to model a variety of data sets. Another advantage of the Weibull analysis is the ability to offer reasonably accurate failure analysis and forecasts with small samples [28]. The probability density function (PDF) of the Weibull distribution is expressed as:

$$f(t) = \frac{\beta}{\theta}\left(\frac{t}{\theta}\right)^{\beta-1} e^{-(t/\theta)^{\beta}} \tag{2.15}$$

where Beta (β) is the shape parameter. For $\beta < 1$, the PDF is similar to the exponential distribution; for $\beta > 3$, the PDF is likely to be symmetric, similar to the normal distribution; for $1 < \beta < 3$, the PDF is skewed. When $\beta = 1$, the failure rate is constant, and the distribution is identical to exponential distribution. Figure 2.19 shows the effect shape parameters on the Weibull distribution probability density function.

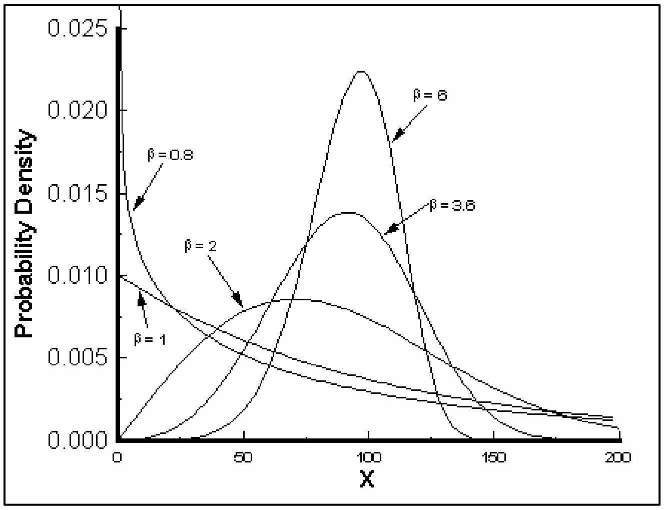

Figure 2.19 The effect shape parameters on the Weibull distribution probability density function

Theta (θ) is the scale parameter, it is also called the characteristic life, which representing the 63.2% of the population are expected to fail. The theta parameter of the Weibull distribution is often used to predict the fatigue life in a fatigue test.

For a Weibull distribution with only β and θ parameters, it is called a two-parameter Weibull distribution. When there is a minimum life t_0 ($T > t_0$) exiting, a three-parameter Weibull distribution ($\beta, \theta \ and \ t_0$) will be the best fit. By applying the three-parameter Weibull distribution, we assume that no failures will occur before the minimum life t_0.

2.6.2.2 Normal Distribution

Normal distribution is often applied to model fatigue and wear-out phenomena. Manufacturing process and nature occurrences also frequently create this type of distribution, if the occurrence is random distributed. A normal distribution is a unimodal bell curve which spreads symmetrically around the central location. A normal distribution exhibits the "3σ" rule: 68.3% of the population is contained within 1 standard deviation from the mean; 95.4% of the population is contained within 2 standard deviation from the mean; 99.7% of the population is contained within 3 standard deviation from the mean.

The PDF formula for the normal distribution is shown in equation 2.16:

$$f(t) = \frac{1}{\sqrt{2\pi}\sigma} exp\left[-\frac{1}{2}\frac{(t-\mu)^2}{\sigma^2}\right] \qquad -\infty < t < +\infty \tag{2.16}$$

Where μ and σ^2 are the mean and variance of the distribution, respectively.

2.6.2.3 Lognormal Distribution

Random variables whose natural logarithms are normally distributed and are said to fit the lognormal distribution. Lognormal distribution fits well with the failure distribution if the failure is the accumulation of many small percentage changes, such as the fatigue degradation based on the crack propagation under cyclic fatigue test. Moreover, electronic corrosion, and electro-migration also fall into this distribution.

The PDF function for lognormal distribution is expressed in equation 2.17:

$$f(t) = \frac{1}{\sqrt{2\pi}t\sigma_n} exp\left[-\frac{(lnt-\mu_n)^2}{2\sigma_n^2}\right] \tag{2.17}$$

Where μ_n and σ_n are the mean and standard deviation of lnt.

Chapter 3 Literature Review

3.1 Introduction

Reliability is defined as the ability of system or component to function under stated conditions for a specific period of time. In terms of SMT, it can be divided to three levels of reliabilities: wafer level, chip level and board level, corresponding to the hierarchy of interconnection levels mentioned in the previous chapter. In this study, we will mainly focus on the reliability of board level, which is known as the reliability of an interconnection. Several reliability tests are conducted (e.g. fatigue test, shear test) to evaluate the quality and reliability of solder interconnection after mounted a component onto a PCB [29]. Solder interconnections, often refers to as solder joints, are exposed to an environment of thermal-mechanical fatigue when subjected to cyclic temperature changes because of the CTE mismatch of soldered components and PCB, which can cause the fatigue failure of solder joints [30]. Fatigue is found to cause the microstructure evolution and deformation of solder joints which will reduce the reliability of solder joints. Meanwhile, studies have demonstrated that aging is universally detrimental to constitutive and failure behaviors of solder joints. Given solder joints in an electronic device during real service life will undergo continued aging, leading aging is one of the factors that limits the reliability of solder joints in real service life. The study of aging effects on different solder materials will: extend current database of mechanical behaviors of different solder alloys over time, provide valuable information on fatigue behaviors of solder joint at various working situation, and finally, put forward feasible solutions to improve the reliability of solder joints under real service conditions. However, numbers of constitutive models regarding the prediction of solder joints fatigue life under various testing conditions have been systematically reviewed.

3.2 Aging Effect on Solder Materials Mechanical Properties

Mechanical properties of solder materials are strongly influenced when exposed to isothermal aging conditions [8, 9, 31, 32]. Generally, we study the aging effects on solder mechanical behaviors in two major aging conditions: room temperature aging (25°C) and elevated temperature aging (75°C, 120°C, 150°C, 180°C etc.). Results showed that aging leads to a large degradation in tensile strength [32-35], shear strength [36-39], creep behaviors [34, 40, 41].

3.2.1 Room Temperature Aging Effect

Room temperature aging was found to have a significant effect on the solder material mechanical properties. Xiao et.al [32] conducted tensile tests for solder alloys for both room temperature (25°C) and elevated temperature under displacement control method. They reported that the tensile strength decreases by 25% under room temperature aging for both Sn-Pb and Sn-3.9Ag-0.6Cu solder alloys. Chuang et.al [9] reported a deterioration of tensile properties for 30-180 days in a 30°C environment for both Sn-9Zn and Sn-9Zn-0.5Al eutectic solder alloys.

Tsui et. al [42] demonstrated that shear strength for Sn-Pb eutectic solder ball keeps constant for the first 12 hours and drops by 10% after 3 days of room temperature aging. Lampe et.al [8] found the softening process varies for different solder joints under room temperature, but eventually takes 6 to 30 days to reach a stable state, which causes a reduction in shear strength and hardness by up to 20%. Coyle et.al [43] reported that both Sn-Pb eutectic solder joints and 62Sn-36Pb-2Ag solder joints undergo an aging softening process when being exposed to room temperature, which leads to an approximate 20% drop for both shear force and hardness. Miyazawa et.al [31] reported an aging softening phenomenon for Sn-Ag, Sn-Zn as well as Sn-PB solder alloys under room temperature aging, however, a slight aging hardness for Sn-Bi eutectic solder alloy was also observed. Li et.al [44] studied the room temperature effect on the shear strength for Sn-0.7Cu, Sn-3.5Ag, Sn-3.8Ag-0.7Cu and Sn-Pb eutectic solder bumps. They reported that shear strength decreases by 5-8% after 51 days of room temperature aging for lead-free solder bumps. A 10-15% degradation of fatigue life was reported by Chilton et.al for single 60Sn-40Pd SMD joints under room temperature aging [45].

A continuous decrease in yield stress and elongation was also observed with increased exposure time under room temperature. As discussed by Ma et.al [34], both ultimate tensile strength and yield strength are significantly reduced (up to 40% decreased) by aging under room temperature after 63 days for SAC305 and SAC405 solder joints. Su et. al studied the long-term (4 years) of room temperature aging on the fatigue behaviors of lead-free solder alloys. It turns out 4 years of room temperature aging leads to a significant decrease for the fatigue life of solder joints (up to 70% drop) and also leads to an increase of the hysteresis loop per cycle. Coyle et. al [43] also reported that the fracture modes of solder joints can be divided into ductile and brittle fracture. Brittle fracture is a low-energy phenomenon, while the ductility fracture needs more energy during the plastic deformation. With the effect of room temperature aging, the failure mode shifts from brittle failure on the earlier stage gradually to a totally ductile failure as the solder joints undergo an age-softening process [34].

3.2.2 Elevated Temperature Aging Effect

Xiao et. al [32] reported a decrease of 33% of tensile strength for 9 days under elevated temperature aging (180 °C). Ding et. al [33] investigated the influence of aging treatment on deformation behaviors of 96.5Sn3.5Ag solder alloys during in situ tensile tests, and results show aging introduces a quick softening effect on solder alloys under 120 hours of elevated temperature aging test. After studying ultimate tensile strength of SAC305 and SAC405, Ma et. al [34] concluded that reduction of ultimate tensile strength followed by a steady linear degradation in the first 20 days of elevated temperature aging. Motalab et. al [35] performed uniaxial tensile testing of SAC305 for 7 different sets of aging. The results show that the largest tensile strength degradation occurs at the first 20 days of aging, then the degradation rate is getting slower.

Chen et. al [37] compared the shear strength behaviors between SnPb and Sn3.5Ag solder bumps with 150°C aging for 1500 hours. It turns out a slight decrease is observed for both solder bumps, 8.9% drop for SnPb solder bumps and 5.3% drop for Sn3.5Ag. Kim et. al [39] observed a 5% of shear strength drop for the first 300 hours under 150°C testing, and almost no shear strength degradation afterwards. Anderson et. al [36] studied the shear strength behaviors for a set of SAC solder alloys. All solder joints are severely softened after 100 and 1000 hours of 150°C thermal aging condition. The results also show that after 1000 hours of elevated temperature aging, the weakest group of 100 hours aging still retains the same ranking. Liu et. al [46] reported the shear strength of SAC387 solder bumps gradually decreases when being subjected to 80°C aging for 20 days. Then the same solder bumps are subjected to higher aging temperatures (150°C and 175°C), and it turns out shear strength drops faster with higher aging temperatures. Darveaux et. al [38] compared shear deformation behaviors among 5 different solder alloys. All solder alloys are observed a 10% to 30% reduction in solder joints strength after 125°C aging for 24 hours. Koo et, al [47] found shear strength for both Sn3.5Ag and 63Sn37Pb are severely affected after aging at 170°C for up to 21 days, however the former shows a better aging resistant than the latter. Comparable results are found by Oliver et. al [48]. They tested 63Sn37Pb and two other lead-free solder alloys (Sn96.5Ag3.5 and Sn96.5Ag3.2Cu0.5) at 100°C and 150°C for 1000 hours. Shear strength degradation rate for 63Sn37Pb is observed higher than the lead-free solder alloys.

Moreover, creep behaviors of solder materials under elevated aging conditions are also investigated. Secondary creep rates are found to increase up to 10X and 100X for SAC305 and SAC405 solder materials, respectively, under elevated temperature aging [34]. Related results about aging induced degradations in creep properties were also reported by Zhang et. al [41]. Furthermore, one general phenomenon was reported: elevated temperature aging often leads to a significant softening for lead-free solder materials during shorter thermal aging time (less than 24 hours). And the elevated temperature aging fails to change the creep properties significantly during longer thermal aging time (larger than 72 hours), which indicates that longer thermal aging time seems to stabilize the creep properties of lead-free solder alloys [40].

3.3 Solder Doping

As discussed earlier in chapter 2, solder doping is observed to have substantial influence on solder joint reliability [6, 19, 49, 50]. Jiang et. al [19] conducted a high-temperature aging test on Sn98.2Ag1Cu0.8 solder joints doped with Ge, Ni, Sb, and Zn on BGA. Results show that Sb doping SAC108 solder joints could increase the undercooling rate during solder solidification and then refine the microstructure. Zn doping could reduce the possibility of interface failure after multi-reflow and high-temperature aging. Anderson et. al [36] studied the shear strength behaviors of a set of SAC solder joints under isothermal fatigue test at 150°C for up to 100 hours. Fe and Co modified SAC solder joints are compared with SAC 305 and Sn-3.5Ag solder joints. Only Fe- and Co- modified SAC solder joints show ductile failure after aging for 1000 hours under elevated temperature. Therefore, Fe or Co doped with high Cu content SAC solder joints are suggested to retain both strength and ductility for extended isothermal aging at elevated temperature. Chuang et. al [51] studied the effect of Ni and Ge on tensile, shear reliability of lead-free solder alloys by comparing test results of SAC355 solder alloys doped with Ni, Ge for both bulk and individual solder joints specimens. Solder alloys doped with 0.07% of Ni shows a better tensile strength, however, shear strength and failure mode for solder joints remain the same regardless of solder compositions. El-Daly et. al [49] reported the strength and ductility of SAC305 solder joints strongly depended on Ni content. SAC305 with 0.05% of Ni demonstrates a superior mechanical property in terms of maximal strength. However, the increasing of Ni content beyond 0.05% shows a corresponding deterioration in the mechanical properties. El-Daly et. al [50] also evaluated the creep behaviors of SAC105 solder alloys doped with 0.06% of Ni and 0.5% of Sb with the application of 24.2 MPa stress at 25°C. Reduction of creep rate is observed which implies an improvement of creep resistance. Comparable results are found by Li et. al [52], who revealed the addition of Sb could increase the ultimate tensile strength (UTS), and UTS reaches the highest value with 1.0% of Sb content in Sn3.5Ag0.7Cu solder alloy.

Moreover, doping effects on the drop impact reliability of SAC solder alloys have also been studied by Liu, Che [53, 54]. Solder joints with doped elements all exhibit significantly higher impact reliability. Liu et. al [54] added small amounts of dopants (Mn & Ce) into SAC family solder alloys, the addition of Mn, Ce is observed to increase solder joints drop test and dynamic bending test reliability than SAC105 and SAC305. Che proved solder joint drop reliability can also be improved by adding Ni into SAC305 solder alloys [53].

3.4 Fatigue Life Prediction Model Applicability to Solder Joints

The reliability of solder joints is vital to the reliability of long-term service of electronic devices. Therefore, studying the failure mechanics of solder joints, and further, developing a lifetime prediction of solder joints are important.

With understanding the basic mechanism of failure process of solder joints, and with proper assumptions, researchers have proposed equations to try to predict the fatigue life of solder joints since the early 1960s [3]. The models reviewed for the purpose of predicting the fatigue life of solder joints can be divided into four major categories: Damage accumulation based fatigue models, plastic strain based fatigue models, creep strain based fatigue models, and energy based fatigue models.

3.4.1 Damage Accumulation Fatigue Models

The increase of fatigue damage with applied loads in a cumulative way will lead to the fatigue failure of materials [55]. With the amount of damage accumulated, the lifetime under certain loads becomes limited. Therefore, it is vital to study the mechanisms of fatigue damage accumulation inside materials until a catastrophic failure happens. Generally, the theories can be classified into two categories: 1. Linear damage cumulative theory and 2. Non-linear damage cumulative theory.

Linear damage cumulative theory predicts the damage caused by a stress cycle which is independent of its load sequences and assumes that the ratio of damage accumulative is independent of the stress level. Linear damage models are used due to their simplicity and close approximation to reality [56].

Among many of those models, the Miner’s rule has been extensively received to estimate the fatigue of metals exposed to cyclic loading conditions with varying stress amplitudes [55].

$$\sum_{i=1}^{k} \frac{n_i}{N_i} = 1 \tag{3.1}$$

Where n_i is the number of cycles accumulated at a given stress amplitude, N_i is the number of cycles to failure at the same stress amplitude. k states there are totally k stress levels.

However, it has been suggested by Hamasha et. al [57] recently that Miner's rule is not valid for predicting the fatigue life of lead-free solder joints, given the reasons that: 1). Lead-free solder material is stress dependent, which means the accumulated damage after specified fraction of fatigue life is different for different stress amplitudes, however, the Miner's rule assumes the material is stress-independent. 2). Lead-free solder material is damage interaction, where the way damage accumulated can be permanently changed by first applying other stress amplitude, however, the Miner's rule assumes the material is damage interaction-free.

Corten and Dolan provided a non-linear accumulative damage model to account for the effects of load interaction during fatigue cycling [58]. It assumes that the damage accumulation is nonlinear and can be expressed in terms of the number of cycles in a power law equation, and the damage was propagated at both high and low stress amplitudes that applied to the material. The damage accumulation according to the Corten-Dolan model is expressed by:

$$\sum_i \left(\frac{n_i}{N_1}\right)\left(\frac{\sigma_i}{\sigma_1}\right)^d = 1 \tag{3.2}$$

Where N_1 is the fatigue life at the highest stress amplitude σ_1, n_i is the number of cycles at stress amplitude σ_i, d is the material constant for the model.

Shun-Peng Zhu et. al [59] proposed a "dynamic" Corten-Dolan's equation, where exponent d is defined as a function that decreases with the increasing loading stress amplitudes.

$$d(\sigma_i) = \mu \frac{\sigma_i^{\lambda}\, \delta_f^{1-\lambda}}{\sigma_i} \tag{3.3}$$

Where λ is load-interaction factor, μ is material constant, σ_i is the ith level stress amplitude, δ_f is initial static strength.

Therefore, new Corten-Dolan’s model can be rewritten as the following equation:

$$N_g = \frac{N_1}{\sum_{i=1}^{k} \alpha_i (\sigma_i/\sigma_1)^{d(\sigma_i)}} \tag{3.4}$$

N_g is number of cycles to failure and N_1 is number of cycles to failure at σ_1.

3.4.2 Plastic Strain Based Fatigue Model

Low cycle fatigue failure of solder joints due to the thermal mismatch strain is viewed as a major cause of failure of solder joints in surface mounted electronic devices [60]. Fatigue is due to plastic deformation and eventually causes the fatigue failure of solder joint. Given the fact that solder joints may undergo severe temperature fluctuations during their life cycle, it is important to consider plastic strain in determining the performance and reliability of solder joints. As stated by Lou, et. al, the applied plastic strain is a function of fatigue life [1]. Since plastic strain influences fatigue, it is applied for evaluating the structural integrity of solder joints in different studies.

The Coffin-Manson model [61] was used to predict the low cycle fatigue life N_f in terms of the plastic strain range $\Delta\varepsilon_p$ for solder alloys.

$$N_f^m \Delta\varepsilon_p = C \tag{3.5}$$

where m and C are fatigue exponent and ductility coefficient, respectively.

However, as proved by Shi et. al [62], fatigue life varies with different frequencies. With decreases of frequency, the time to failure increases, which leads to a lower fatigue life. When frequency is above 10^{-3} Hz, fatigue life decreases weakly with decreasing frequency. However, when the frequency reduced from 10^{-3} to 10^{-4} Hz, the time to failure increase drastically, which leads to a larger drop in fatigue life. Therefore, when applying Coffin-Manson model to describe the fatigue behavior of solder alloys for any frequencies, large differences are seen in fatigue life at different frequencies. As a result, the frequency-modified Coffin-Manson model was introduced in equation 3.6:

$$\left[N_f v^{(k-1)}\right]^m \Delta\varepsilon_p = C \tag{3.6}$$

Where v is frequency exponent and k is frequency exponent. k is calculated differently in two frequency ranges roughly as 0.91 and 0.42 for 10^{-3} to 1 Hz and 10^{-3} to 10^{-4} Hz, respectively.

Engelmaier modified the Coffin-Manson model by incorporating parameters such as cyclic frequency, solder and substrate temperature into the equation, developing as the Engelmaier model [63].

$$N_f = \frac{1}{2}\left(\frac{\Delta\gamma}{2\epsilon_f'}\right)^{1/c} \tag{3.7}$$

Where, N_f is the mean cycle to failure, $\Delta\gamma$ is cyclic shear strain range, ϵ_f' is fatigue ductility coefficient, c is fatigue ductility exponent, and c is equal to $-0.442 - 6 \times 10^{-4}\overline{T}_S + 1.74 \times 10^{-2}\ln(1+f)$ for near-eutectic tin-lead solder alloy. $\overline{T}_S$ is the mean cyclic solder joint temperature, f is the cyclic frequency.

Further, Engelmaier put forward an acceleration transform which compares results from different test conditions by normalizing the data to one common comparison condition (condition 2) or to predict operating condition (condition 2) reliability from the accelerated test results (condition 1) [60].

$$\overline{N}_f(2) = \frac{1}{2}\left[\left[2\overline{N}_f(1)\right]^{c1}\frac{\Delta\gamma_2}{\Delta\gamma_1}\right]^{1/c2} \tag{3.8}$$

Where $\overline{N}_f(2)$ is the fatigue life in use condition 2, $\overline{N}_f(1)$ is the fatigue life in accelerated test (condition 1), c1 is the fatigue exponent in condition 1 and c2 is the fatigue exponent in condition 2.

For leadless surface mount solder joints, the total solder joint cyclic shear strain range $\Delta\gamma$ in either condition is given by:

$$\Delta\gamma = \mathrm{F}\frac{d}{2h}\Delta(\alpha\Delta T) \tag{3.9}$$

Where F is empirical factor for second-order effects, d is the longest distance on component between solder joints, h is solder joint height, $\Delta(\alpha\Delta T)$ is thermal expansion differential.

Later, Engelmaier combined a two-parameter Weibull distribution into his model to address the performance fluctuation within a component [64]. The fatigue life $N_f(x\%)$, at a given acceptable failure probability x can be predicted by:

$$N_f(x\%) = \frac{1}{2}\left[\frac{F}{2\epsilon_f'}\,\frac{L_D\Delta\alpha\Delta T_e}{h}\right]^{1/c}\left[\frac{\ln(1-0.01x)}{\ln 0.5}\right]^{1/\beta} \tag{3.10}$$

Where L_D is the maximal distance between component solder joints measured from solder joint centers, $\Delta\alpha$ is the absolute difference in coefficients of thermal expansion of component and substrate, CTE mismatch, β is Weibull shape parameter for Weibull distribution.

Solomon proposed a low cycle fatigue model correlates the plastic shear strain to the fatigue life cycles for near eutectic solder joints at 4 different temperatures (-50℃, 35℃, 125℃ and 150℃) [65]:

$$\Delta\gamma_p\, N_f^{\alpha} = \theta \tag{3.11}$$

Where $\Delta\gamma_p$ is the plastic shear strain range, α and θ are constants. For 60/40 Tin-lead solder material from -50℃ to 150℃, α and θ are estimated to be 0.51 and 1.14, respectively.

Norris-Landzberg et. al [66] had proposed a fatigue life prediction method based on three factors: the maximum temperature T_{max}, the frequency of the temperature cycle f and the thermal excursion range ΔT based on the Coffin-Manson model. Those factors are all known to have a significant impact on the reliability of solder joints. By taking the ratio of the lifetime in field N_{field} and test N_{test} environment, this requires no information on the test vehicle, neither the geometry nor the material properties.

$$A.F. = \frac{N_{field}}{N_{test}} \tag{3.12}$$

$$A.F. = \left(\frac{\Delta T_{test}}{\Delta T_{field}}\right)^{1.9} \times \left(\frac{f_{field}}{f_{test}}\right)^{1/3} e^{\left[(Ea/k)\left(\left(\frac{1}{Tmax},field\right)-\left(\frac{1}{Tmax},test\right)\right)\right]} \tag{3.13}$$

$A.F.$ is called the acceleration factor. The subscripts "$field$" and "$test$" denote different conditions. The activation value Ea estimates to be 0.122eV for Sn-Pb solder alloy and k is Boltzmann's constant.

3.4.3 Creep Damage Based Fatigue Model

The occurrence of time-dependent deformation (creep) is the result of a constant load or strain on a material that deforms over time to reduce the load. The creep behavior of solder material often happens when solder material is exposed to elevated temperature.

Syed et. al [67] proposed two fatigue life equations based on creep strain and creep energy density to predict fatigue life for SnAgPb and SnPb solder alloy simplified from Monkmann-Grant's equation (equation 3.16) [68] and Miner's rule (equation 3.1) [55]. In this equation, the authors assumed the damage in solder joints during thermal cycling tests is mainly from the steady state creep strain accumulation.

When considering an approach using fracture mechanics, the creep strain based model is proposed for low and high stress regions:

$$N_f = (C_{\mathrm{I}}\varepsilon_{acc}^{\mathrm{I}} + C_{\mathrm{II}}\varepsilon_{acc}^{\mathrm{II}})^{-1} \tag{3.14}$$

Then when switching creep strain related constants to energy density constants, we have the energy density model:

$$N_f = (W_{\mathrm{I}}w_{acc}^{\mathrm{I}} + W_{\mathrm{II}}w_{acc}^{\mathrm{II}})^{-1} \tag{3.15}$$

N_f is the number of cycles to failure for both equations. C_{I} and C_{II} represents the constants related to creep strain based model respectively, ε_{acc} represents accumulated creep strain per cycle. And W_{I} and W_{II} represents constants related to dissipated creep energy density based model respectively. w_{acc} represents accumulated creep energy density per cycle.

Syed et. al [69] then combined the Monkmann-Grant equation and Miner' rule to have a new life prediction model, where the cyclic loading is considered as a special case of creep.

In the Monkmann-Grant equation, the time to rupture is inversely related to the steady state creep strain rate, ε_{cr}.

$$t_r = \frac{C}{\dot{\varepsilon}_{cr}} \tag{3.16}$$

Then equation 3.16 is provided for the cyclic creep fatigue life prediction under varying and repeated stress for one single creep mechanism:

$$N_f = \left(\frac{E_{cr}}{C}\right)_{per\ cycle}^{-1} \tag{3.17}$$

E_{cr} is the accumulated creep strain for the whole cycle, and is equals to $\sum_{i=1}^{n} \Delta t_i \times \varepsilon_{cri}$. Δt_i is the time spent at a given stress level within one cycle. The creep ductility c for the creep mechanism.

For two creep mechanisms, the equation becomes:

$$N_f = \left(\frac{E_1}{C_1} + \frac{E_2}{C_2}\right)_{per\ cycle}^{-1} \tag{3.18}$$

The constants are determined as 50 and 15.87 for c_1 and c_2, respectively, for Sn-Pb eutectic solder alloy.

By applying Manson's strain range partitioning method (SRP), Kariya et. al [70] partitioned the entire reversed inelastic strain range into four generic components with creep and plasticity: ε_{pp}: time-independent plasticity reversed by time-independent plasticity; ε_{pc}: time-independent plasticity reversed by creep; ε_{cp}: creep reversed by time-independent plasticity; ε_{cc}: creep reversed by creep.

$$\Delta\varepsilon_{ij} = A_{ij} \times N_{ij}^{-m_{ij}}\ (i, j = p, c\ where\ p\ denotes\ plasticity\ and\ c\ denotes\ creep) \tag{3.19}$$

N_{ij} is the cyclic life corresponds to the specific partitioned strain range $\Delta\varepsilon_{ij}$ and m is the slope of Coffin-Manson plot. $\Delta\varepsilon_{cp}$, $\Delta\varepsilon_{pc}$, $\Delta\varepsilon_{cc}$ are determined from the hysteresis loops in a series of tests that featured the three generic inelastic components.

With all the partitioned cyclic fatigue lives are known, Miner's rule are used to predict creep-fatigue life for each solder alloy.

$$\frac{1}{N_f} = \frac{1}{N_{pp}} + \frac{1}{N_{cc}} + \frac{1}{N_{cp}} + \frac{1}{N_{pc}} \tag{3.20}$$

For Sn-3.5Ag solder alloy, the equation is provided by the author:

$$\frac{1}{N_f} = \left(\frac{\Delta\varepsilon_{pp}}{1.06}\right)^{1.92} + \left(\frac{\Delta\varepsilon_{cp}}{1.92}\right)^{1.67} + \left(\frac{\Delta\varepsilon_{pc}}{4.76}\right)^{0.98} + \left(\frac{\Delta\varepsilon_{cc}}{0.24}\right)^{1.56} \tag{3.21}$$

3.4.4 Energy Based Fatigue Model

The idea that using hysteresis energy as a damage indicator relies on the assumption that, during cyclic stress-strain test, energy was absorbed cycle by cycle because of the plastic deformation and will remain in the solder joints until one point, equals to the energy that is enough to cause the fracture or crack in the solder joints [71]. Many studies tend to correlate hysteresis energy to fatigue life given that energy can capture the fatigue condition within solder joints with more accuracy than creep or strain [72].

Stowell et.al [71] developed one of the earliest fatigue life prediction models by assuming the total energy to the fracture of the material (W_f) is a known quantity and can be calculated from the static stress-strain hysteresis loop. Then the correlation between the energy required to fracture (W_f) and the energy losses for cycling between positive stress level (+σ) to negative stress level (-σ) (W_m) is used to predict the number of cycles to failure (N).

Given the criterion for fatigue life shown in equation 3.22:

$$N \times W_m = W_f \tag{3.22}$$

Cycles to failure (N) is calculated from the cyclic stress-strain equations in hysteresis loop:

$$N = 2\,\frac{\frac{\sigma_f}{\sigma_0} \times \frac{\epsilon_f - \left(\sigma_f/2E\right)}{\epsilon_0} - \cos\frac{\sigma_f}{\sigma_0} + 1}{\frac{\sigma}{\sigma_0}\sin\frac{\sigma}{\sigma_0} - 2\left(\cos\frac{\sigma}{\sigma_0} - 1\right)} \tag{3.23}$$

Where σ_f and ϵ_f are true stress and strain at fracture. E, σ_0 and ϵ_0 are the known constants.

Similarly, Pan et.al [73] provided a strain energy based fatigue life prediction model called Critical Accumulated Strain Energy (CASE) failure criterion, based on the assumption that total hysteresis energy of isothermal fatigue failure for solder joints is almost constant for low strain loading.

$$C = N_f^* \left(a\dot{E}_p + b\dot{E}_c\right) \tag{3.24}$$

Where C is the strain energy density and geometry dependent. In this study, C was reported to be 4.55 MPa/mm^3 from historical experimental data. N_f^* is the number of cycles to failure. $(a\dot{E}_p + b\dot{E}_c)$ is the strain energy density accumulation rate per cycle contributing to the fatigue life. E_p and E_c are the time-dependent plastic and time-dependent creep energy generated within the solder joints and can be calculated using finite element analysis. The weighting factors A and b represented the corresponding energies.

Kujawski et.al [74] proposed a method to predict the fatigue life in low- and high- cycle fatigue using strain energy density. In their theory, the strain energy density is viewed as a constant damage parameter in low and high life region.

$$\Delta W_t = W_f\left(2N_f\right)^d + \Delta W_{end} \tag{3.25}$$

In this equation, ΔW_t is the total cyclic strain energy and is the combination of the cyclic plastic strain energy enclose within the stress-strain hysteresis loop ΔW and the linear elastic strain energy. W_f and d can be determined through the best fit of the experiment. ΔW_{end} elastic strain energy density associated with the material endurance level.

Oldham et.al [75] proposed similar creep-fatigue life prediction method by assuming a constant fatigue damage parameter:

$$N_f = \frac{E_{intrinsic}}{w} \tag{3.26}$$

It assumed that there exists an “intrinsic material property” – $E_{intrinsic}$ which represents the average of all the hysteresis energy failure density (HEFD) for each test in one experiment, and was viewed as a constant value of hysteresis damage energy at failure.

When compared to W_t, energy density dissipated in one cycle (w) multiplying the total number of cycles to failure (N_f), $W_t \geq E_{intrinsic}$ means a failure happens. Then dividing intrinsic energy $E_{intrinsic}$ by the energy density dissipated per cycle (w), we have the fatigue life for this material. In this paper, the author proposed an $E_{intrinsic}$ value equal to 4.64 J/mm^3 with a standard deviation of 2.15 J/mm^3 for 9Cr-1Mo steel.

Morrow’s energy model [76] has been widely used to estimate the fatigue life of solder joint with the equation listed below:

$$N_f^m W_p = C \tag{3.27}$$

Where m is fatigue exponent and C is material ductility coefficient. W_p represents the plastic strain energy density for the static state loop.

Recently, researchers found the Morrow’s model ignores the effect of frequency and temperature on fatigue life, therefore, causing errors when predicting fatigue life at different frequencies and temperatures [62, 77].

Solomon et.al [77] introduced a frequency modified energy model by incorporating frequency modified strain energy density W_p/v^n, and frequency modified fatigue life $N_f v^{(k-1)}$.

$$\left[N_f v^{(k-1)}\right]^m \frac{W_p}{v^n} = C \tag{3.28}$$

In this equation, v is frequency and k is frequency exponent determined from relationship between fatigue life and frequency. N is another frequency exponent determined from the relationship between strain energy density and frequency.

Chapter 4 Sample Preparation and Experimental Methodology

4.1 Introduction

In this chapter, the specimens used in this work are presented. Instead of a traditional bulk sample, individual solder joints were mounted on customized PCB with 3 different types of surface finishes. Compared with traditional bulk samples, individual solder joints have two unique advantages: 1. They are a better reflection of solder joint application in the real service environment; 2. The effects of IMC and surface finishes on the reliability of solder joints can be tested using individual solder joint.

Fatigue and shear testing were carried out using an Instron micromechanical test system. Material properties of solder alloys of interest were tested and analyzed. After that, constitutive empirical models were applied to characterize the stress-strain behaviors of solder alloys.

4.2 Sample Preparation

4.2.1 Test Board Design

The test boards are made of a double layer of FR-4 glass-epoxy material. Each test board includes 120 square test vehicles (12 x 10 vehicles) with dimensions of 10mm x 10mm each. Each test vehicle includes 9 solder joints with 3mm pitch size soldered on the Solder-Mask-Defined (SMD) pads. The solder joint specimens are developed by directly placing fluxed 30mils (0.75mm) solder spheres on the 20mils (0.55mm) copper pads on the customized PCB. Testing boards with three different surface finishes are tested: Organic Solderability Preservative (OSP), Immersion Silver (ImAg), and Electroless Nickle Immersion Gold (ENIG). Figure 4.1 shows a schematic of the test vehicles:

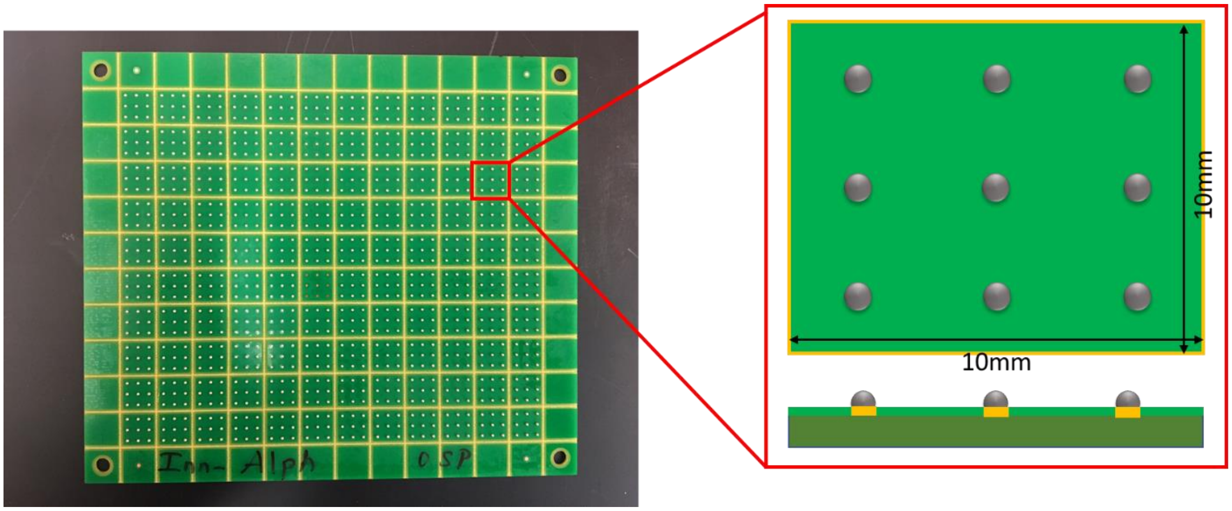

Figure 4.1 Test board design schematic

4.2.2 Solder Materials Selection

Eight lead-free solder alloys with dopants were supplied by 3 suppliers. Table 4.1 summarized all the tested doped solder materials. Doped solder alloys are created by adding a fourth or more element into SAC family solder alloys. In this research, the addition of Ni, Sb, and Bi are added into the solder materials.

Table 4.1 Solder material information

Supplier	**Materials**	**Compositions**
A	SAC305	Sn-3Ag-0.5Cu
B	Innolot	Sn-3.8Ag-0.7Cu-3Bi-1.4Sb-0.15Ni
C	Innolot	Sn-3.5Ag-0.7Cu-3Bi-1.5Sb-0.125Ni
B	MaxRel II	Sn-3.8Ag-0.8Cu-3Bi

A	CycloMax	Sn-3.41Ag-0.52Cu-3.3Bi
A	Ecolloy	Sn-0.92Cu-2.46Bi
B	SAC-X-Plus	Sn-0.3Ag-0.7Cu-0.05Ni-0.08Bi
B	SAC-Ni	Sn-1.2Ag-0.5Cu-0.05Ni

4.2.3 Sample SMT Assembly

All the test samples are assembled in Electronics Packaging Lab in Universal Instruments Corporation (UIC). Once the design was finalized and approved, two stencils with different diameters of openings were designed for assembly. One stencil is set for solder paste/flux application and another is for solder sphere placement. The machine used in stencil printing was a DEK Galaxy (see Figure 4.2). The sticky flux was first applied on the board, and the boards were inspected using a microscope and automatic optical inspection (AOI) device to see whether the flux was properly applied based on the requirement. Once the criteria are passed, solder spheres were applied to fill all the apertures on the second stencil manually using a brush, then boards were ready for reflow.

Figure 4.2 DEK Galaxy stencil printing machine

The reflow process was accomplished using an 8 zone Pyramax 100N reflow oven (see Figure 4.3) within a nitrogen gas environment. The reflow thermal profile has been determined through testing to make sure the solder joints have the appropriate wetting and less board damage. Based on the different solder joint properties, 2 reflow profiles were created. Detail reflow profiles are shown in Figure 4.4. Batch 1 has longer preheat time (from 35°C to 150°C), which is 300 seconds, while batch 2 only has a preheat time of 200 seconds. The peak time for both profiles is 238°C. Max temperature rising rate is about 0.75 degrees per second.

Figure 4.3 Pyramax 100N reflow oven

After the reflow process, x-ray inspection was conducted to check for quality issues in the solder joints in the assemblies (e.g. voids). Any manufacturing defects was reworked.

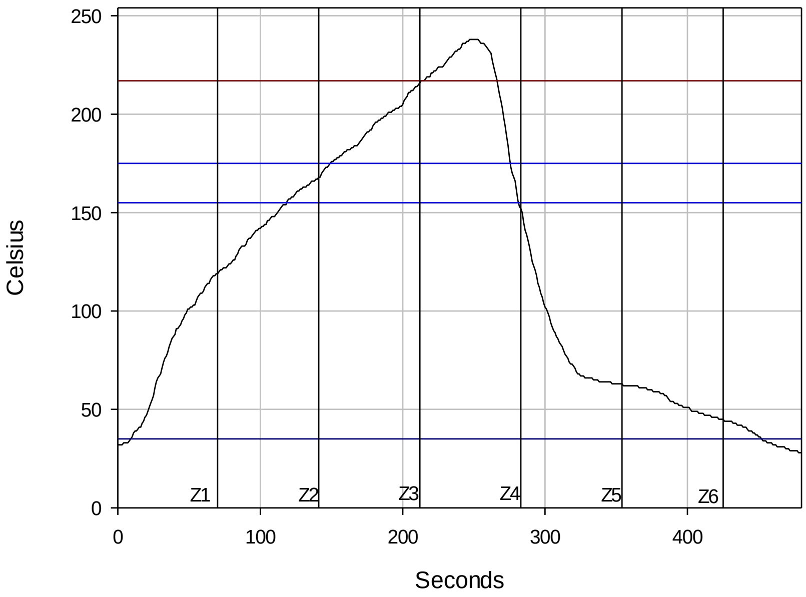

Figure 4.4 Reflow profile

4.3 Instruments Used in Mechanical Testing and Image Analysis

4.3.1 Instron 5948 Micro-mechanical Test System & Calibration

All tests in this study were carried out on a multifunctional Instron 5948 Micromechanical Tester, shown in Figure 4.5. The 5948 model MicroTester offers solutions for testing small assemblies or miniature specimens by combining an ultra-high precision drive system with high-accuracy load measurement. The MicroTester has the ability to perform tension, compression, shear, and low-cycle fatigue tests with a load force range of less than 2mN up to 2kN. Micro-position displacement control is obtained using preloaded ball-screw drive system that is equipped with both a rotary encoder and a 10nm resolution encoder.

To apply shear and fatigue tests on the solder joint and adjust the location, a fixture was designed and manufactured for this test (Figure 4.6). A microtester probe was installed on a stainless-steel rod which was attached to a 50N load cell. The test vehicle was glued on a sample holder which sat on the surface of an x-y stage so that the location of the test board could be adjusted easily to fit the single solder joint into the testing probe.

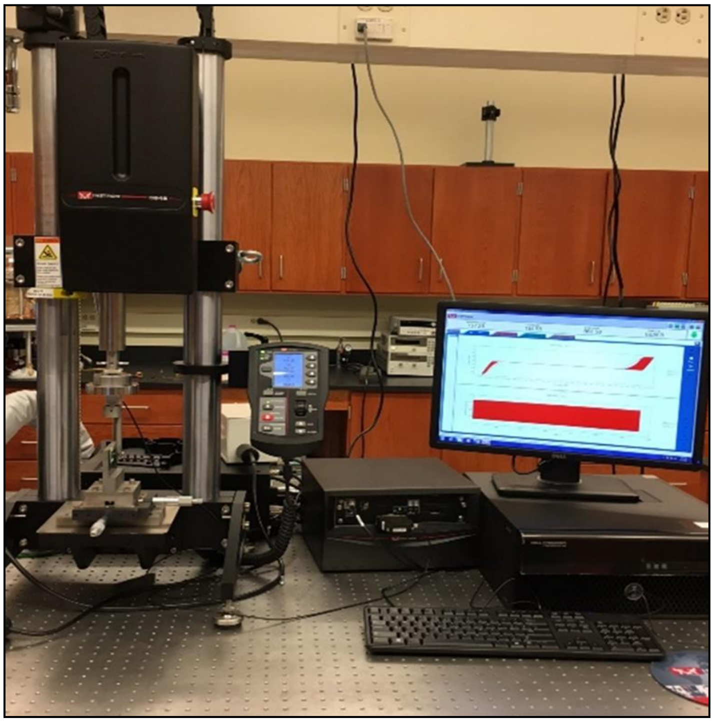

Figure 4.5 Instron MicroTester system

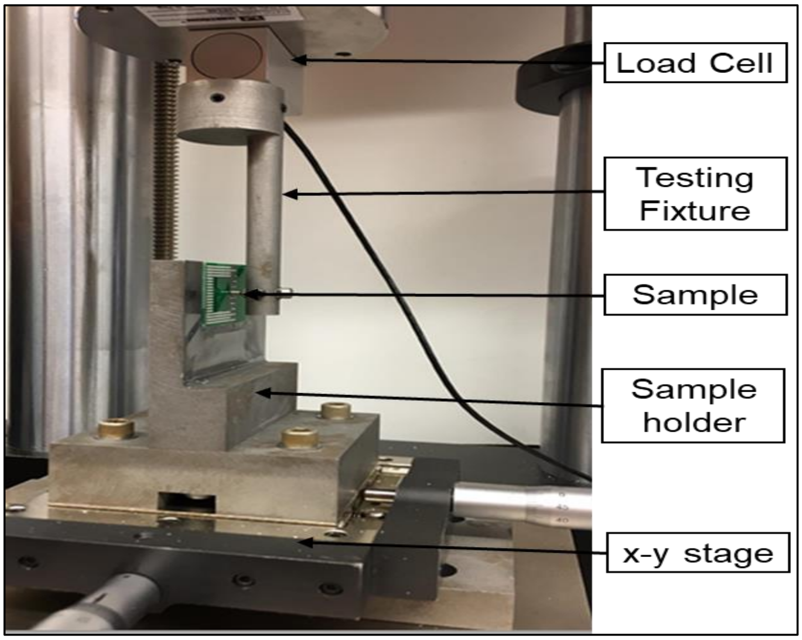

Figure 4.6 Instron MicroTester fixture design

Figure 4.7 shows the side-view schematic of the testing configuration. The grey solid body represents the testing probe. The inner diameter of the probe is 40mils (1.02mm), while the offset from the copper pad is set to be 0.05mm for each test to promise the shear stress concentrated at the same place for each tested solder joint. Typically, before each test, an individual solder joint will be set up in the center of the hollow (1.02mm in diameter) of the customized shear probe, and shear force parallel to the plane of the substrate is achieved by contacting solder joint with the wall of the shear probe. During the testing, the shear probe moves downward first until it contacts the solder joint. Then shear motion continues until the pre-set stress amplitude is reached. After that, the shear probe reverses its moving direction until the same stress amplitude is reached at the opposite of the solder joint, in this way, a cycle of stress-control shear fatigue is completed. The first few cycles lead to a partial flattening of the contact area of the solder joint, but no significant further flattening situation is observed [78]. Fatigue failure of an individual solder joint is defined as the time a sharp drop of hysteresis loop is detected during the shear fatigue testing. Fatigue life of individual solder joint under given stress amplitude is defined as the number of cycles until the fatigue failure of this solder joint.

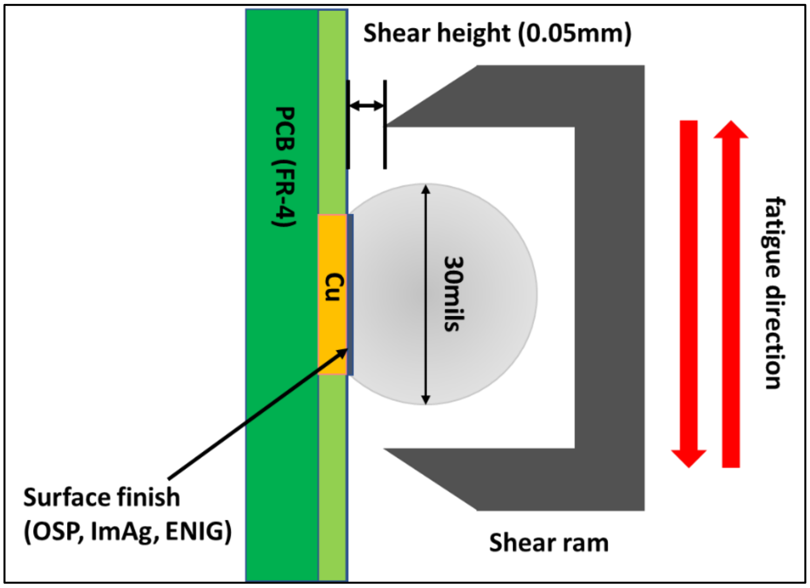

Figure 4.7 Schematic view of the shear fatigue fixture tip with a solder sphere

Calibration of the Instron machine is required after using for a period of time, which involves validation of the accuracy of the instrument's responsibility for achieving displacement and force measurement. Generally speaking, calibration of an instrument means comparing the testing instrument to one device that has already been calibrated to an accepted traceable standard. The aim of calibration of a universal testing device is to reduce uncertainties in test results by ensuring the accuracy of the measurement, and it is important to maintain an up-to-date calibration schedule so that the testing errors could be minimized and accurate conclusions about test specimens in research could be achieved.

Several recognized calibration standards were published by American Society for Testing and Materials (ASTM), which involves the calibration of strain and load rate (ASTM E2309), speed and displacement (ASTM E2658), and measurement of dynamic force (ASTM E467), torque (ASTM E2624), tension and compression (ASTM E4).

Different calibration standards require different calibration devices and procedures. In this work, we mainly conducted ASTM E2309 and ASTM E2658 calibration standards. The calibration devices used in this work were digital linear scales and displacement measuring transducers to calibrate the displacement and time pieces (e.g. stop watches). The combined estimate of uncertainty for the calibration devices shall be equal to or less than 1/3 the allowable error for the measuring system. The estimated measurement uncertainty of the calibration devices shall have a confidence level of 95%.

Prior to the calibration, it is important to minimize any misalignment between the calibration device and testing device to optimize the result. Meanwhile, temperature needs to be closely monitored. At least 15mins of operation time is required for the component to be energized, and to allow all the devices to reach thermal stability.

During the calibration, the testing machine needs to be adjusted to its maximum verification displacement to ensure that the maximum displacement can be achieved, and the machine can have adequate space for the calibration device. Then put the calibration device in the testing machines and let them align to each other as closely as possible to eliminate the errors. Based on the displacement verification standard ASTM E2309, the method for using displacement calibration devices is through the ‘follow-the-displacement’ method where: “the displacement reading on the calibration device is followed until the testing machine reaches a nominal graduation on the displacement readout scale of the measurement system”. Then the displacement from the calibration device is recorded. After selecting suitable displacement increments, obtain zero reading for both the machine and the calibration device, and adjusting the testing machine slowly and smoothly for all verification measurements. The percent error for the displacement values within the verified range of the displacement measuring system shall not exceed the required Classification criteria. Moreover, based on the verification standard for material testing speed ASTM E2658, the method for using speed calibration device is through the ‘stop and start method’ where: “the displacement at where the verification run will start or stop will be firstly determined, then start moving the crosshead, start the displacement calibration device readout and time calibration device once the preset start displacement is reached. Once the crosshead has reached the predetermined stop displacement as indicated by the displacement calibration device, stop the crosshead from moving. then compute the indicated speed error in percentage.” Then repeat the verification run to acquire the second run for the repeatability. The percent error for the speed indication shall not exceed the required classification criteria.

Finally, the calibration/verification interval needs to be discussed and agreed. It is recommended that the interval shall not exceed 18 months. Meanwhile, calibration needs to be immediately carried out after repairs or if there is a reason to double the accuracy of the measuring device.

4.3.2 ZEISS Axio Imager.M2m Optical Microscopy

Prior to the test, microstructure analyses were conducted and IMC thinness for all solder alloys were recorded. A ZEISS Axio Imager.M2m optical microscope with an Axiocam 503 color microscope camera (Figure 4.8) was used to analysis the samples. The ZEISS Axio Imager.M2m optical microscope uses a structured light produced by an LED to illuminate the specimens, with 5 objective magnifications (50, 100, 200, 500, and 1000x). Axiocam 503 color has a 3-megapixl color camera with a 2/3” sensor and an image diagonal of 11mm. The highest resolution is 4.54 µm pixel size. It features a dynamic range of 1:2,500 for precise reproduction and can take live images of up to 38 images per second at full resolution. After the mechanical tests, failure modes were also inspected using the same optical microscope.

Figure 4.8 ZEISS Axio Imager.M2m optical microscope

4.3.3 Hitachi S-2460N SEM

A scanning electron microscope (SEM) shown in Figure 4.9 has also been used to examine the solder surface morphology, microstructure and failure mechanisms. By scanning the sample with a focused beam of electrons, images can be produced with higher resolution and depth of focus. Moreover, there are various types of signals that result from the interaction of electron beam with the sample atoms, including secondary electrons (SE), backscattered electrons (BSE), and characteristic X-ray (EDS) et.al. Secondary electron detection (SE) is the most common imaging mode, which collects low-energy (<50 eV) secondary electrons that are ejected from conduction or valence bands of the specimen atoms by inelastic scattering interactions with beam electrons [79]. Because of the low energy, electrons are initiated within few nanometers from the sample surface so that SE image can provide information about surface morphology and surface topography. In addition, backscattered electron detection (BSE) mode collects high energy electrons originated deeper in the electron beam, which are reflected out of the specimen interaction volume by elastic scattering interaction with specimen atom. Image from BSE mode is brighter than SE mode, since the heavy elements from BSE are brighter. Therefore, BSE mode is normally used to detect contrast between area with different compositions [79]. Characteristic X-ray (Energy-dispersive X-ray spectroscopy, EDS) was used to characterize elements or map the element distribution from the sample, by interacting source of X-ray excitation with a sample. Its characterization ability is based on the fundamental principle that each element has a unique atomic structure allowing a unique set of peaks on its electromagnetic emission spectrum. Figure 4.10 explained the various depths of the produced signals within the sample, and schematic of EDS.

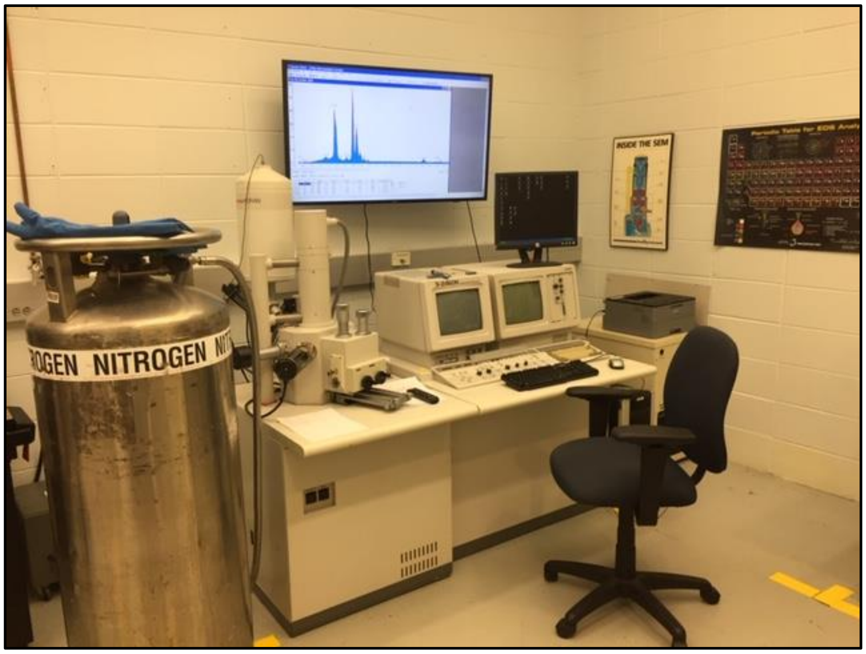

Figure 4.9 Hitachi S-2460N SEM with QuartzXOne EDS system

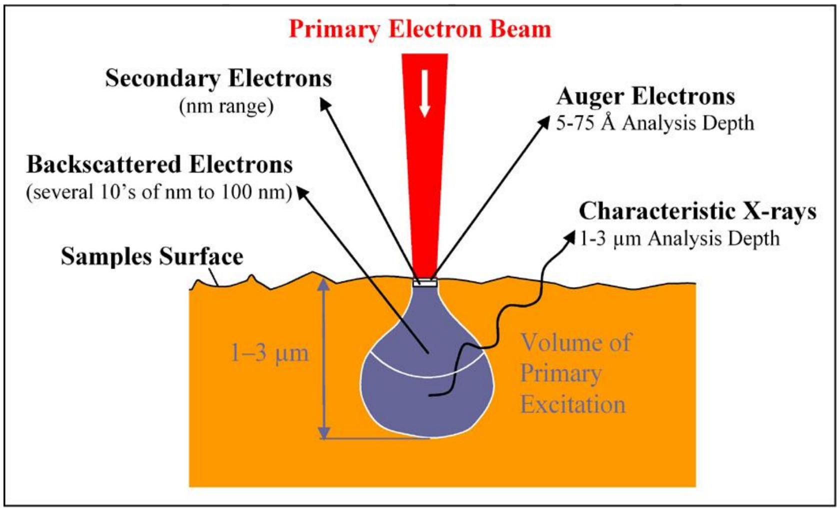

Figure 4.10 Schematic of EDS, Energy-Dispersive X-ray Spectroscopy

4.4 Proposed Test Plan

4.4.1 Study I

The objective of this study is to investigate the effect of long-term room temperature aging on the fatigue behavior of SnAgCu based lead-free solder alloys. In this study, 5 types of lead-free solder alloys (SAC305, SAC105, SAC-Ni, SAC-X-Plus, and Innolot) were aged under room temperature

(25°C) for 4 years. Shear fatigue testing were conducted to characterize the effect of room temperature aging on characteristic fatigue life and hysteresis loop of the solder alloys of interest. The test setup followed the mechanical test setup in the previous section. For the fatigue tests, each solder alloy is tested under 4 varies stress amplitudes, the amplitude level varies with the mechanical properties of solder alloys. Table 4.2 summarizes the fatigue test plan (partial).

Table 4.2 Fatigue test matrix for study I

Solder Materials	Aging Conditions	Stress Level (MPa)	Replicates
SAC305	No Aging	16	10
		20	8
		24	9
		28	10
	4 Years Aging	16	7
		20	8
		24	7
		28	7
SAC105	No Aging	12	7
		16	7
		20	8
		24	7
	4 Years Aging	12	7
		16	7
		20	7
		24	7

The Weibull distribution was applied to analyze the failure data among various solder alloys. Example of a Weibull distribution analysis was shown in Figure 4.11. As discussed in section 2.6.2 (reliability distribution), the Weibull distribution was selected to analyze the failure data because it has the flexibility to model a variety of data sets and the ability to offer reasonably accurate failure analysis and forecasts with small samples. Scale parameter (θ) was used as the characteristic life of a solder joint under a given condition, which is the number of cycles at 63.2% of the overall population to fail.

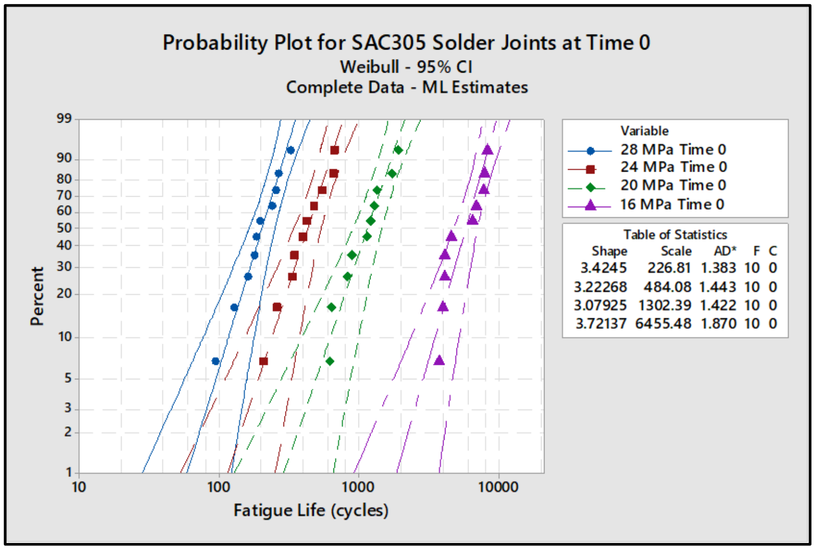

Table of Statistics

Shape	Scale	AD*	F	C
3.4245	226.81	1.383	10	0
3.22268	484.08	1.443	10	0
3.07925	1302.39	1.422	10	0
3.72137	6455.48	1.870	10	0

Figure 4.11 Example of Weibull distribution analysis

Characteristic life was plotted as a function of stress amplitude for a solder joint under each aging condition, known as the N-S curve. Figure 4.12 shows a N-S curve for the Ecolloy solder joint under the no aging condition. A power equation (Equation 4.1) was used to fit the data in this figure: N_{63} is the characteristic life at given stress amplitude, P represents the stress amplitude, A and c are material constants. The absolute value of the power value c represents material ductility, where the smaller the absolute value c, the higher the material ductility.

$$N_{63} = \mathrm{A} * P^{-c} \tag{4.1}$$

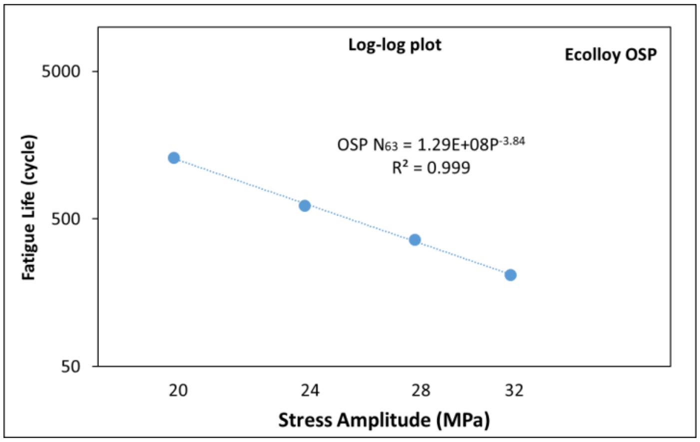

Figure 4.12 Stress amplitude vs. characteristic life for Ecolloy solder joint at 0 aging

Cyclic stress and strain were continuously recorded during the experiment. Typical hysteresis loop (cyclic fatigue stress-strain curve) for single cycle is shown in Figure 4.13. Inelastic work per cycle and plastic strain range are determined based on the hysteresis loop. The inelastic work per cycle is the area enclosed within the loop and is calculated using numerical integration method, the plastic strain is the width of the loop. Later, the inelastic work per cycle or the plastic strain range is plotted as a function of cycle number, and the evolution of those material parameters along with the cyclic test was demonstrated and discussed.

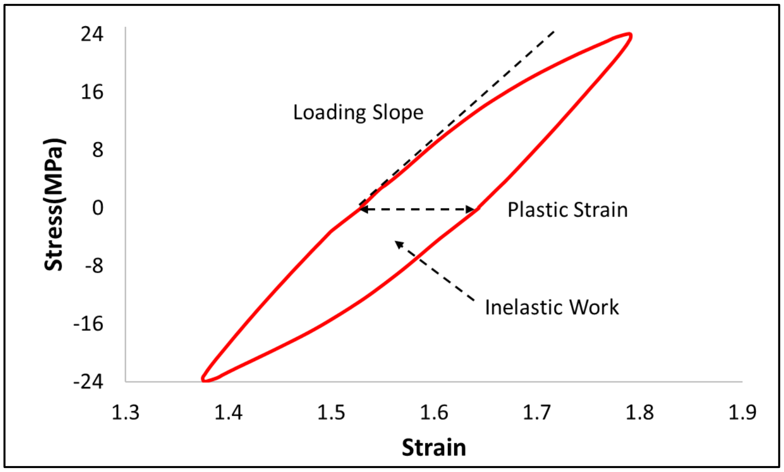

Figure 4.13 Hysteresis loop for SAC305 solder joint under 24MPa

Finally, two empirical models (Coffin-Manson model and Morrow energy model) were applied to fit plastic strain and inelastic work per cycle, respectively against the characteristic fatigue life of each type of solder alloy.

4.4.2 Study II

The objectives of the study II (and study III) are to provide better understanding of shear and fatigue properties of individual doped solder joints and investigate the effect of surface finishes on the integrity/reliability of doped solder joints versus SAC305 solder joints. In study II, shear testing was conducted to evaluate the shear properties of doped solder joints with various surface finishes and the effect of shear strain rate on the solder joint was investigated. Four commercially used doped solder joints and SAC305 solder joints were evaluated as testing samples. Three types of surface finishes were applied on the copper pads of the PCB, which were Organic Solderability Preservative (OSP), Immersion Silver (ImAg), and Electroless Nickle Immersion Gold (ENIG). Solder ball shear testing was conducted at 4 different shear speeds: 0.33, 0.033, 0.0033, and 0.00033mm/s (strain rate: 1, 0.1, 0.01, and 0.001sec^{-1}) at ambient temperature. The experiment setup is the same as the mechanical test setup mentioned in the previous section (Section 4.3: Mechanical Testing Setup). The test matrix for this study is shown in table 4.3 (partial).

Shear strength was systematically recorded as the peak values of shear force over the cross-section area of solder joints, which serves as one of the important indicators for the reliability of solder joints. Main effect plot and interaction plot were conducted to analyze which factors (surface finish, solder joints materials) contribute the most in terms of solder joint reliability. Typically, main effect plot displays the means for each value of a categorial variable to determine whether a main effect is present for that variable and interaction plot displays the means for the levels of one factor on the x-axis and a separate line for each level of another factor to show how the relationship between one categorical factor and a continuous response depends on the value of the second categorical factor. Prior to the test, the solder joints' microstructure and IMC thinness were analyzed using SEM. Failure modes of shear test of various solder alloys were also identified to correlate the failure mechanism to the test result.

Table 4.3 Shear test matrix for study II

Solder Materials	**Surface Finish**	**Strain Rate Level (sec^{-1})**	**Replicates**
SAC305	OSP	0.001	7
	OSP	0.01	8
	OSP	0.1	7
	OSP	1	7
	ImAg	0.001	7
	ImAg	0.01	7
	ImAg	0.1	7
	ImAg	1	7
	ENIG	0.001	7
	ENIG	0.01	9
	ENIG	0.1	7
	ENIG	1	7
Innolot-H	OSP	0.001	7
	OSP	0.01	7
	OSP	0.1	8
	OSP	1	7
	ImAg	0.001	7
	ImAg	0.01	7
	ImAg	0.1	7
	ImAg	1	7
	ENIG	0.001	7
	ENIG	0.01	7
	ENIG	0.1	9
	ENIG	1	13

4.4.3 Study III

Shear testing is a quick experiment to screen the integrity of various solder alloys and not really in the category of reliability testing. In study III, cyclic shear fatigue testing was conducted to evaluate the effect of surface finish to the overall reliability of 5 commercially used doped solder joints and SAC305 solder joints. Three types of surface finishes were applied on the copper pads of the PCB, which were Organic Solderability Preservative (OSP), Immersion Silver (ImAg), and Electroless Nickle Immersion Gold (ENIG). Fatigue tests were conducted under 4 stress amplitudes according to the mechanical properties of each type of solder alloy under stress control. The experimental setup is the same as study II. Table 4.4 summarizes test matrix between study II and study III.

Table 4.4 Mechanical test matrix for study II and study III

Test Method	Shear Testing	Fatigue Testing
Applied Load	Shear	Cyclic shear
Load Rate	1, 0.1, 0.01, 0.001sec^{-1}	0.01sec^{-1}
Sample Size	480	400
Stress Amplitude	N/A	16, 20, 24, 28, 32MPa
Testing Height	0.05mm	0.05mm
Surface Finish	OSP, ImAg, ENIG	OSP, ImAg, ENIG

Characteristic fatigue life and hysteresis analysis was used were analyzed to determine the effect of various surface finishes on the reliability of solder joints. The Weibull distribution was used to model the failure rate distribution of each solder alloy. The scale parameter was taken as the characteristic fatigue life of solder alloys under each stress amplitude. The stress-strain curve of fatigue testing was systematically recorded as hysteresis loop, and was fitted by an empirical model, then the area enclosed within the fitting curve was defined as work dissipation per cycle. Work per cycle is viewed as one of characterizations for solder alloys, and work per cycle for each solder alloy in this study was compared. After fatigue testing, failure modes of various types of solder joints with surface finishes were analyzed by optical microscope. Detail testing matrix is shown in table 4.5 (partial).

Table 4.5 Fatigue test matrix for study III

Solder Materials	**Surface Finish**	**Stress Amplitude (MPa)**	**Replicates**
CycloMax	OSP	32	8
	OSP	28	8
	OSP	24	7
	ImAg	32	7
	ImAg	28	7
	ImAg	24	7
	ENIG	32	9
	ENIG	28	8
	ENIG	24	9
SAC-Ni	OSP	20	7
	OSP	24	7
	OSP	28	8
	ImAg	20	7
	ImAg	24	7
	ImAg	28	7
	ENIG	20	7
	ENIG	24	7
	ENIG	28	7

4.5 Failure Analysis

Test samples need to be cross-sectioned prior to microscopic examination. Sample preparation procedure can be summarized into 3 steps: sectioning, mounting, and grinding & polishing. Samples were first cut into certain sizes, to fit into the molds. The samples were cold mounted using an epoxy system (blended epoxy resin and hardener). Once set, the samples were released carefully to minimize the possibility of cracking of the epoxy. After that, they were ground on a Pace Technologies NANO 1000T grinder-polisher machine (Figure 4.14). Grinding involves using sandpaper: paper backings with hard, imbedded “grit” particles (mainly SiC) with a variety of diameter ranges. Sandpaper with grit of 240, 320, 400, 600, 800, and 1200 were used in sequence for grinding. The target of grinding was to reach the body of solder joints, where a plane passing through the solder joints, and control the surface roughness of epoxy to a level for the preparation of polishing. A polishing pad was loaded onto the working wheel and polishing was conducted on top of it. A 3μm polycrystalline diamond suspension and 0.02μm non-crystallizing colloidal silica polishing suspension were applied for the semi-final and final polishing, respectively. A final polished sample is shown in Figure 4.15.

Upon completion of the polishing process, A ZEISS Axio Imager.M2m optical microscope and SEM were used to examine any failure modes occurring during the test.

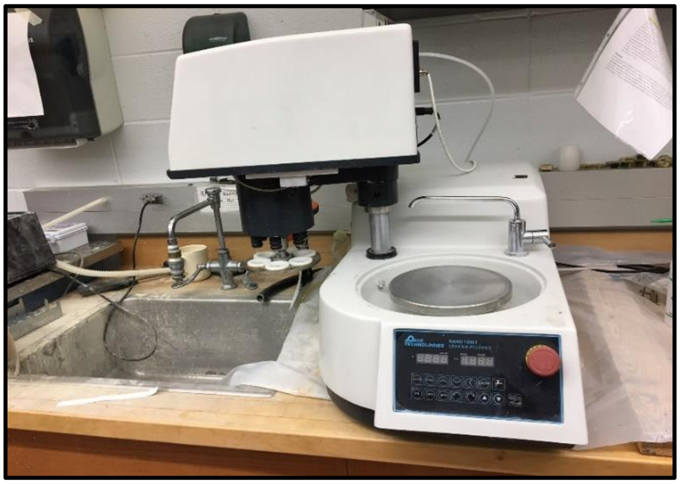

Figure 4.14 Pace Technologies NANO 1000T grinder-polisher machine

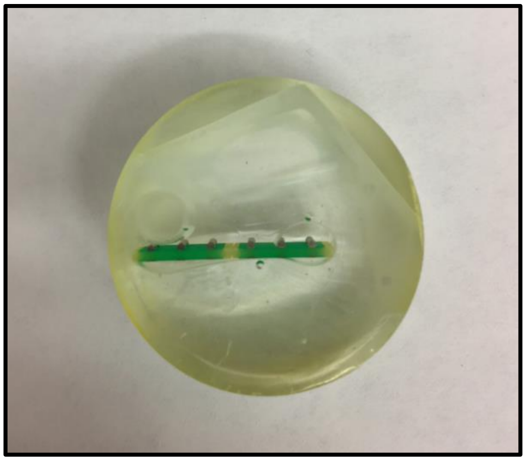

Figure 4.15 Cross-sectioned sample with final polishing

Chapter 5 Effect of Long-Term Room Temperature Aging on the Fatigue Properties of SnAgCu Solder Joint

5.1 Introduction

The fatigue failure of solder joints in printed circuit boards (PCB) is one of the limiting factors for the reliability in long-term service of electronic products. Since isothermal aging or thermal cycling environments was known to change the microstructure [80], and further, impact the mechanical response and failure behavior of solder joints in electronic assemblies, aging effect is investigated as one of the leading factors for low fatigue life of solder joints. The aging effect during thermal cycling tests has been well studied by extensive research, and generally accepted as being universally detrimental to reliability, which leads to a large degradation of mechanical properties including shear strength, drop reliability, creep and crack behavior. However, room temperature aging was also found to have a significant effect on the solder ball properties [8, 42, 43].

While the room temperature aging effect has been well studied about the solder mechanical behaviors such as shear strength and softening process, very limited data were published for a long-term dwelling under room temperature (e.g. aging at room temperature for more than 4 years) on the solder cyclic loading and fatigue behaviors. In this chapter, the effect of long-term room temperature aging on the fatigue life and cyclic loading behavior of individual solder alloy is studied.

5.2 Effect of Room Temperature Aging on the Fatigue Life

A two-parameter Weibull distribution was introduced to characterize the fatigue life of solder joints under different aging conditions. Figures 5.1 and 5.2 showed the Weibull distribution of SAC305 under no aging and aged for 4 years conditions. It is obvious that the fatigue life varies for the same stress amplitude for both conditions. This variation can be extrapolated mainly because of the random Sn orientation and secondary precipitate distribution [81]. The scale parameter represents the characteristic life which is the number of cycles at 63.2% of total populations to fail, the shape parameter represents the slope of the curve on a Weibull plot. To represent the fatigue life as a function of stress amplitudes, a power equation is introduced to fit the fatigue data:

$$N = aP^{-c} \tag{5.1}$$

Where N represents the fatigue life of solder joints under given stress amplitude. P is pre-selected peak stress amplitudes, a and c are material constants. For each set of aging conditions, the fatigue life (N) vs. stress amplitude (P) are demonstrated on a log-log scale. The power value c explains the ductility of the material; the smaller number means the higher ductility.

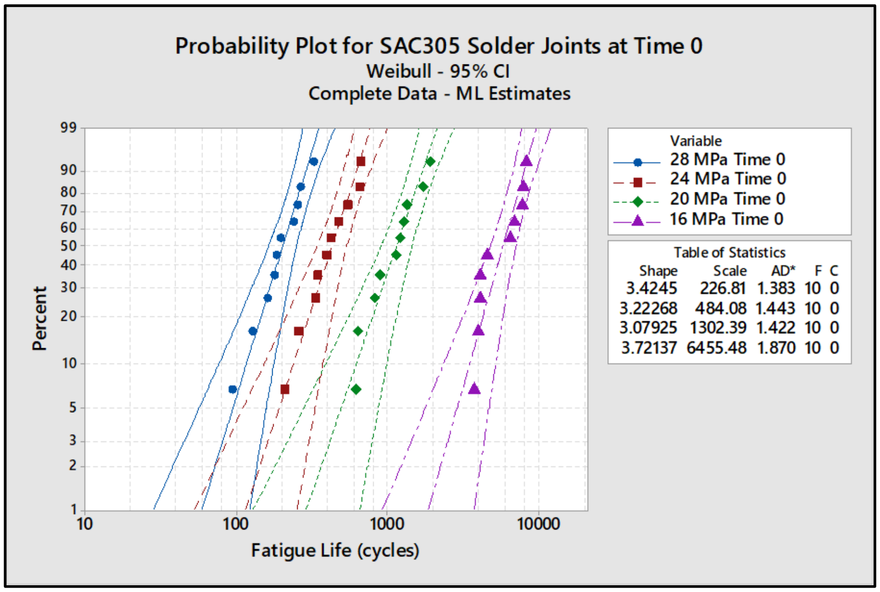

Figure 5.1 Weibull plots of the fatigue life of SAC305 solder joints at different stress amplitudes under no-aging condition

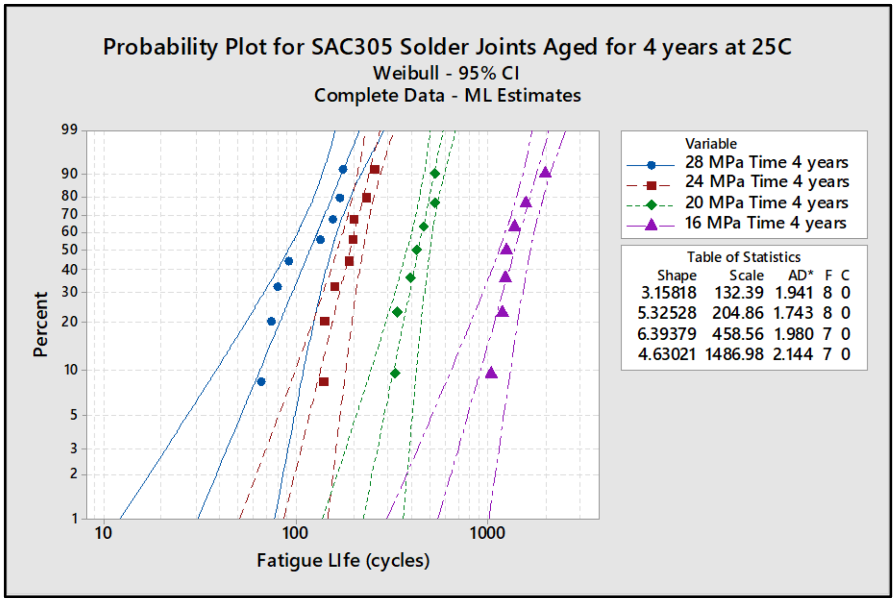

Figure 5.2 Weibull plots of the fatigue life of SAC305 solder joints at different stress amplitudes after 4 years of room temperature aging

In Figures 5.3 and 5.4, log-log plots of the characteristic fatigue life (N_{63}) versus stress amplitudes (P) and the lifetime at 10% cumulative probability of failure (B10) versus stress amplitudes (P) for SAC305 solder joint tested at no aging and 4 years aging conditions are shown respectively. The power equations offered a good approximation for both plots (R^2 close to 0.99 for both no aging and 4 years aging). As expected, both characteristic fatigue life and B10 life decreased by increasing the stress amplitudes with a power value of -c. More importantly, the fatigue life after aging was significantly lower than before aging at any given stress amplitudes. The power value c was also lower after aging, which indicated an increase in ductility.

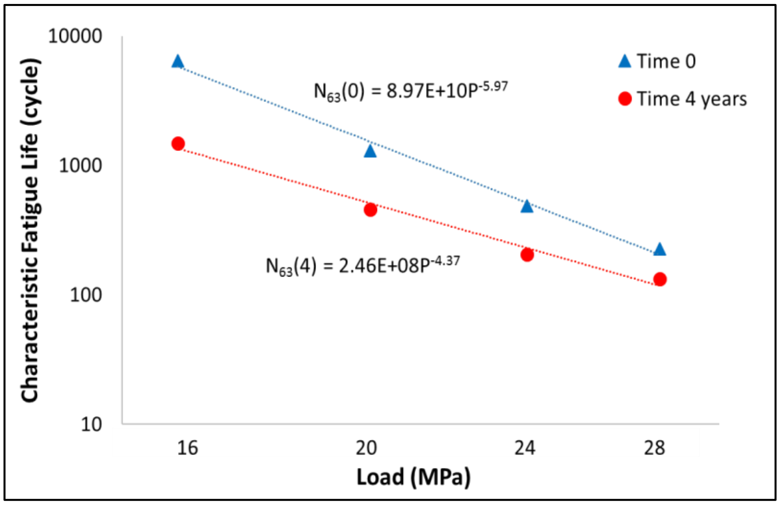

Figure 5.3 Characteristic fatigue life vs. stress amplitude (log-log scale) under 2 aging conditions for SAC305 solder alloy

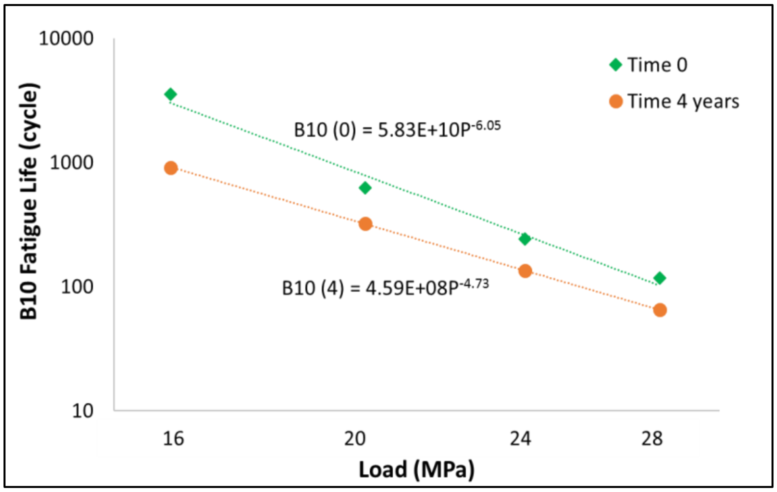

Figure 5.4 B10 fatigue life vs. stress amplitude (log-log scale) under 2 aging conditions for SAC305 solder alloy

To illustrate the fatigue life plots more visibly, fatigue life degradation bar charts (fatigue life vs. peak stress amplitudes) were demonstrated in Figures 5.5 and 5.6 for SAC305 solder joints. Figure 5.5 was the degradation bar chart for characteristic life before and after 4 years of room temperature aging, and Figure 5.6 was the degradation bar chart for B10 life before and after 4 years of room temperature aging. After 4 years of room temperature aging, the characteristic life dropped 41%, 58%, 65% and 77% for stress amplitudes 28MPa, 24MPa, 20MPa, and 16MPa, respectively. Likewise, B10 life dropped 45%, 45%, 48% and 74% for stress amplitudes 28MPa, 24MPa, 20MPa and 16MPa.

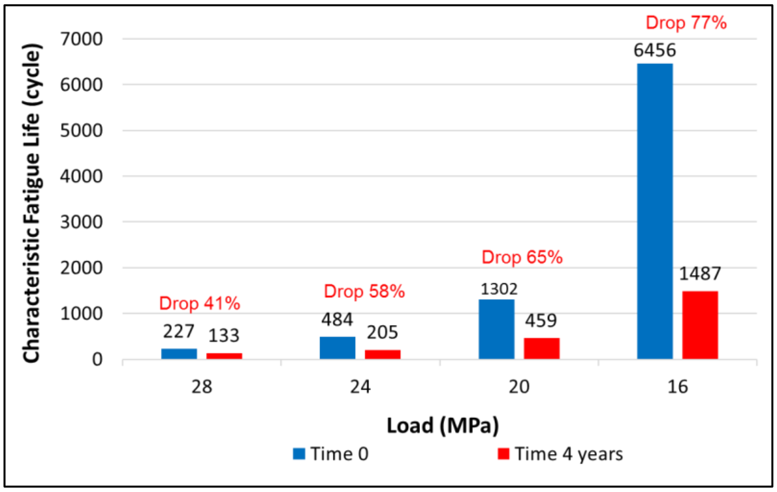

Figure 5.5 Characteristic life degradation for SAC305 solder joints after aging

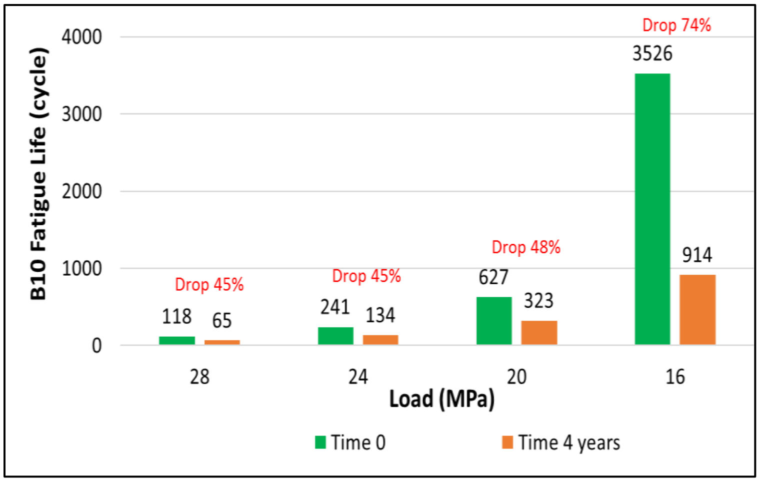

Figure 5.6 B10 life degradation for SAC305 solder joints after aging

After baseline comparison material SAC305 solder alloy, effect of room temperature aging on the low silver alternative SAC105 solder alloy was tested. Figure 5.7 and 5.8 demonstrated the Weibull distribution for SAC105 at 0 aging and after 4 years of room temperature aging.

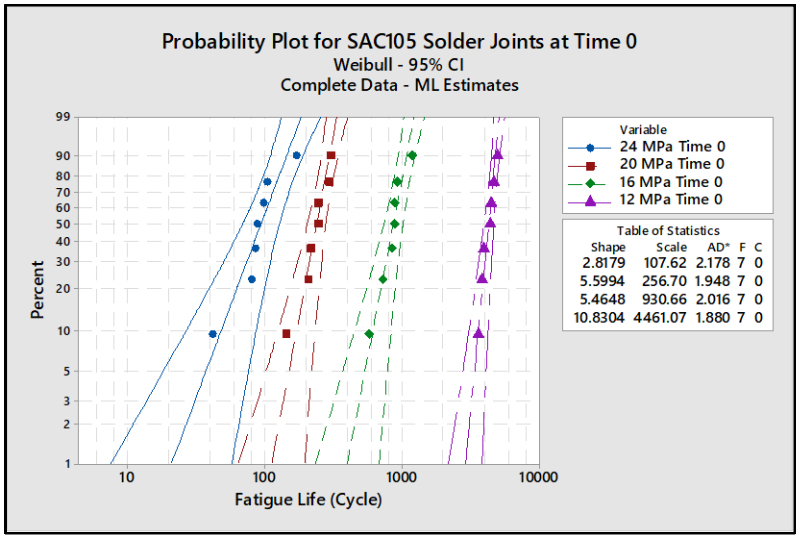

Figure 5.7 Weibull plots of the fatigue life of SAC305 solder joints at different stresses amplitudes under no-aging condition

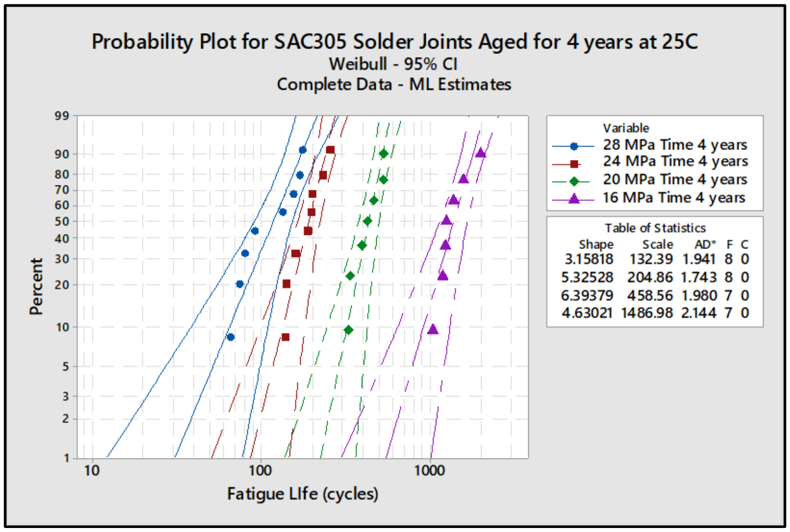

Figure 5.8 Weibull plots of the fatigue life of SAC305 solder joints at different stress amplitudes after 4 years of room temperature aging

Then characteristic life and B10 life were plotted as a function of stress amplitude for SAC105 solder alloy under both 0 aging and 4 years aging, as shown in Figure 5.9 and Figure 5.10.

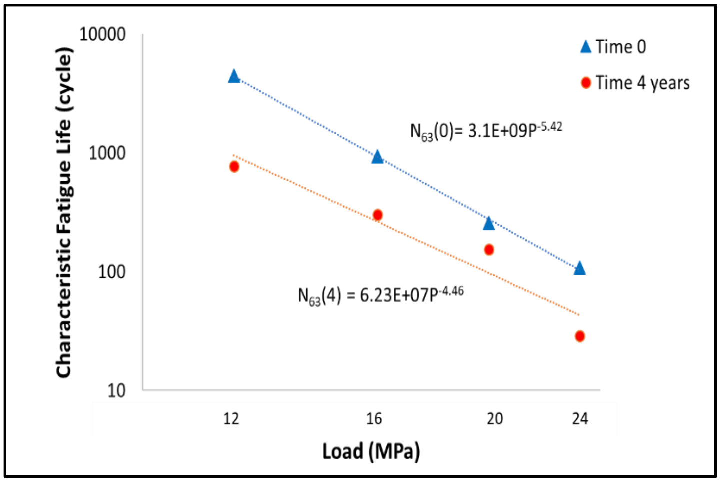

Figure 5.9 Characteristic fatigue life vs. stress amplitude (log-log scale) under 2 aging conditions for SAC105 solder alloy

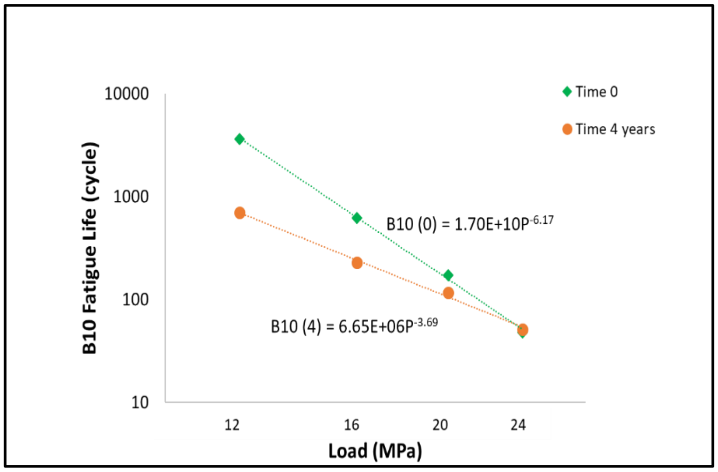

Figure 5.10 B10 fatigue life vs. stress amplitude (log-log scale) under 2 aging conditions for SAC105 solder alloy

The same trend was observed when comparing to SAC305 solder joint, as 4 years of room temperature aging significantly decreased both characteristic life and B10 life, while increased the ductility of this solder alloy.

Bar char comparisons for SAC105 before and after 4 years of room temperature aging were conducted as well to demonstrate the degradation of solder joint after aging, as shown in Figure

5.11 and 5.12. Figure 5.11 highlighted the characteristic life comparison while Figure 5.12 highlighted the B10 life comparisons.

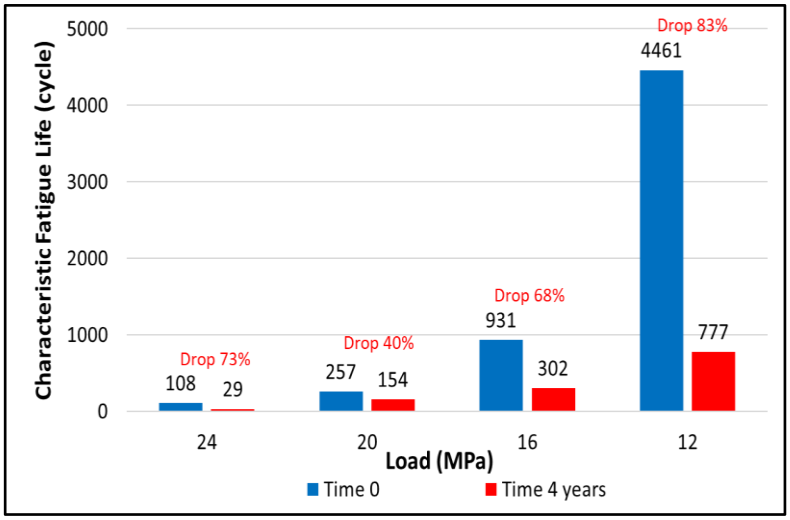

Figure 5.11 Characteristic life degradation for SAC105 solder joints after aging

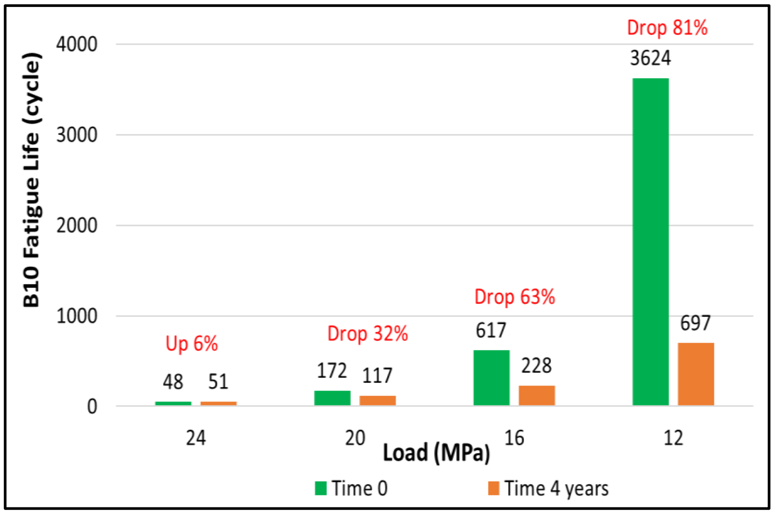

Figure 5.12 B10 life degradation for SAC105 solder joints after aging

As comparing to SAC305, the similar trend was also observed, as the fatigue life dropped after aging and the life degradation was more severe for lower stress amplitude than for higher stress amplitude.

Characteristic life vs. stress amplitudes for SAC-Ni was examined and the results are shown in Figure 5.13 and 5.14. Figure 5.13 compared characteristic life before and after 4 years of room temperature aging and Figure 4.14 compared B-10 life before and after 4 years of room temperature aging. Results showed that both fatigue life decreased after 4 years of aging, and ductility of this material was increased.

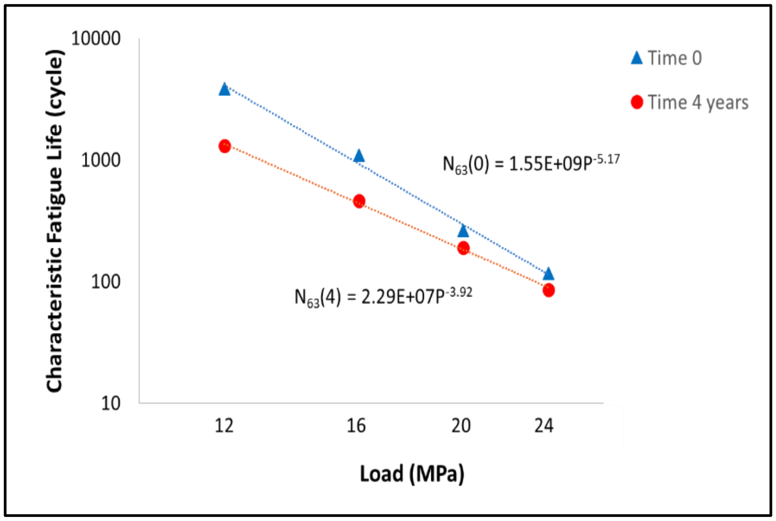

Figure 5.13 Characteristic fatigue life vs. stress amplitude (log-log scale) under 2 aging conditions for SAC-Ni solder alloy

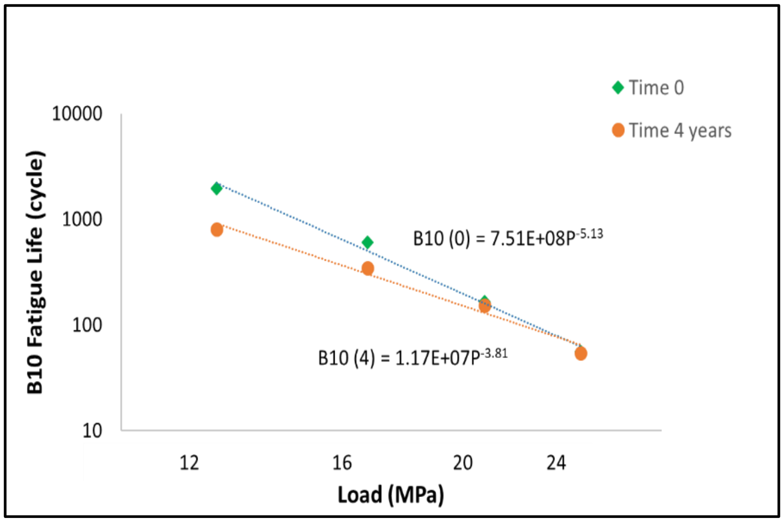

Figure 5.14 B10 fatigue life vs. stress amplitude (log-log scale) under 2 aging conditions for SAC-Ni solder alloy

Bar chart associated with SAC-Ni solder alloy was conducted to further explain the aging degradation, as shown in Figure 5.15 and Figure 5.16. A significantly drop in both characteristic life and B10 life was observed, however, the degradation rate was less than SAC305 or SAC105.

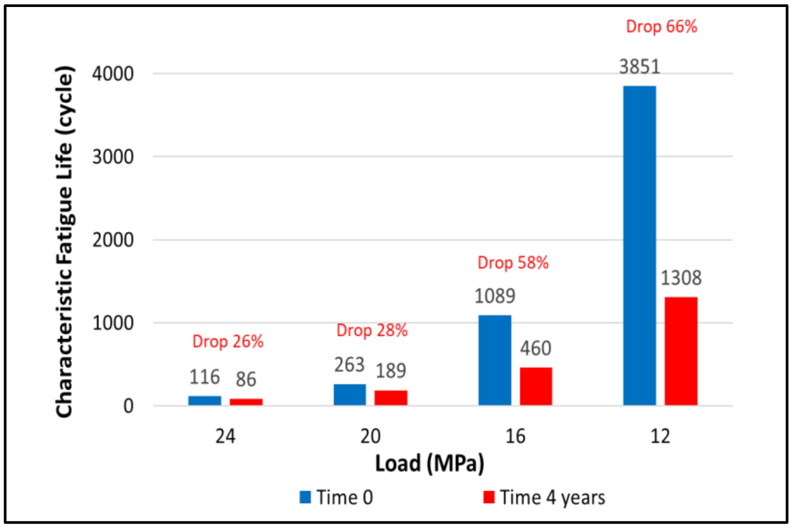

Figure 5.15 Characteristic life degradation for SAC-Ni solder joints after aging

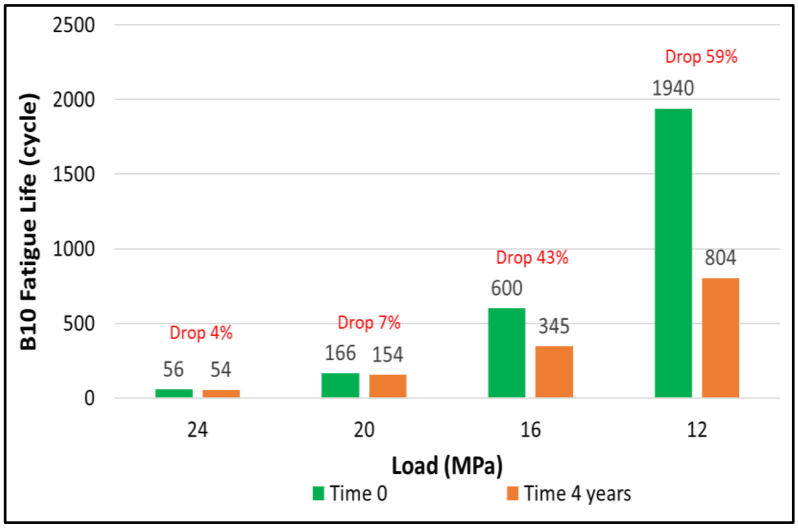

Figure 5.16 B10 life degradation for SAC-Ni solder joints after aging

Similarly, both characteristic life and B10 life for SAC-X-Plus was plotted as a function of stress amplitude, shown in Figure 5.17 and 5.18. A degradation was observed for both characteristic life and B10 life, and the ductility of the material was increased with 4 years of aging.

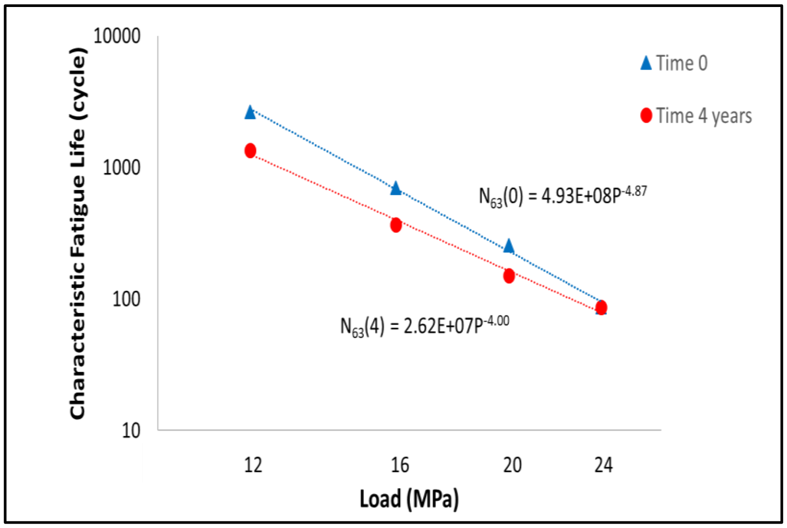

Figure 5.17 Characteristic fatigue life vs. stress amplitude (log-log scale) under 2 aging conditions for SAC-X-Plus solder alloy

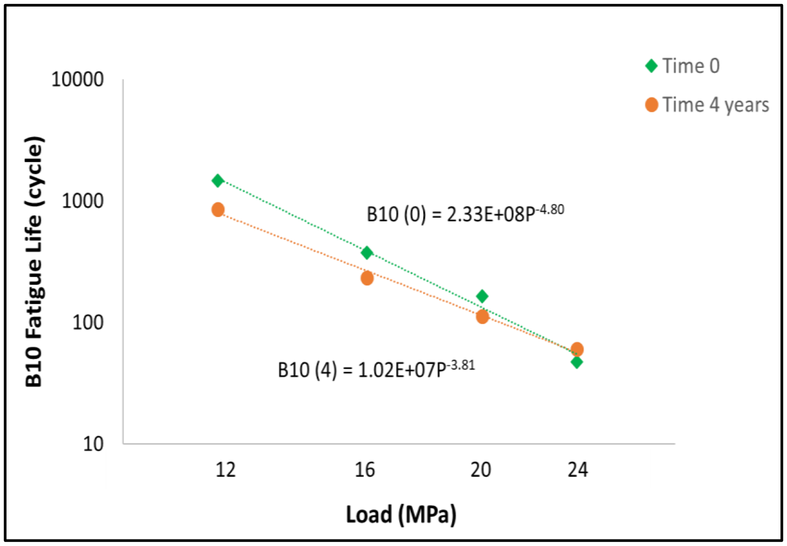

Figure 5.18 B10 fatigue life vs. stress amplitude (log-log scale) under 2 aging conditions for SAC-X-Plus solder alloy

Bar chart comparisons for SAC-X-Plus was conducted to demonstrate the degradation after long-term room temperature aging for characteristic life and B10 life as shown in Figure 5.19 and 5.20. Both characteristic life and B10 life decreased with SAC-X-Plus solder alloy, as we have observed for the rest of the alloys, however, a smaller degradation rate was illustrated.

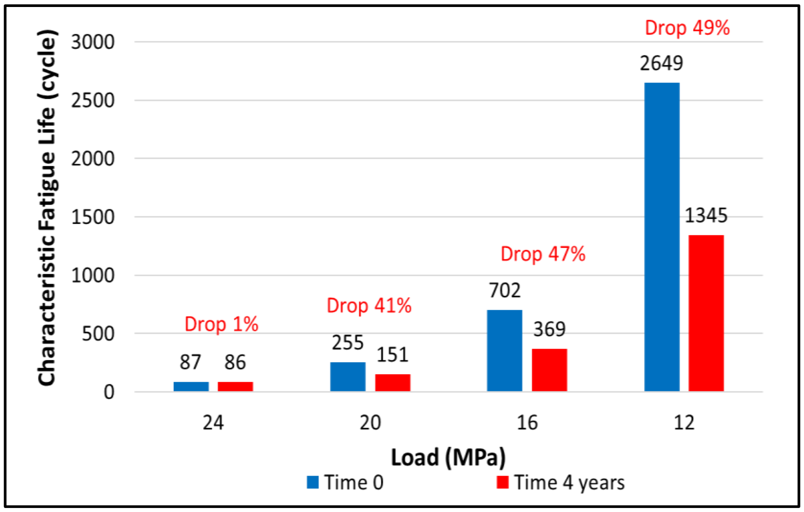

Figure 5.19 Characteristic life degradation for SAC-X-Plus solder joints after aging

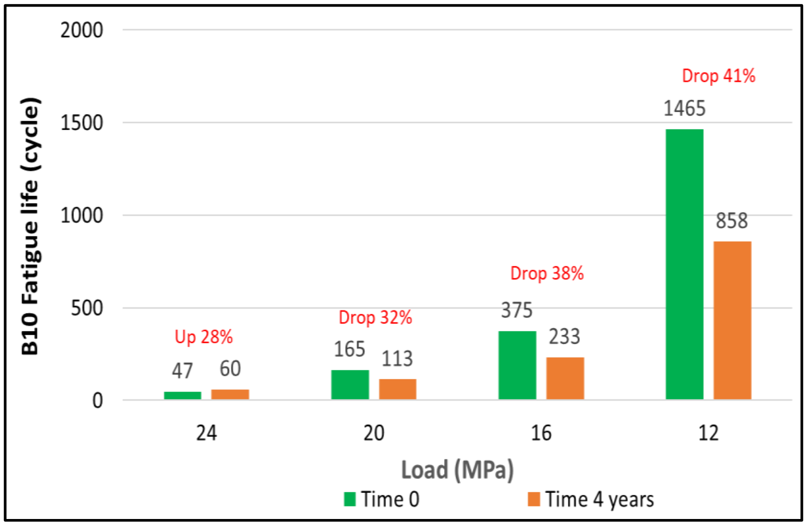

Figure 5.20 B10 life degradation for SAC-X-Plus solder joints after aging

The last solder alloy studied was Innolot. Different than the rest of the alloys, long-term room temperature aging didn’t demonstrate a significant effect on the fatigue life of Innolot, especially when testing at higher stress amplitude. Both characteristic life and B10 life as a function of stress amplitude were shown in Figure 5.21 and 5.22. Although fatigue life associated with Innolot solder alloy wasn’t affect much with room temperature aging, when comparing the material ductility, the ductility of Innolot was also increased after 4 years of room temperature aging.

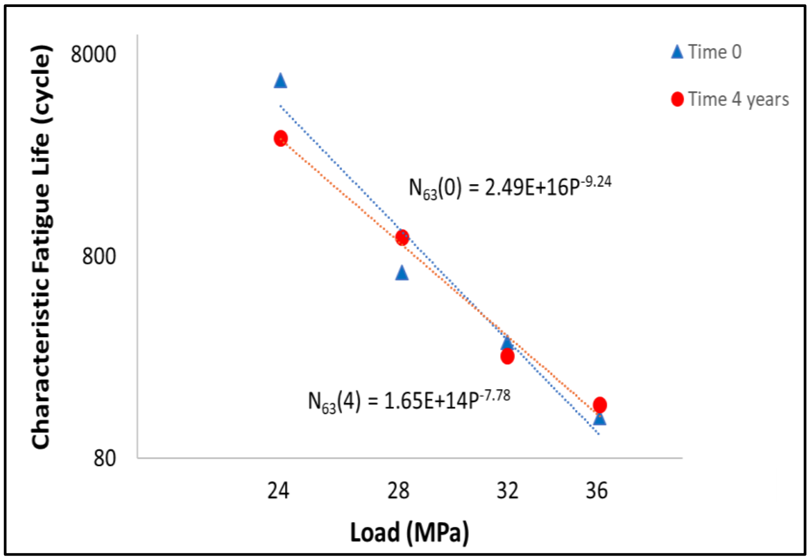

Figure 5.21 Characteristic fatigue life vs. stress amplitude (log-log scale) under 2 aging conditions for Innolot solder alloy

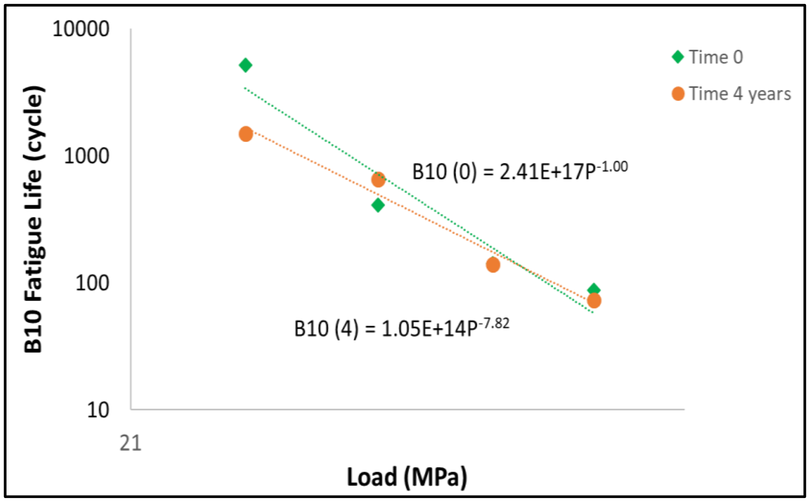

Figure 5.22 B10 fatigue life vs. stress amplitude (log-log scale) under 2 aging conditions for Innolot solder alloy

Room temperature aging effect on both characteristic life and B10 life for Innolot solder alloy was plotted in a bar chart, as shown in Figure 5.23 and 5.24. Both characteristic life and B10 life dropped under 24MPa, while almost no changes at higher stress amplitude was observed. Given the anisotropy nature of solder material, fatigue life varies from joint to joint, even testing at the same condition. This can also explain why at some stress levels, fatigue life after 4 years of room temperature ends up higher than the non-aging condition, aside from experimental error, the strong variability in the solder material can also contribute to this phenomenon.

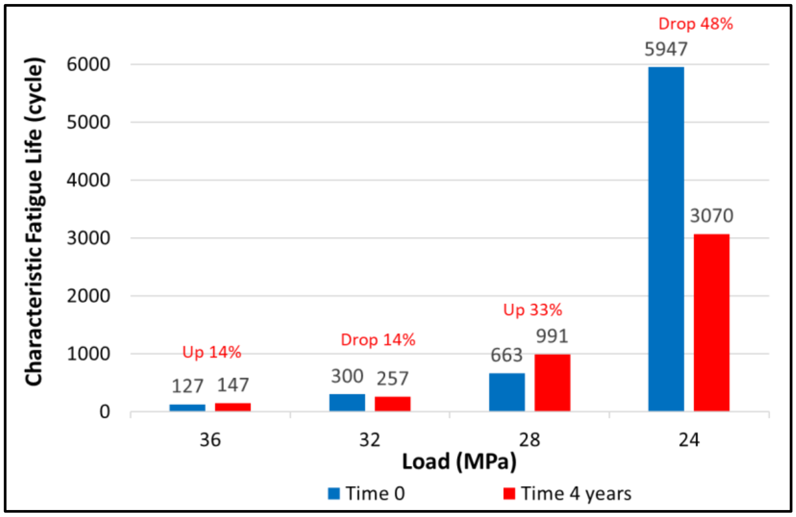

Figure 5.23 Characteristic life degradation for Innolot solder joints after aging

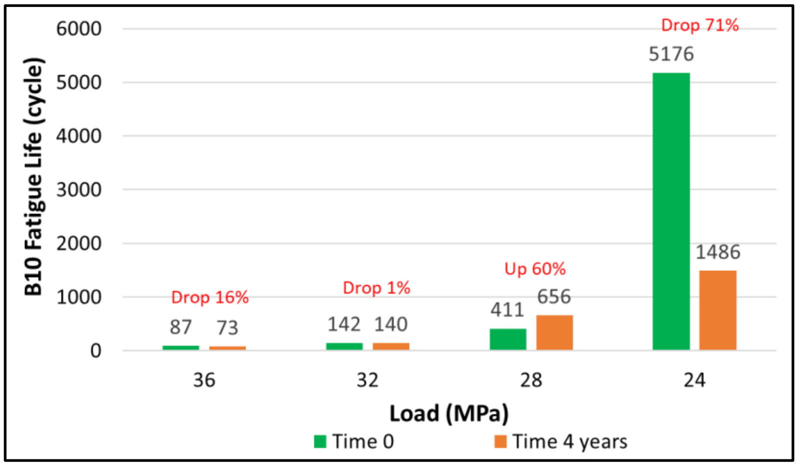

Figure 5.24 B10 life degradation for Innolot solder joints after aging

Table 5.1 summarized the average degradation for both characteristic and B10 fatigue life after 4 years of room temperature aging for all alloys. Life degradation after aging for non-doped solder alloys (SAC305 and SAC105) was relatively larger than the doped alloys. The characteristic fatigue life degradation was 60% for SAC305 and 66% for SAC105 after aging. However, adding doped elements (such as Ni, Bi, and Sb) to the SAC solder alloy reduced the degradation after aging. The characteristic life degradations after aging were 45% for SAC-Ni (doped with 0.1% Ni), 35% for SAC-X-Plus (doped with 0.05% Ni and 0.08% Bi), and only 4% for Innolot (doped with 0.1% Ni, 2.83% Bi, and 1.48% Sb). This showed that adding dopants into the SAC solder alloy will mitigate the effects of room temperature aging as the degradation rates of doped solder alloys decrease compared to the non-doped solder alloys.

Table 5.1 Average degradation of characteristic life and B10 life after 4 years of room temperature aging

	Avg. Degradation of Characteristic Life	**Avg. Degradation of B10 Life**
SAC305	60%	53%
SAC105	66%	42%
SAC-Ni	45%	28%
SAC-X-Plus	35%	21%
Innolot	4%	7%

The characteristic fatigue life as a function of stress amplitudes for all 5 solder alloys before and after aging were illustrated in Figures 5.25 and 5.26 on a log-log scale. In Figure 5.25, with 3.6% Ag and 2.83% Bi, Innolot was the most fatigue resistant alloy, followed by the SAC305 with 3% Ag. While with only 0.3% Ag and 0.08% Bi, SAC-X-Plus showed the least fatigue resistant. SAC-Ni and SAC105, with 1.2% and 1.0% Ag, showed almost the same fatigue resistance. This indicated that higher Ag and Bi alloys tended to be more fatigue resistant. After four years' aging, shown in Figure 5.26, Innolot and SAC305 still had the largest and second-largest fatigue resistance. However, SAC105 solder alloy turned out to demonstrate the least fatigue resistance after 4 years of room temperature aging. Solder joints had higher Ag and Bi also showed higher aging resistance as well.

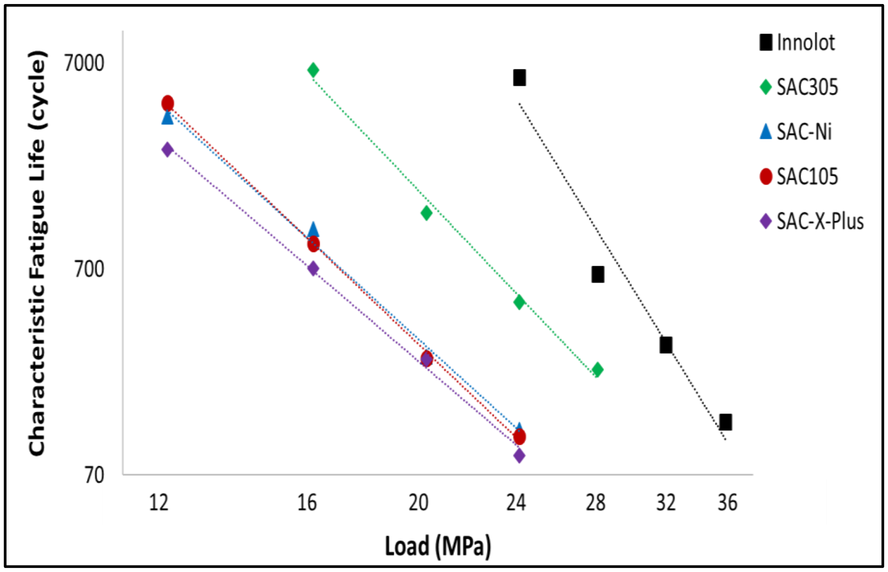

Figure 5.25 Characteristic life as a function of stress amplitudes under no-aging conditions

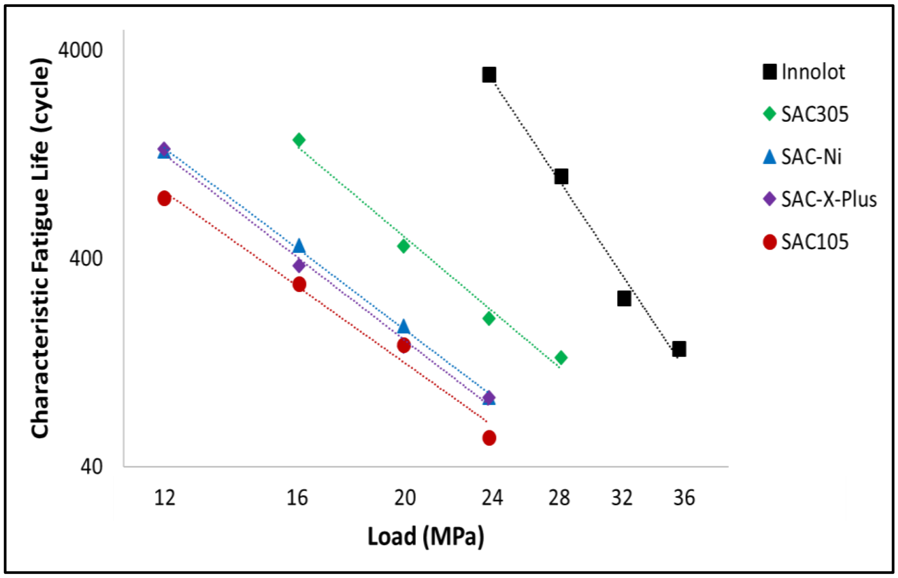

Figure 5.26 Characteristic life as a function of stress amplitudes after 4 years of room temperature aging

5.3 Effect of Room Temperature Aging on the Evolution of Hysteresis Loop

Figure 5.27 shows a hysteresis loop, or a stress-strain loop, for individual SAC305 solder joint cycled under 24MPa. Inelastic work per cycle and plastic strain range were determined based on the hysteresis loop. The inelastic work per cycle is the area enclosed within the loop, and the plastic strain is the width of the loop at 0MPa. The inelastic work per cycle was plotted continuously with the corresponding cycle number to have an inelastic work per cycle vs. characteristic fatigue life curve, as shown in Figure 5.28. Three main regions are detected in this work curve. Region 1 includes a rapid decrease in the work per cycle for the first few cycles due to the initial flattening and solder joint hardening. Region 2 accounts for about 90% of the total cycles and involves a steady-state level of the work per cycle. Region 3 accounts for around 10% of the total cycles and involves a continuous increase in the work per cycle until complete failure, which is mainly due to crack propagation.

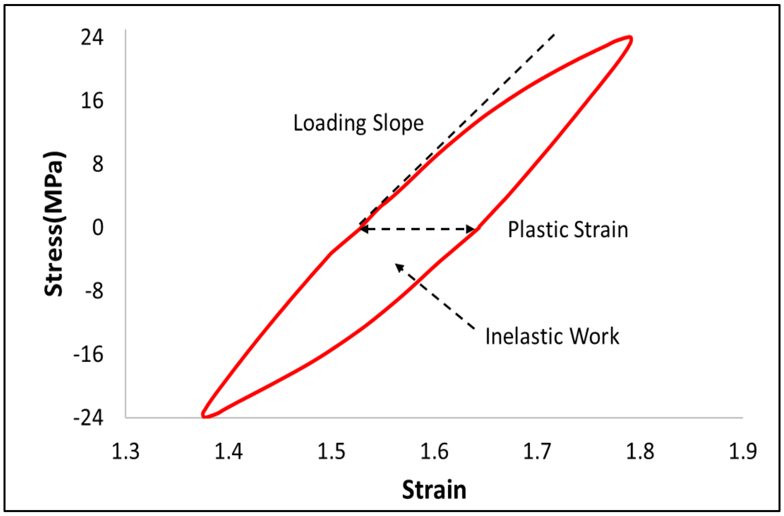

Figure 5.27 Hysteresis loop for a SAC305 solder joint cycled at 24 MPa

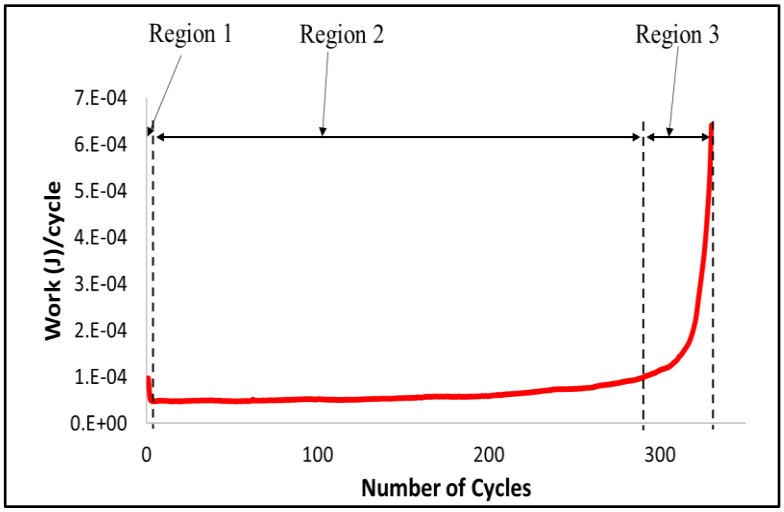

Figure 5.28 Inelastic work per cycle vs. the number of cycles for a SAC305 solder joint cycled at 24MPa

Figure 5.29 shows the effect of stress amplitude on the inelastic work per cycle vs. the number of cycles curve for SAC305 solder joints. As expected, larger stress amplitude lad to a larger inelastic work per cycle and consequently, smaller number of cycles to achieve complete failure. Figure 5.30 shows a comparison of the hysteresis loops in the steady-state region for SAC305 solder joints cycled at 4 different stress amplitudes. It was obvious that higher stress amplitude resulted in a higher inelastic work per cycle (larger area) and higher plastic strain range (wider loop).

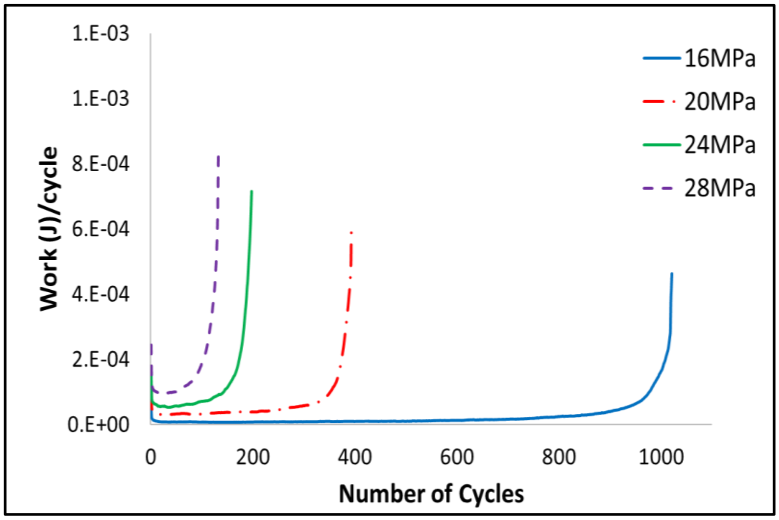

Figure 5.29 Inelastic work per cycle vs. the number of cycles for SAC305 solder joints at different stress amplitudes

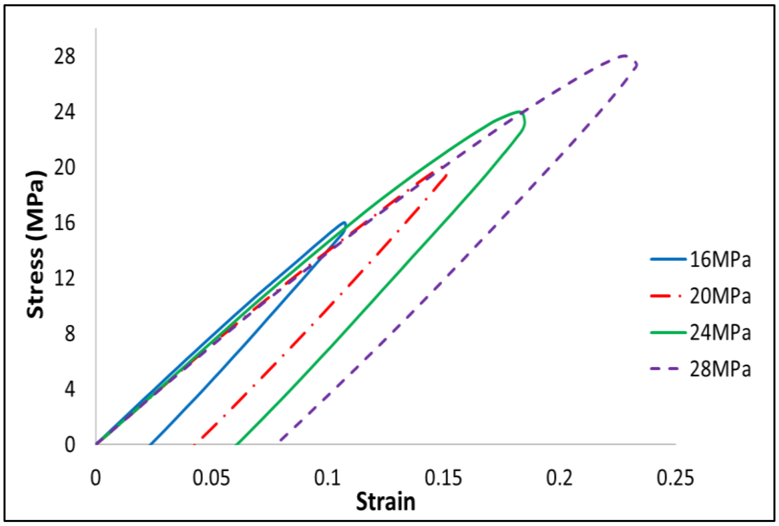

Figure 5.30 Hysteresis loops for SAC305 solder joints in the steady-state region for different stress amplitudes

Figures 5.31, 5.32, and 5.33 show that the evolution of hysteresis loops before and after 4 years of room temperature aging for SAC105, SAC305 and Innolot solder joints. Representative loops for each solder alloy are selected based on the requirement that the inelastic work for the given representative loop that is closest to the average inelastic work of 7 replicates tested under the same stress amplitude. From those figures, we can observe that aging lad to an increase of inelastic work (the area enclosed in the hysteresis loop) and plastic strain for SAC105, SAC305, and Innolot solder alloys. The same trends were seen for SAC-Ni and SAC-X-Plus solder alloys as well.

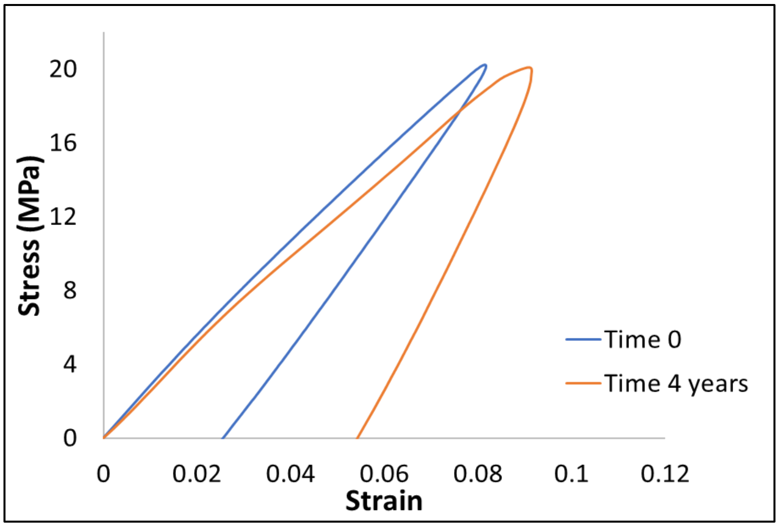

Figure 5.31 Comparison of hysteresis loops for SAC105 solder joints cycled at 20 MPa before and after aging

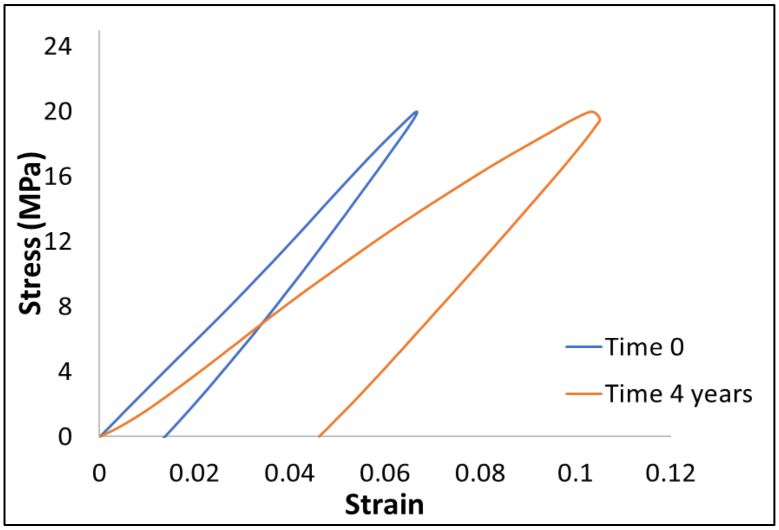

Figure 5.32 Comparison of hysteresis loops for SAC305 solder joints cycled at 20 MPa before and after aging

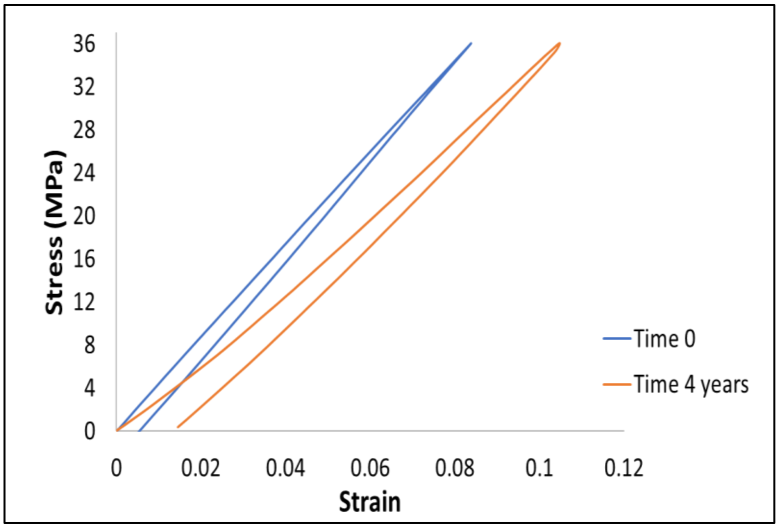

Figure 5.33 Comparison of hysteresis loops for Innolot solder joints cycled at 36 MPa before and after aging

The characteristic fatigue life (N_{63}) under different stress amplitudes has been correlated with average inelastic work per cycle (W) shown in Figures 5.34-5.38 for SAC305, SAC105, SAC-Ni, SAC-X-Plus, and Innolot, respectively. The value of average inelastic work per cycle (W) was calculated as the area within the hysteresis loop in the steady-state region for a given stress amplitude. For each type of solder alloys under both aging conditions, the N_{63} vs. W was shown as a nearly linear correlation when plotted on a log-log scale. With R^2 larger than 98% for most of the cases, this suggests the Morrow energy fatigue equation [76] can accurately represent the following data:

$$N_{63}^{m}\, W = C \tag{5.2}$$

$$N_{63} = C^{\frac{1}{m}} W^{\frac{-1}{m}} \tag{5.3}$$

Where N_{63} is the characteristic fatigue life of solder joint (cycles to failure), W is inelastic work per cycle. C and m are the fatigue ductility and fatigue exponent respectively.

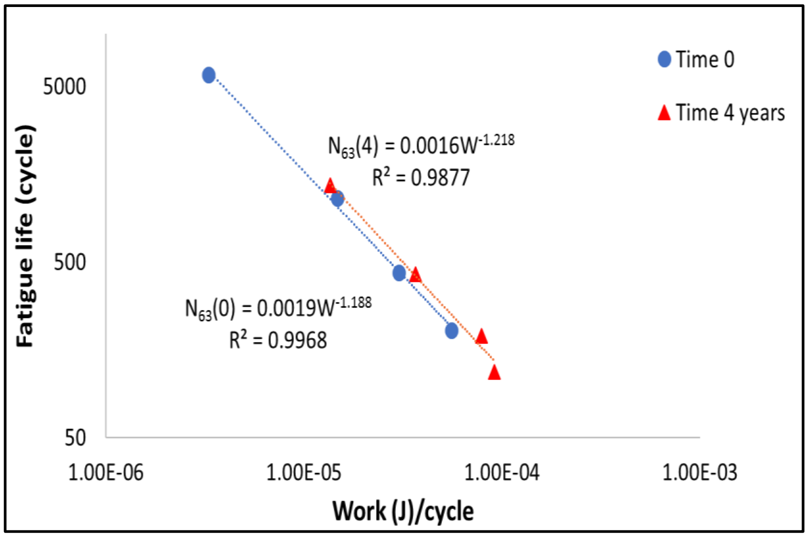

Figure 5.34 Characteristic fatigue life vs. Inelastic work per cycle for SAC305 solder joints with 2 aging conditions

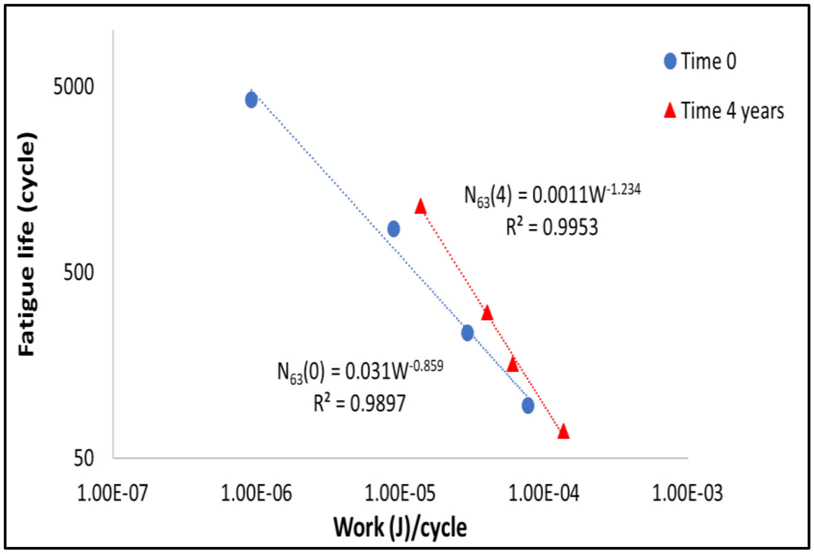

Figure 5.35 Characteristic fatigue life vs. Inelastic work per cycle for SAC105 solder joints with 2 aging conditions

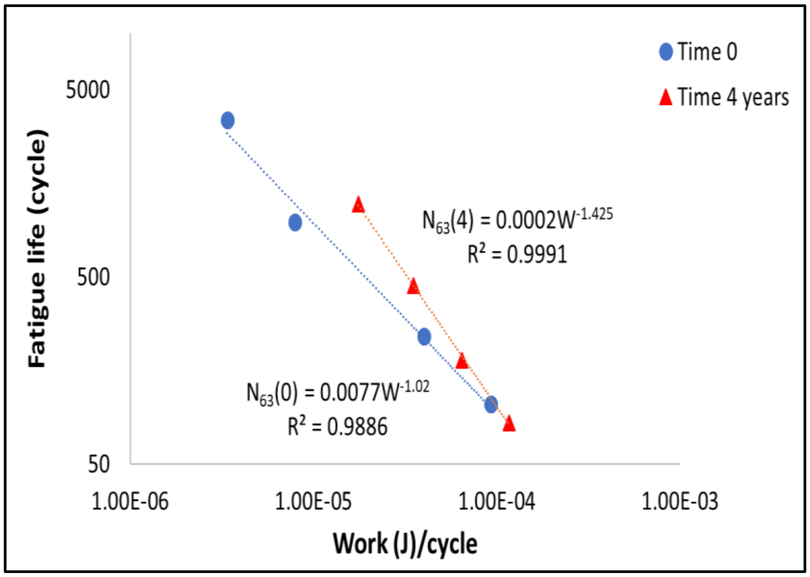

Figure 5.36 Characteristic fatigue life vs. Inelastic work per cycle for SAC-Ni solder joints with 2 aging conditions

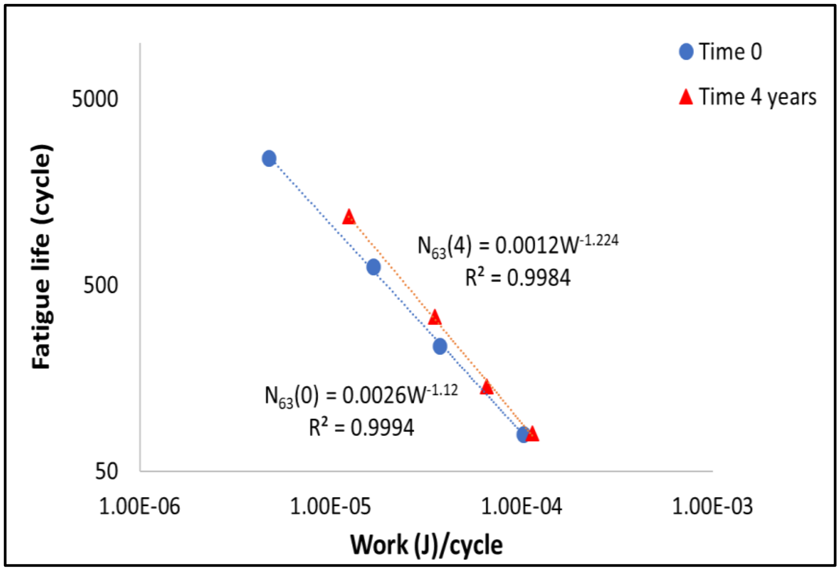

Figure 5.37 Characteristic fatigue life vs. Inelastic work per cycle for SAC-X-Plus solder joints with 2 aging conditions

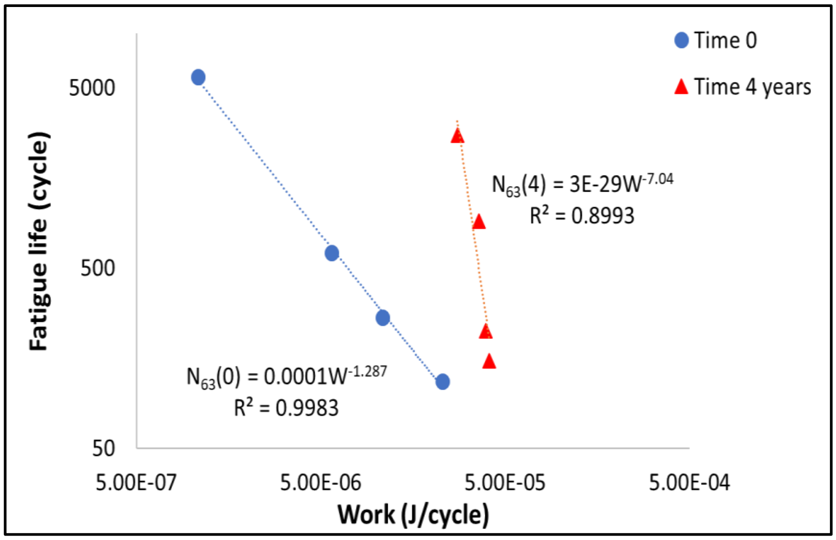

Figure 5.38 Characteristic fatigue life vs. Inelastic work per cycle for MaxRel (Innolot) solder joints with 2 aging conditions

The Morrow fatigue model coefficients m and C, calculated by the least-square regression analysis, are shown in Table 5.2. Generally, the fatigue exponent m and the fatigue ductility C decreased after 4 years of aging. From Figures 5.39-5.43, we can observe that for SAC305 solder alloy, the Morrow model fits are almost parallel because of the similar values of fatigue exponent m. The largest shift happens for Innolot solder joints. The material ductility coefficient for Innolot decreased by a factor of 8 and the fatigue exponent decreased by a factor of 6 after exposure to room temperature aging for 4 years.

Table 5.2 Morrow Model Coefficients for 5 solder alloys

	Fatigue Ductility, C		Fatigue Exponent, m	
	Time 0	**Time 4 years**	**Time 0**	**Time 4 years**
SAC305	0.0051	0.0050	0.8418	0.8210
SAC105	0.0175	0.0040	1.1641	0.8104
SAC-Ni	0.0085	0.0025	0.9804	0.7018
SAC-X-Plus	0.0049	0.0041	0.8929	0.8170
Innolot	0.0008	0.0001	0.7770	0.1420

Same fatigue data was recast to correlate the characteristic fatigue life (N_{63}) to plastic strain (ε_p) for all alloys as shown in Figures 5.17. For each type of the solder alloy under both aging conditions, the N_{63} vs. ε_p is shown as a nearly linear correlation when plotted on a log-log scale. The Coffin-Manson fatigue law was used to fit the data.

$$N_{63}^{\alpha}\varepsilon_p = \theta \tag{5.4}$$

$$N_{63} = \theta^{\frac{1}{\alpha}}\varepsilon_p^{\frac{-1}{\alpha}} \tag{5.5}$$

Where ε_p is the plastic strain range, N_{63} is the characteristic fatigue life (cycles to failure). α is fatigue exponent and θ is the fatigue ductility coefficient.

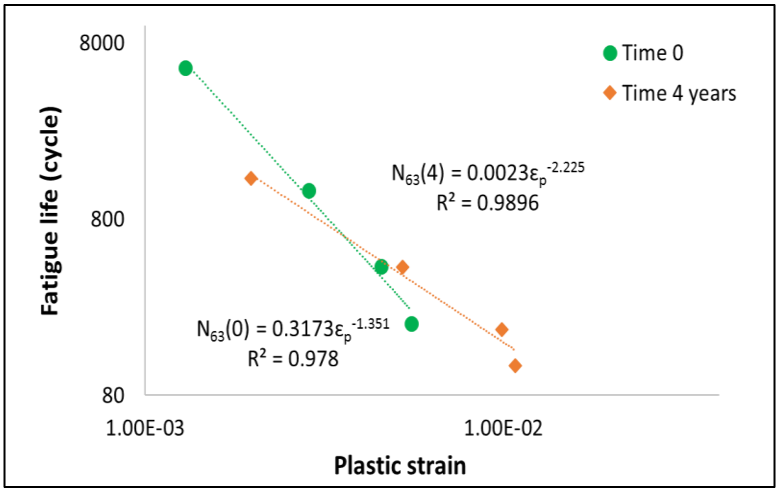

Figure 5.39 Characteristic fatigue life vs. plastic strain for SAC305 solder joints with 2 aging conditions

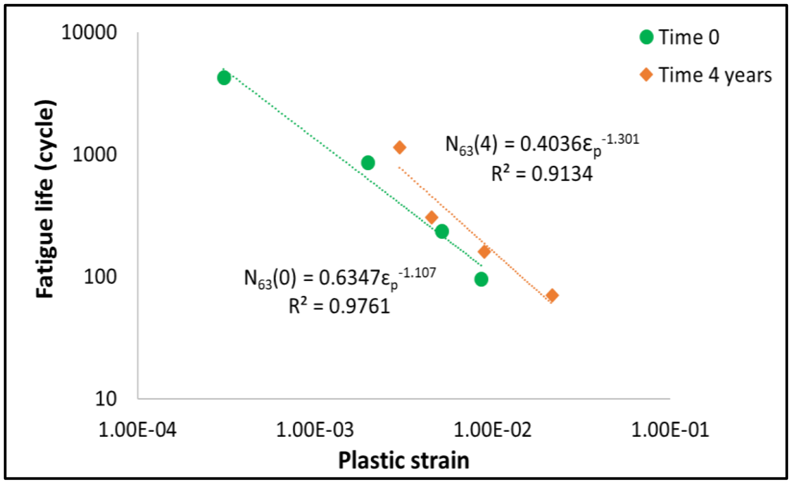

Figure 5.40 Characteristic fatigue life vs. plastic strain for SAC105 solder joints with 2 aging conditions

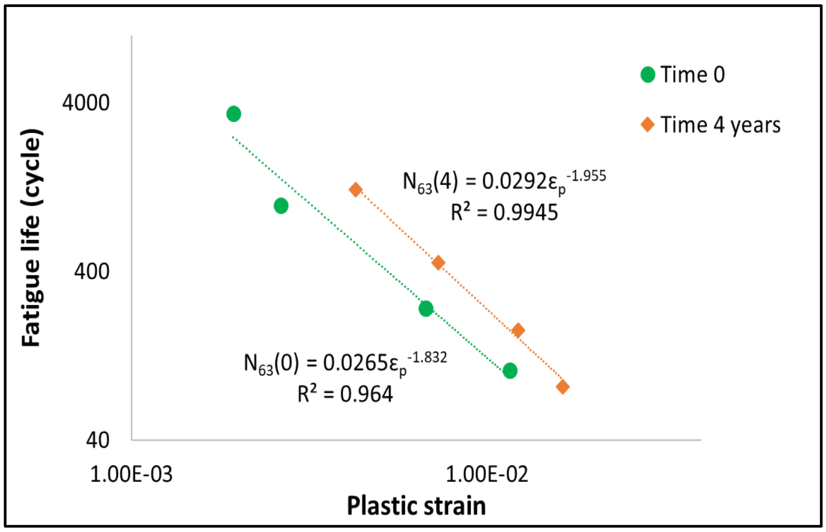

Figure 5.41 Characteristic fatigue life vs. plastic strain for SAC-Ni solder joints with 2 aging conditions

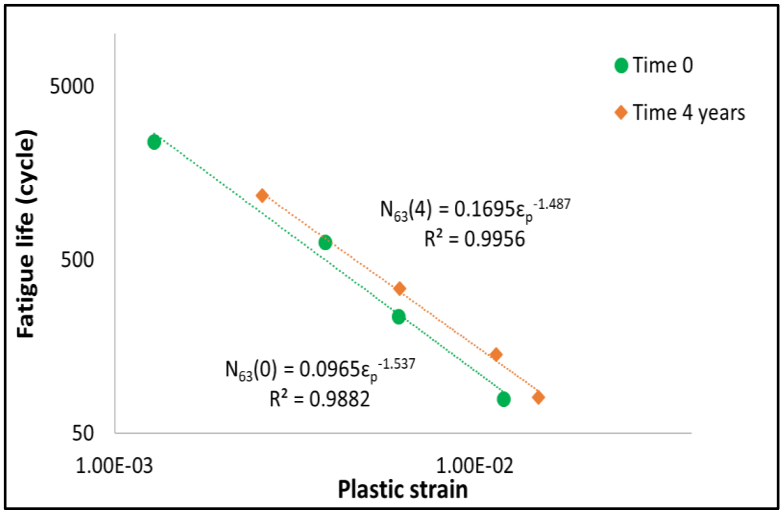

Figure 5.42 Characteristic fatigue life vs. plastic strain for SAC-X-Plus solder joints with 2 aging conditions

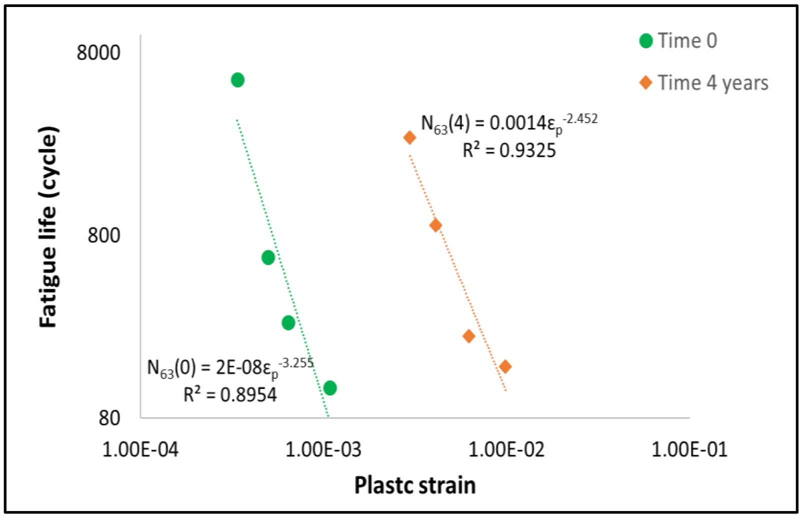

Figure 5.43 Characteristic fatigue life vs. plastic strain for MaxRel (Innolot) solder joints with 2 aging conditions

The Coffin-Manson model coefficients α and θ, calculated by the least-square regression analysis, are shown in Table 5.3. From Figures 5.17, we can observe the Coffin-Manson model fits are almost parallel because of the similar values of fatigue ductility exponent α. The largest shift happens for Innolot solder alloy, similar to that of the Morrow model. The fatigue ductility coefficient of Innolot decreased by a factor of 40 after exposure to room temperature for 4 years.

Table 5.3 Coffin-Manson Coefficients for 5 solder alloys

	Fatigue Ductility Coefficient, θ		**Fatigue Exponent, α**	
	Time 0	**Time 4 years**	**Time 0**	**Time 4 years**
SAC305	0.0652	0.4276	0.4494	0.7402
SAC105	0.6632	0.4979	0.9033	0.7686
SAC-Ni	0.1378	0.1641	0.5459	0.5115
SAC-X-Plus	0.2184	0.3031	0.6506	0.6725
Innolot	0.0017	0.0686	0.3072	0.4078

Chapter 6 Effect of Surface Finish on the Shear Properties of SnAgCu-Based Solder Alloys

6.1 Introduction

Ball Grid Array (BGA) components with lead free solder joints have been very popular within the past decade given their superior advantages over other surface mount components. However, reliability concerns have arisen with further investigation of the mechanical properties of lead-free solder joints [82-85]. Solder joints tend to fail easily when being exposed to the thermal or mechanical cycling environment given the strain damage caused by the mismatch of Coefficient of Thermal Expansion (CTE) between the Printed Circuit Board (PCB) and BGA component materials [80, 84-90]. The reliability of solder joints can be improved by doping, or micro-alloying, small percentages of rare-earth elements such as Ni, Bi, In, Mg, and Co into the bulk of the solder joint [91, 92]. It has been reported that the doping can improve the tensile and shear strengths, and fatigue resistance [83, 87, 93-96]. Ma, et al. found that adding Bi to the solder joints leads to increase the IMC layer thickness and increase the shear strength. The fracture mode also changed from ductile to mixed ductile-brittle fracture with increasing the amount of Bi [97]. As reported by Zhou et al., the addition of Bi could increase the Ultimate Tensile Strength (UTS). However, if Bi content exceeds 4%, the results are reversed, given excess Bi tends to embrittle the solder joints [98]. Gao, et al. indicated SnAgCu (SAC) solder joint with 1% Ni increases the shear strength [93].

Similarly, as stated by Li, et al., the addition of Sb could increase Ultimate Tensile Strength (UTS), and UTS reaches the maximal with 1% of Sb content in Sn3.5Ag0.7Cu solder alloys [99].

Another influential factor of the solder joint reliability is the surface finish on the Cu pads [100-108]. Surface finish has proven to be effective in terms of preventing the oxidation of Cu pads [104], improving wettability [102], and protecting the pads from corrosion [106]. Moreover, the formation of the Intermetallic Compound (IMC) on solder joints is strongly affected by the type of surface finishes [104]. Different types of surface finishes lead to different IMC layer thickness [109]. The growth of IMC in a reasonable range is beneficial to the reliability of solder joints, since it creates a firmer bond between solder joints and the Cu pad underneath. However, the excessive growth of IMC turns out to be detrimental because the brittle nature of IMC will strongly degrade the mechanical properties of the solder joints. Organic Solderability Preservative (OSP), Immersion Silver (ImAg) and Electronic Ni/Au (ENIG) are commercially available choices of surface finishes [101]. OSP surface finish has no metal content and is mainly used to prevent the copper pads from oxidation without affecting the metallurgy of the solder joint [110]. ImAg surface finish provides good solderability with relatively a cheaper cost. However, neither OSP nor ImAg surface finish has a good shelf life and is more vulnerable to contamination under room temperature storage. ENIG surface finish provides excellent solderability, good tarnish resistance, and longer shelf life. A nickel layer is used as a diffusion barrier to prevent the Cu from diffusing into solder alloy, therefore, effectively control the growth of IMC during thermal environments. Gold is plated on the nickel layer in order to improve the wettability and increase the corrosion resistance. Upon many advantages, the brittle failure of the ENIG surface finish has been observed [104, 105, 107, 108]. A premature failure by apparent delamination between the solder joints and the nickel layer was observed with ENIG surface finish [111, 112]. However, no study was focused on investigating the effect of surface finish on the mechanical properties of the doped lead-free solder joints.

In this chapter, the effect of common surface finishes, including OSP, ImAg, and ENIG, on the mechanical shear properties of doped lead-free solder joints is investigated. Since the solder alloys are viscoelastic material, the shear tests were done at different four shear strain rates (speed of shear). Five different doped solder alloys were used with the three surface finish. The shear strength and shear energy were measured and correlated to the microstructural analysis of the fracture surfaces as well.

6.2 IMC Morphology Characterization

During the reflow process, OSP surface finish either decomposes or reacts with flux, and IMC grows at the interface between the solder alloy and the copper pad. Figure 6.1 shows a typical cross-section view of SEM micrograph of interfacial microstructure for CycloMax solder alloy with OSP surface finish. Scallop-shape Cu_6Sn_5 IMC was detected along the Cu pad. For ImAg surface finish, the similar morphology was observed. Ag layer deposited on top of the Cu pad was dissolved into the molten solder during the initial reflow, so IMC grew at the interface between solder alloys and the Cu pad. As shown in Figure 6.2, a SEM micrograph of interfacial microstructure for CycloMax solder alloy with ImAg surface finish, scallop-shape a Cu_6Sn_5 IMC was detected on the interface. In the case of the ENIG surface finish, the Au layer on the top was dissolved into solder alloy during reflow, leaving the Ni layer exposed to the molten solder. Therefore, the Ni atom from the Ni layer reacted with Cu and Sn from the solder alloy. As indicated in Figure 6.3, a SEM micrograph of interfacial microstructure for CycloMax solder alloy with ENIG surface finish, $(Ni, Cu)_6Sn_5$ was observed. It is worth mentioning that the Ni layer in-between the IMC and the Cu pad served as a diffusion barrier, which prevented the Cu pad atom from diffusing into the solder alloy. Therefore, most of the Cu atoms in the (Ni, Cu)$_6$Sn$_5$ IMC layer are initiated from the solder alloy instead of the Cu pad. The observations of the IMC morphology aligned with the previous research.

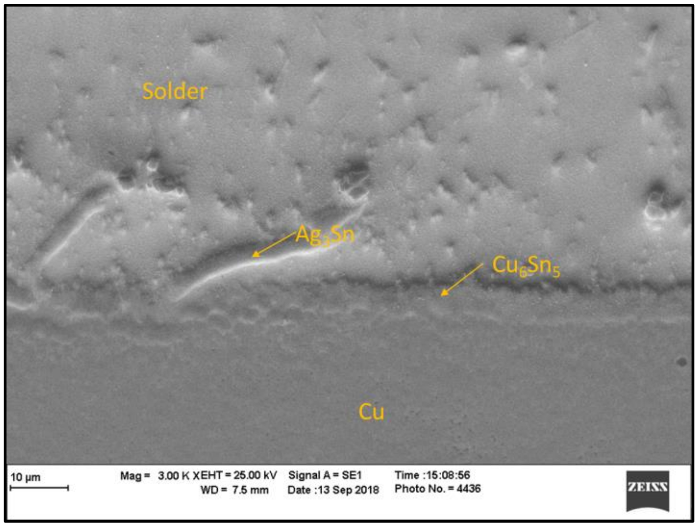

Figure 6.1 IMC morphology of OSP surface finish with CycloMax solder alloy

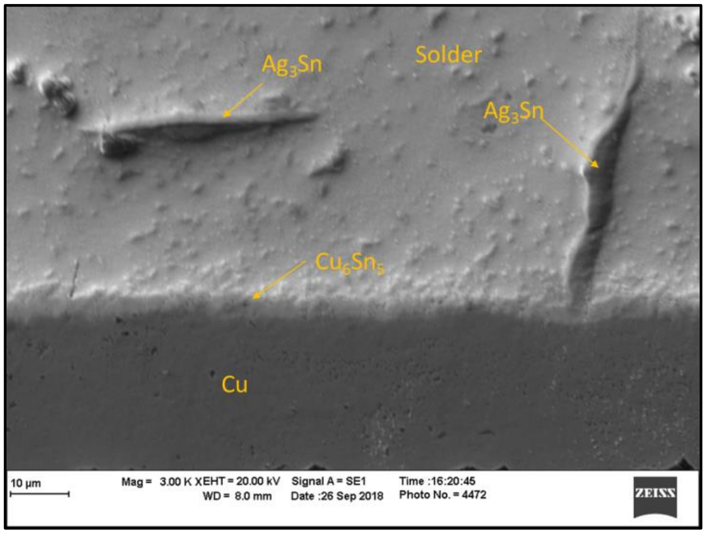

Figure 6.2 IMC morphology of ImAg surface finish with CycloMax solder alloy

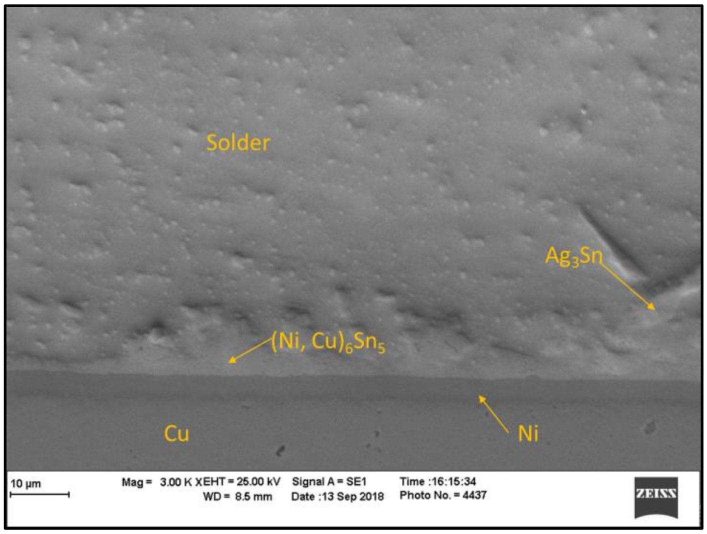

Figure 6.3 IMC morphology of ENIG surface finish with CycloMax solder alloy

The size and distribution of Ag_3Sn second precipitates were also affected by the types of surface finishes. As shown in Figures 6.1-6.3, the needle-like, big planate shape Ag_3Sn precipitates only appeared at the interfacial region of the solder joint. Since Ag atoms from the ImAg surface finish would diffuse into solder alloys during reflow, an increase of Ag content at the interfacial region resulted, which lead to a corresponding increase of size and distribution of Ag_3Sn precipitate as shown in Figure 6.2. Since the intermetallic compounds (Ag_3Sn, Cu_6Sn_5, $(Ni, Cu)_6Sn_5$) have higher strength and modulus than β-Sn, a higher concentration of IMC particles in a reasonable range would increase the effective modulus of solder joints. On another hand, a coarsening of the second precipitates (because of aging or numbers of reflow) would drive a significant reduction of solder joint strength.

6.3 Shear Strength Results

Average shear strength of doped solder alloys is plotted as a function of shear strain rate with various surface finishes (Figures 6.4 to 6.8). Shear strength (τ) could be expressed in terms of applied shear strain rate (γ) in an approximately power equation:

$$\tau = \mathrm{a}\,[\ln(\gamma)]^{b} \tag{6.1}$$

where a and b are material condition constants.

It is evident from Figures 6.4-6.8, shear strength increased with the increase of shear strain rate due to the viscoplastic property of solder alloys. Shear strength vs. strain rates data fits equation 1 with a high R^2 value. The ImAg surface finish demonstrated the best shear strength for SAC305, Ecolloy, and SAC-X-plus solder alloys, followed by an OSP surface finish. The OSP surface finish was observed to have the best shear strength for Innolot and CycloMax, followed by ImAg. The ENIG surface finish demonstrated the least shear strength among the 5 solder alloys. Moreover, for Innolot and CycloMax solder alloys with ENIG surface finish, shear strength slightly increased with the increase of strain rates, and it is significantly lower than that of OSP and ImAg surface finishes at all strain rates.

After that, a two-way ANOVA was conducted firstly on SAC305 to investigate whether the shear strength of typical solder material was influenced by the two influential factors (shear strain rate/ surface finish). Based on the results, all the effects including shear strain rate, surface finish, and the interaction were all statistically significant (p=0.000, 0.001, 0.037). Given the presence of an interaction, simple main effects were needed to be investigated. In this study, the effect of single surface finish (OSP, ImAg, ENIG) on the shear strength under various shear strain rates was investigated, and the results showed they all the surface finishes demonstrated statistically significant impact on the shear strength result (p values were all less than 0.05).

After SAC305, two-way ANOVA was also conducted on Innolot solder alloys, where the mechanical behavior was different than SAC305 to investigate whether the shear strength of that was influenced by the two influential factors (surface finish/shear strain rate), or if there is still an interaction on both effects. Like the result for SAC305, both factors and the interaction were all statistically significant (p=0.000, 0.000, 0.000). However, when investigating the single surface finish effect on the shear strength, OSP and ImAg showed statistically significant differences of the means of shear strength, while the result for ENIG surface finish was not statistically significant (p=0.987). Analysis of variances tables were attached in Appendix B (Table B1-B3)

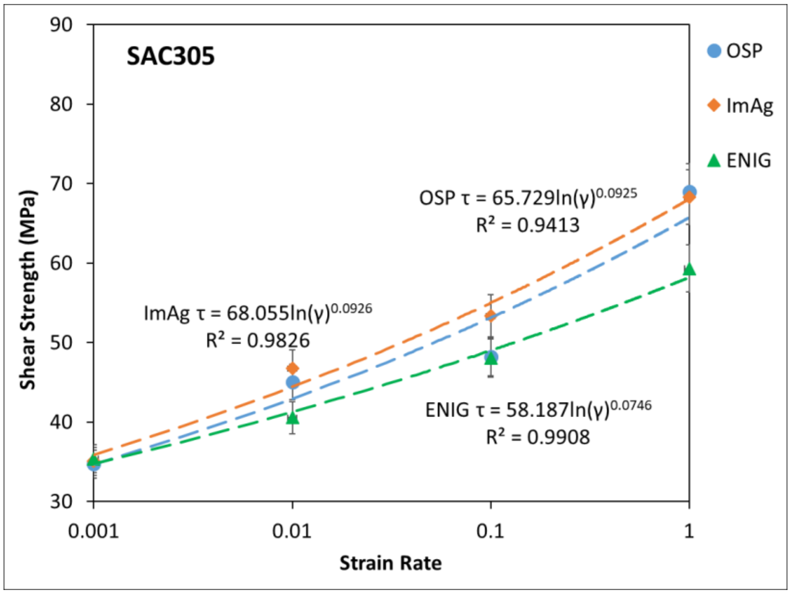

Figure 6.4 Shear strength vs. strain rate for SAC305 solder alloy

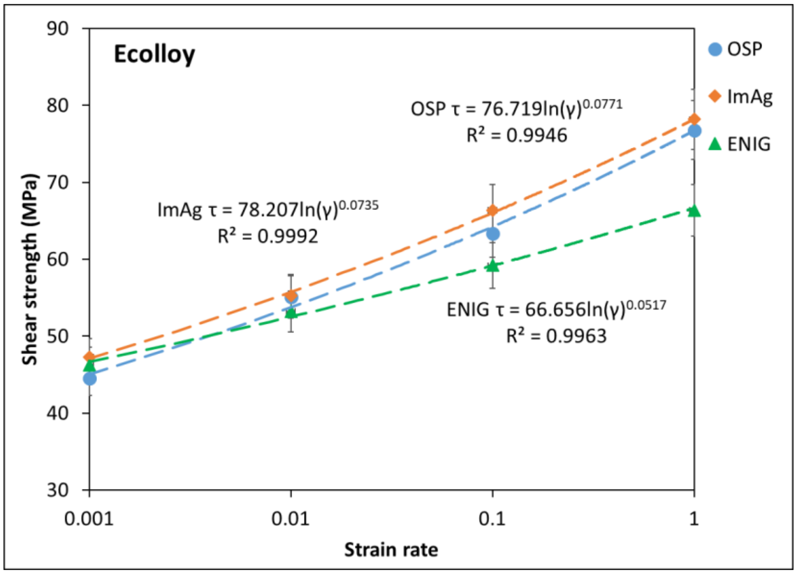

Figure 6.5 Shear strength vs. strain rate for Ecolloy solder alloy

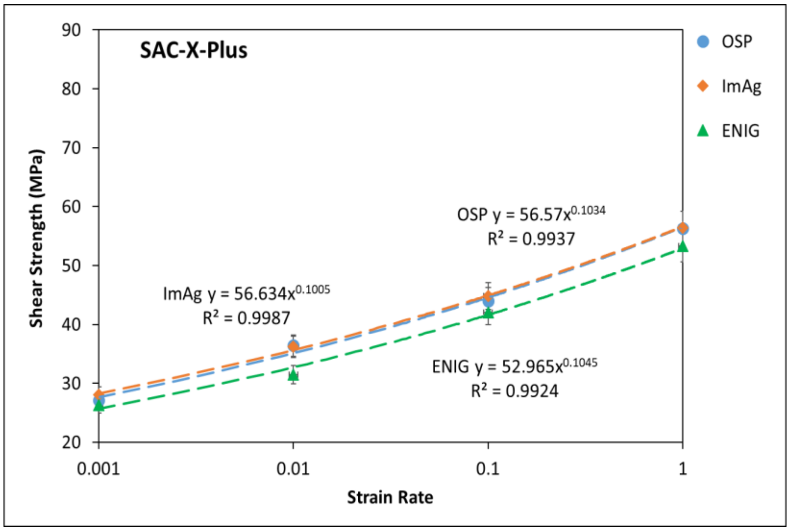

Figure 6.6 Shear strength vs. strain rate for SAC-X-Plus solder alloy

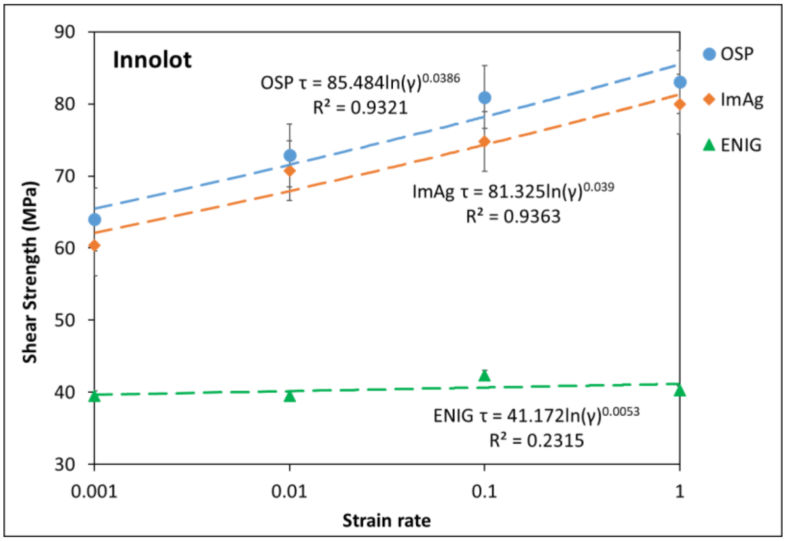

Figure 6.7 Shear strength vs. strain rate for Innolot solder alloy

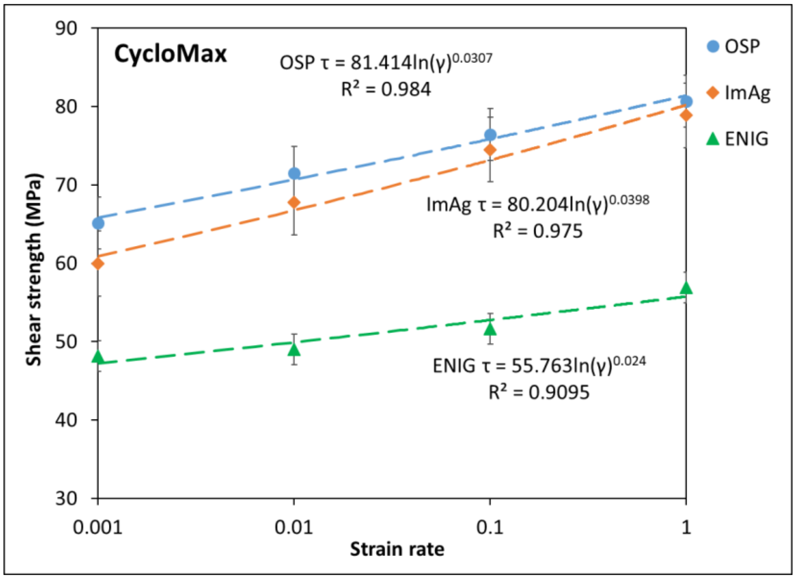

Figure 6.8 Shear strength vs. strain rate for CycloMax solder alloy

Figures 6.9 and 6.10 further expounded this situation, where shear strengths of 5 different solder alloys associated with 3 different surface finishes were compared at the 2 extreme strain rates (the slowest: γ=0.001sec^{-1}, the fastest γ=1sec^{-1}). At the 0.001sec^{-1} strain rate, CycloMax and Innolot demonstrated better shear strengths with OSP and ImAg surface finishes. For the ENIG surface finish, Ecolloy replaced Innolot in the second place. At 1sec^{-1} strain rate, Innolot and CycloMax still demonstrated the better two shear strengths for OSP and ImAg. However, the differences in shear strength among solder alloys were reduced. For the ENIG surface finish, shear strengths for CycloMax and Innolot were further degraded, and Ecolloy had the highest shear strength. Summaries of the constants a and b for the 5 solder alloys with 3 surface finishes were shown in Table 6.1.

After that, one-way ANOVA test was conducted to test the equality of means and to assess the differences between pairs of means among various solder types.

At the highest shear rate 1sec^{-1}, shear strength with various solder alloy types was compared at ImAg, OSP, and ENIG surface finish. At ImAg surface finish, the p value for shear strength of one-way ANOVA is less than 0.05 (p=0.000), which indicated that the mean differences between each solder alloy is statistically significant. Then the Tukey comparisons results were tested to see whether the differences between a pair of solder alloys were statistically different. Tukey simultaneous confidence interviews showed that the ranges for SAC-X-Plus with CycloMax, Innolot, SAC305, Ecolloy, SAC305 with CycloMax, Innolot, and Ecolloy doesn’t include zero, which indicated that the differences between those means were significant. The confidence intervals for the remaining pairs of means all included zero, which indicated the differences were not statistically different. Three groups were detected: Group A: Innolot, CycloMax, Ecolloy; Group B: SAC305; Group C: SAC-X-Plus. At OSP surface finish, the p value for shear strength ANOVA was also less than 0.05 (p=0.000), which indicated that the mean differences between each solder alloy was statistically different. Tukey simultaneous confidence interview showed that pairs between SAC-X-Plus with Innolot, CycloMax, SAC305, and Ecolloy, SAC305 with Innolot and CycloMax were statistically different. Three groups were detected: Group A: Innolot, CycloMax, Ecolloy; Group B: Ecolloy, SAC305; Group C: SAC-X-Plus. Moreover, at ENIG surface finish, the p value for shear strength ANOVA was less than 0.05 as well (p=0.000), indicated that there was statistically different between each solder alloy. Tukey simultaneous confidence interview showed that pairs between CycloMax with Ecolloy, Innolot, Innolot with CycloMax, SAC305, SAC-X-Plus, Ecolloy were statistically significant between each other. Three groups were detected: Group A: Ecolloy, SAC305; Group B: SAC305, CycloMax and SAC-X-Plus; Group C: Innolot (analysis tables were attached in Appendix B).

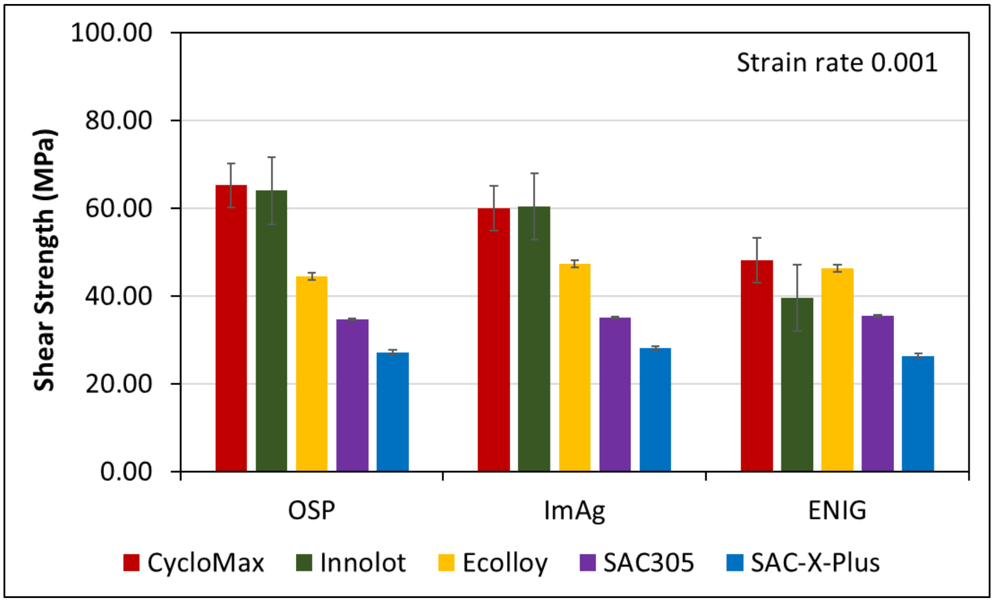

Figure 6.9 Shear strength comparison (γ=0.001sec-1)

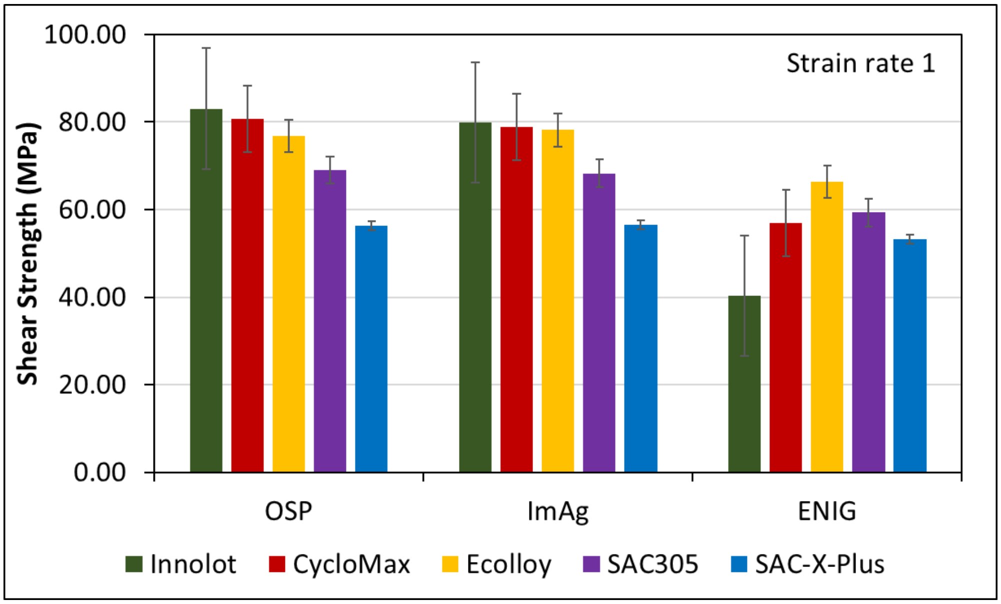

Figure 6.10 Shear strength comparison (γ=1sec-1)

Table 6.1 Summary of shear strength constants

	Constant a			**Constant b**		
	ImAg	**OSP**	**ENIG**	**ImAg**	**OSP**	**ENIG**
SAC305	68.06	65.73	58.19	0.093	0.093	0.075
Ecolloy	78.21	76.72	66.66	0.076	0.077	0.052
SAC-X-Plus	56.63	56.57	52.96	0.100	0.103	0.105
CycloMax	80.20	81.41	55.76	0.04	0.031	0.024
Innolot	81.33	85.48	41.17	0.039	0.039	0.005

An analysis of variance (ANOVA) was conducted to further investigate the effect of surface finish and solder alloy selection on the shear strength. In particular, the main effect analysis was conducted to examine those 2 effects separately as shown in Figure 6.11. During the main effect analysis, the impact factors (surface finishes, and solder alloys) were analyzed one at a time, ignoring the influences from the remaining factors. The OSP and ImAg surface finishes were associated with a higher shear strength compared to the ENIG surface finish. CycloMax solder alloy was associated with the highest shear strength and SAC-X-Plus was associated with the lowest shear strength. An interaction analysis was conducted to study the interaction effects between 2 impact factors jointly, as shown in Figure 6.12. Innolot and CycloMax with OSP surface finish were associated with the heighest shear strength, while Innolot and SAC-X-plus with ENIG surface finish were associated with the lowest shear strength.

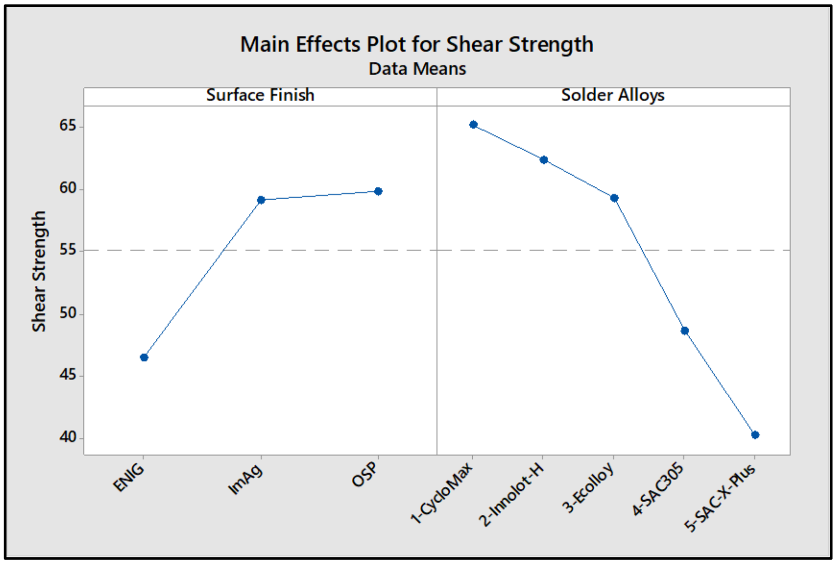

Figure 6.11 Main effect analysis for shear strength

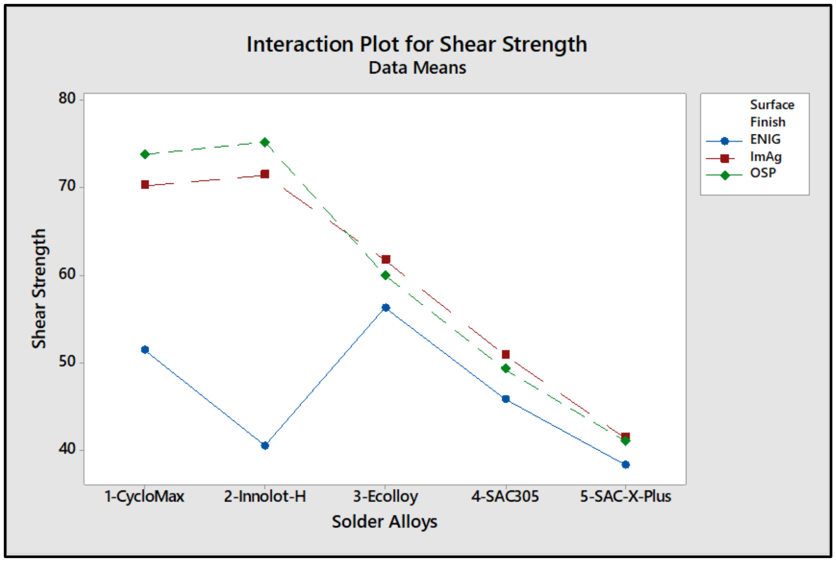

Figure 6.12 Interaction analysis for shear strength

Figure 6.13 shows the shear strength comparisons for an ImAg surface finish when considering the effect of Bismuth (Bi) and Silver (Ag). Solder alloys with higher Bi and Ag content (Innolot & CycloMax) demonstrated better shear strength compared to solder alloy that only contains Bi (Ecolloy) or Ag (SAC305). The solder alloy with the lowest Bi and Ag content (SAC-X-Plus) demonstrated the least shear strength. From the literature, it was indicated that small additions of

Bi would dissolve into the Sn matrix and improve the strength [98, 113]. Adding certain larger atoms (e.g. Bismuth, Antimony, Indium, etc.) would distort to the Sn crystalized lattice when dissolving in the Sn matrix, which would result in blocking the movement of dislocation cell structure and slowing down the deformation of solder alloys by ‘solid solution hardening [114]’, thus improving the mechanical properties and increasing the durability. Since the Ag_3Sn is the only phase containing Ag in the SAC solder alloy, increasing the Ag content leads to a corresponding increase of Ag_3Sn precipitates, thus improve the strength of the solder alloy [115, 116]. After that, a one-way ANOVA was conducted to test the equality of means and to assess the differences in pairs of groups. The p-value for the ANOVA is less than 0.05 (p=0.000), which indicated that there were statistically significant differences among the three groups (solder alloy with high Bi & Ag, with higher Bi or Ag, or without higher Bi and Ag). Tukey test demonstrated that none of the confidence interview for the pairs of groups contained zero, which indicated that all of the pairs of groups were statistically different between each other, while solder alloys with higher Ag and Bi demonstrated the best shear strength (analysis table was attached in Appendix B).

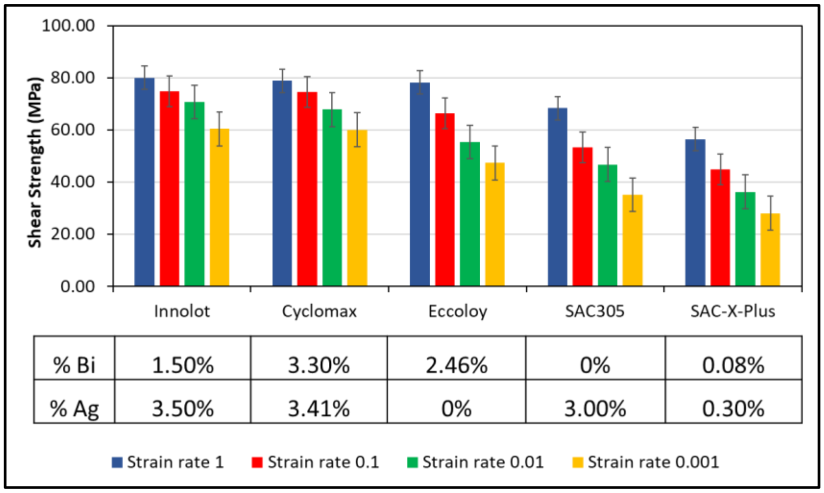

% Bi	1.50%	3.30%	2.46%	0%	0.08%
% Ag	3.50%	3.41%	0%	3.00%	0.30%

Figure 6.13 Effect of Bi & Ag on the shear strength with ImAg surface finish

6.4 Shear Failure Modes Analysis

In this investigation, shear testing was evaluated both quantitatively (shear strength and shear energy) and qualitatively (failure modes). Specifically, failure modes of shear testing were categorized into three groups: ductile failure, brittle failure, and mixed failure. Since Solder-Mask-Define (SMD) pads were used and the relatively lower shear strain rate, no pad lifting failure was observed. Ductile and brittle failures could be easily determined by observing the shape of stress-strain curves. Stress-strain curve for ductile failure was identified by a steep force increasing as the shear probe contacted the solder joint up to a peak (ultimate shear point), then followed by a long smooth decrease in force as the ductile bulk solder was pushed by the shear probe. In contrast, the stress-strain curve for brittle failure was identified by a steep force increased to a peak, followed by a sharp drop in force as solder joints were quickly fractured from the Cu pad. Typical stress-strain curves for ductile and brittle failures were shown in Figure 6.14.

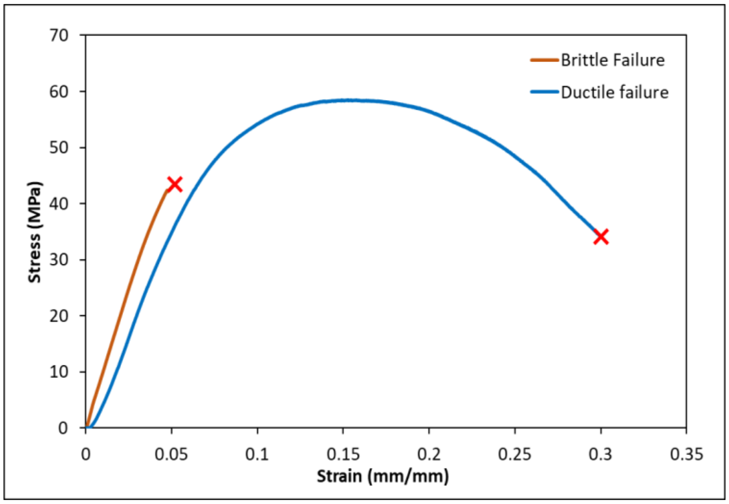

Figure 6.14 Typical stress-strain curve

Cross-section view and failure surface of the ductile failure are shown in Figures 6.15 and 6.16. A portion of solder remained on top of the Cu pad when the majority of solder joint was sheared off which indicates crack propagation through the bulk solder, indicating a transgranular failure. This is the desired failure mechanism because it shows a robust interconnection between the solder joint and the Cu pad. Ecolloy, SAC305, and SAC-X-Plus with three surface finishes showed ductile failures for all of the strain rates. Innolot and CycloMax with OSP and ImAg surface finishes showed ductile failures at lower strain rates. Typical stress-strain curves for ductile failure with various shear strain rates were shown in Figure 6.17.

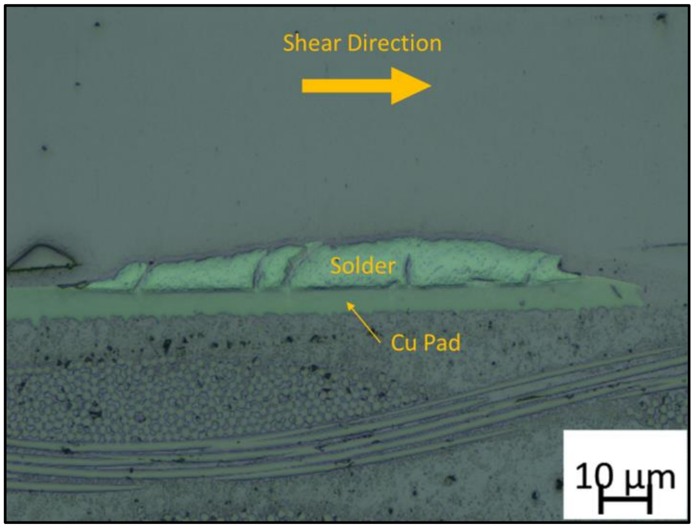

Figure 6.15 Cross-section view of ductile failure

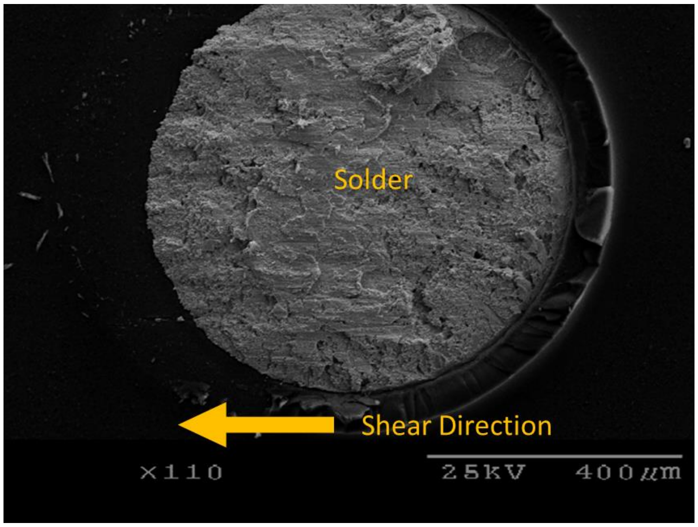

Figure 6.16 Top view of the fracture surface of the ductile failure

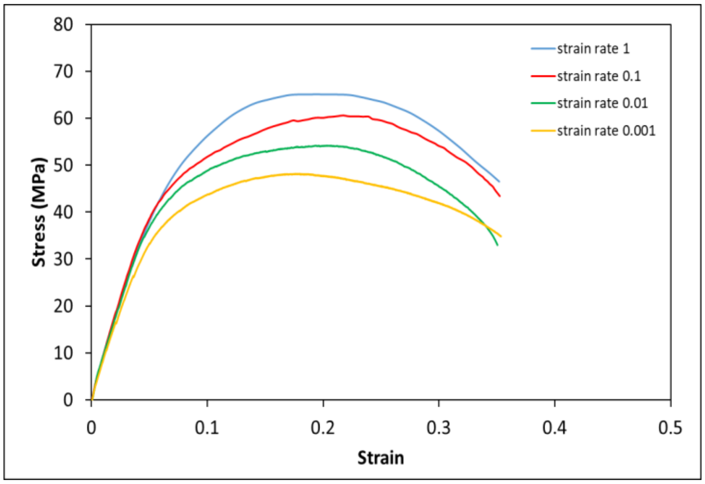

Figure 6.17 Stress-strain curves for ductile failure of SAC305 with OSP surface finish

Figure 6.18 and 6.19 showed the cross-section view and the fracture surface of the brittle failure that associated with CycloMax solder joint with ENIG surface finish. A clean separation of the CycloMax solder joint from the Cu pad surface was observed, leaving mainly a Ni layer from the ENIG surface finish and less amount of (Ni, Cu)$_6$Sn$_5$ IMC on top of the Cu pad, which indicated that the fracture propagated between the IMC and Ni layers. Figure 6.20 showed the stress-strain curves of the typical brittle failure at various strain rates. The brittle failure mode was dominant at all strain rates for Innolot and CycloMax with ENIG surface finish.

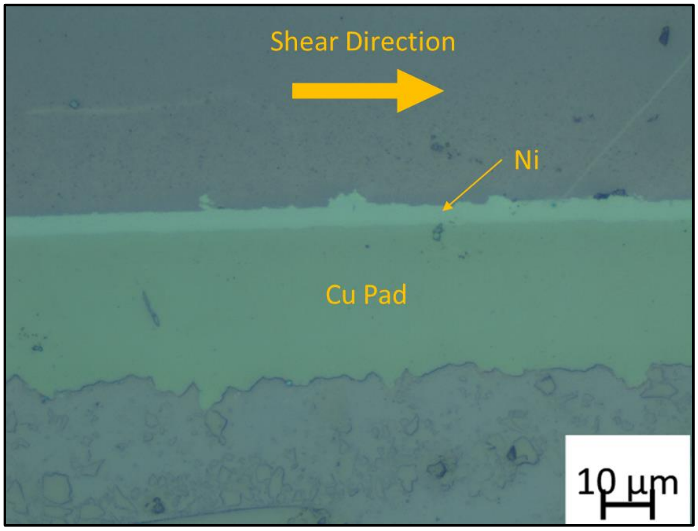

Figure 6.18 Cross-section view of the brittle failure with ENIG surface finish

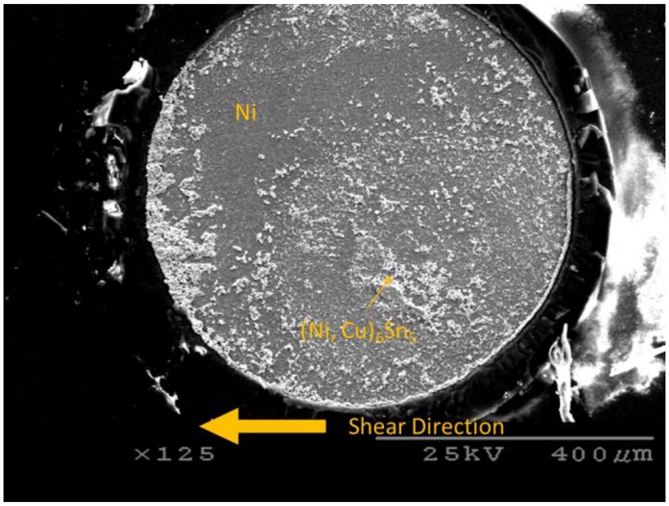

Figure 6.19 Top view of the fractured surface of the brittle failure for ENIG surface finish

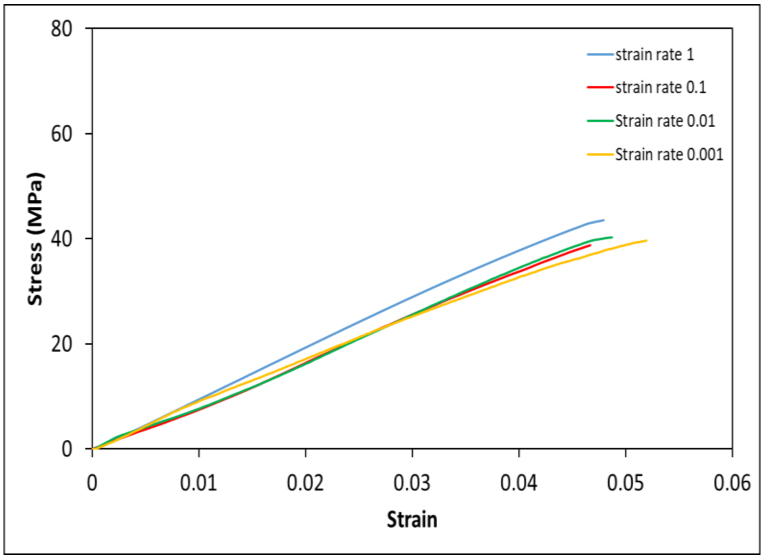

Figure 6.20 Stress-strain curves for brittle failure of CycloMax with ENIG surface finish

Beside the ENIG surface finish, brittle failure was also observed for OSP and ImAg surface finishes with CycloMax alloy when tested at the highest shear strain rate (1 sec^{-1}). Figure 6.21 and 6.22 shows the cross-section view and the fracture surface of the brittle failure of CycloMax with OSP surface finish. Based on the EDS analysis, a portion of Cu_6Sn_5 IMC left after solder joint was sheared off, indicating a separation happened between IMC and Cu pad.

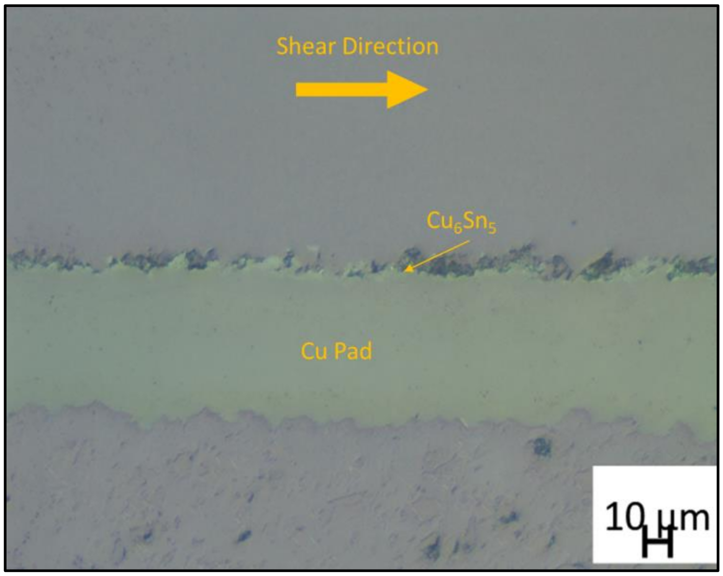

Figure 6.21 Cross-section view of brittle failure with OSP surface finish

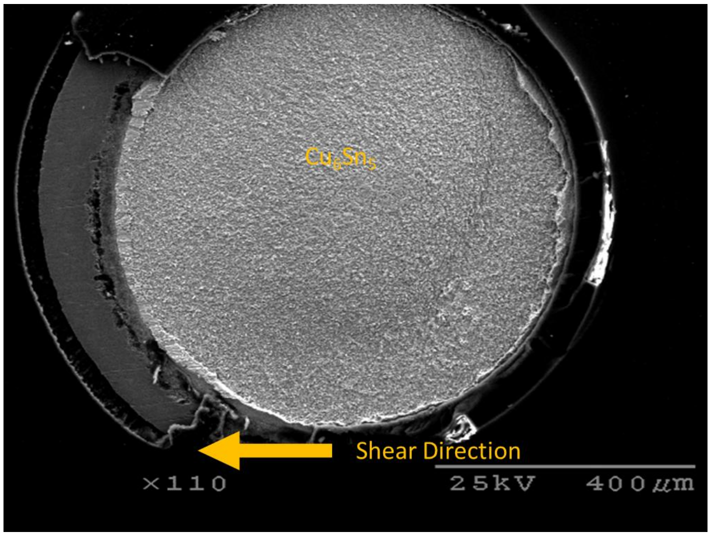

Figure 6.22 Top view of the fractured surface of the brittle failure for OSP surface finish

The third failure mode was a mix of both ductile and brittle failure as shown in Figures 6.23 and 6.24. The fracture surface of the mixed failure displays both properties of ductile failure (Cu pad covered by solder) and brittle failure (only Cu_6Sn_5 IMC left on the Cu pad), which indicates that the solder joint is in a transitional state between the two distinguished failure modes during shear testing. Stress-strain curves of the mixed failure mode for CycloMax with OSP surface finish were shown in Figure 6.25. At 0.1sec^{-1} strain rate, both the shapes of brittle and ductile curves were detected. Pure brittle failure was observed for strain rates larger than 0.1sec^{-1}, and pure ductile failure was observed for strain rates less than 0.1sec^{-1}. In conclusion, for OSP and ImAg surface finishes with CycloMax or Innolot solder alloys, a transition from ductile failure to brittle failure was observed with the increase of shear strain rate. For ENIG surface finish with those solder alloys, brittle failure resulted regardless of strain rates. These observations were in agreement with previous reports [102-104, 107, 108].

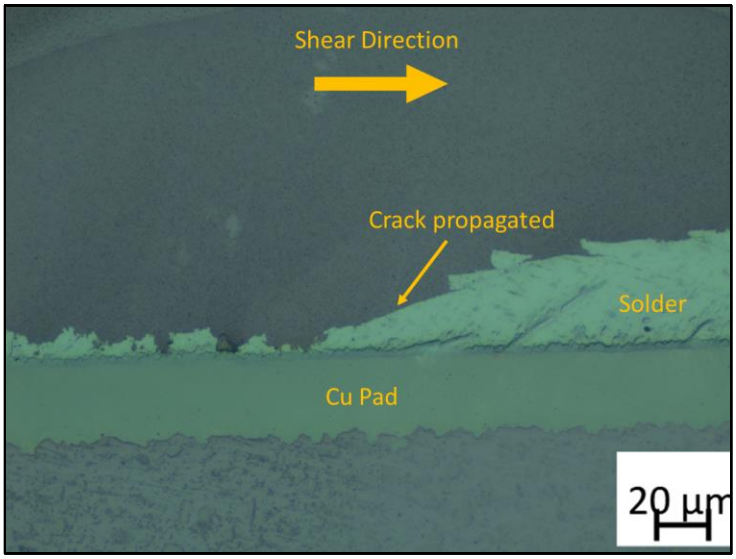

Figure 6.23 Cross-section view of the mixed failure mode

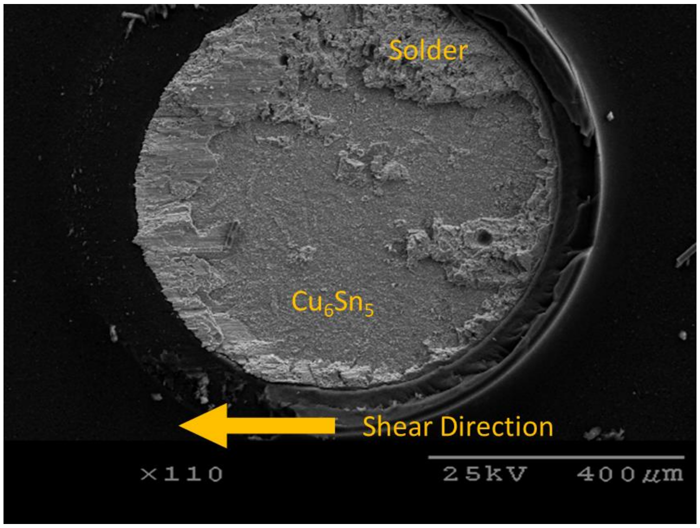

Figure 6.24 Top view of the fractured surface of the mixed failure mode for OSP surface finish

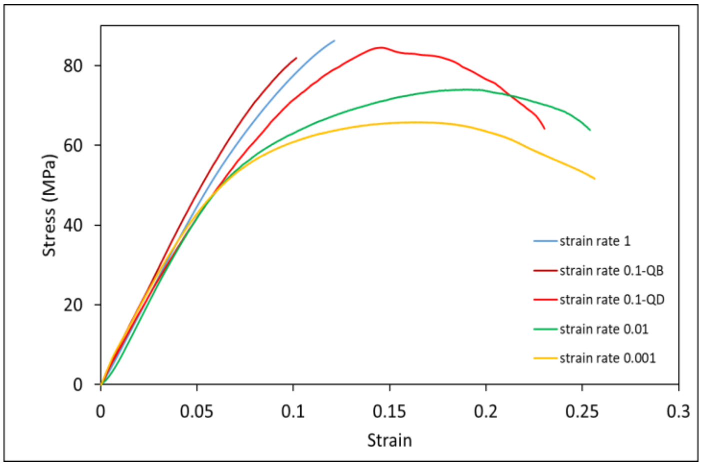

Figure 6.25 Stress-strain curves of the mixed failure mode of CycloMax with OSP surface finish

A flow stress theory was provided by Erich [117] explaining the differences in solder joint behaviors (failure modes) in response to various surface finishes and strain rates. During shear testing, a bulk solder flow stress received from the shear probe is compared among copper peel strength and intermetallic strength, where the flow stress of bulk solder is dependent on the speed of shear testing due to the viscoplastic property of solder alloy. The goal is to find the "weakest interconnection" of solder joints, where the fracture is suspected to initiate from and propagate. When the copper peel strength is less than the bulk solder flow stress, a pad cratering failure occurs.

When the flow stress of bulk solder is less than either peel stress or intermetallic stress, the fracture will propagate within the bulk solder, which leads to the occurrence of a ductile failure.

CycloMax and Innolot are strong alloys due to the high percentage of Ag and Bi content. Therefore, their intermetallic strength turns out to be the lowest, and thus the separation between the IMC and the Cu pad was observed for OSP and ImAg surface finishes, and the separation between the IMC and Ni layer was observed for the ENIG surface finish. For the mixed failure though, differences between bulk solder flow stress and intermetallic strength are minimal, tiny changes of stress near the interface, because of microvoids or impurities of materials, can lead to a change of failure mode, where part of the Cu pad shows ductile failure while the other part shows brittle failure.

6.5 Shear Energy Results

Shear energy was measured as the integrated area under the stress-strain curve [105, 118] as another method to evaluate the shear test. Shear energy was plotted as a function of the shear strain rate, as shown in Figures 6.26 to 6.30. For the solder alloys that exhibit ductile failure (SAC305, Ecolloy, and SAC-X-Plus), shear energy increased with the increase of shear strain rate. ImAg surface finish demonstrated the largest shear energy among those solder alloys, followed by OSP, then ENIG. Trends observed from shear energy vs. strain rate was consistent with those observed from shear strength vs. strain rate. The two failure modes (ductile vs. brittle) were observed from shear energy vs. strain rate plots for Innolot and CycloMax with 3 surface finishes as separated by a red dash line. Shear energy data above that line represented a ductile failure, while below represented a brittle failure. For the ductile failure, shear energy still increased as the increase of strain rates due to the viscoplastic behavior of the bulk solder. For the brittle failure part, shear energy was much lower than that of ductile failure. Shear energy for OSP and ImAg surface finish remained almost the same, which indicated a similarity in intermetallic toughness (between IMC and the solder joint) for both surface finishes. The ENIG surface finish exhibited much lower shear energy, which implied a weaker interfacial toughness (between Ni layer and IMC) compared to OSP or ImAg surface finish. Transition failure mode was detected as both failure modes were observed from the same strain rate (Figures 6.29 and 6.30).

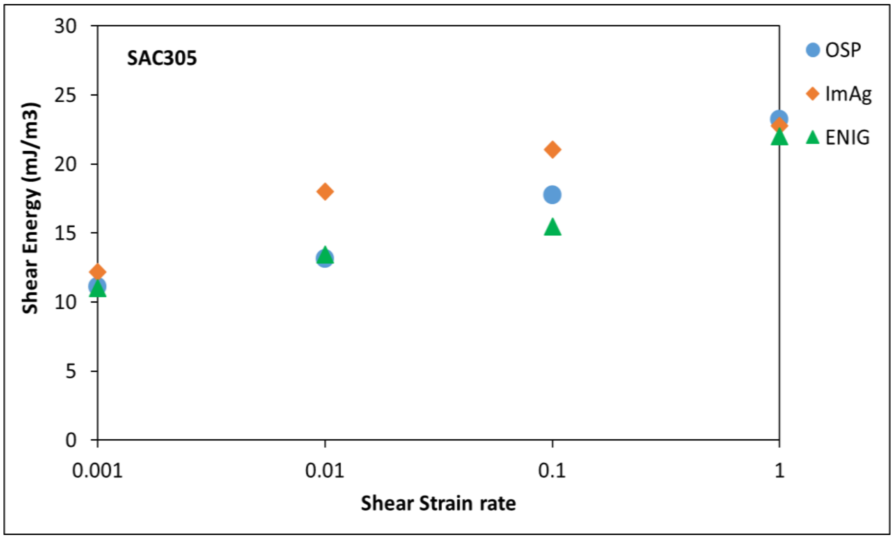

Figure 6.26 SAC305 solder alloy shear energy vs. strain rate

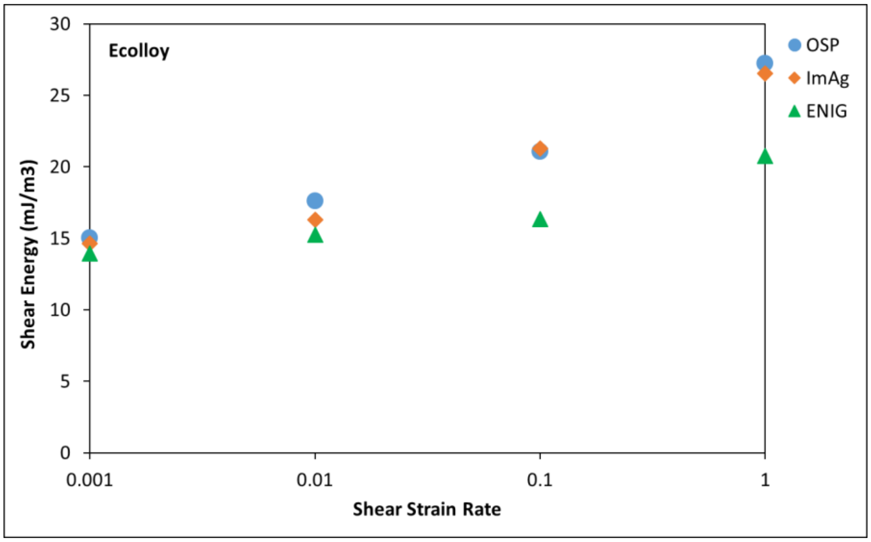

Figure 6.27 Ecolloy solder alloy shear energy vs. strain rate

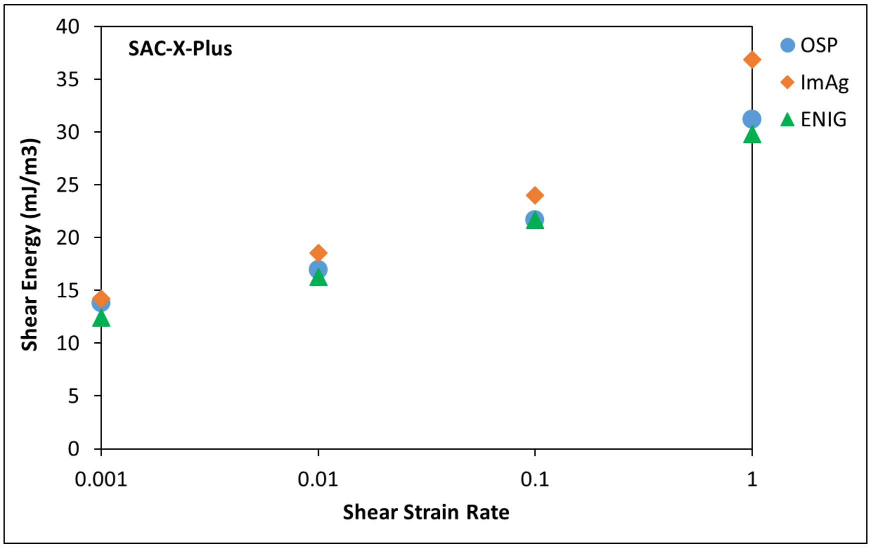

Figure 6.28 SAC-X-Plus solder alloy shear energy vs. strain rate

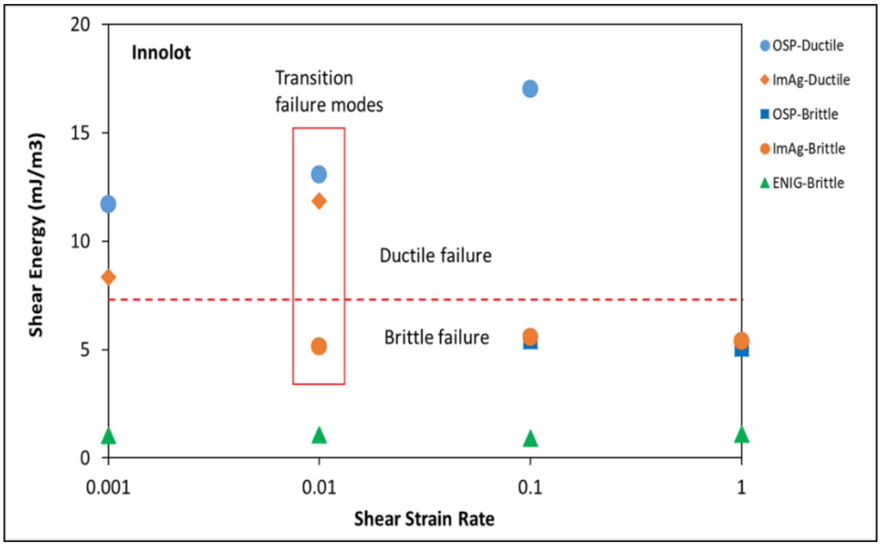

Figure 6.29 Innolot solder alloy shear energy vs. strain rate

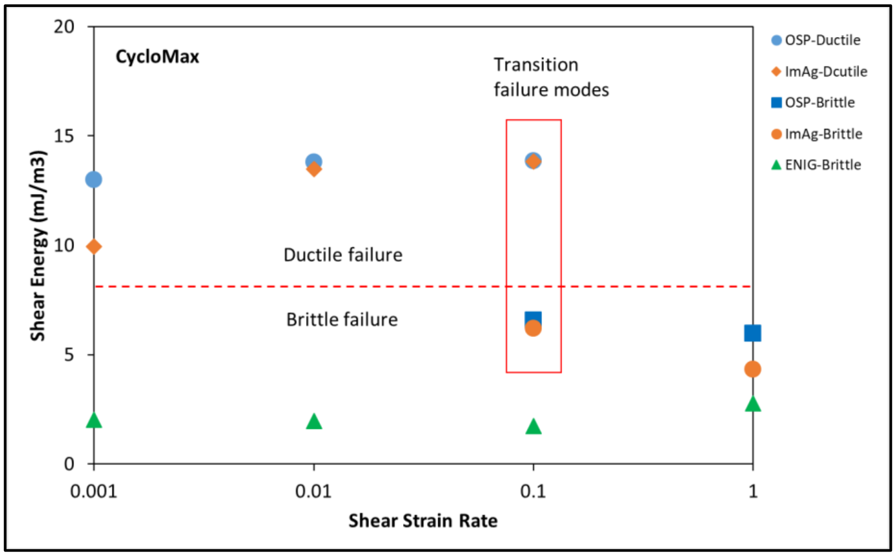

Figure 6.30 CycloMax solder alloy shear energy vs. strain rate

In addition, shear energy was viewed as a more sensitive quantitative way in detecting the failure modes over shear strength [105]. As shown in Figure 6.14, the shear strength of ductile failure was only 25% larger than that of brittle failure, while shear energy of ductile failure could be many times more than brittle failure. Moreover, it was found that failure modes correlated better with shear energy than with shear strength [118, 119]. As shown in Figures 6.31-6.33, shear energy was compared to shear strength with various solder alloys for ImAg, OSP, and ENIG surface finishes, respectively. Taking the ImAg surface finish (Figure 6.31) as an example, CycloMax and Innolot solder alloy at higher strain rates (1, 0.1 sec^{-1}) still demonstrated high shear strength, while failure modes had shifted from ductile failure to brittle failure based on the microstructure analysis. In contrast, we can identify the shift of failure modes from shear energy by observing an unusual shear energy drop for CycloMax and Innolot at higher strain rate instructed by the red arrow. A similar situation was observed from OSP and ENIG surface finishes as well, where significant shear energy drops between CycloMax and Innolot indicating the occurring of brittle failure.

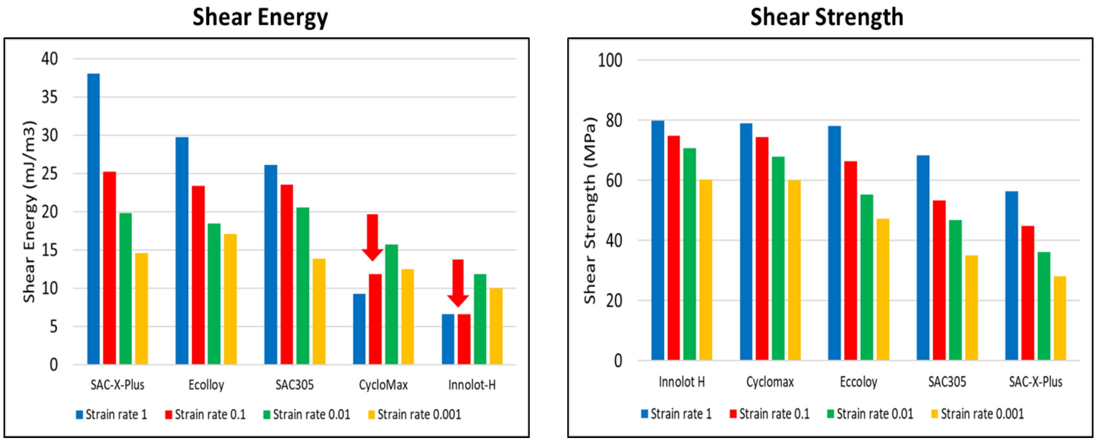

Shear Energy

Shear Strength

Figure 6.31 Shear energy vs. shear strength comparisons for ImAg surface finish

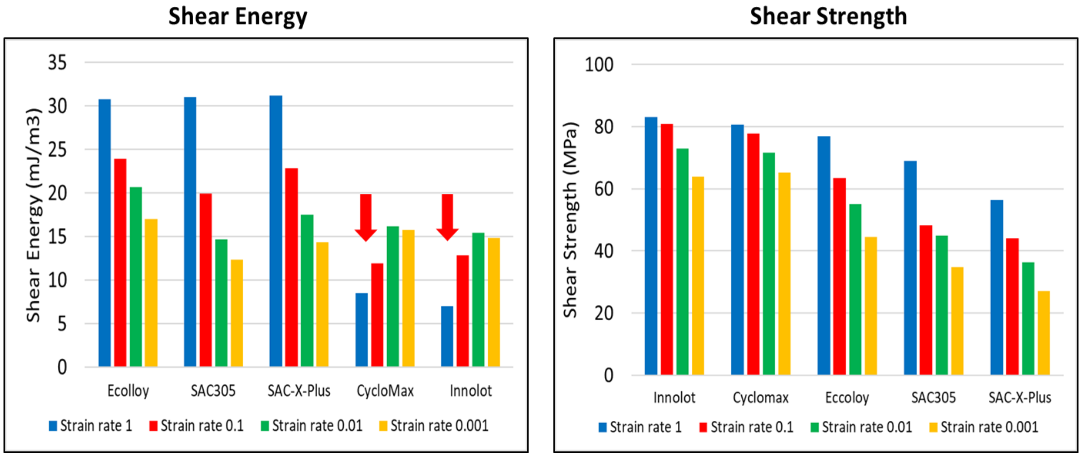

Shear Energy

Shear Strength

Figure 6.32 Shear energy vs. shear strength comparisons for OSP surface finish

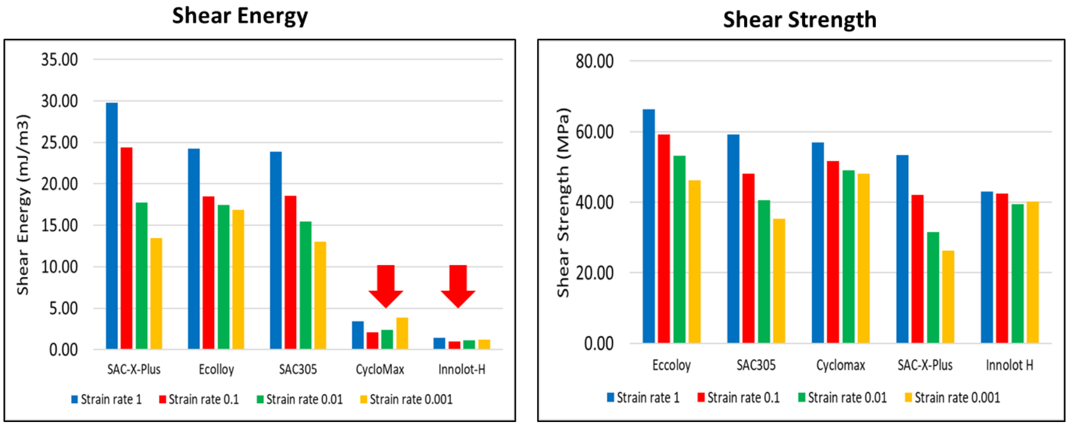

Shear Energy

Shear Strength

Figure 6.33 Shear energy vs. shear strength comparisons for ENIG surface finish

Chapter 7 Effect of Surface Finish on the Reliability of SnAgCu-Based Solder Alloys Under Fatigue Test

7.1 Introduction

The reliability of an electronic assembly is normally limited by the fatigue failure of one of the solder interconnections under long-term service conditions. Since lead (Pb) in the traditional eutectic tin/lead solder alloy has been banned under regulations proposed in Japan and the EU (RoHS and WEEE), the electronic packaging industry has moved to lead-free electronics. Currently, SnAgCu (SAC) family has become the most popular solder choice in the market. However, it is well recognized that the characteristic behaviors of SAC-based solder alloy are much more complex and haven't been thoroughly studied compared to the traditional tin/lead solder alloy [120]. SAC-based solder alloys have shown many favorable characteristics such as excellent wettability and fair reliability, which make them effective solder alloys and potential candidates to replace eutectic tin/lead solder alloy. However, questions still exist for the reliability of lead-free solder materials under long-term extreme service conditions. Therefore, a fundamental understanding of parameters that would have affected the behaviors of lead-free solder materials under long-term extreme environments is essential before manufacturers can use these solders without any reliability concerns.

For SAC-based solder joints in realistic applications, they are typically exposed to cyclic loading, either through thermal cycling or mechanical cycling. In general, the failure mechanisms for thermal cycling is totally different from mechanical cycling. In cases of thermal cycling, failure is caused by the mismatches of the coefficient of thermal expansion (CTE) between board and package. Based on the damage accumulation model proposed by Liang, et al., during thermal cycling, precipitates coarsening, and recrystallization starts at the corner of a joint where the stress concentration is the highest. Global recrystallization is accomplished by crack initiation and propagation. Finally, a complete crack propagates through the whole recrystallized region along the grain boundaries. However, the isothermal mechanical cycling does not lead to the major recrystallization as in thermal cycling. Transgranular failure was the dominant failure mode for the isothermal mechanical cycling, where the crack goes through the bulk solder. Cracks nucleate at defects (scratches or voids) or because of the plastic deformation induced by the cyclic loading. As provided by Andersson et al., the crack propagation path varies depending on the strain range level. Cracks tend to propagate through the bulk of solder joints at high strain ranges whereas cracks propagate along the interface and the bulk solder at lower strain ranges [6].

Currently, accelerated testing was widely used to predict the service life of microelectronic products. However, results of accelerated testing would be misleading, even useless if the testing could not reflect the performance in service. Bulk sample (e.g., dog-bone shape sample) has been used for years in testing the mechanical and fatigue behaviors of solder materials, and an inherent assumption is made that relations developed for the bulk sample can be directly applied to the solder joint, independent of sample size and microstructure. However, studies have revealed that mechanical and fatigue behaviors of bulk samples are different from actual solder joints. This is mainly due to the different microstructures, geometry sizes and pad finishes [121]. Since the solder joint demonstrates a much more complex structure, by testing the bulk sample, several vital factors are ignored that can affect the fatigue behaviors of solder joints [6]. Solder joints in as-received condition can consist of either single Sn grain or three grains ‘cyclically twined’ into a beach ball structure [122]. Studies have confirmed that shear fatigue behavior of SnAgCu solder joints heavily depends on the number and the orientation of the Sn grains. The formation of intermetallic compounds (IMC) between solder joints and substrates (or surface finishes) has been proven to impact the fatigue life of solder joints. By cycling the individual solder joints in low-cycle shear testing, we can investigate the interaction effects of IMC and solder materials. It also allows us to monitor the ‘in-situ’ load vs. displacement of individual solder joints, and the damage accumulation during cycling can be quantitatively measured by analyzing the hysteresis loop (load-displacement curve).

Solder doping, referring to micro-alloying of rare-earth elements such as Ni, Bi, and Sb, to the SnAgCu-based alloy can effectively improve the thermal or mechanical reliability of solder joints. The effect of surface finishes on the thermal or shear behaviors of solder joints has been studied. In general, Ni/Au surface finish (ENIG) has shown better reliability in thermal cycling with aging since the Ni layer is used as a diffusion barrier to control the growth of IMC in thermal environments. However, Ni/Au surface finishes were associated with brittle fracture in high-speed shear testing, where the fracture was propagated along the interface of the solder joint and the nickel layer, causing a relatively low shear strength. No study has focused on investigating the effect of surface finish on the reliability of doped solder joint in a cyclic shear testing.

In this research, the effect of common surface finishes (OSP, ImAg, ENIG) on the mechanical reliability of doped lead-free solder joints was investigated in cyclic shear testing. Five different doped lead-free solder joints were tested with three surface finishes within four different stress amplitudes. Characteristic fatigue life and hysteresis loop were analyzed and correlated to the IMC microstructure and fracture surface as well.

7.2 Effect of Surface Finish on the Characteristic Fatigue Life

Figure 7.1 showed a cross-section view of SAC305 solder joints after reflow including the IMC layer that grows at the interface between solder joint and copper pad with different surface finishes. During the reflow, OSP surface finish reacts with the flux and evaporates inside the reflow oven, while ImAg surface finishes dissolve into the molten solder. Thus, after reflow, the surface finish layer does not exist, and only the Scallop-shape Cu_6Sn_5 IMC layer can be detected along the Cu pads, as shown in Figure 7.1. In the case of ENIG surface finish, the Au layer dissolves into the molten solder during the reflow, leaving Ni layer which reacts with Cu and Sn from the solder joint. Thus a $(Ni, Cu)_6Sn_5$ IMC layer was detected in between the solder joint and the copper pad as shown in Figure 7.1. Needle-like Ag_3Sn precipitate was also observed at the interfacial region of the solder joint for all the three surface finishes. Since IMC (Ag_3Sn, Cu_6Sn_5, $(Ni, Cu)_6Sn_5$) has higher strength and modules than β-Sn and can result in blocking the plastic deformation of the solder joint, thus a higher concentration of IMCs in a realistic range can improve the effective modulus and fatigue resistant of the solder joint.

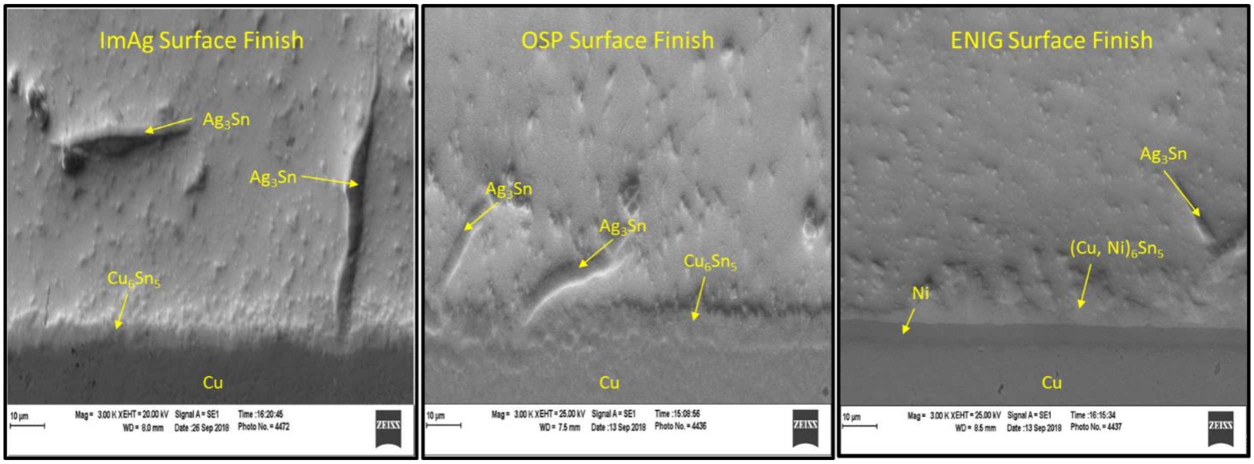

Figure 7.1 Cross-section view of IMC for OSP, ImAg, and ENIG surface finish

A two-parameter Weibull distribution shown in Figure 7.2 was utilized to characterize the fatigue life of the solder joints with three surface finishes. A two-parameter Weibull distribution is expressed in Equation 7.1:

$$R(t) = e^{-(\frac{t}{\theta})^{\beta}} \tag{7.1}$$

where *R(t)* is the reliability or the probability of survival, β is the shape parameter, θ is the scale parameter, and t is the time or number of cycles. The scale parameter is defined as the characteristic fatigue life which is the number of cycles at 63.2% probability of failure.

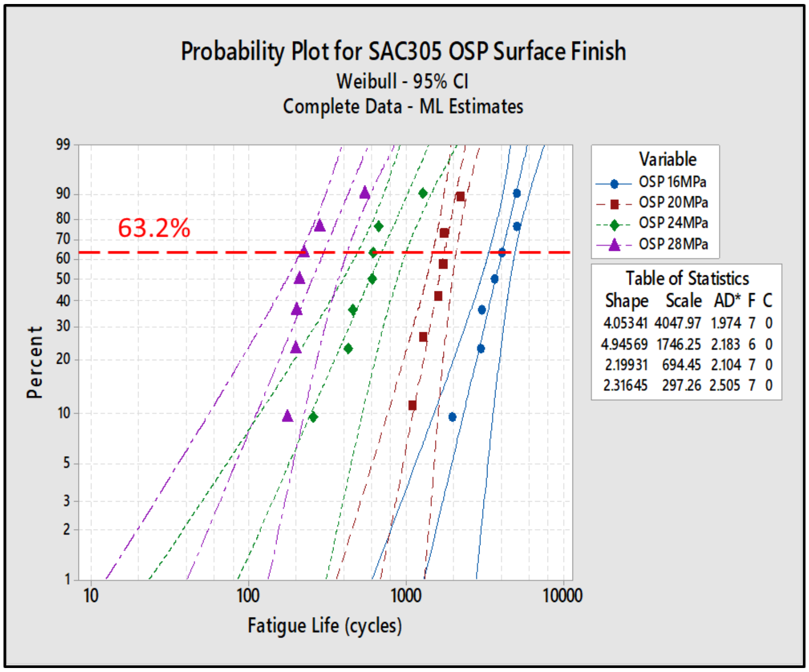

Figure 7.2 Weibull distribution of SAC305 solder joints with OSP surface finish cycled at different stress amplitudes

Weibull plots for SAC305, Ecolloy, SAC-X-Plus, Innolot, and CycloMax solder alloys with three surface finishes were shown in Appendix A (Figures A1-A15).

Characteristic fatigue life from the Weibull distribution was then plotted as a function of stress amplitude on a *log-log scale*. Figure 7.3 shows the characteristic fatigue life vs. stress amplitude

(20-32MPa) for Ecolloy solder joints with OSP surface finish on a log-log scale. It is clear that increasing stress amplitude leads to less characteristic fatigue life. This trend is true for all solder materials and surface finishes. An empirical power equation (Equation 7.2) was used to fit the characteristic fatigue life (N_{63}) in terms of stress amplitude (P):

$$N_{63} = \mathrm{A} * P^{-c} \tag{7.2}$$

Where A is a material constant, and c is the stress exponent. The absolute value of the stress exponent (c) represents the ductility of this material. The smaller the absolute value of this stress exponent, the larger the material ductility.

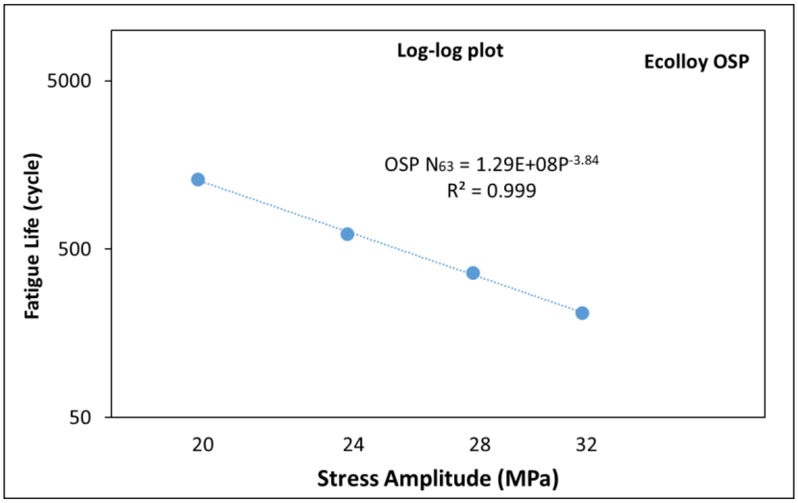

Figure 7.3 Characteristic fatigue life of Ecolloy solder joints with OSP surface finish as a function of stress amplitude

Figures 7.4-7.8 show the characteristic fatigue life vs. stress amplitude for SAC305, Ecolloy, SAC-X-Plus, Innolot, and CycloMax solder joints, respectively, with OSP, ImAg, and ENIG surface finishes on a log-log plot. All data points in these figures fit the power equation (Equation 2) with an excellent goodness-of-fit ($R^2 > 0.95$). The characteristic fatigue life associated with an ImAg surface finish was the largest for SAC305, Ecolloy, and SAC-X-Plus solder alloys. The characteristic fatigue life with an OSP surface finish was the largest for Innolot and CycloMax solder alloys. The ENIG surface finish was observed to have the least fatigue life among all the solder alloys. The largest decrease in fatigue life was observed for Innolot solder alloy when switching from an OSP to an ENIG surface finish, where the fatigue life dropped by 90%. Moreover, the ductility of each solder alloys associated with various surface finishes was exanimated. For SAC305, Ecolloy, and CycloMax solder alloys, the absolute value of stress exponent *c* for ENIG surface finish is larger than that for OSP and ImAg, indicating the ductility of the ENIG surface finish was less than that of OSP and ImAg . While for SAC-X-Plus and Innolot, no such trend in ductility was observed.

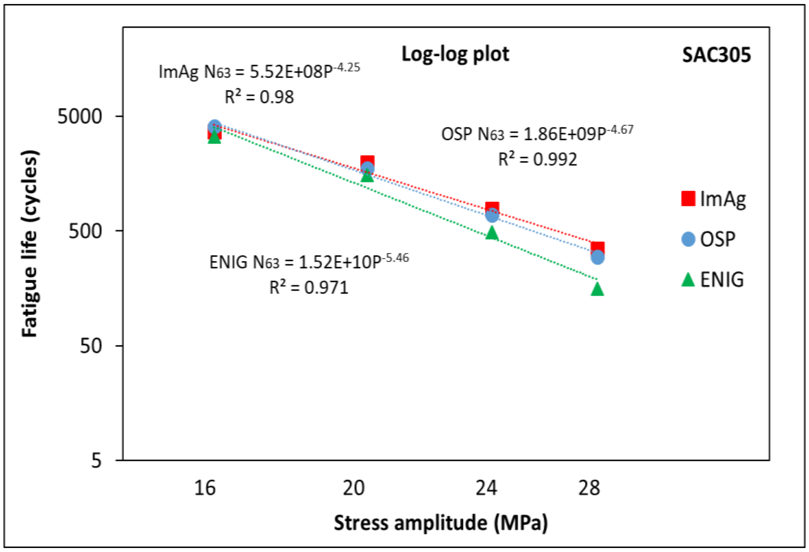

Figure 7.4 Characteristic fatigue life as a function of stress amplitudes for SAC305 solder alloy

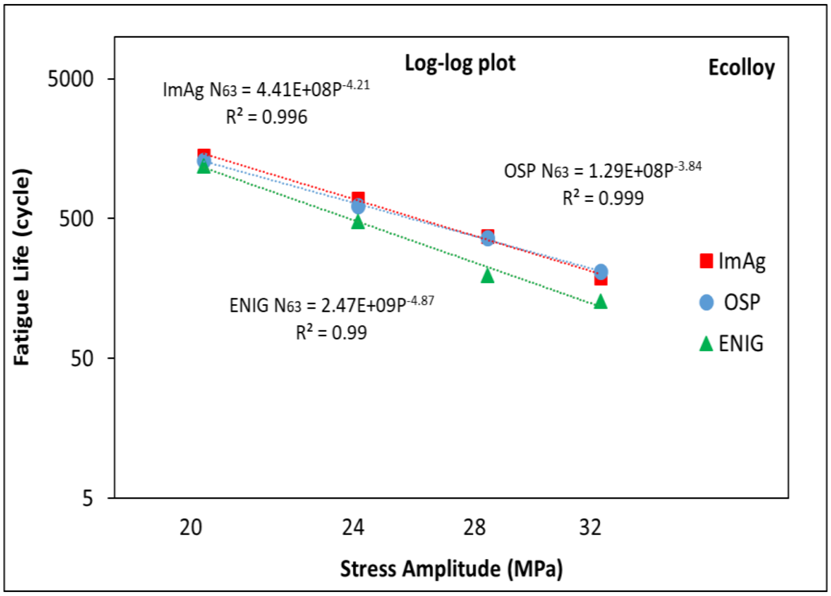

Figure 7.5 Characteristic fatigue life as a function of stress amplitudes for Ecolloy solder alloy

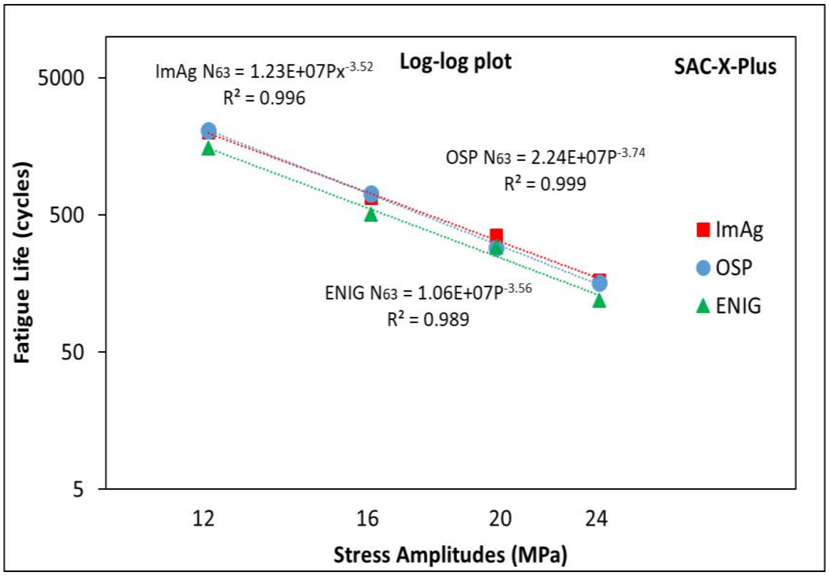

Figure 7.6 Characteristic fatigue life as a function of stress amplitudes for SAC-X-Plus solder alloy

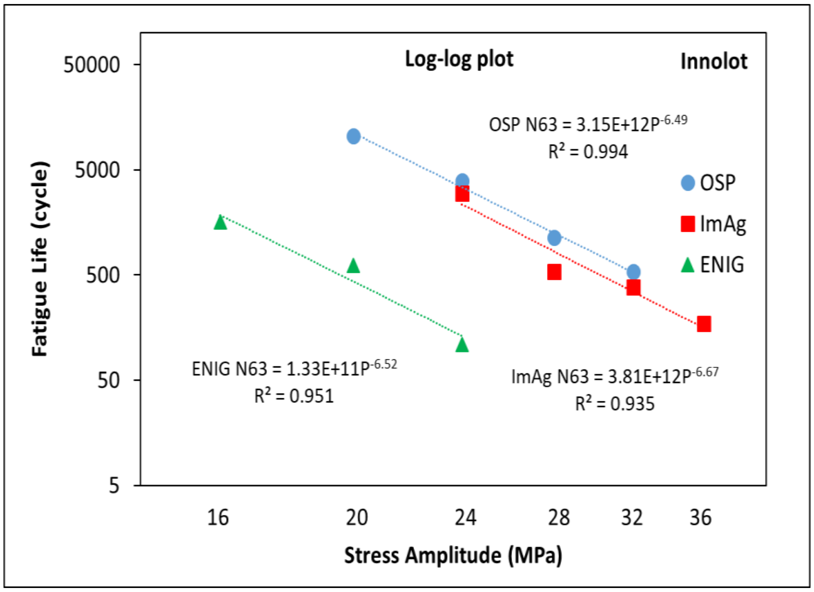

Figure 7.7 Characteristic fatigue life as a function of stress amplitudes for Innolot solder alloy

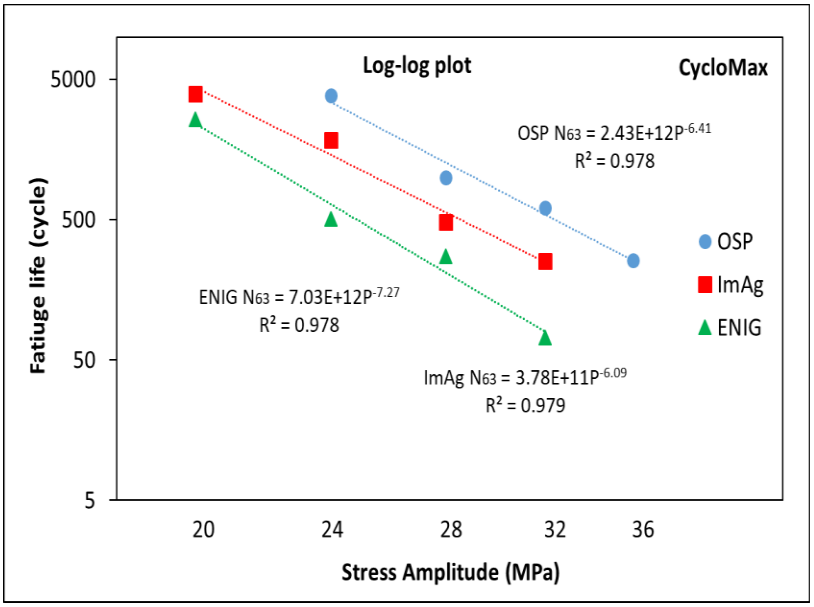

Figure 7.8 Characteristic fatigue life as a function of stress amplitudes for CycloMax solder alloy

Characteristic fatigue life of all the solder alloys was compared under OSP, ImAg, and ENIG surface finishes as shown in Figures 7.9-7.11. For OSP surface finish, CycloMax demonstrated the best fatigue life, followed by Innolot, SAC305, Ecolloy, and then SAC-X-Plus. A similar trend was observed for the ImAg surface finish. When comparing fatigue life of each solder alloy with its solder composition, it can be concluded that solder alloys with both higher Ag and Bi content (CycloMax and Innolot) demonstrated the highest fatigue life. Adding Bi to the SAC-based solder alloy can improve the mechanical properties by distorting the Sn crystalized lattice through ‘solid solution hardening’. 3% of Bi in the solder alloy was suggested as a “sweet spot”; less than this value is not enough to cause significant improvement; while more than a 3% can increase the embrittlement of the solder material. In addition, increasing the amount of Ag in the solder alloy would lead to a corresponding increase of Ag_3Sn precipitates, improving the strength and fatigue resistance of the solder. When examining the ductility of each solder alloy, SAC-X-Plus was associated with the highest ductility while both Innolot and CycloMax were associated with the lowest ductility. It indicated that the effect of both Bi and Ag would harden the solder material, and enhance the fatigue resistance, at the expense of material ductility. For the ENIG surface finish, a similar trend was observed except for the Innolot solder alloy. Fatigue life of Innolot dropped from 2nd place to the 4th place. SAC-X-Plus remained associated with the highest ductility while Innolot and CycloMax had the lowest ductility.

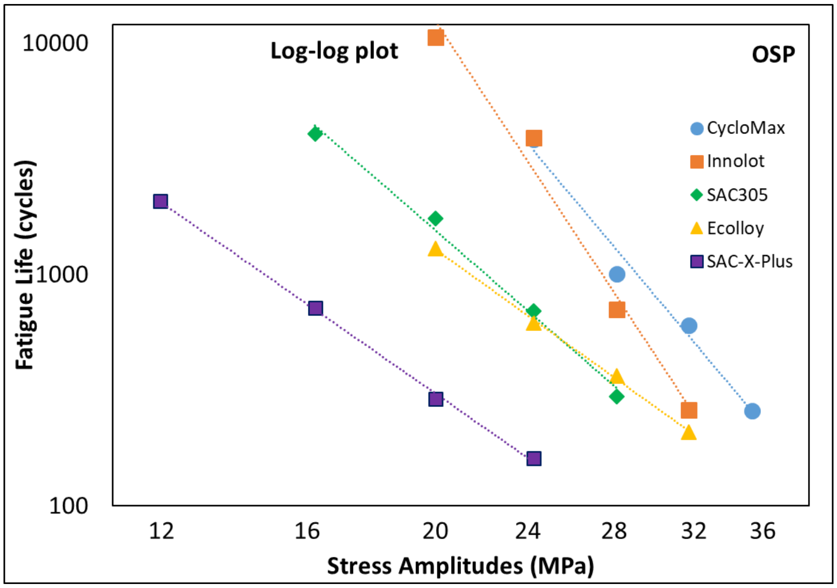

Figure 7.9 Fatigue life comparisons for OSP surface finish

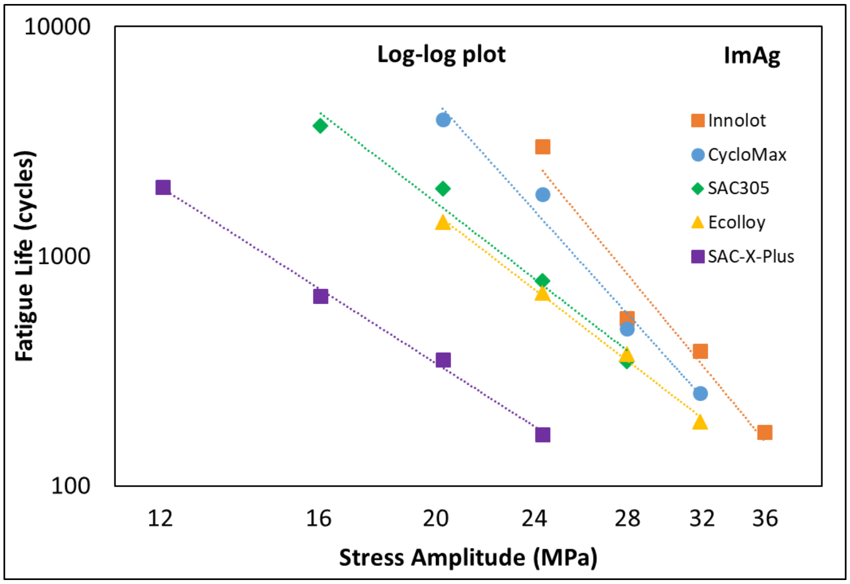

Figure 7.10 Fatigue life comparisons for ImAg surface finish

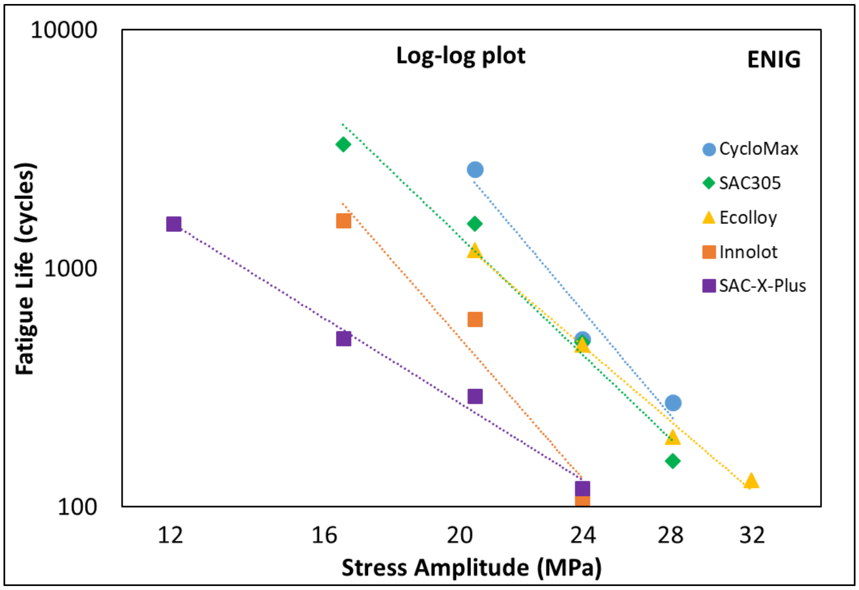

Figure 7.11 Fatigue life comparisons for ENIG surface finish

Then, fatigue life was compared at various stress amplitudes (20, 24, 28MPa) and results were shown in Figure 7.12-7.14. For three different surface finishes, no significant fatigue life differences were observed for SAC305 and Ecolloy solder alloys. However, for Innolot and

CycloMax solder alloys, OSP demonstrated the largest fatigue life, followed by ImAg, and the ENIG demonstrating the least fatigue life.

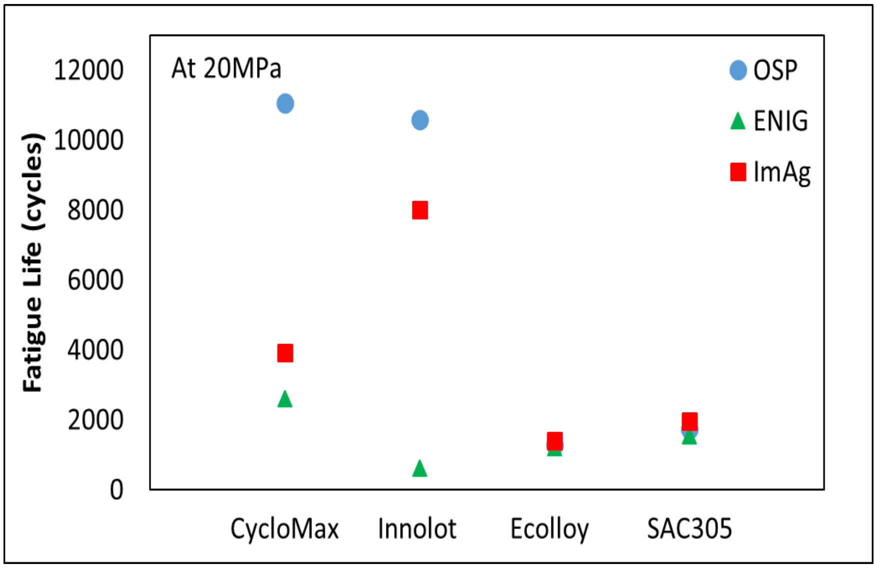

Figure 7.12 Fatigue life comparisons for solder alloys under 20MPa

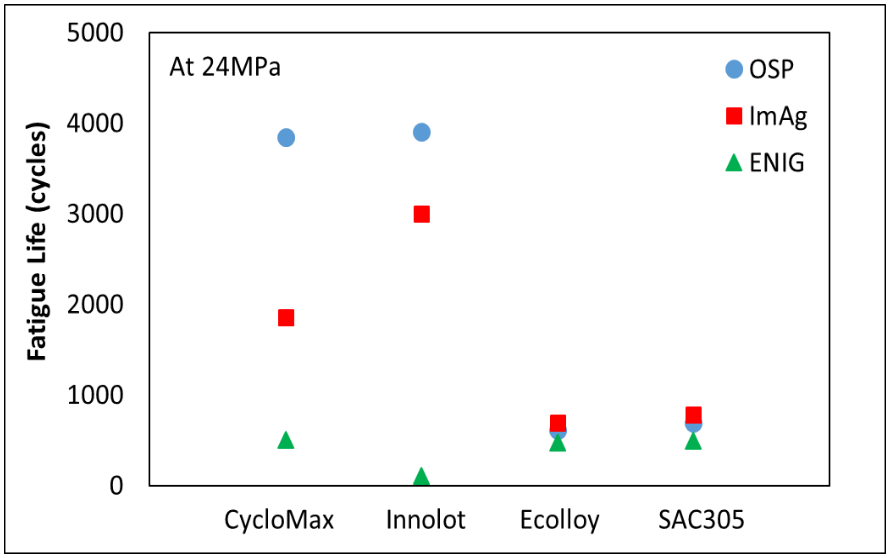

Figure 7.13 Fatigue life comparisons for solder alloys under 24MPa

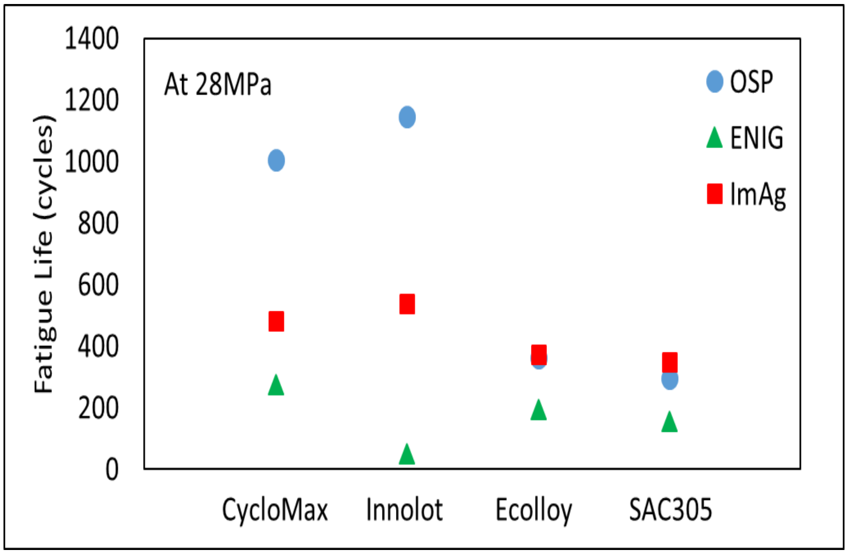

Figure 7.14 Fatigue life comparisons for solder alloys under 28MPa

7.3 Effect of Surface Finish on the Solder Failure Mechanisms

In this investigation, the fracture surfaces after shear fatigue testing were analyzed. Three failure modes were detected: brittle failure (failure through IMC interface), ductile failure (failure through bulk solder), and near-IMC failure (failure through bulk solder near IMC). Since fatigue life of Innolot experienced a significant drop when switching to an ENIG surface finish, failure modes of OSP vs. ENIG surface finishes of Innolot solder alloy were examined as shown in Figure 7.15. For Innolot with an OSP surface finish, the fracture surface was somewhat coarse, instead of smooth. Based on the failure modes definitions published by the author in a forthcoming paper, Song et al., and others, a smooth fracture surface identified the brittle failure, while a coarse surface could be the implication of either ductile failure or quasi-ductile/quasi-brittle failure or near-IMC failure. Brittle failure was always associated with the substantial changes in the solder joint behaviors (Ultimate shear strength, shear energy, fatigue life, etc.), while when looking into the behavior of Innolot with OSP surface finish, no such change was observed. An energy-dispersive spectroscopy (EDS) element mapping, which explains in section 4.3.3, was captured to further expound this situation shown in Figure 7.16. Green dots represent elements of Sn and orange dots represent elements of Cu. For Innolot with an OSP surface finish, a significant amount of Sn and Cu elements were detected. Comparing to Figure 7.16, SAC305 with OSP surface finish (confirmed ductile failure), only very few amounts of Cu (few orange dots) were detected. Combining the facts stated above (neither brittle failure nor ductile failure), we can conclude that the failure modes for Innolot with OSP surface finish for all the stress amplitudes (24-36MPa) are in between ductile and brittle failure. Since Song's classification (quasi-ductile/brittle) needs to estimate the percentage of the area without solder, the author would like to define this failure mode as a near-IMC failure. For Innolot with ENIG surface finish (Figure 7.15 on the right), brittle failure was defined since a classic, nearly smooth, fracture surface was observed. Thin trails left on the basal surface because of the bottom of the solder ball was dragged across the whole pad area, indicating the shear direction. For EDS element mapping on the right of Figure 7.16, most of the areas were covered by pink dots (Ni element), indicating a Ni layer left on the fracture surface. This observation was coordinated with several other publications, where embrittlement of ENIG surface finish was mentioned. The most prevalent failure mechanism is the separation between the Ni layer and IMC ($(Cu, Ni)_6Sn_5$). While most of the cases happened after elevated temperature aging or isothermal cycling at elevated temperature, this study observed that the ENIG surface finish embrittlement could also happen at room temperature fatigue cycling under given situation (Innolot solder joint with ENIG surface finish).

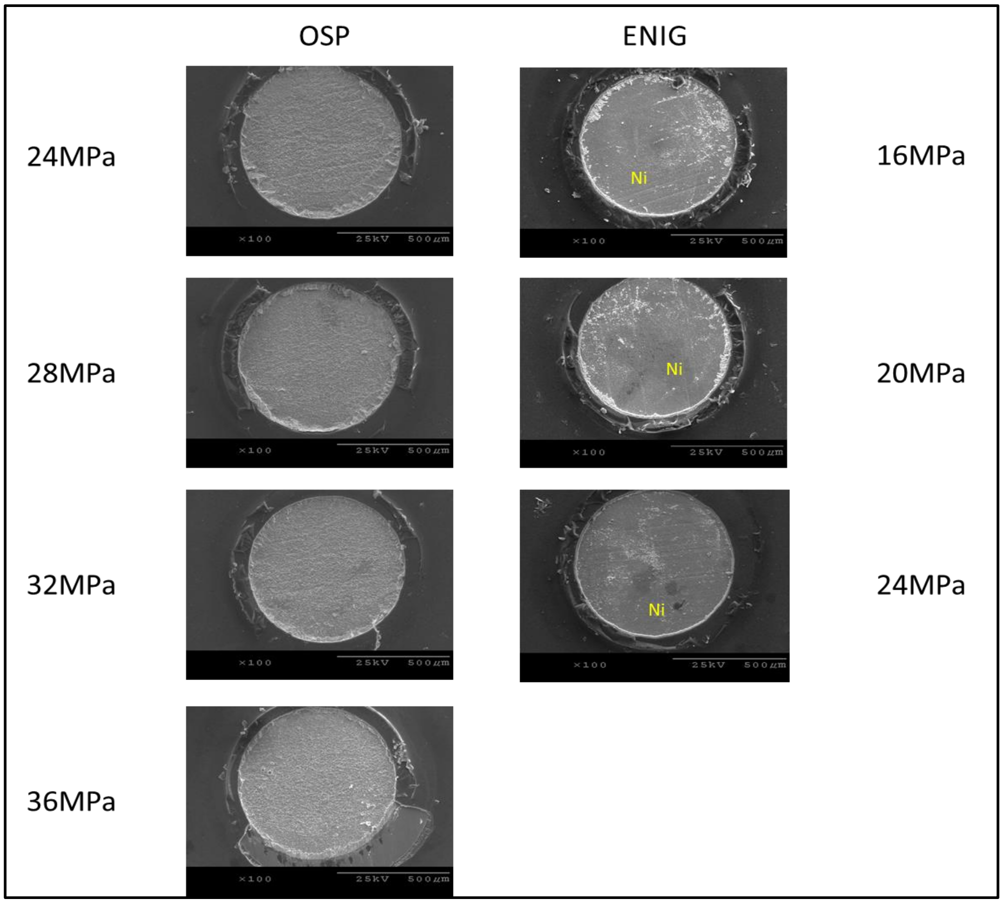

Figure 7.15 Fractured surface of Innolot with OSP and ENIG surface finish

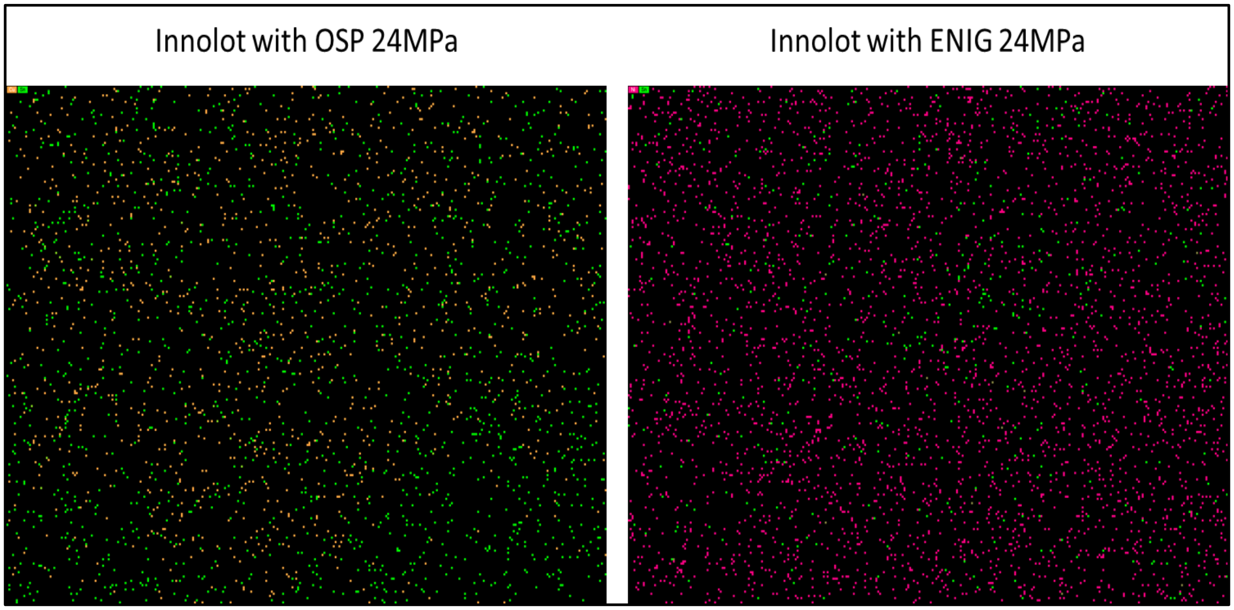

Figure 7.16 EDS mapping for Innolot with OSP VS. ENIG surface finish

Failure modes of SAC305 solder alloy with 3 surface finishes were also analyzed. Fracture surfaces and EDS element mapping are shown in Figures 7.17 and 7.18. Fracture surface morphology was ductile, and Sn was detected covering most of the pad area as shown in Figure 7.17. Green dots representing Sn elements dominate the whole mapping picture. Ductile failure was concluded for SAC305 with OSP and ENIG surface finish at all levels of stress amplitudes, except for SAC305 with an ENIG surface finish at 32MPa. Partial Ni was detected for 2 of 7 replicates cycled at 32MPa, as shown in the lower right of Figure 7.17, indicating near-IMC failure.

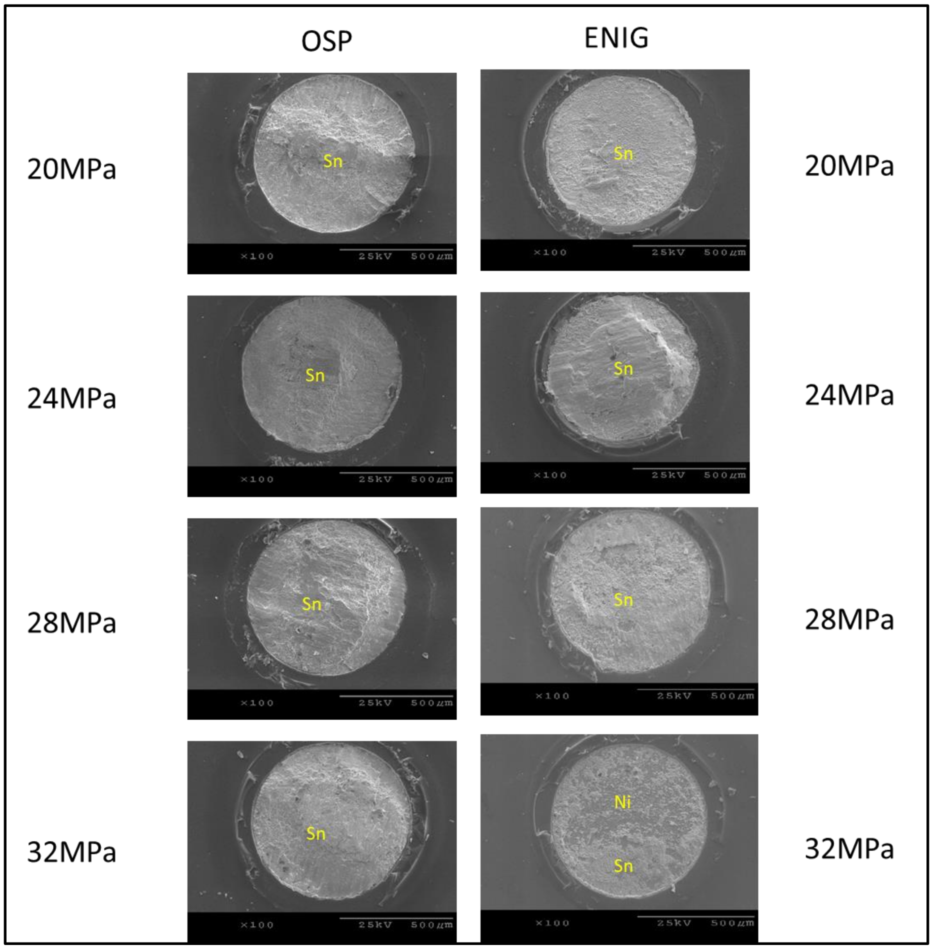

Figure 7.17 Fractured surface of SAC305 with OSP and ENIG surface finish

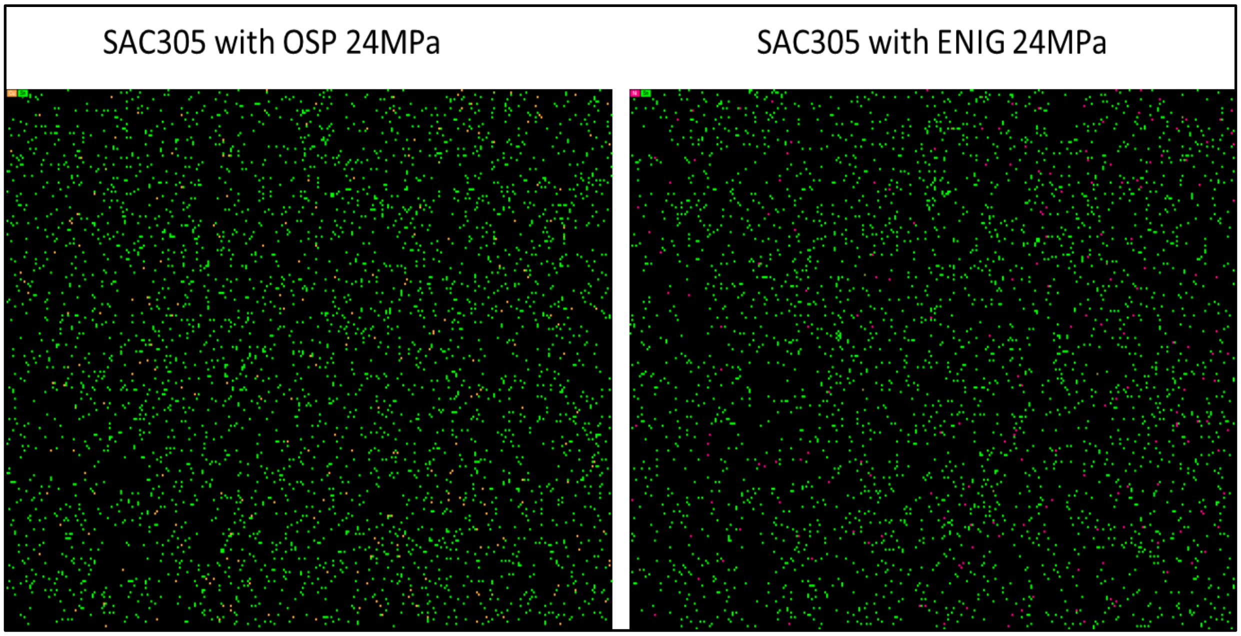

SAC305 with OSP 24MPa

SAC305 with ENIG 24MPa

Figure 7.18 EDS mapping for SAC305 with OSP vs. ENIG surface finish

7.4 Effect of Surface Finish on the Hysteresis Loop

A hysteresis loop and the energy dissipation per cycle were also compared as another method to evaluate the effects of surface finishes on the shear fatigue of solder joints. The data acquisition frequency was set to be $20s^{-1}$, with an average cycling frequency of 0.2cycle/s yields 100 data points per cycle, which is enough to plot hysteresis loops with good accuracy, as shown in Figure 4.13. The energy dissipation per cycle was calculated as the area within the hysteresis loop. Work or energy is assumed to be absorbed cycle by cycle in fatigue test and accumulates eventually resulting in the fatigue failure. Therefore, the energy dissipation per cycle can be used to predict fatigue life. In general, larger energy dissipation per cycle leads to a faster fatigue failure of the solder joint. During the fatigue test, hysteresis loop evolution for solder joints normally go through three stages where in the first stage the hysteresis loop increases due to the strain hardening process, then it keeps almost the same for a long period of time, where it enters the second stage known as the steady state. At last, solder joint hysteresis loop increases again which demonstrates the initiation and propagation of cracks within the solder alloy. Hysteresis loop evolution was shown in Appendix A (Figures A16-A19). Moreover, the work per cycle was plotted as a function of number of cycles during a whole fatigue test at various stress amplitudes, figures for SAC305 and CycloMax with different surface finishes were shown in Appendix A (Figures A20-A33). Meanwhile, hysteresis loop increases with the increasing of stress amplitudes, the evolution was shown in Appendix A (Figures A34-A37).

Figure 7.19 presents a hysteresis loop comparison between all tested solder alloys with OSP surface finish cycled at 24MPa. SAC-X-Plus was observed to have the largest hysteresis loop, followed by Ecolloy, SAC305, Innolot, and then CycloMax. Hysteresis loop comparisons for ImAg and ENIG surface finishes have shown the same trend as that of an OSP surface finish as shown in Figure 7.20 and 7.21. The hysteresis loop trend for the 5 solder alloys in this research is consistent with the trends for characteristic fatigue life and ductility, where the characteristic fatigue life trend was inversely proportional to the hysteresis loop trend, while the ductility trend was proportional to it. Higher ductility of solder alloy was detrimental to its fatigue resistance since higher ductility induced a larger plastic deformation per cycle under the same stress amplitude, which, therefore, led to faster crack initiation and propagation, and finally, less fatigue life.

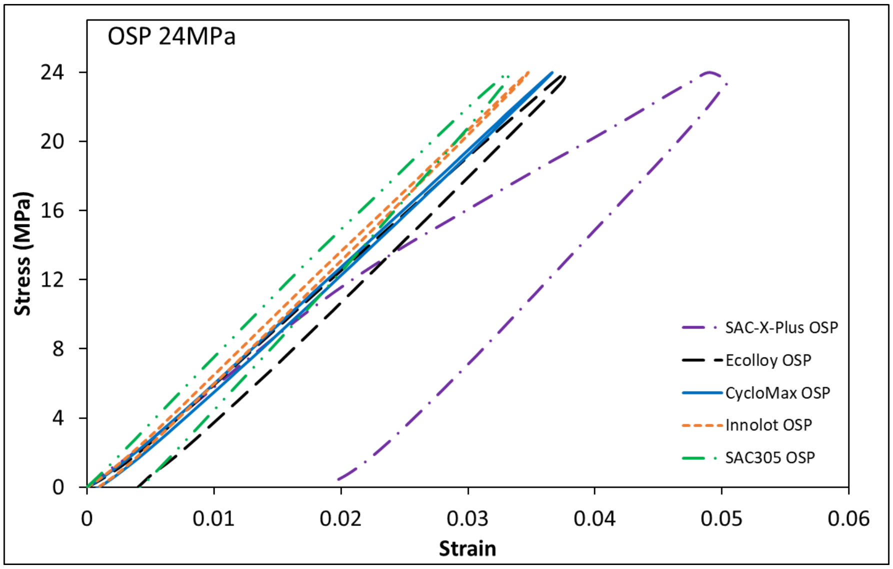

Figure 7.19 Hysteresis loop comparison for all solder alloys with OSP surface finish

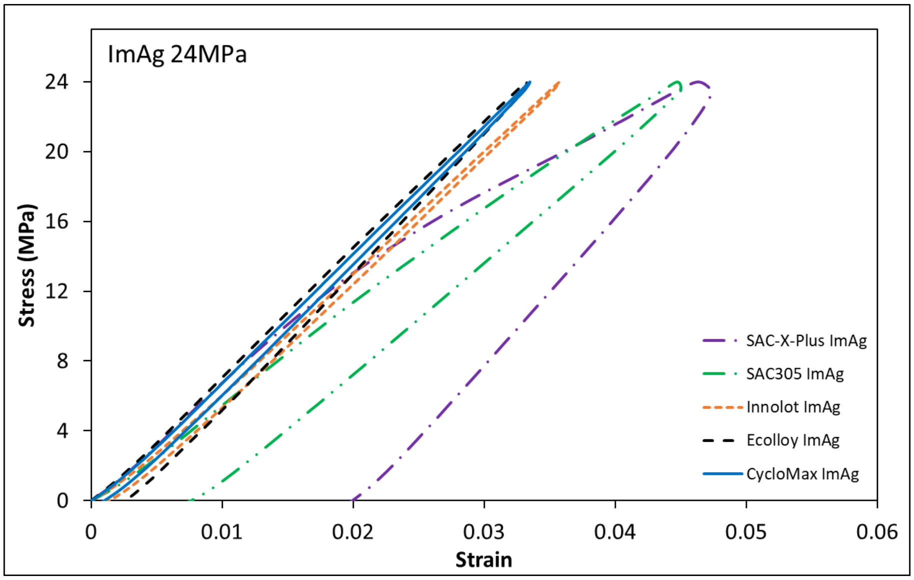

Figure 7.20 Hysteresis loop comparison for all solder alloys with ImAg surface finish

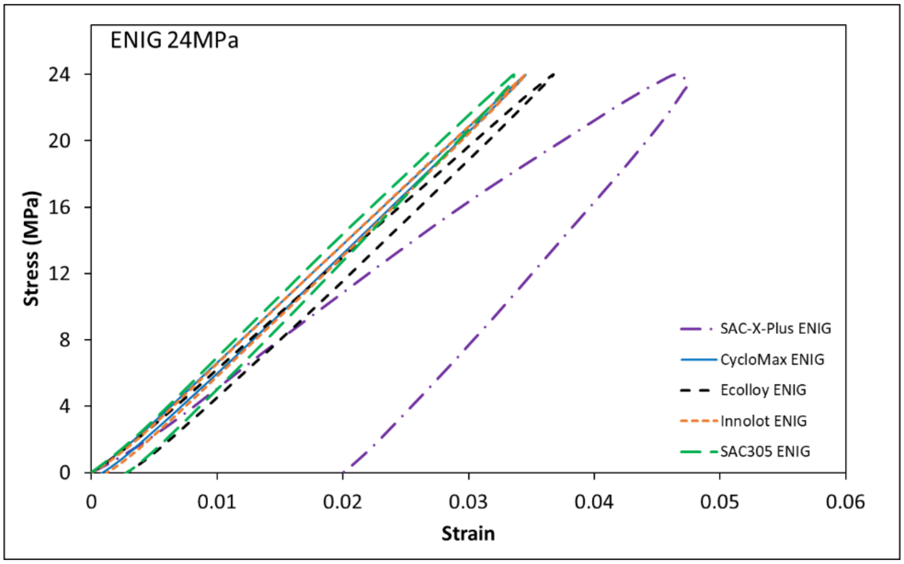

Figure 7.21 Hysteresis loop comparison for all solder alloys with ENIG surface finish

A hysteresis loop comparison for both SAC305 and Innolot is shown in Figures 7.22 and 7.23. Slight differences were observed for hysteresis loops of SAC305 with 3 surface finishes, where the loop for the ImAg surface finish is slightly larger than OSP followed by ENIG. There is no significant difference between the hysteresis loops for Innolot with 3 surface finishes. However, a similarity in the hysteresis loop means similarity of work dissipation per cycle, thus comparability in the fatigue resistance among surface finishes (Innolot ENIG vs. Innolot OSP). Based on the failure mechanisms discussion in the previous section, Innolot with an ENIG surface finish demonstrated a brittle failure during shear fatigue testing, where the fatigue life was much less than other surface finishes (OSP, ImAg). Thus, there is an implication of lower fatigue resistance of the ENIG surface finish with Innolot. This calls into a question of how to interpret the contradiction of fatigue resistance and hysteresis loop. The key to this question is based upon the understanding of which part of the solder joint was being tested for different failure mechanisms. For Innolot with OSP and ImAg surface finishes, the result is a near-IMC failure, meaning still the bulk failure, but crack is closer to the intermetallic region. However, for Innolot with the ENIG surface finish, it is the interface between the IMC and Ni layer that was tested due to the brittle failure mechanism. In the study conducted by Fahim, et al., the elastic modulus and hardness of an ENIG plating finish interface were similar to that of Ag3Sn or Cu6Sn5, all much larger than that of β-Sn. Moreover, the total energy to failure (the accumulated energy throughout the whole fatigue failure process) at 24MPa for Innolot with either OSP or ImAg surface finish surpassed that for ENIG surface finish by a factor of 20, which indicated a much worse fatigue resistance of the ENIG surface finish interface compared to the others given the classic fatigue theory. Even the energy per cycle is almost similar for all the 3 surface finishes (given a similarity of the ENIG interface to the other precipitates), in fact, the fatigue resistance of ENIG surface finish for Innolot solder alloy was much lower than the other two, due to excessive brittleness of ENIG interface associated with Innolot solder alloy. Figure 7.24 shows the average work per cycle for the solder alloys with the surface finishes cycled at 24MPa.

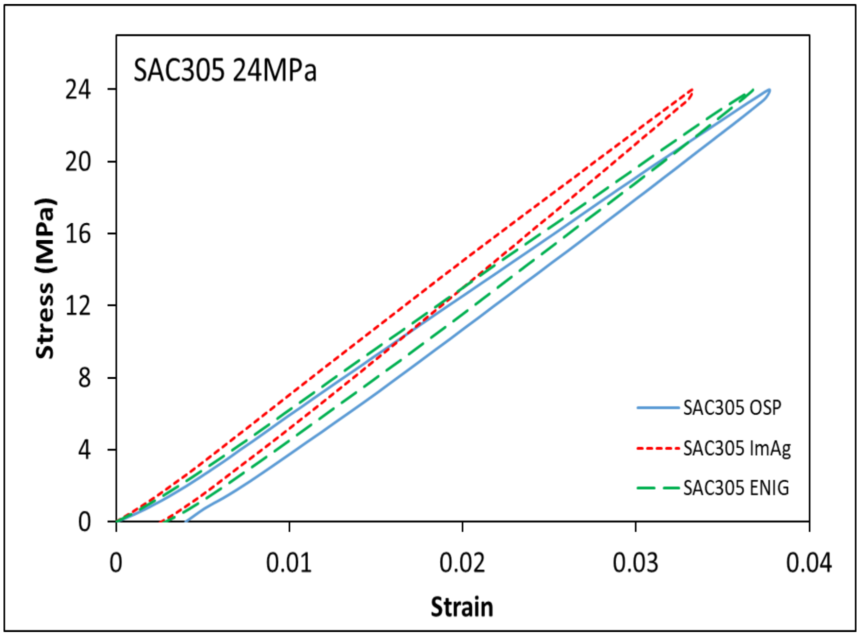

Figure 7.22 Hysteresis loop comparison for SAC305 with 3 surface finishes

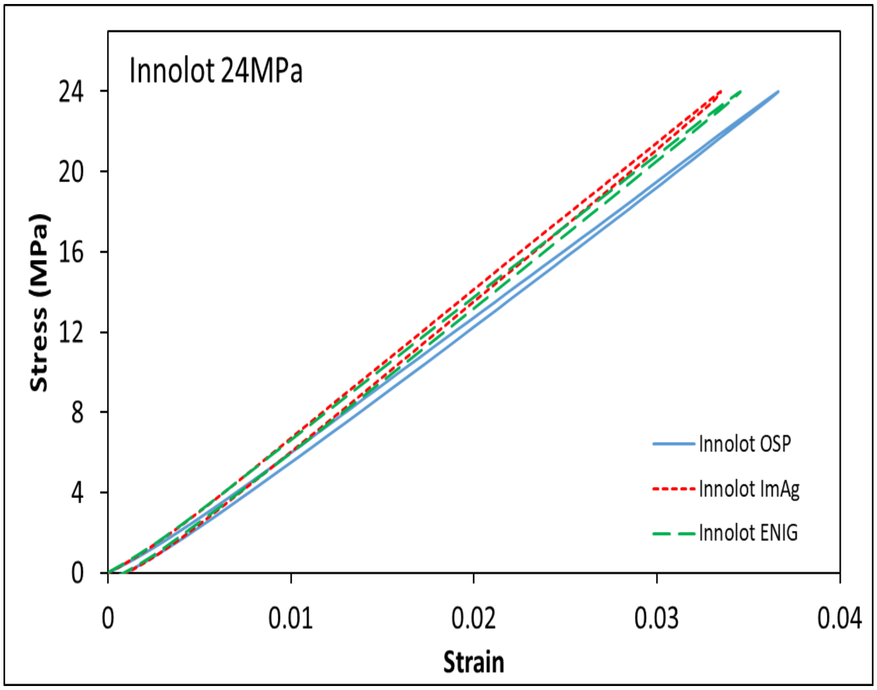

Figure 7.23 Hysteresis loop comparison for Innolot with 3 surface finishes

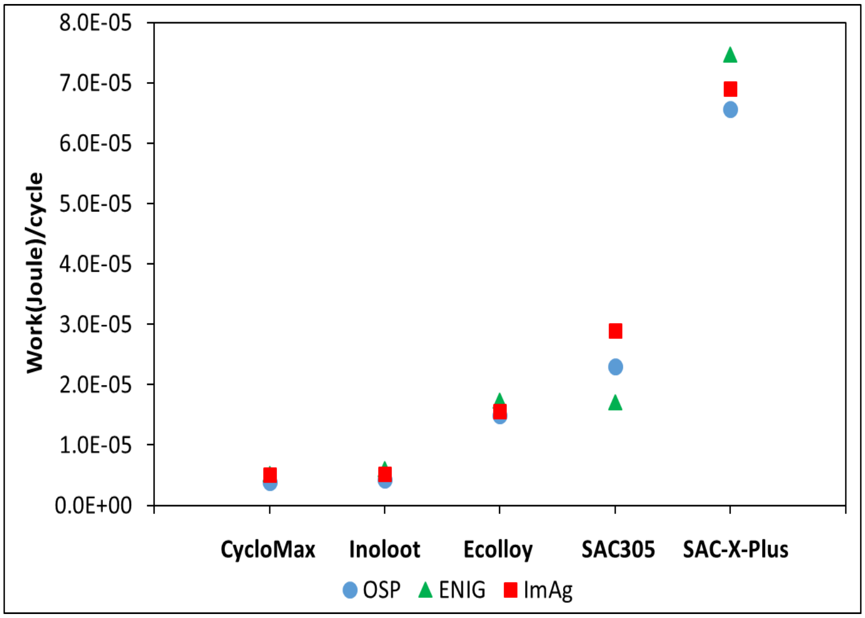

Figure 7.24 Average work per cycle comparison among solder alloys with surface finishes cycled at 24MPa

7.5 Morrow Energy Model for Shear Fatigue Testing

The Morrow energy model was applied to correlate inelastic work per cycle (W) with characteristic fatigue life of solder joint (N_{63}) as shown in Equation 3 and 4:

$$N_{63}^{\beta}W = \varphi \tag{7.3}$$

$$W = \varphi N_{63}^{-\beta} \tag{7.4}$$

Where β is the fatigue exponent, and φ is the material ductility coefficient.

Figures 7.25-7.29 show the Morrow energy model fitted curves with 3 surface finishes for SAC305, Ecolloy, SAC-X-Plus, Innolot, and CycloMax, respectively. For each surface finish, the average work per cycle (W) vs. the characteristic life (N_{63}) is shown as a nearly linear correlation when plotted on a log-log scale with R^2 larger than 90% for all the cases. The coefficients β and φ calculated by the least-square regression analysis are shown in Table 7.1. The material ductility coefficient φ for Innolot and CycloMax solder alloys were smaller than the rest of solder alloys regardless of surface finish.

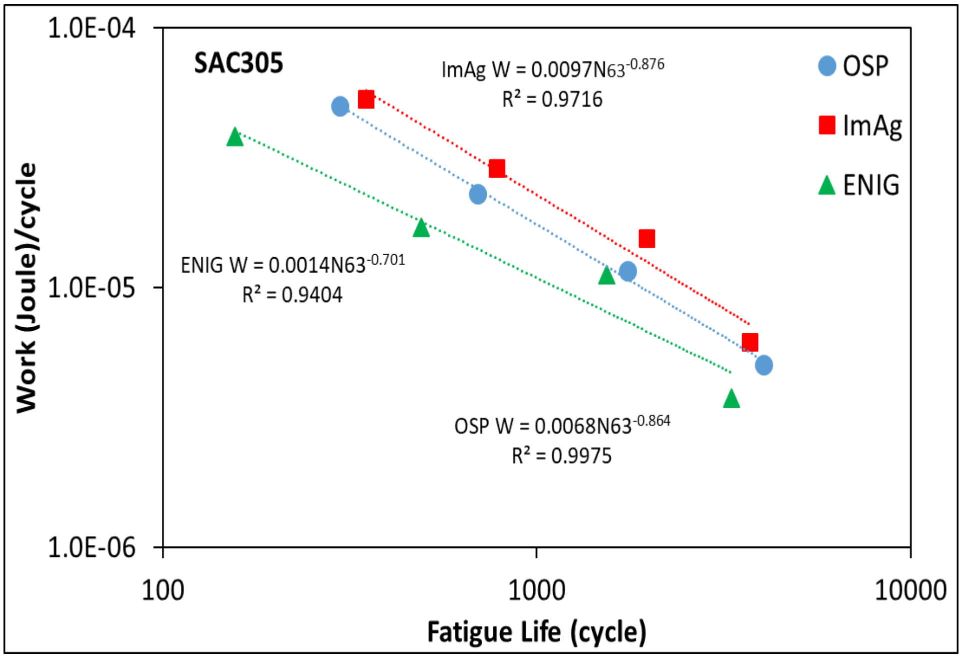

Figure 7.25 Morrow energy model for SAC305 solder alloy

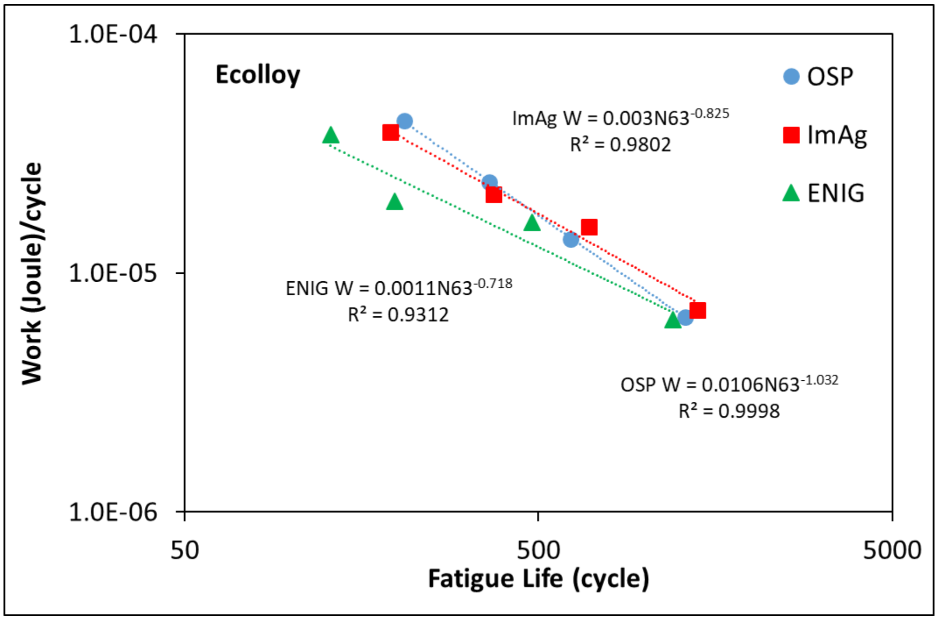

Figure 7.26 Morrow energy model for Ecolloy solder alloy

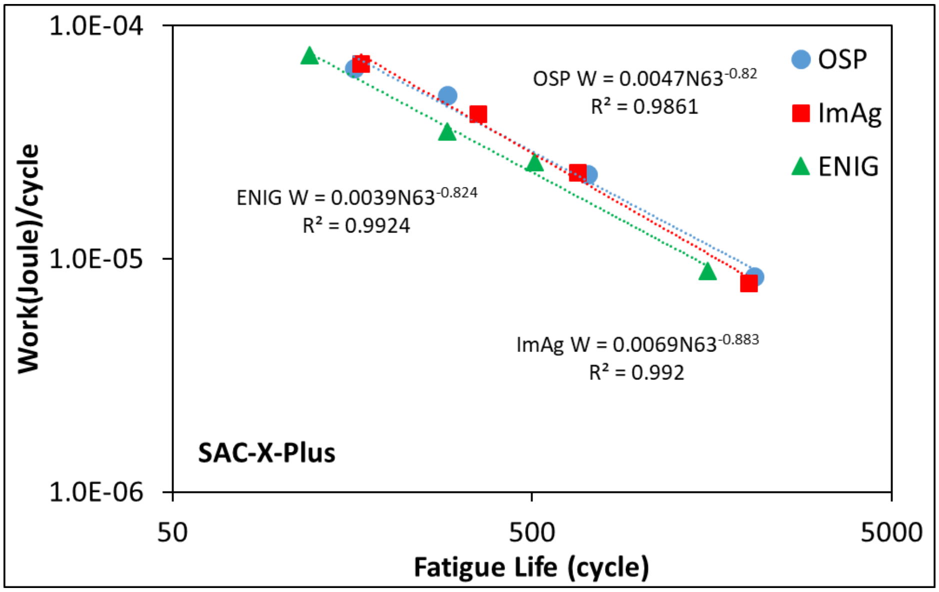

Figure 7.27 Morrow energy model for SAC-X-Plus solder alloy

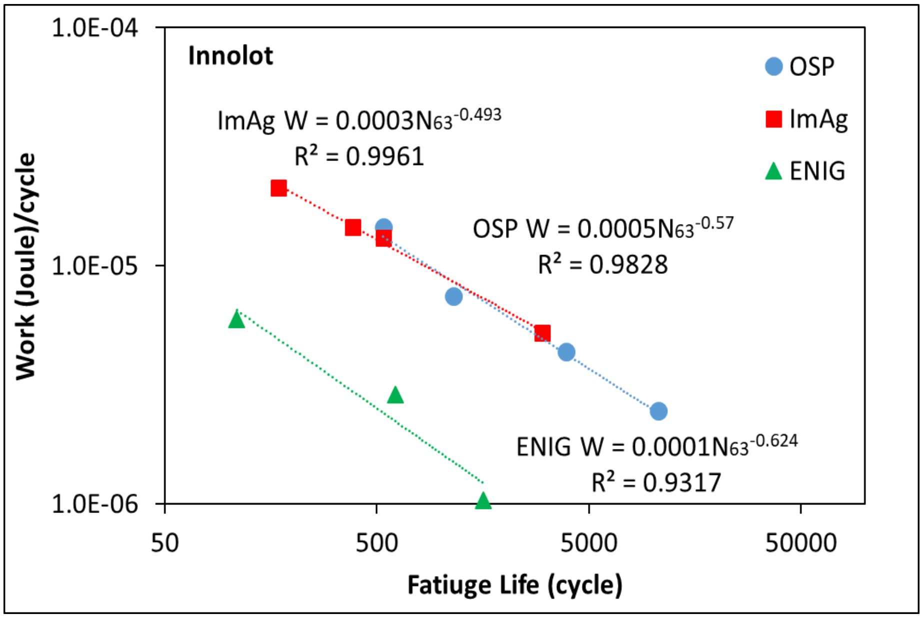

Figure 7.28 Morrow energy model for Innolot solder alloy

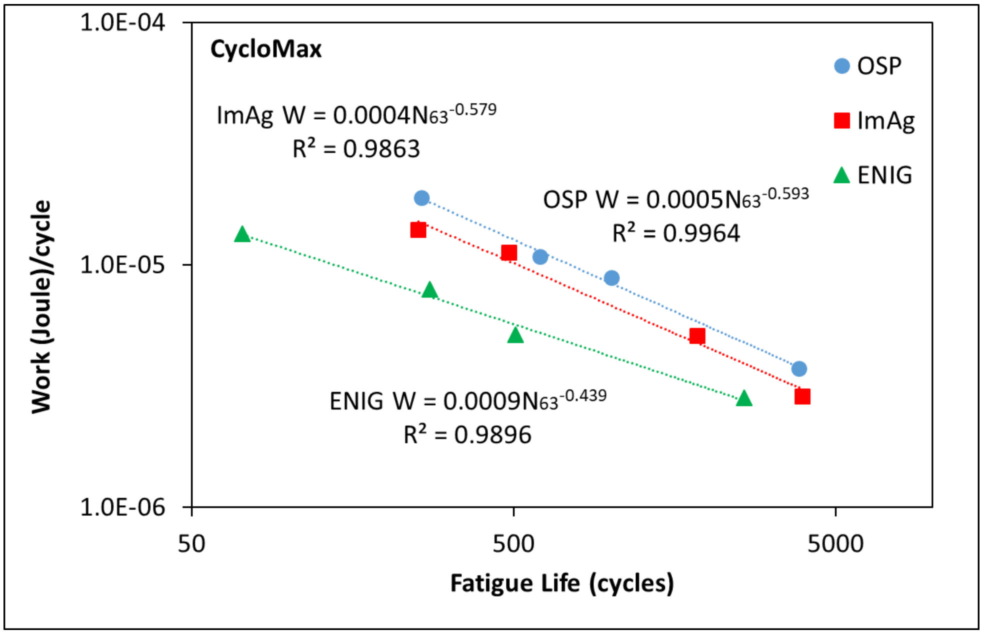

Figure 7.29 Morrow energy model for CycloMax solder alloy

Table 7.1 Morrow model constants

	OSP		**ImAg**		**ENIG**	
	φ	β	φ	β	φ	β
SAC305	0.0068	0.864	0.0097	0.876	0.0014	0.701
Ecolloy	0.0106	1.032	0.003	0.825	0.0011	0.718
SAC-X-Plus	0.0047	0.82	0.0069	0.883	0.0039	0.824
CycloMax	0.0005	0.593	0.0004	0.579	0.0009	0.439
Innolot	0.0005	0.57	0.0003	0.493	0.0001	0.624

Chapter 8 Results and Conclusions

8.1 Results and Conclusions

The reliability of solder joints under realistic applications was restricted by several impact factors, such as aging, IMC, solder material, or surface finishes. This dissertation investigates the effect of shear testing and cyclic shear fatigue testing on the reliability of lead-free solder joint with different solder dopants, surface finish, room temperature aging duration. Three surface finishes (OSP, ImAg, ENIG) were tested in combination of 5 doped materials (SAC+Bi, Ni, Sb). A test vehicle consists of 9 individual solder joints on a double layer PCB. Test vehicles were subjected to 4 years of room temperature aging (25°C) and shear or cyclic shear testing in order to evaluate the effects of various impact factors on the reliability of individual solder joints. A two-parameter Weibull distribution was used to generate the characteristic life and B10 life (early failure) for data analysis. A SEM and polarized light microscope were used for failure analysis, including solder surface morphology, microstructure evolution, crack initiation and propagation. Conclusions for this dissertation were summarized as follows:

1) Long-term room temperature aging led to a significant drop in the fatigue life with various doped solder alloys, and the life degradation after aging was correlated with doping elements. Solder alloys doped with Bi, Ni, and Sb demonstrated less life degradation than SAC305 or SAC105 solder alloys.

2) Long term room temperature aging increased the inelastic work per cycle and plastic strain range for all the solder joints cycling at given stress amplitude. Solder joints with Bi doped demonstrated stronger aging resistance compared to the rest of the doped solder joints.
3) Shear strength increased with the increasing of shear strain rate due to the viscoplastic characteristic of solder alloys.
4) OSP and ImAg surface finishes demonstrated better shear strength than an ENIG surface finish at all shear strain rates.
5) Solder alloys with higher Bi and Ag content (CycloMax & Innolot) showed better shear strength.
6) Ball shear testing produced a high incidence of brittle failure with the increase of shear strain rates, regardless of surface finishes.
7) Solder alloys with higher Bi and Ag content (CycloMax & Innolot) were more susceptible to brittle failure, thus attention must be made to improve the interfacial toughness. SEM/EDS analysis of fracture surfaces indicated that for the ENIG surface finish, fracture occurred at interfacial region between the Ni layer and the IMC; while for OSP/ ImAg surface finishes, fracture occurred at interfacial region between the IMC and the Cu pad.
8) Shear energy increased with the increase of shear strain rates for ductile failure, while remained almost the same for brittle failures. Shear energy was viewed as a more sensitive quantitative method in determining the failure modes over shear strength since shear energy of ductile failure was many times more than that of brittle failure.
9) Characteristic fatigue life decreased with the increasing of stress amplitudes, since larger stress amplitude leads to a larger damage per cycle.

10) OSP and ImAg surface finishes demonstrated larger fatigue life than an ENIG surface finish at all stress amplitudes, regardless of solder alloys.
11) Solder alloys with higher Ag and Bi content (CycloMax and Innolot) demonstrated larger fatigue life, since higher Ag and Bi increase the strength of bulk solder.
12) Innolot solder alloy with an ENIG surface finish was determined to form brittle failure during shear fatigue testing under all the stress amplitudes (16, 20, 24MPa), where the separation occurred at the interfacial region between the Ni layer and the IMC. Fatigue resistance associated with this combination was observed as significantly worse than the others (e.g. Innolot with OSP, Innolot with ImAg).
13) Increasing stress amplitude resulted in an increase in the hysteresis loop. It is more dependent on the ductility of solder alloys. The higher the solder alloy ductility, the larger the hysteresis loop.

8.2 Future Work

All the cyclic shear fatigue testing so far is *stress-controlled*, the fatigue behaviors of doped solder joints under *strain-controlled* shall be investigated as well, to create a better understanding of the effects of various impact factors on the individual solder joints under fatigue testing.

In addition, the effects of elevated temperature aging on the doped solder joint need to be studied, since all the solder joint properties collected currently are based on either room-temperature aging or no aging.

Cyclic shear fatigue testing under elevated temperature shall be conducted, since in almost all the realistic applications, the older joint is normally exposed to the elevated temperatures in harsh applications. By cycling solder joints under elevated temperature, we can have results closer to the realistic conditions.

References

[1] J. H. Lau, "Electronics manufacturing with lead-free," *Halogen-free & Conductive-adhesive materials,* vol. 17, 2003.

[2] J. W. Dally, P. Lall, and J. C. Suhling, *Mechanical design of electronic systems*: College House Enterprises, 2008.

[3] R. Prasad, *Surface mount technology: principles and practice*: Springer Science & Business Media, 2013.

[4] G. Bhattacharyya and Z. Soejoeti, "A tampered failure rate model for step-stress accelerated life test," *Communications in statistics-Theory and methods,* vol. 18, pp. 1627-1643, 1989.

[5] M. Wickham, J. Nottay, and C. Hunt, *A review of mechanical test method standards for lead-free solders*: National Physical Laboratory, 2001.

[6] C. Andersson, Z. Lai, J. Liu, H. Jiang, and Y. Yu, "Comparison of isothermal mechanical fatigue properties of lead-free solder joints and bulk solders," *Materials Science and Engineering: A,* vol. 394, pp. 20-27, 2005.

[7] Y. Jaradat, A. Qasaimeh, M. Obaidat, and P. Borgesen, "Assessment of solder joint fatigue life under realistic service conditions," *Journal of electronic materials,* vol. 43, pp. 4472-4484, 2014.

[8] B. Lampe, "Room temperature aging properties of some solder alloys," *Welding Journal,* vol. 55, p. 330, 1976.

[9] C.-M. Chuang, T.-S. Lui, and L.-H. Chen, "Effect of aluminum addition on tensile properties of naturally aged Sn-9Zn eutectic solder," *Journal of Materials Science,* vol. 37, pp. 191-195, 2002.

[10] M. I. Montrose, *EMC and the printed circuit board: design, theory, and layout made simple* vol. 6: John Wiley & Sons, 2004.

[11] J. H. Lau and Y.-H. Pao, *Solder joint reliability of BGA, CSP, flip chip, and fine pitch SMT assemblies*: McGraw-Hill Professional Publishing, 1997.

[12] J. H. Lau, *Ball grid array technology*: McGraw-Hill Professional, 1995.

[13] G. Zweig, "Guest View: BGAs: Inspect the Process, Not the Product," *Circuits Assembly,* vol. 5, p. 92, 1994.

[14] K.-J. Wolter, "System integration by advanced electronics packaging," in *Bio and Nano Packaging Techniques for Electron Devices*, ed: Springer, 2012, pp. 31-48.

[15] A. Elshabini, G. Wang, and F. Barlow, "Future trends in electronic packaging," in *Smart Structures and Materials 2006: Smart Electronics, MEMS, BioMEMS, and Nanotechnology*, 2006, p. 61720Z.

[16] J. E. Morris, "Nanopackaging: Nanotechnologies and electronics packaging," in *Nanopackaging*, ed: Springer, 2008, pp. 1-14.

[17] M. Abtew and G. Selvaduray, "Lead-free solders in microelectronics," *Materials Science and Engineering: R: Reports*, vol. 27, pp. 95-141, 2000.

[18] G. Humpston and D. M. Jacobson, *Principles of soldering*: ASM international, 2004.

[19] D.-s. Jiang, Y.-p. Wang, and C. Hsiao, "Effect of minor doping elements on lead free solder joint quality," in *Electronics Packaging Technology Conference, 2006. EPTC'06. 8th*, 2006, pp. 385-389.

[20] W. Richard, "Deformation and fracture mechanics of engineering materials," 1976.

[21] R. Ross, L. Wen, G. Mon, E. Jetter, and J. Winslow, "Creep-Fatigue Behavior of Microelectronic Solder Joints," *MRS Online Proceedings Library Archive,* vol. 225, 1991.

[22] C. Boller and T. Seeger, *Materials data for cyclic loading: Low-alloy steels* vol. 42: Elsevier, 2013.

[23] G. Di Giacomo and G. Di Giacomo, *Reliability of electronic packages and semiconductor devices*: McGraw-Hill New York, 1997.

[24] H.-J. Christ, "Effect of environment on thermomechanical fatigue life," *Materials Science and Engineering: A,* vol. 468, pp. 98-108, 2007.

[25] W. Q. Meeker and G. J. Hahn, *How to plan an accelerated life test: Some practical guidelines*: ASQC Statistics Division, 1985.

[26] C. E. Ebeling, *An introduction to reliability and maintainability engineering*: Tata McGraw-Hill Education, 2004.

[27] G.-A. Klutke, P. C. Kiessler, and M. A. Wortman, "A critical look at the bathtub curve," *IEEE Transactions on reliability,* vol. 52, pp. 125-129, 2003.

[28] W. Weibull, "A statistical distribution function of wide applicability," *Journal of applied mechanics,* vol. 18, pp. 293-297, 1951.

[29] N. Azira, N. M. Nan, M. Idris, and M. Bukhari, "Board Level Reliability (BLR)–board design, test and application."

[30] M. Matin, W. Vellinga, and M. Geers, "Thermomechanical fatigue damage evolution in SAC solder joints," *Materials Science and Engineering: A,* vol. 445, pp. 73-85, 2007.

[31] Y. Miyazawa and T. Ariga, "Microstructural change and hardness of lead free solder alloys," in *Environmentally Conscious Design and Inverse Manufacturing, 1999. Proceedings. EcoDesign'99: First International Symposium On*, 1999, pp. 616-619.

[32] Q. Xiao, H. J. Bailey, and W. D. Armstrong, "Aging effects on microstructure and tensile property of Sn3. 9Ag0. 6Cu solder alloy," *Journal of Electronic Packaging*, vol. 126, pp. 208-212, 2004.

[33] Y. Ding, C. Wang, Y. Tian, and M. Li, "Influence of aging treatment on deformation behavior of 96.5 Sn3. 5Ag lead-free solder alloy during in situ tensile tests," *Journal of Alloys and Compounds*, vol. 428, pp. 274-285, 2007.

[34] H. Ma, J. C. Suhling, P. Lall, and M. J. Bozack, "Reliability of the aging lead free solder joint," in *Electronic Components and Technology Conference, 2006. Proceedings. 56th*, 2006, p. 16 pp.

[35] M. Motalab, Z. Cai, J. C. Suhling, J. Zhang, J. L. Evans, M. J. Bozack*, et al.*, "Improved predictions of lead free solder joint reliability that include aging effects," in *Electronic Components and Technology Conference (ECTC), 2012 IEEE 62nd*, 2012, pp. 513-531.

[36] I. Anderson and J. Harringa, "Elevated temperature aging of solder joints based on Sn-Ag-Cu: Effects on joint microstructure and shear strength," *Journal of electronic materials*, vol. 33, pp. 1485-1496, 2004.

[37] W.-M. Chen, P. McCloskey, and S. C. O'Mathuna, "Isothermal aging effects on the microstructure and solder bump shear strength of eutectic Sn37Pb and Sn3. 5Ag solders," *Microelectronics Reliability*, vol. 46, pp. 896-904, 2006.

[38] R. Darveaux, "Shear deformation of lead free solder joints," in *Electronic Components and Technology Conference, 2005. Proceedings. 55th*, 2005, pp. 882-893.

[39] K.-S. Kim, C.-H. Yu, and J.-M. Yang, "Aging treatment characteristics of solder bump joint for high reliability optical module," *Thin solid films*, vol. 462, pp. 402-407, 2004.

[40] S. Wiese, M. Roellig, and K.-J. Wolter, "Creep of eutectic SnAgCu in thermally treated solder joints," in *Electronic Components and Technology Conference, 2005. Proceedings. 55th*, 2005, pp. 1272-1281.

[41] Y. Zhang, Z. Cai, J. C. Suhling, P. Lall, and M. J. Bozack, "The effects of SAC alloy composition on aging resistance and reliability," in *Electronic Components and Technology Conference, 2009. ECTC 2009. 59th*, 2009, pp. 370-389.

[42] Y.-K. Tsui, S. R. Lee, and X. Huang, "Experimental investigation on the degradation of BGA solder ball shear strength due to room temperature aging," in *Electronic Materials and Packaging, 2002. Proceedings of the 4th International Symposium on*, 2002, pp. 478-481.

[43] R. J. Coyle, P. P. Solan, A. J. Serafino, and S. A. Gahr, "The influence of room temperature aging on ball shear strength and microstructure of area array solder balls," in *Electronic Components & Technology Conference, 2000. 2000 Proceedings. 50th*, 2000, pp. 160-169.

[44] L. Li, J.-W. Jang, and B. Allmen, "Shear property and microstructure evaluation of Pb-free solder bumps under room temperature and multiple reflow/high temperature aging," in *Advanced Packaging Materials: Processes, Properties and Interfaces, 2001. Proceedings. International Symposium on*, 2001, pp. 347-353.

[45] A. Chilton, M. Whitmore, and W. Hampshire, "Fatigue failure in a model SMD joint," *Soldering & Surface Mount Technology*, vol. 1, pp. 21-24, 1989.

[46] C. Liu, P. Conway, D. Li, and M. Hendriksen, "Analysis of the micro-mechanical properties in aged lead-free, fine pitch flip chip joints," *Journal of Electronic Packaging,* vol. 126, pp. 359-366, 2004.

[47] J.-M. Koo and S.-B. Jung, "Effect of displacement rate on ball shear properties for Sn–37Pb and Sn–3.5 Ag BGA solder joints during isothermal aging," *Microelectronics Reliability,* vol. 47, pp. 2169-2178, 2007.

[48] J. Oliver, J. Liu, and Z. Lai, "Effect of thermal ageing on the shear strength of lead-free solder joints," in *Advanced Packaging Materials: Processes, Properties andInterfaces, 2000. Proceedings. International Symposium on*, 2000, pp. 152-157.

[49] A. El-Daly, A. El-Taher, and T. Dalloul, "Enhanced ductility and mechanical strength of Ni-doped Sn–3.0 Ag–0.5 Cu lead-free solders," *Materials & Design,* vol. 55, pp. 309-318, 2014.

[50] A. El-Daly, A. Hammad, A. Fawzy, and D. Nasrallh, "Microstructure, mechanical properties, and deformation behavior of Sn–1.0 Ag–0.5 Cu solder after Ni and Sb additions," *Materials & Design,* vol. 43, pp. 40-49, 2013.

[51] C.-M. Chuang, P.-C. Shih, and K.-L. Lin, "Mechanical strength of Sn-3.5 Ag-based solders and related bondings," *Journal of electronic materials,* vol. 33, pp. 1-6, 2004.

[52] G. Li, B. Chen, X. Shi, S. C. Wong, and Z. Wang, "Effects of Sb addition on tensile strength of Sn–3.5 Ag–0.7 Cu solder alloy and joint," *Thin Solid Films,* vol. 504, pp. 421-425, 2006.

[53] F. Che, W. Zhu, E. S. Poh, X. Zhang, and X. Zhang, "The study of mechanical properties of Sn–Ag–Cu lead-free solders with different Ag contents and Ni doping under different

strain rates and temperatures," *Journal of Alloys and Compounds,* vol. 507, pp. 215-224, 2010.

[54] W. Liu, N.-C. Lee, A. Porras, M. Ding, A. Gallagher, A. Huang*, et al.*, "Achieving high reliability low cost lead-free SAC solder joints via Mn or Ce doping," in *Electronic Components and Technology Conference, 2009. ECTC 2009. 59th*, 2009, pp. 994-1007.

[55] E. Wilkins, "Cumulative damage in fatigue," in *Colloquium on Fatigue/Colloque de Fatigue/Kolloquium über Ermüdungsfestigkeit*, 1956, pp. 321-332.

[56] Z. Lv, H.-Z. Huang, S.-P. Zhu, H. Gao, and F. Zuo, "A modified nonlinear fatigue damage accumulation model," *International Journal of Damage Mechanics,* vol. 24, pp. 168-181, 2015.

[57] A. Qasaimeh, Y. Jaradat, and P. Borgesen, "Damage evolution in lead free solder joints in isothermal fatigue," *Journal of Electronic Packaging,* vol. 137, p. 021012, 2015.

[58] H. Corten and T. Dolan, "Cumulative fatigue damage," in *Proceedings of the international conference on fatigue of metals*, 1956, p. 235.

[59] S.-P. Zhu, H.-Z. Huang, Y. Liu, L.-P. He, and Q. Liao, "A practical method for determining the Corten-Dolan exponent and its application to fatigue life prediction," *Int. J. Turbo Jet-Engines,* vol. 29, pp. 79-87, 2012.

[60] W. Engelmaier and A. I. Attarwala, "Surface-mount attachment reliability of clip-leaded ceramic chip carriers on FR-4 circuit boards," *IEEE transactions on components, hybrids, and manufacturing technology,* vol. 12, pp. 284-296, 1989.

[61] L. F. Coffin Jr, "A study of the effects of cyclic thermal stresses on a ductile metal," *trans. ASME,* vol. 76, pp. 931-950, 1954.

[62] X. Shi, H. Pang, W. Zhou, and Z. Wang, "Low cycle fatigue analysis of temperature and frequency effects in eutectic solder alloy," *International Journal of fatigue*, vol. 22, pp. 217-228, 2000.

[63] P. Chauhan, M. Osterman, S. R. Lee, and M. Pecht, "Critical review of the Engelmaier model for solder joint creep fatigue reliability," *IEEE Transactions on Components and Packaging Technologies,* vol. 32, pp. 693-700, 2009.

[64] W. Engelmaier, "The use environments of electronic assemblies and their impact on surface mount solder attachment reliability," *IEEE transactions on components, hybrids, and manufacturing technology,* vol. 13, pp. 903-908, 1990.

[65] H. Solomon, "Fatigue of 60/40 solder," *IEEE Transactions on Components, Hybrids, and Manufacturing Technology,* vol. 9, pp. 423-432, 1986.

[66] K. Norris and A. Landzberg, "Reliability of controlled collapse interconnections," *IBM Journal of Research and Development,* vol. 13, pp. 266-271, 1969.

[67] A. Syed, "Accumulated creep strain and energy density based thermal fatigue life prediction models for SnAgCu solder joints," in *Electronic Components and Technology Conference, 2004. Proceedings. 54th*, 2004, pp. 737-746.

[68] F. C. Monkman, "An empirical relationship between rupture life and minimum creep rate in creep-rupture tests," in *Proc of the ASTM*, 1956, pp. 593-620.

[69] A. Syed, "Predicting solder joint reliability for thermal, power, and bend cycle within 25% accuracy," in *Electronic Components and Technology Conference, 2001. Proceedings., 51st*, 2001, pp. 255-263.

[70] Y. Kariya, T. Morihata, E. Hazawa, and M. Otsuka, "Assessment of low-cycle fatigue life of Sn-3.5 mass% Ag-X (X= Bi or Cu) alloy by strain range partitioning approach," *Journal of Electronic Materials,* vol. 30, p. 1184, 2001.

[71] E. Stowell, "A study of the energy criterion for fatigue," *Nuclear Engineering and Design,* vol. 3, pp. 32-40, 1966.

[72] M. G. Bevan and M. Wittig, "Complex fatigue of soldered joints-comparison of fatigue models," in *Electronic Components and Technology Conference, 1997. Proceedings., 47th*, 1997, pp. 127-133.

[73] T.-Y. Pan, "Critical accumulated strain energy (case) failure criterion for thermal cycling fatigue of solder joints," *Journal of Electronic Packaging,* vol. 116, pp. 163-170, 1994.

[74] D. Kujawski, "Fatigue failure criterion based on strain energy density," *Journal of Theoretical and Applied Mechanics,* vol. 27, pp. 15-22, 1989.

[75] J. Oldham and J. Abou-Hanna, "A numerical investigation of creep-fatigue life prediction utilizing hysteresis energy as a damage parameter," *International Journal of Pressure Vessels and Piping,* vol. 88, pp. 149-157, 2011.

[76] J. Morrow, "Cyclic plastic strain energy and fatigue of metals," in *Internal friction, damping, and cyclic plasticity,* ed: ASTM International, 1965.

[77] H. Solomon and E. Tolksdorf, "Energy approach to the fatigue of 60/40 solder: Part I—Influence of temperature and cycle frequency," *Journal of Electronic Packaging,* vol. 117, pp. 130-135, 1995.

[78] M. Mustafa, Z. Cai, J. C. Suhling, and P. Lall, "The effects of aging on the cyclic stress-strain behavior and hysteresis loop evolution of lead free solders," in *Proceedings of the 61st Electronic Components and Technology Conference,* 2011, pp. 927-939.

[79] J. I. Goldstein, D. E. Newbury, J. R. Michael, N. W. Ritchie, J. H. J. Scott, and D. C. Joy, *Scanning electron microscopy and X-ray microanalysis*: Springer, 2017.

[80] P. Borgesen, S. Hamasha, L. Wentlent, D. Watson, and C. Greene, "Interpreting accelerated test results for lead free solder joints," in *Pan Pacific Microelectronics Symposium (Pan Pacific), 2016*, 2016, pp. 1-9.

[81] L. Wentlent and P. Borgesen, "Statistical Variations of Solder Joint Fatigue Life Under Realistic Service Conditions," *IEEE Transactions on Components, Packaging and Manufacturing Technology,* vol. 5, pp. 1284-1291, 2015.

[82] J. H. Lau and Y.-H. Pao, *Solder joint reliability of BGA, CSP, flip chip, and fine pitch SMT assemblies* vol. 1: McGraw-Hill New York, 1997.

[83] S. Su, N. Fu, F. J. Akkara, and S. Hamasha, "Effect of Long-Term Room Temperature Aging on the Fatigue Properties of SnAgCu Solder Joint," *Journal of Electronic Packaging,* vol. 140, p. 031005, 2018.

[84] S. Hamasha, F. Akkara, S. Su, H. Ali, and P. Borgesen, "Effect of Cycling Amplitude Variations on SnAgCu Solder Joint Fatigue Life," *IEEE Transactions on Components, Packaging and Manufacturing Technology,* 2018.

[85] P. Borgesen, S. Hamasha, M. Obaidat, V. Raghavan, X. Dai, M. Meilunas*, et al.*, "Solder joint reliability under realistic service conditions," *Microelectronics Reliability,* vol. 53, pp. 1587-1591, 2013.

[86] S. Hamasha and P. Borgesen, "Effects of Strain Rate and Amplitude Variations on Solder Joint Fatigue Life in Isothermal Cycling," *Journal of Electronic Packaging,* vol. 138, p. 021002, 2016.

[87] S. Hamasha, S. Su, F. Akkara, A. Dawahdeh, P. Borgesen, and A. Qasaimeh, "Solder joint reliability in isothermal varying load cycling," in *Thermal and Thermomechanical Phenomena in Electronic Systems (ITherm), 2017 16th IEEE Intersociety Conference on*, 2017, pp. 1331-1336.

[88] F. Akkara, S. Su, S. Thirugnanasambandam, A. Dawahdeh, A. Qasaimeh, J. Evans*, et al.*, "Effects of Long-Term Aging on SnAgCu Solder Joints Reliability in Mechanical Cycling Fatigue," in *SMTA International Conference, Rosemont, IL, Sept*, 2017, pp. 17-21.

[89] S. Hamasha, Y. Jaradat, A. Qasaimeh, M. Obaidat, and P. Borgesen, "Assessment of Solder Joint Fatigue Life Under Realistic Service Conditions," *Journal of electronic materials*, vol. 43, 2014.

[90] S. Su, F. J. Akkara, M. Abueed, M. Jian, J. Suhling, and P. Lall, "Fatigue Properties of Lead-free Doped Solder Joints," in *2018 17th IEEE Intersociety Conference on Thermal and Thermomechanical Phenomena in Electronic Systems (ITherm)*, 2018, pp. 1243-1248.

[91] C. Zhao, "Board Level Reliability of Lead-Free Solder Interconnections with Solder Doping Under Harsh Environment," 2017.

[92] C. Zhao, T. Sanders, Z. Hai, C. Shen, and J. L. Evans, "Reliability Analysis of Lead-Free Solder Joints with Solder Doping on Harsh Environment," in *International Symposium on Microelectronics*, 2016, pp. 000117-000122.

[93] L. Gao, S. Xue, L. Zhang, Z. Sheng, F. Ji, W. Dai*, et al.*, "Effect of alloying elements on properties and microstructures of SnAgCu solders," *Microelectronic Engineering*, vol. 87, pp. 2025-2034, 2010.

[94] S. Sridhar, A. Raj, S. Hamasha, J. Evans, M. Bozack, and W. Johnson, "Reliability Study of Doped Lead Free Solder Paste Alloys by Thermal Cycling Testing," in *SMTA International Conference Proceedings*, 2017.

[95] A. Qasaimeh, S. Hamasha, Y. Jaradat, and P. Borgesen, "Damage evolution in lead free solder joints in isothermal fatigue," *Journal of Electronic Packaging,* vol. 137, p. 021012, 2015.

[96] A. Raj, S. Sridhar, S. Thirugnanasambandam, T. Sanders, S. Hamasha, J. Evans, *et al.*, "Comparative Study on Impact Of Various Low Creep Doped Lead Free Solder Alloys," in *SMTA International Conference Proceedings*, 2017.

[97] Y. Ma, H. Luo, W. Liu, Y. Huang, Q. Yu, and Y. Li, "Effects of Bi addition on interfacial reactions and mechanical properties of In–3Ag–xBi/Cu solder joints," *Journal of Materials Science: Materials in Electronics,* vol. 27, pp. 103-110, 2016.

[98] J. Zhou, Y. Sun, and F. Xue, "Properties of low melting point Sn–Zn–Bi solders," *Journal of alloys and compounds,* vol. 397, pp. 260-264, 2005.

[99] G. Li, B. Chen, X. Shi, S. C. Wong, and Z. Wang, "Effects of Sb addition on tensile strength of Sn–3.5 Ag–0.7 Cu solder alloy and joint," *Thin Solid Films,* vol. 504, pp. 421-425, 2006.

[100] F. J. Akkara, C. Zhao, R. Athamenh, S. Su, M. Abueed, S. Hamasha, *et al.*, "Effect of Solder Sphere Alloys and Surface Finishes on the Reliability of Lead-Free Solder Joints in Accelerated Thermal Cycling," in *2018 17th IEEE Intersociety Conference on Thermal and Thermomechanical Phenomena in Electronic Systems (ITherm)*, 2018, pp. 1374-1380.

[101] M. Arra, D. Shangguan, D. Xie, J. Sundelin, T. Lepistö, and E. Ristolainen, "Study of immersion silver and tin printed-circuit-board surface finishes in lead-free solder applications," *Journal of electronic materials,* vol. 33, pp. 977-990, 2004.

[102] J.-M. Kim, M.-H. Jeong, S. Yoo, C.-W. Lee, and Y.-B. Park, "Effects of surface finishes and loading speeds on shear strength of Sn–3.0 Ag–0.5 Cu solder joints," *Microelectronic Engineering,* vol. 89, pp. 55-57, 2012.

[103] C.-B. Lee, I.-Y. Lee, S.-B. Jung, and C.-C. Shur, "Effect of surface finishes on ball shear strength in BGA joints with Sn-3.5 mass% Ag solder," *Materials transactions,* vol. 43, pp. 751-756, 2002.

[104] P. Liu, P. Yao, and J. Liu, "Effects of multiple reflows on interfacial reaction and shear strength of SnAgCu and SnPb solder joints with different PCB surface finishes," *Journal of Alloys and Compounds,* vol. 470, pp. 188-194, 2009.

[105] F. Song, S. R. Lee, K. Newman, B. Sykes, and S. Clark, "Brittle failure mechanism of SnAgCu and SnPb solder balls during high speed ball shear and cold ball pull tests," in *Electronic Components and Technology Conference, 2007. ECTC'07. Proceedings. 57th*, 2007, pp. 364-372.

[106] J.-W. Yoon and S.-B. Jung, "Effect of immersion Ag surface finish on interfacial reaction and mechanical reliability of Sn–3.5 Ag–0.7 Cu solder joint," *Journal of Alloys and Compounds,* vol. 458, pp. 200-207, 2008.

[107] K. Newman, "BGA brittle fracture-alternative solder joint integrity test methods," in *Electronic Components and Technology Conference, 2005. Proceedings. 55th*, 2005, pp. 1194-1201.

[108] F. Song, S. R. Lee, K. Newman, B. Sykes, and S. Clark, "High-speed solder ball shear and pull tests vs. board level mechanical drop tests: correlation of failure mode and loading speed," in *Electronic Components and Technology Conference, 2007. ECTC'07. Proceedings. 57th*, 2007, pp. 1504-1513.

[109] F. Akkara, M. Abueed, M. Rababah, C. Zhao, S. Su, J. Suhling*, et al.*, "Effect of Surface Finish and High Bi Solder Alloy on Component Reliability in Thermal Cycling," in *2018 IEEE 68th Electronic Components and Technology Conference (ECTC)*, 2018, pp. 2032-2040.

[110] J. J. Sundelin, S. T. Nurmi, T. K. Lepistö, and E. O. Ristolainen, "Mechanical and microstructural properties of SnAgCu solder joints," *Materials Science and Engineering: A*, vol. 420, pp. 55-62, 2006.

[111] T. Edwards, "Solder Joint Similarities of BGAs, CSPs and Other Surface-Mounted Devices," *Chip Scale Review*, pp. 38-45, 1997.

[112] M. ZEQUN, "Interfacial Fracture Mechanism of BGA Package on Electroless Ni/Au," in *Conf. ASTM International Engineering Congress & Exposition*, 1997.

[113] M. Huang and L. Wang, "Effects of Cu, Bi, and In on microstructure and tensile properties of Sn-Ag-X (Cu, Bi, In) solders," *Metallurgical and Materials Transactions A,* vol. 36, pp. 1439-1446, 2005.

[114] C. Kanchanomai, Y. Miyashita, and Y. Mutoh, "Low-cycle fatigue behavior of Sn-Ag, Sn-Ag-Cu, and Sn-Ag-Cu-Bi lead-free solders," *Journal of Electronic Materials,* vol. 31, pp. 456-465, 2002.

[115] M. Sona and K. Prabhu, "Review on microstructure evolution in Sn–Ag–Cu solders and its effect on mechanical integrity of solder joints," *Journal of Materials Science: Materials in Electronics,* vol. 24, pp. 3149-3169, 2013.

[116] Y. Takamatsu, H. Esaka, and K. Shinozuka, "Formation Mechanism of Eutectic Cu6Sn5 and Ag3Sn after Growth of Primary β-Sn in Sn-Ag-Cu Alloy," *Materials transactions*, vol. 52, pp. 189-195, 2011.

[117] R. Erich, R. J. Coyle, G. M. Wenger, and A. Primavera, "Shear testing and failure mode analysis for evaluation of BGA ball attachment," in *Electronics Manufacturing Technology Symposium, 1999. Twenty-Fourth IEEE/CPMT*, 1999, pp. 16-22.

[118] J. Y. H. Chia, B. Cotterell, and T. C. Chai, "The mechanics of the solder ball shear test and the effect of shear rate," *Materials Science and Engineering: A*, vol. 417, pp. 259-274, 2006.

[119] C.-L. Yeh and Y.-S. Lai, "Insights into correlation between board-level drop reliability and package-level ball impact test," in *Electronic Components and Technology Conference, 2006. Proceedings. 56th*, 2006, p. 7 pp.

[120] P. Borgesen, L. Wentlent, T. Alghoul, S. Joshi, R. Sivasubramony, M. Yadav*, et al.*, "A mechanistic model for the life of solder joints under realistic long-term service conditions," in *Thermal, Mechanical and Multi-Physics Simulation and Experiments in Microelectronics and Microsystems (EuroSimE), 2018 19th International Conference on,* 2018, pp. 1-11.

[121] B. Arfaei, Y. Xing, J. Woods, J. Wolcott, P. Tumne, P. Borgesen*, et al.*, "The effect of Sn grain number and orientation on the shear fatigue life of SnAgCu solder joints," in

Electronic Components and Technology Conference, 2008. ECTC 2008. 58th, 2008, pp. 459-465.

[122] A. Qasaimeh, Y. Jaradat, L. Wentlent, L. Yang, L. Yin, B. Arfaei, *et al.*, "Recrystallization behavior of lead free and lead containing solder in cycling," in *Electronic Components and Technology Conference (ECTC), 2011 IEEE 61st*, 2011, pp. 1775-1781.

Appendices

Appendix A

Additional Figures Used in the Dissertation

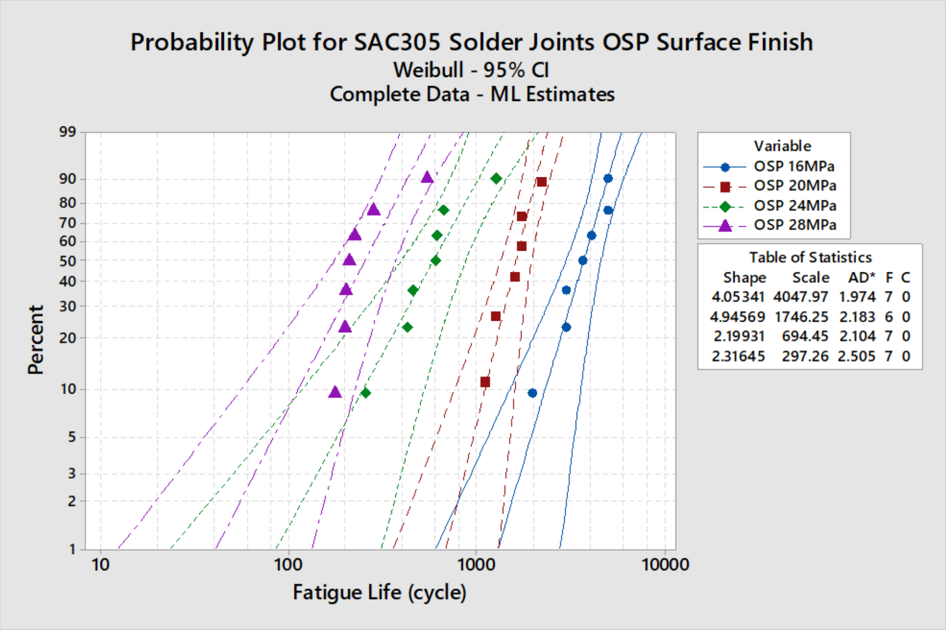

Shape	Scale	AD*	F	C
4.05341	4047.97	1.974	7	0
4.94569	1746.25	2.183	6	0
2.19931	694.45	2.104	7	0
2.31645	297.26	2.505	7	0

Figure A1. Weibull plot for SAC305 with OSP surface finish

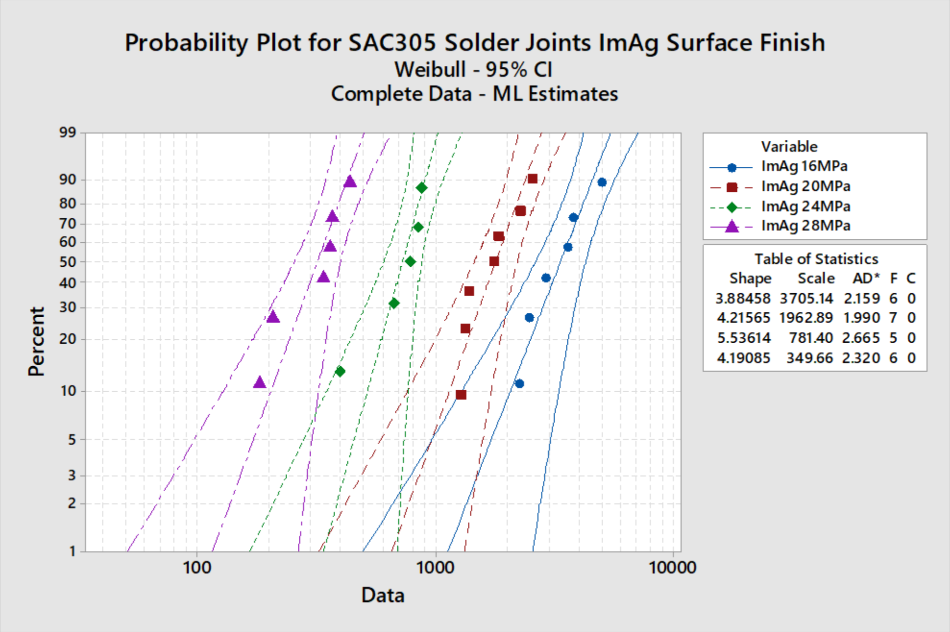

Shape	Scale	AD*	F	C
3.88458	3705.14	2.159	6	0
4.21565	1962.89	1.990	7	0
5.53614	781.40	2.665	5	0
4.19085	349.66	2.320	6	0

Figure A2. Weibull plot for SAC305 with ImAg surface finish

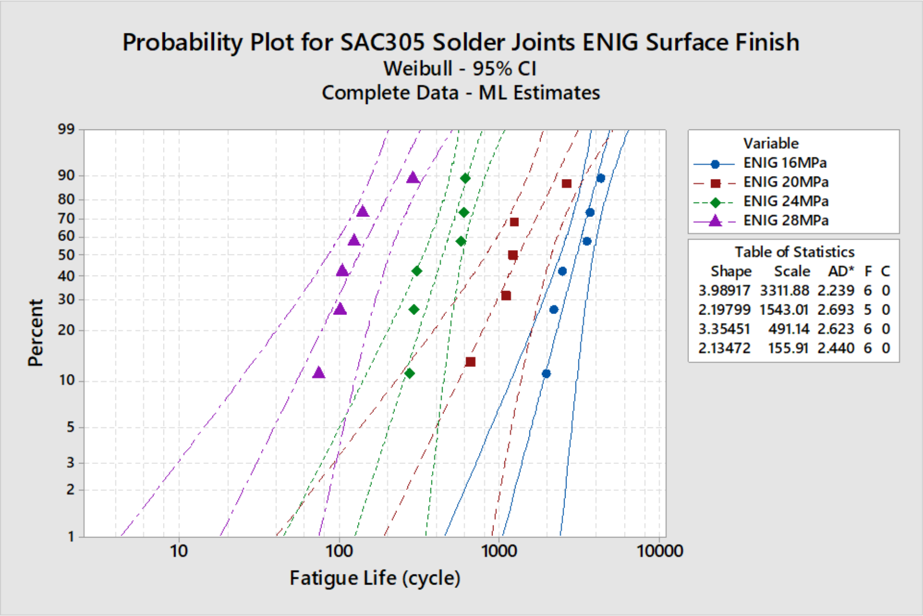

Figure A3. Weibull plot for SAC305 with ENIG surface finish

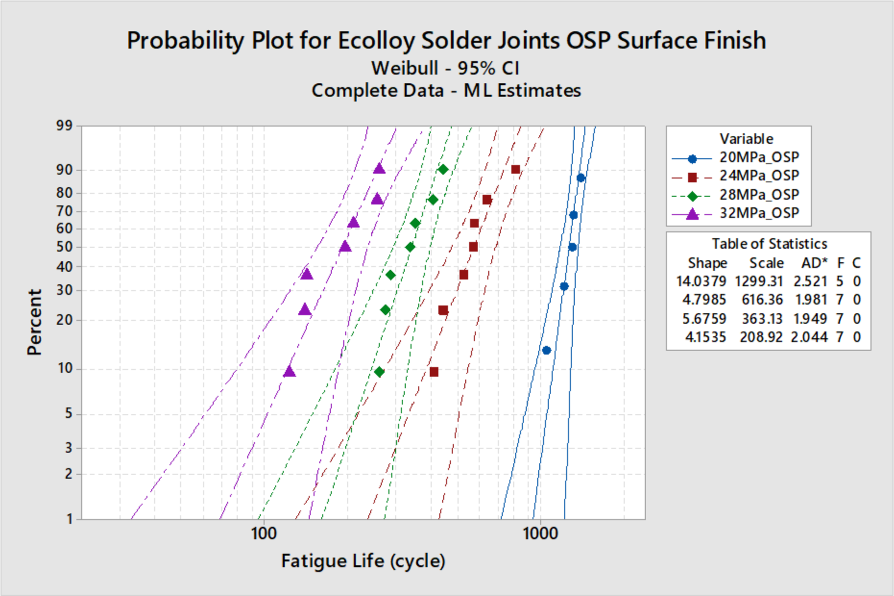

Figure A4. Weibull plot for Ecolloy with OSP surface finish

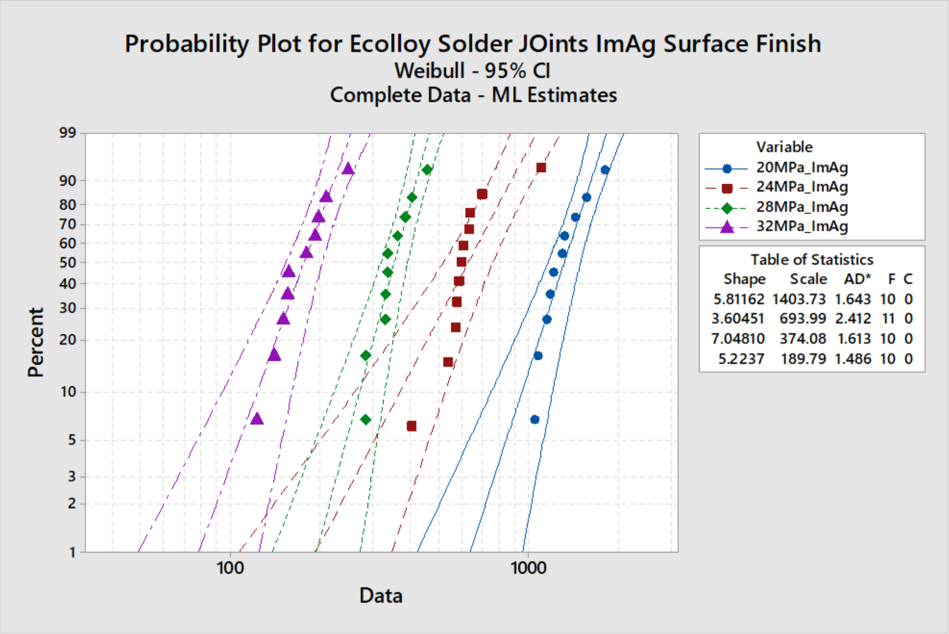

Figure A5. Weibull plot for Ecolloy with ImAg surface finish

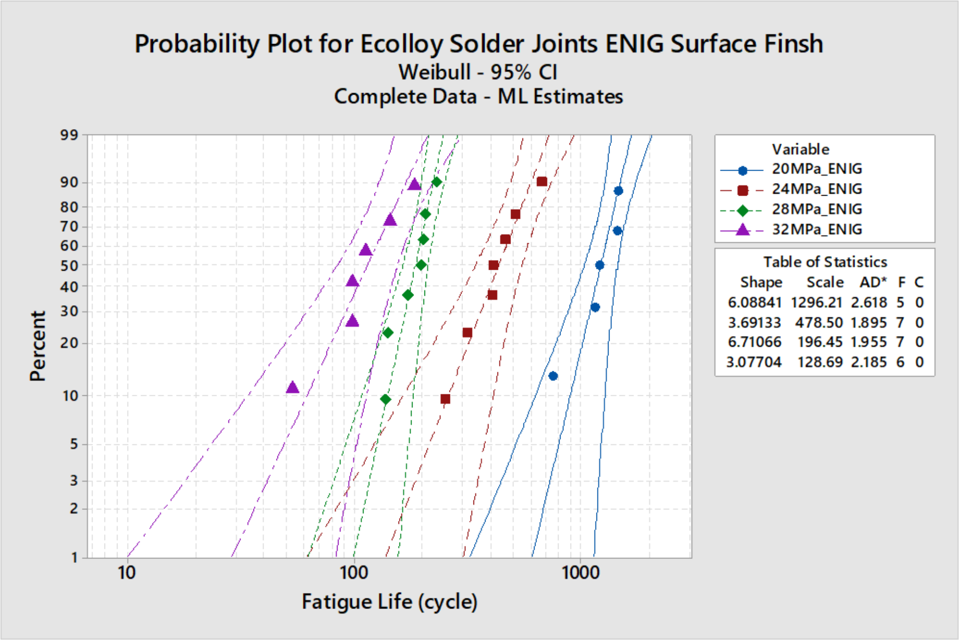

Figure A6. Weibull plot for Ecolloy with ENIG surface finish

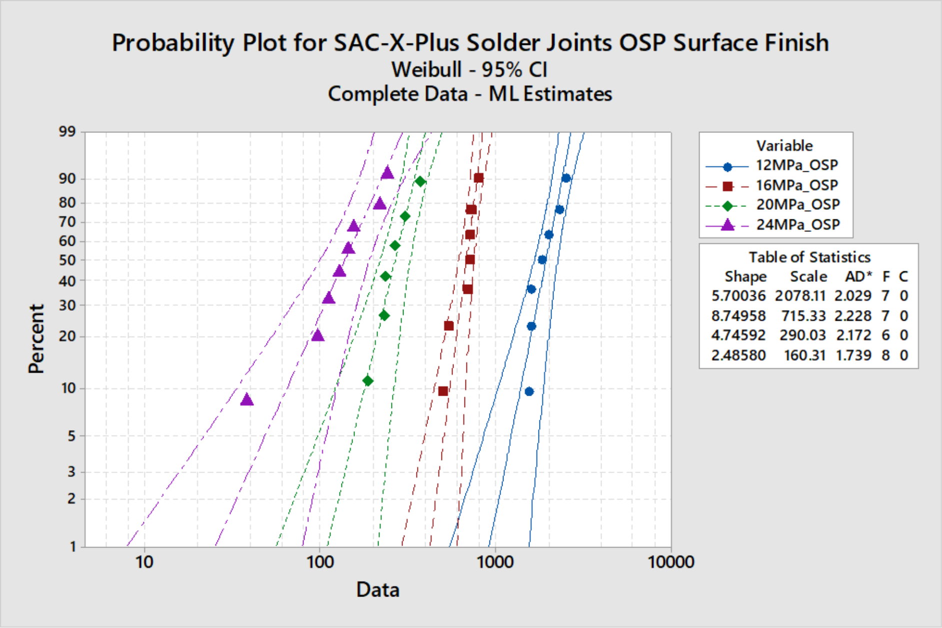

Figure A7. Weibull plot for SAC-X-Plus with OSP surface finish

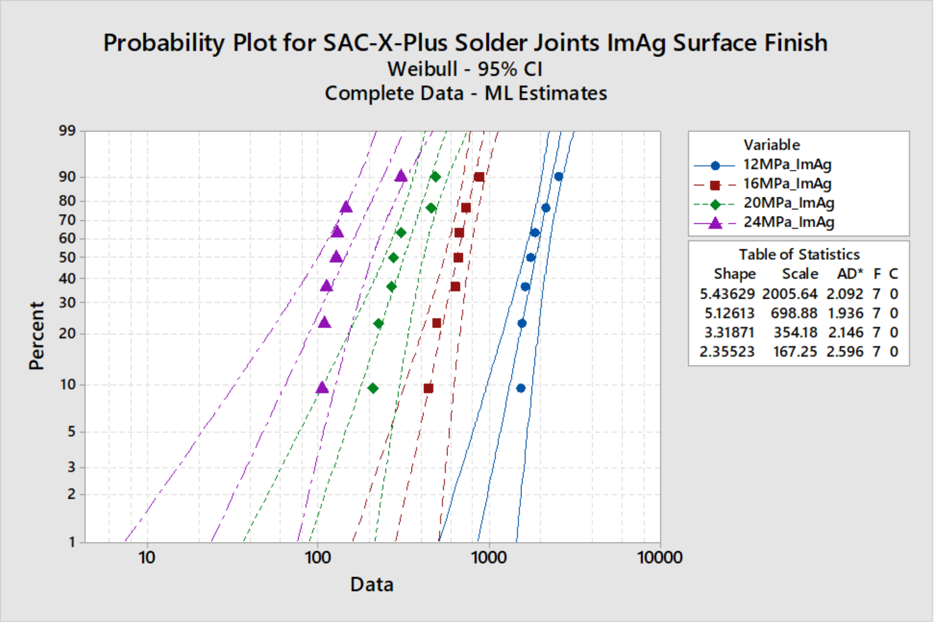

Figure A8. Weibull plot for SAC-X-Plus with ImAg surface finish

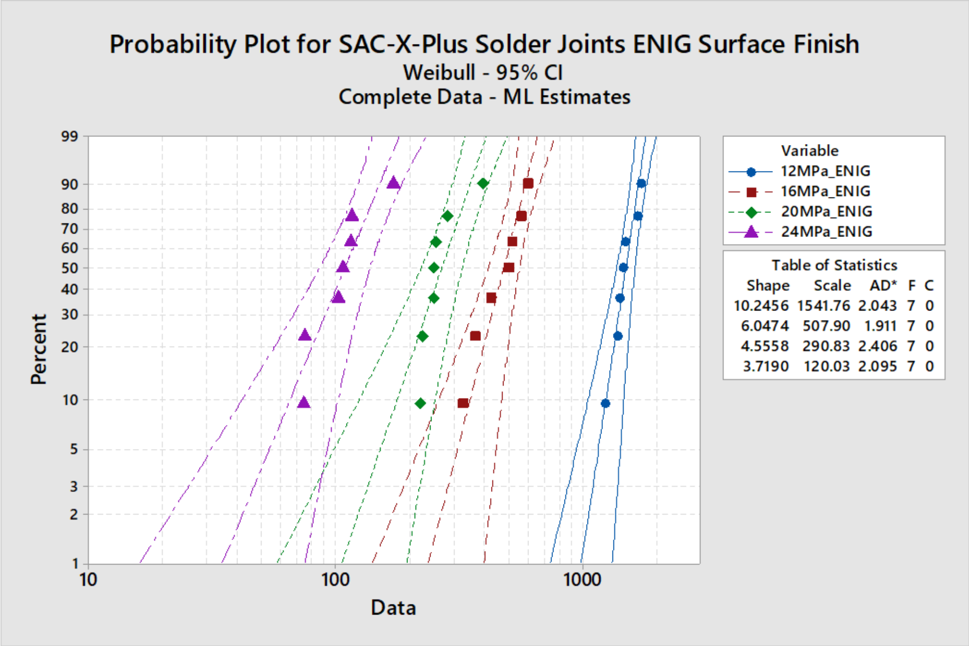

Figure A9. Weibull plot for SAC-X-Plus with ENIG surface finish

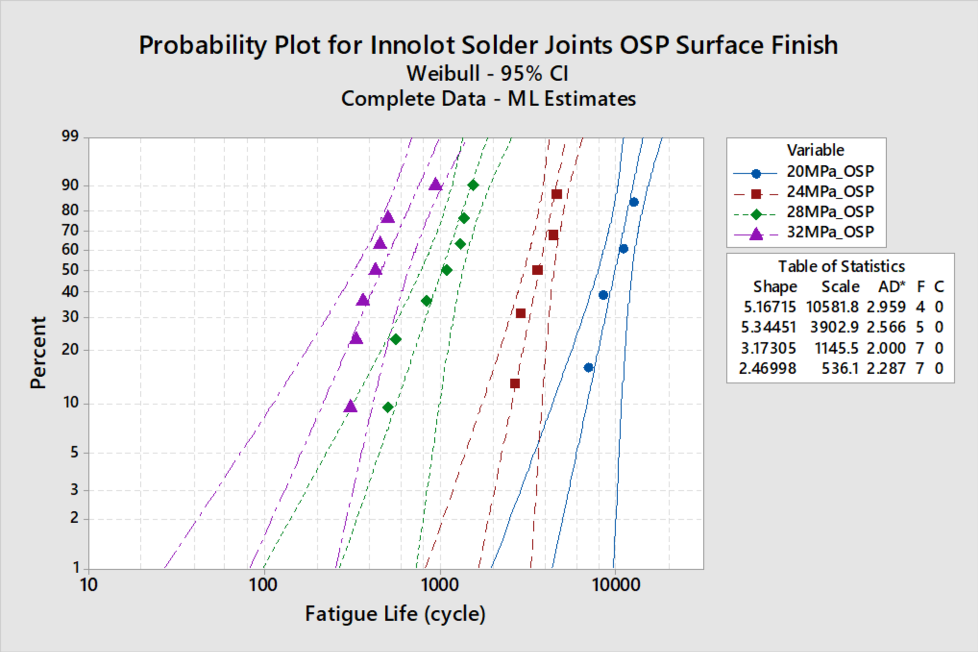

Figure A10. Weibull plot for Innolot with OSP surface finish

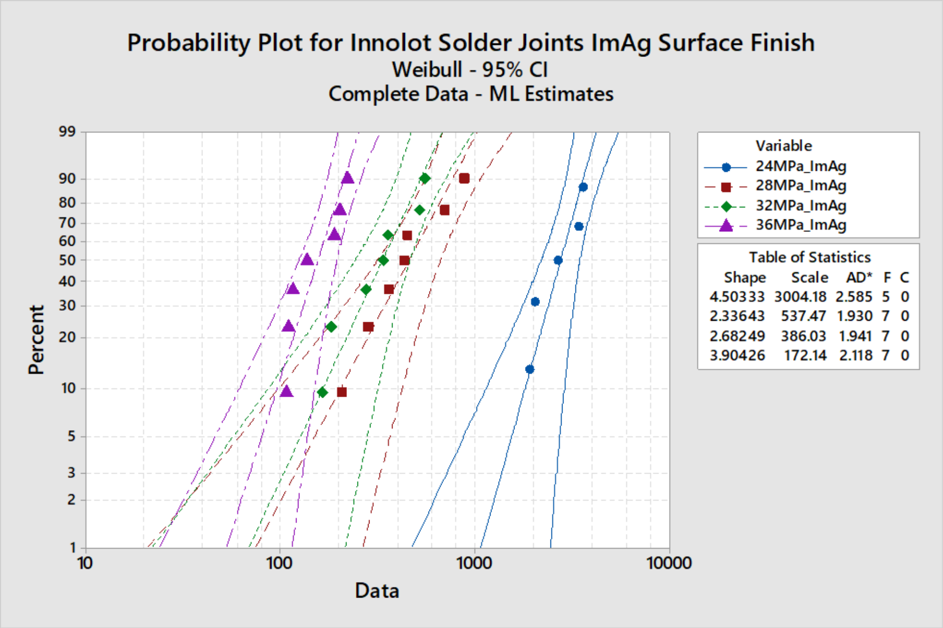

Figure A11. Weibull plot for Innolot with ImAg surface finish

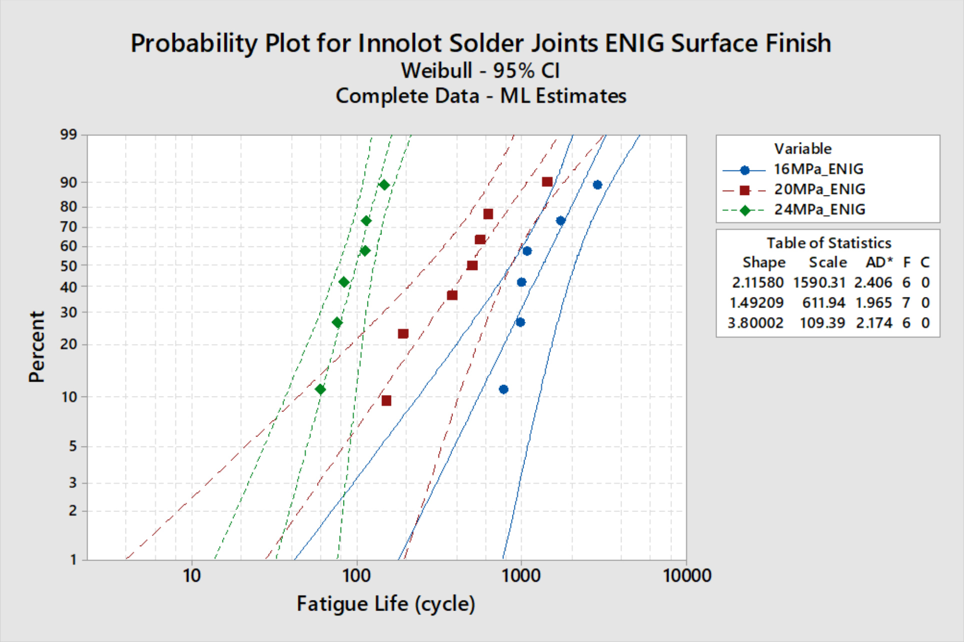

Figure A12. Weibull plot for Innolot with ENIG surface finish

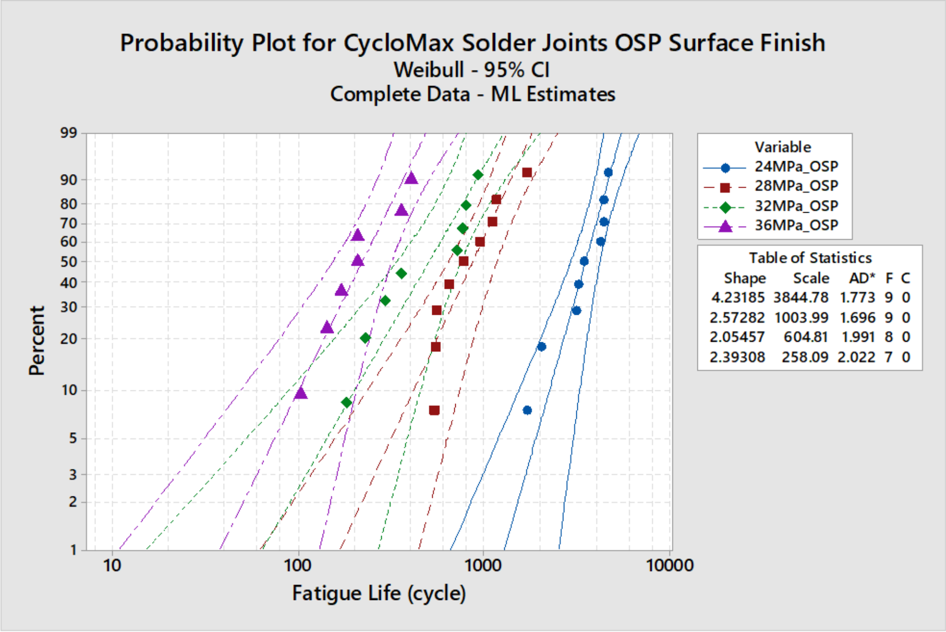

Figure A13. Weibull plot for CycloMax with OSP surface finish

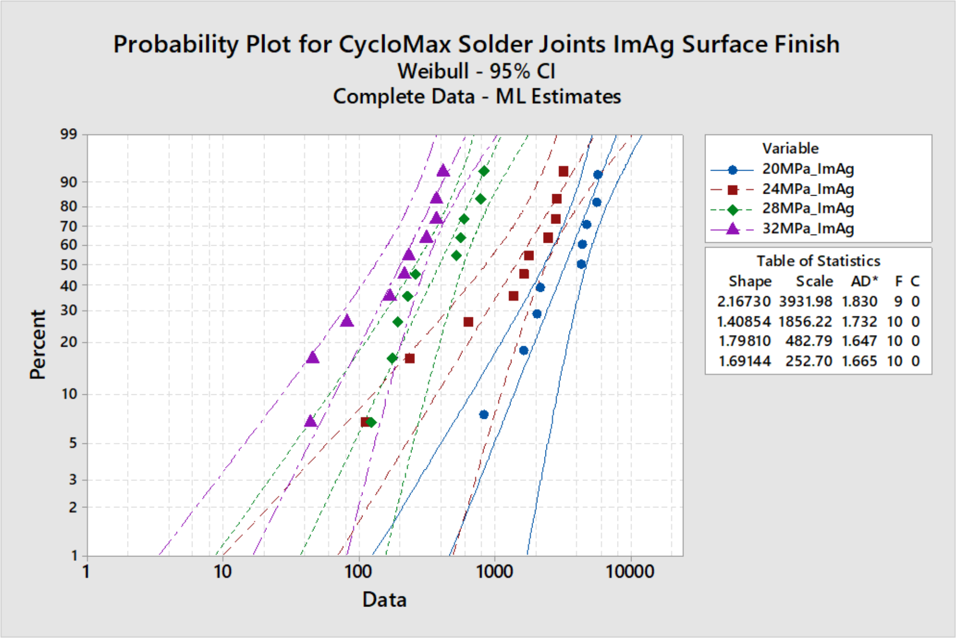

Figure A14. Weibull plot for CycloMax with ImAg surface finish

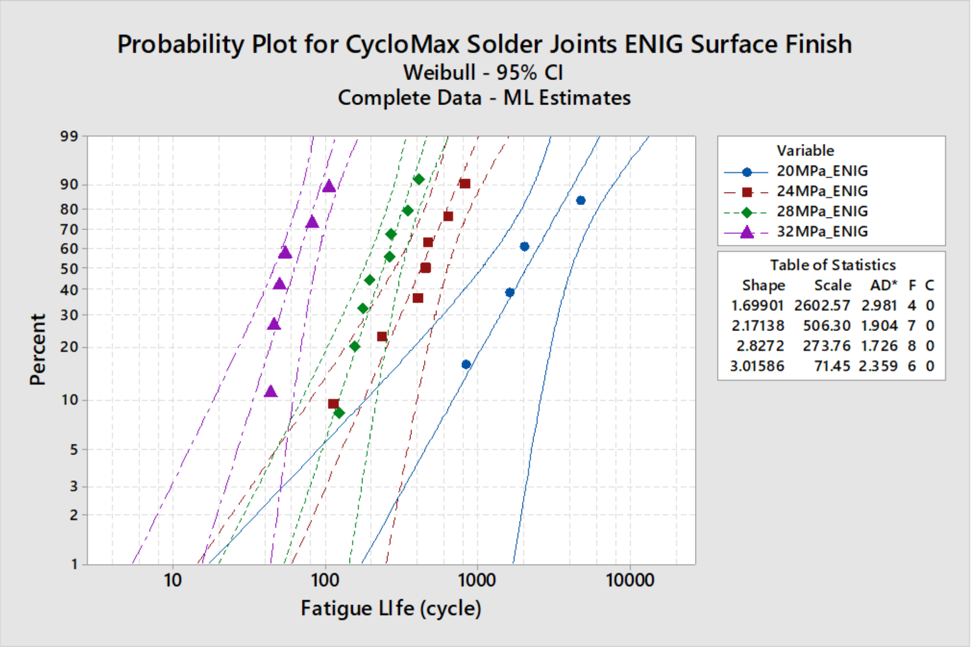

Figure A15. Weibull plot for CycloMax with ENIG surface finish

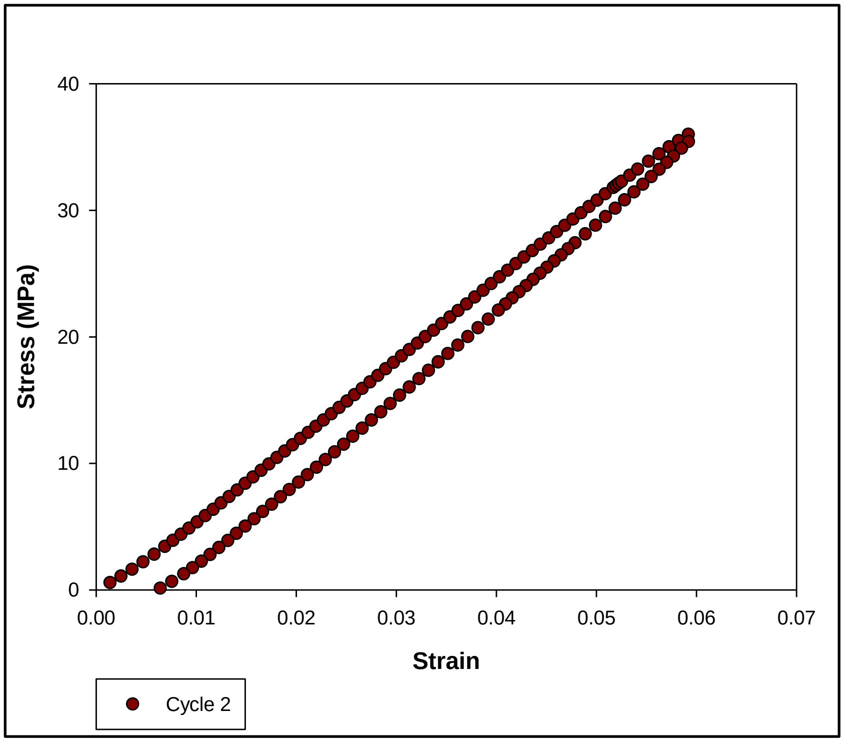

Figure A16. Hysteresis loop at cycle 2 for SAC305

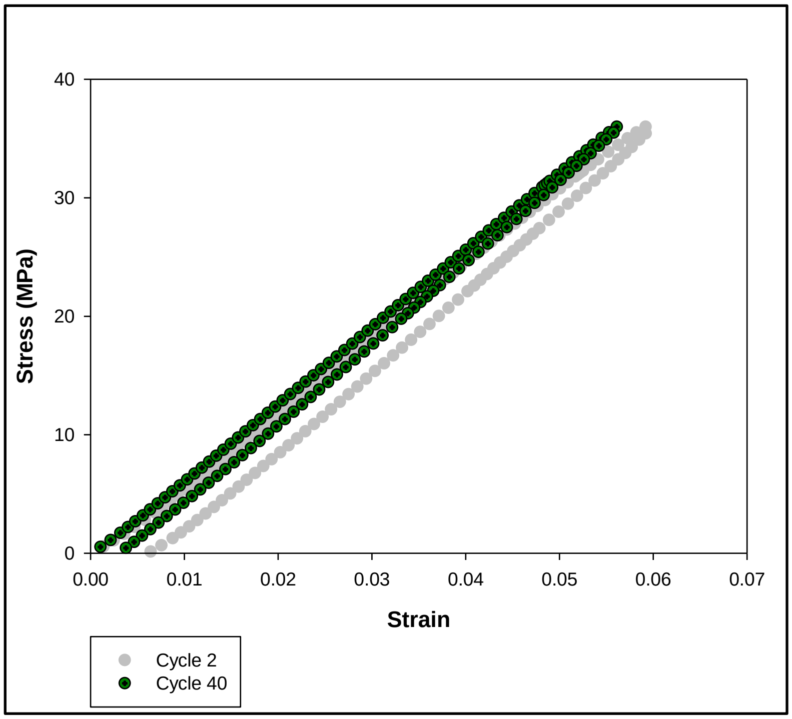

Figure A17. Hysteresis loop at cycle 40 for SAC305

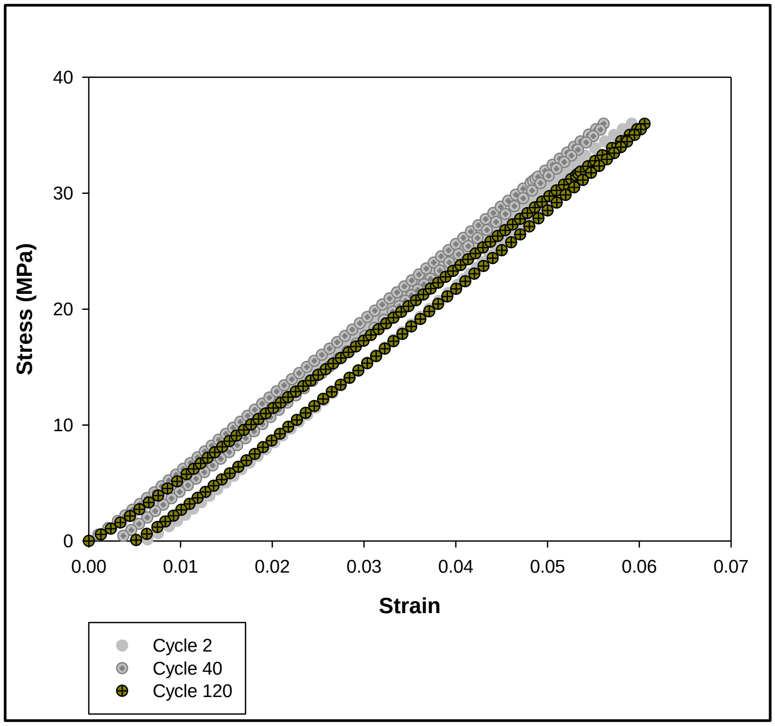

Figure A18. Hysteresis loop at cycle 120 for SAC305

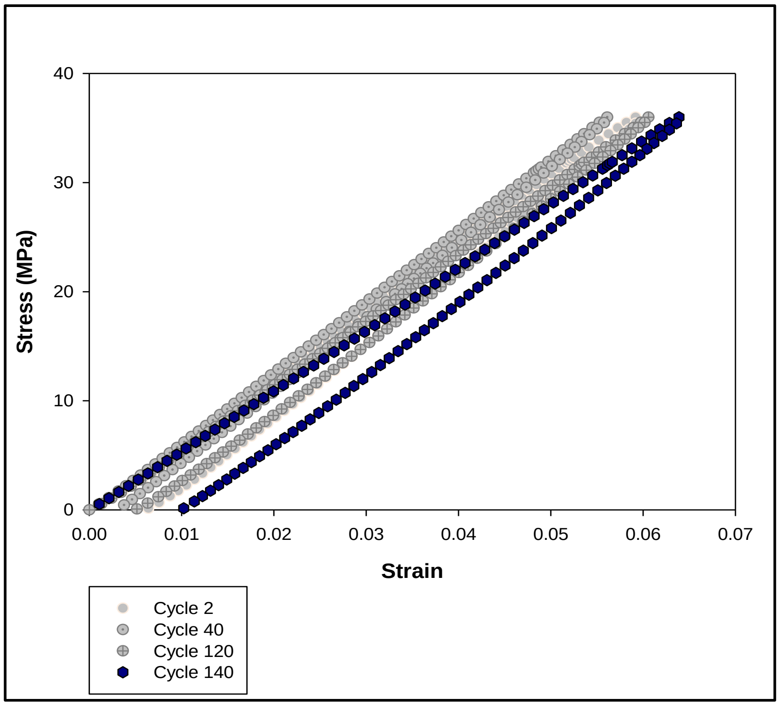

Figure A19. Hysteresis loop at cycle 140 for SAC305

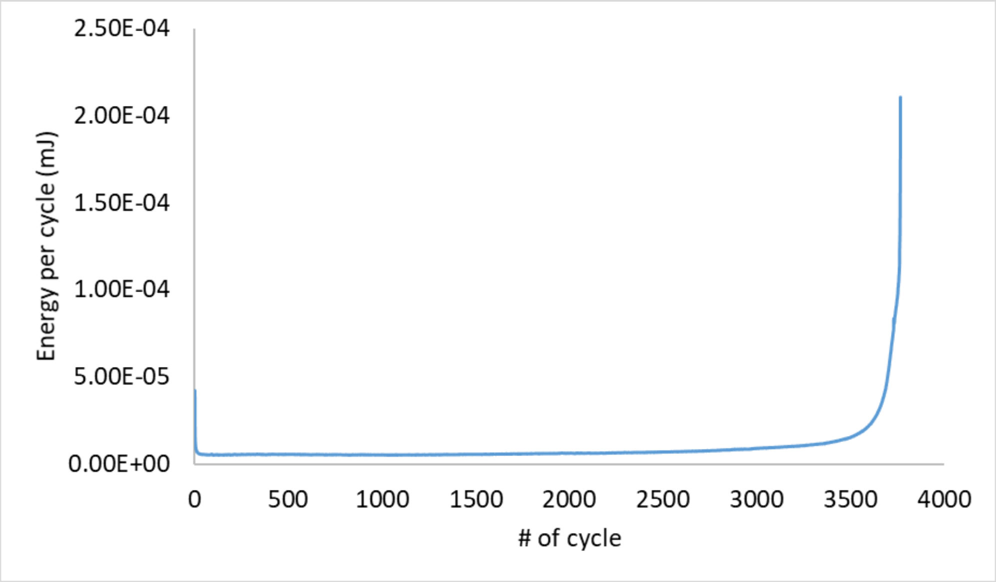

Figure A20. Work per cycle as a function of cycle number for SAC305 OSP at 16MPa

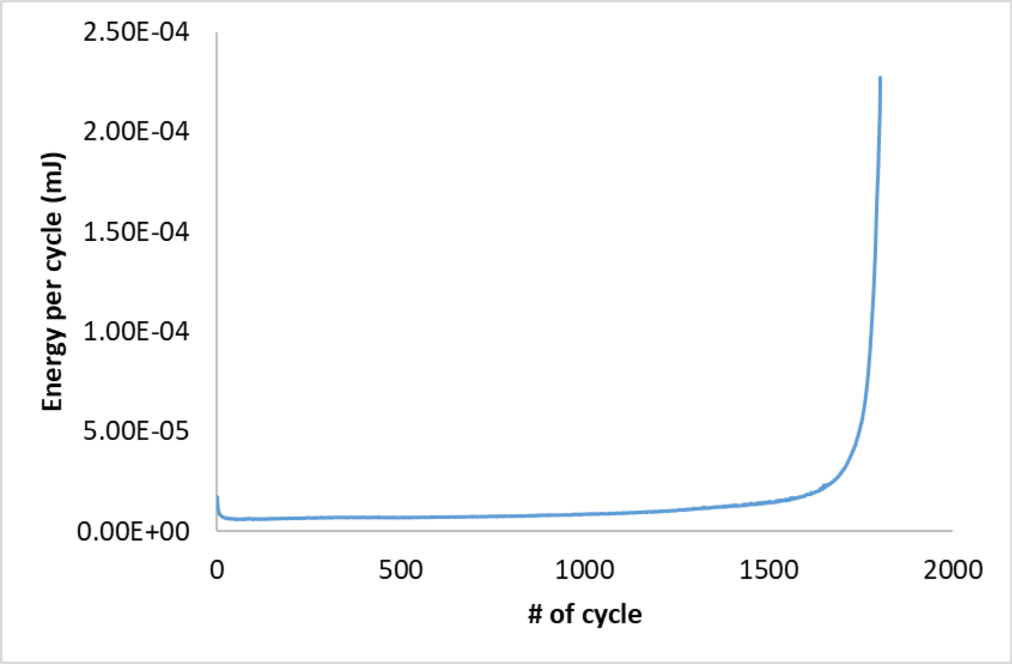

Figure A21. Work per cycle as a function of cycle number for SAC305 OSP at 20MPa

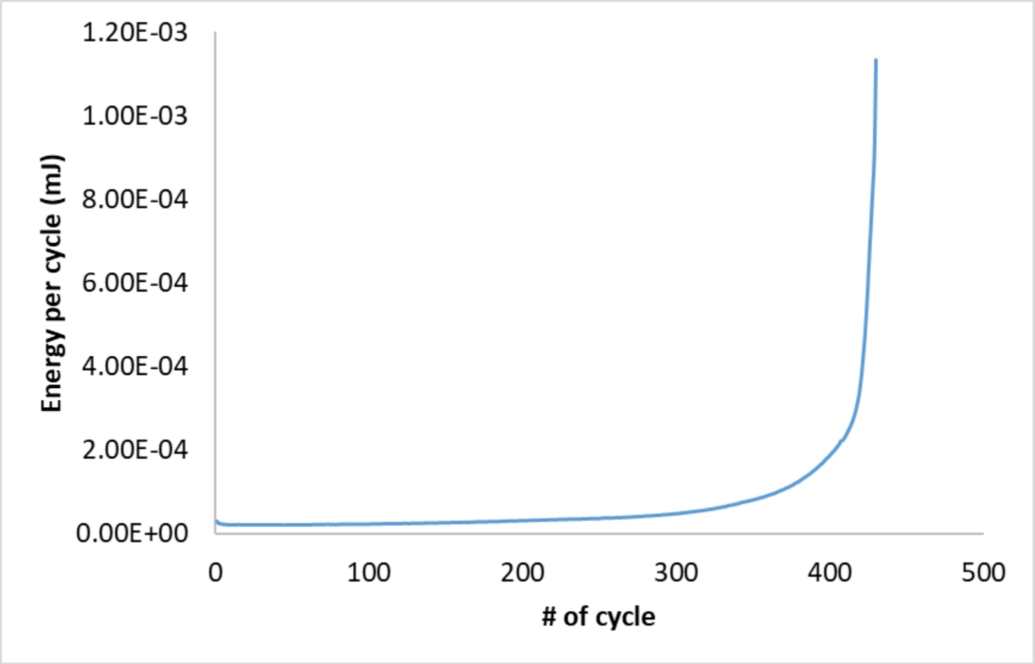

Figure A22. Work per cycle as a function of cycle number for SAC305 OSP at 24MPa

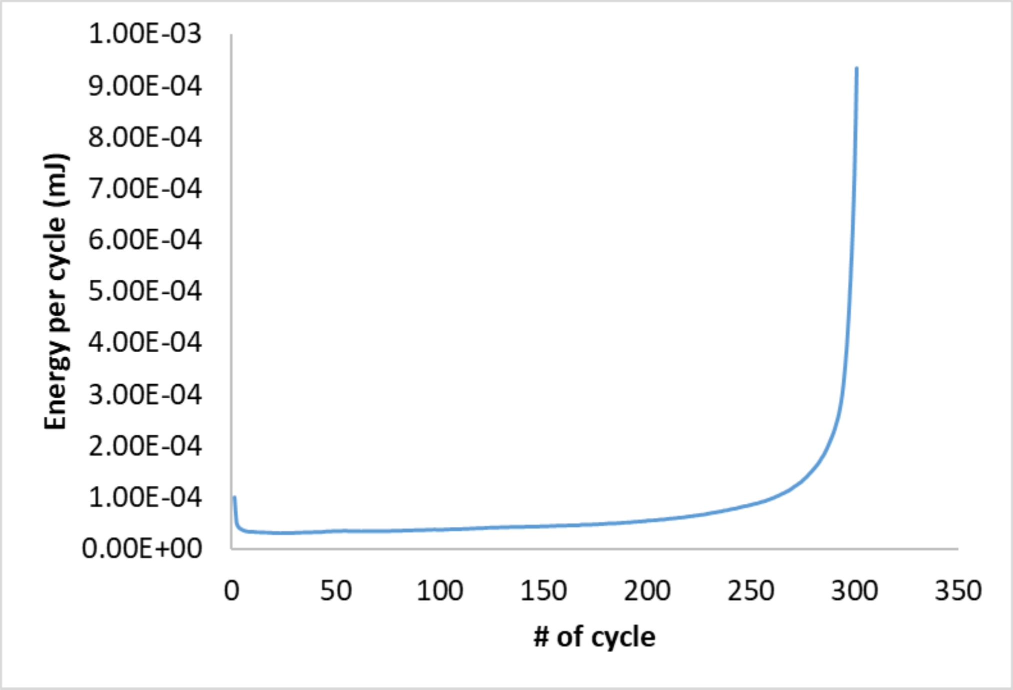

Figure A23. Work per cycle as a function of cycle number for SAC305 OSP at 28MPa

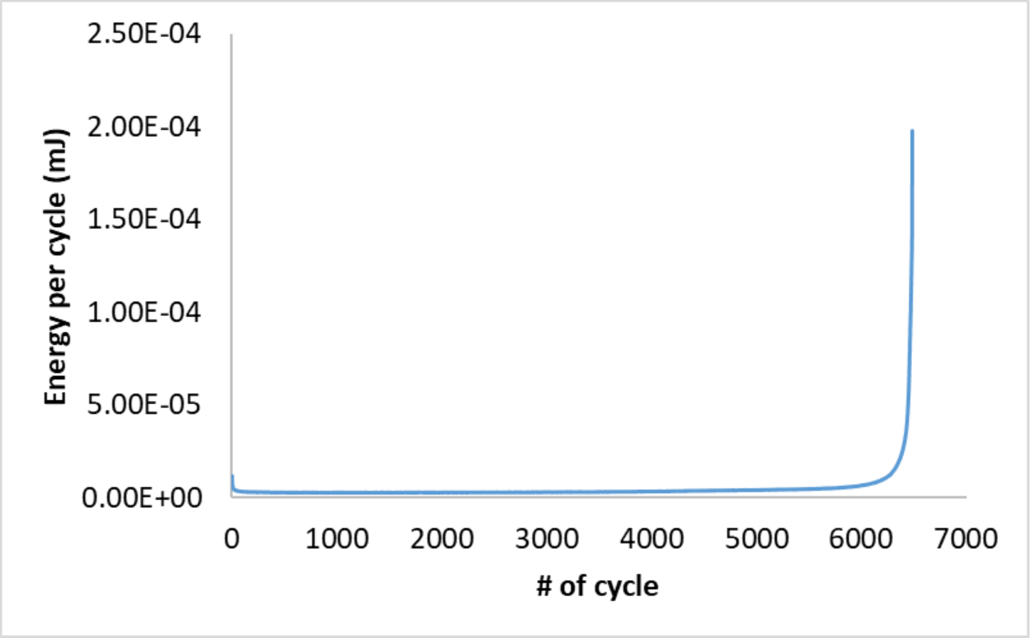

Figure A24. Work per cycle as a function of cycle number for SAC305 ImAg at 16MPa

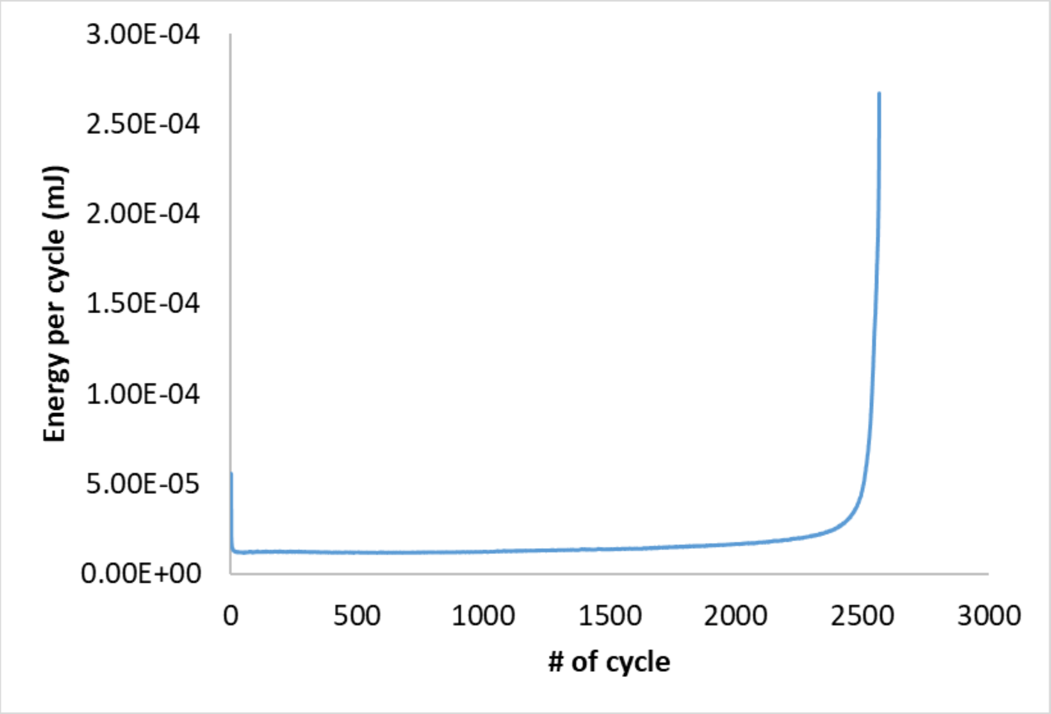

Figure A25. Work per cycle as a function of cycle number for SAC305 ImAg at 20MPa

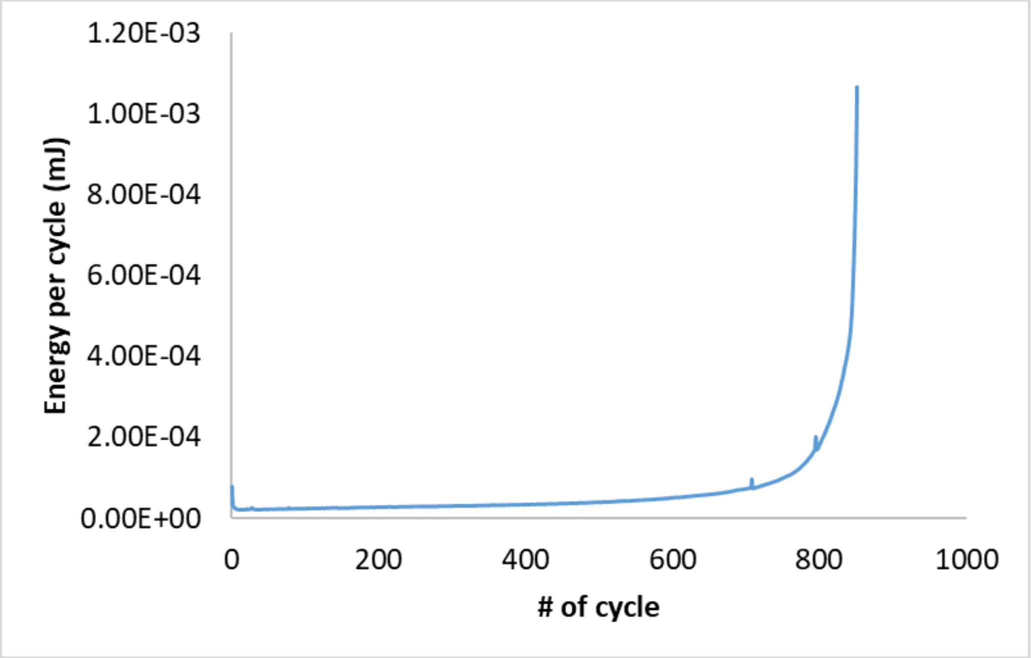

Figure A26. Work per cycle as a function of cycle number for SAC305 ImAg at 24MPa

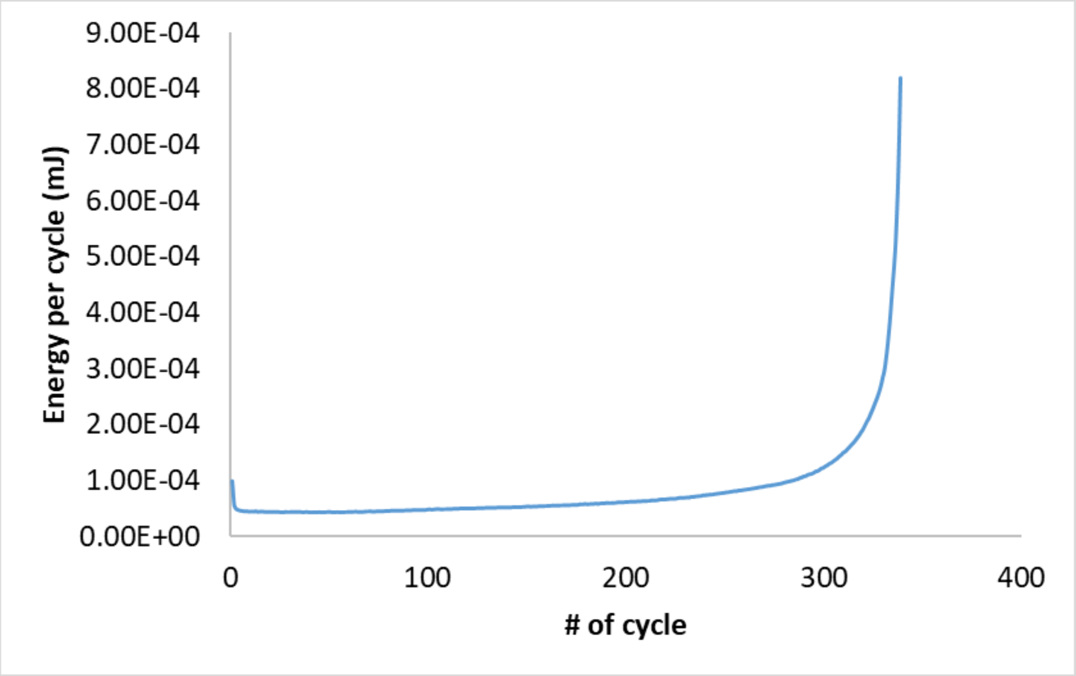

Figure A27. Work per cycle as a function of cycle number for SAC305 ImAg at 28MPa

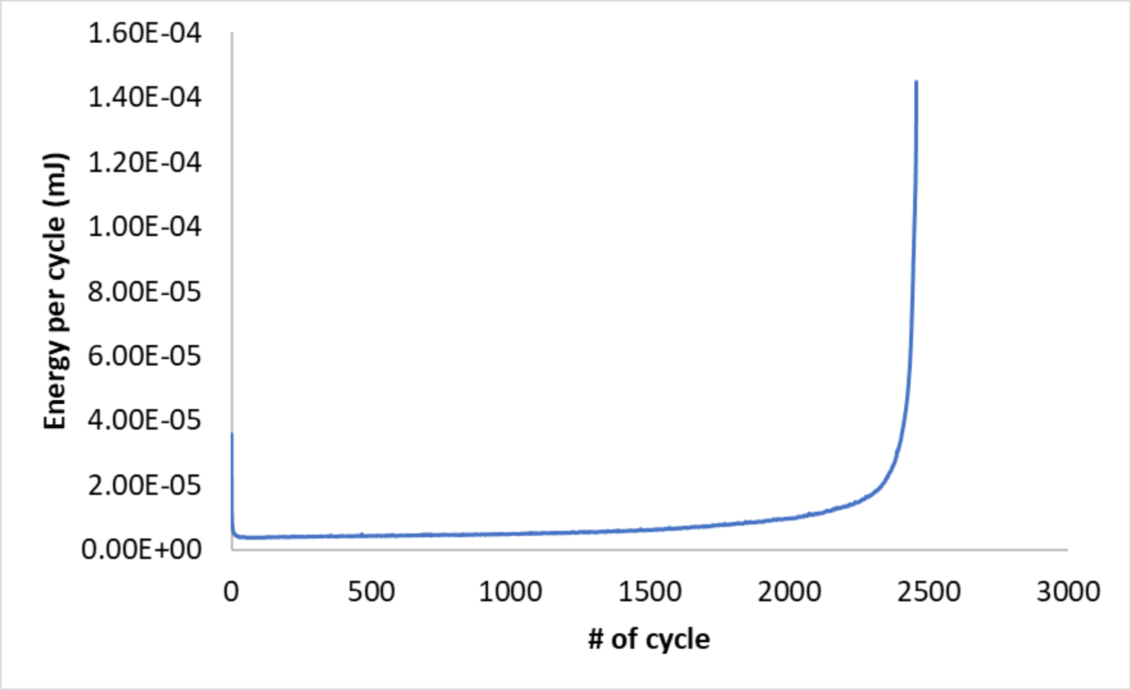

Figure A28. Work per cycle as a function of cycle number for SAC305 ENIG at 16MPa

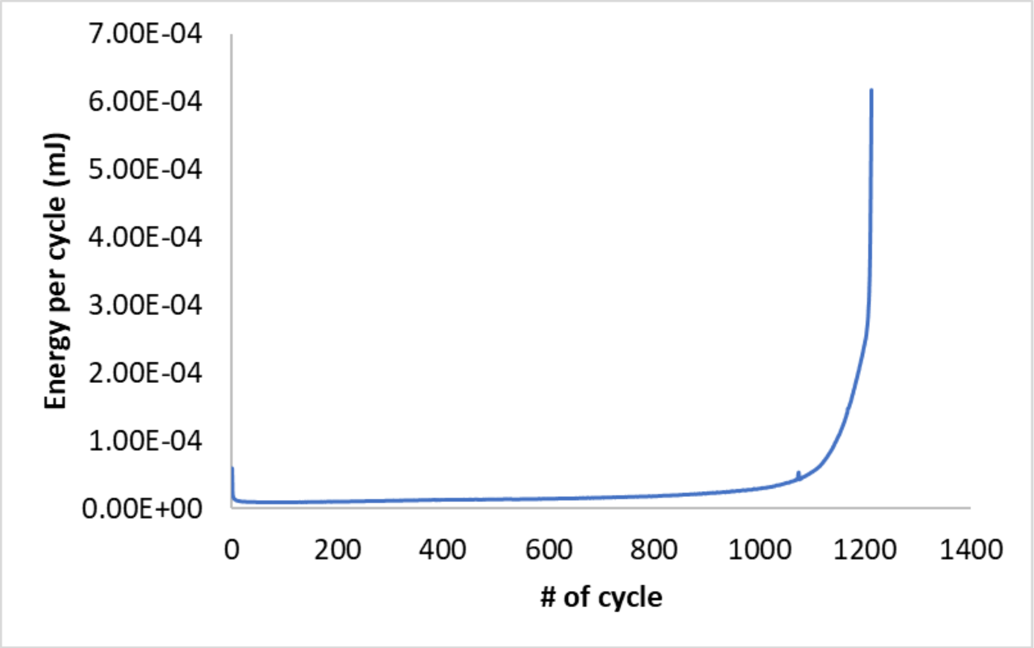

Figure A29. Work per cycle as a function of cycle number for SAC305 ENIG at 20MPa

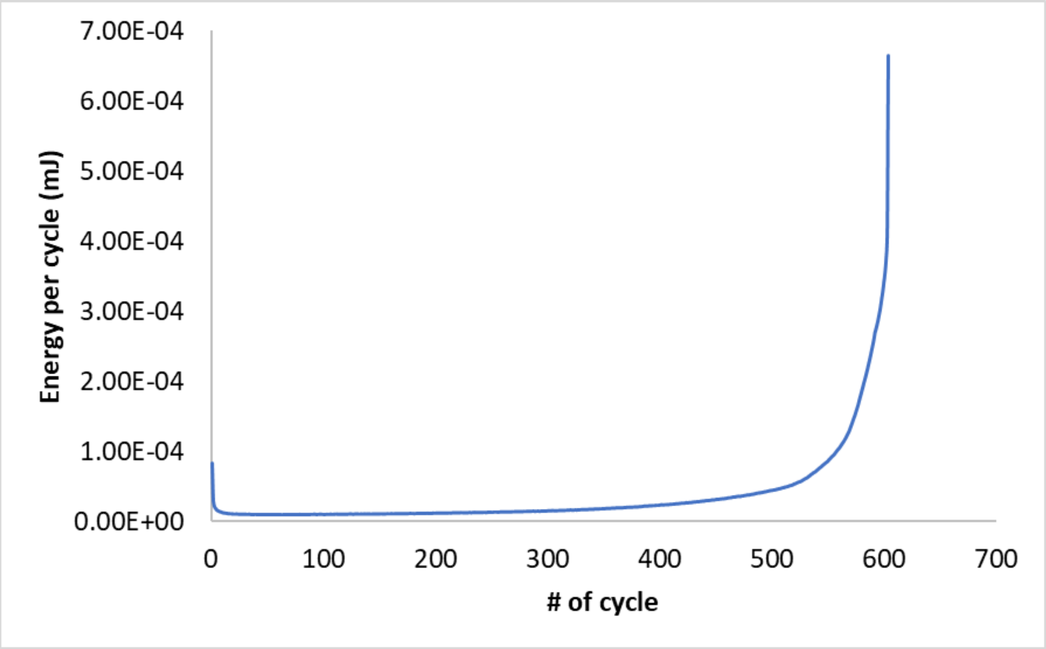

Figure A30. Work per cycle as a function of cycle number for SAC305 ENIG at 24MPa

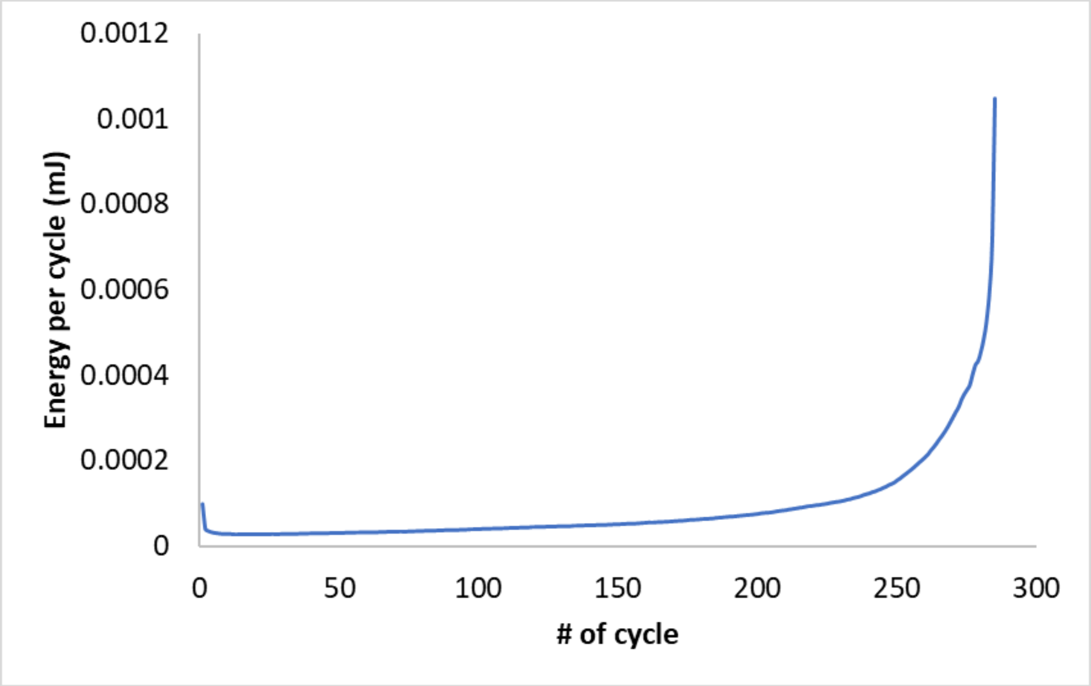

Figure A31. Work per cycle as a function of cycle number for SAC305 ENIG at 28MPa

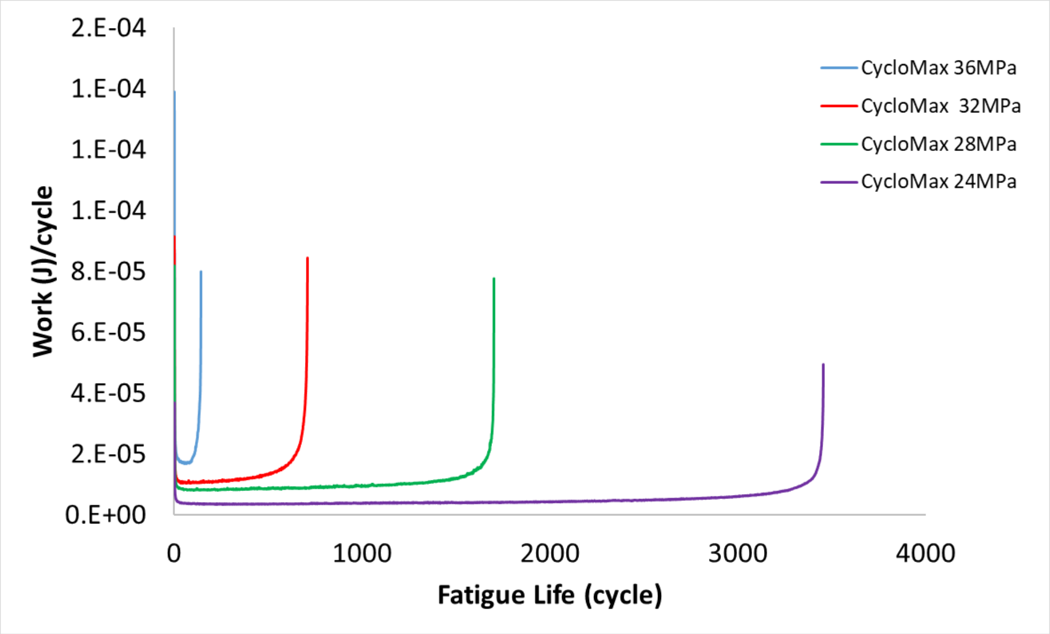

Figure A32. Work per cycle as a function of cycle number for CycloMax OSP at 4 stress amplitudes

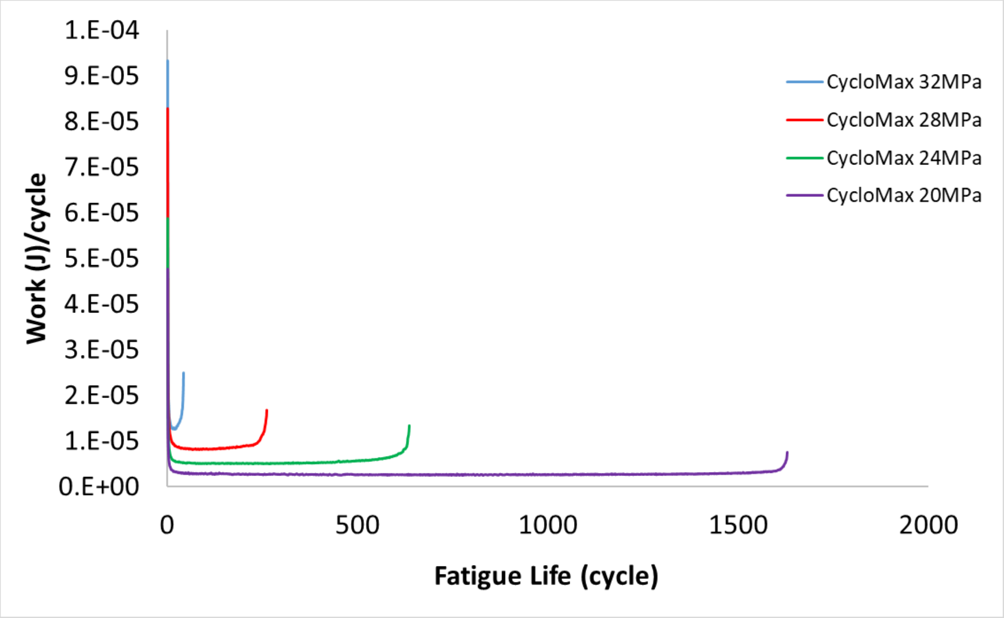

Figure A33. Work per cycle as a function of cycle number for CycloMax ENIG at 4 stress amplitudes

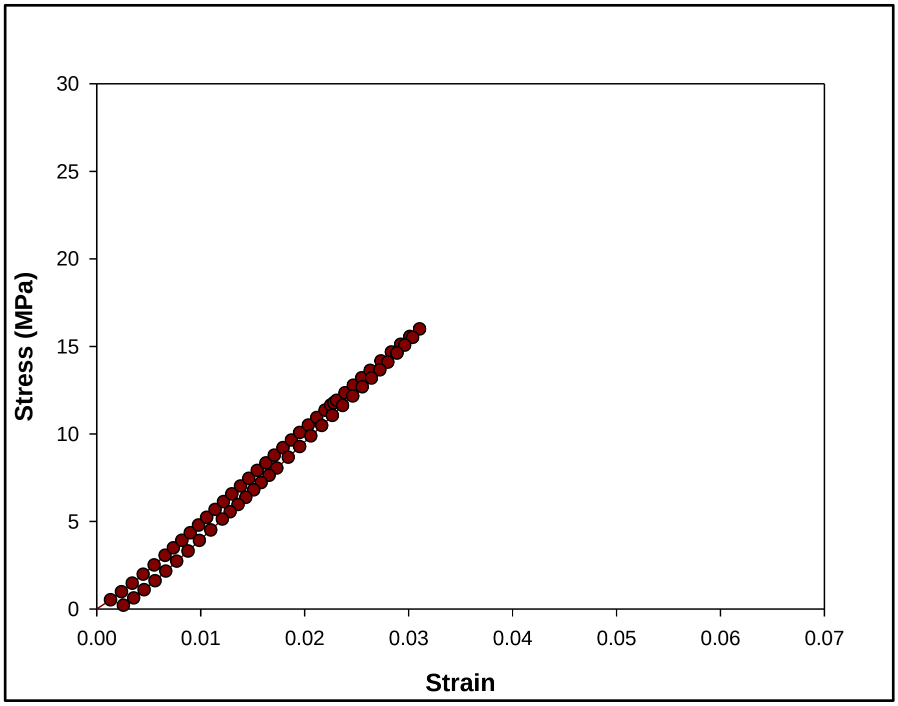

Figure A34. Hysteresis loop for SAC305 at 16MPa

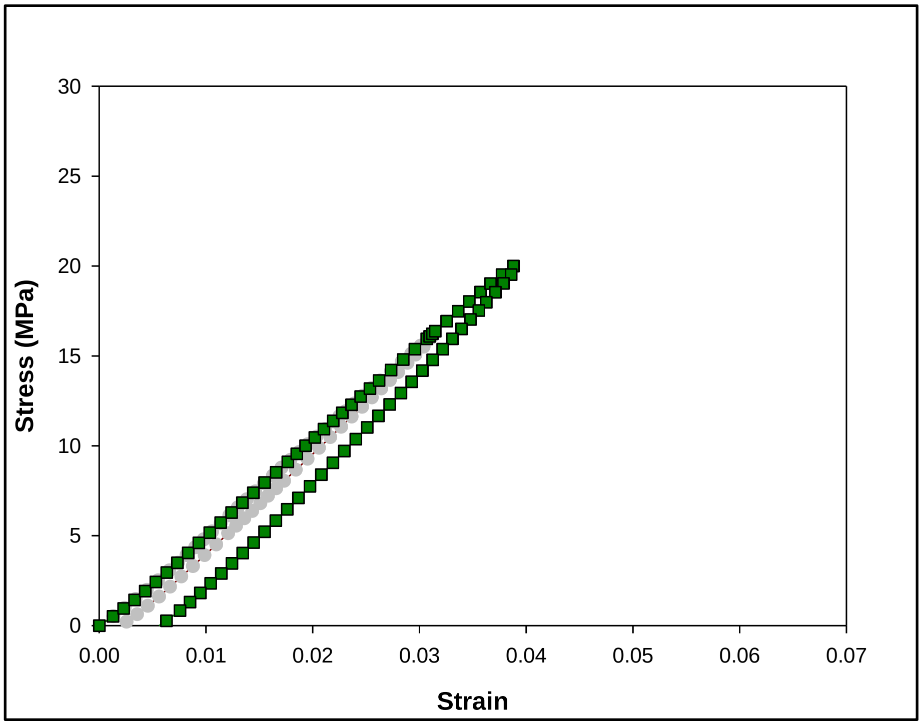

Figure A35. Hysteresis loop for SAC305 at 20MPa

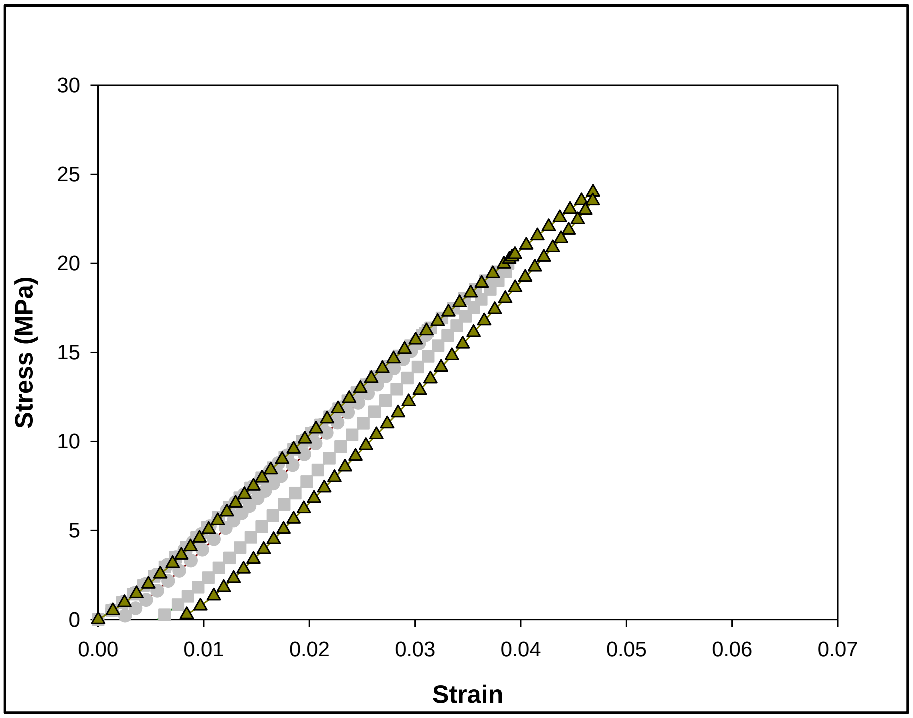

Figure A36. Hysteresis loop for SAC305 at 24MPa

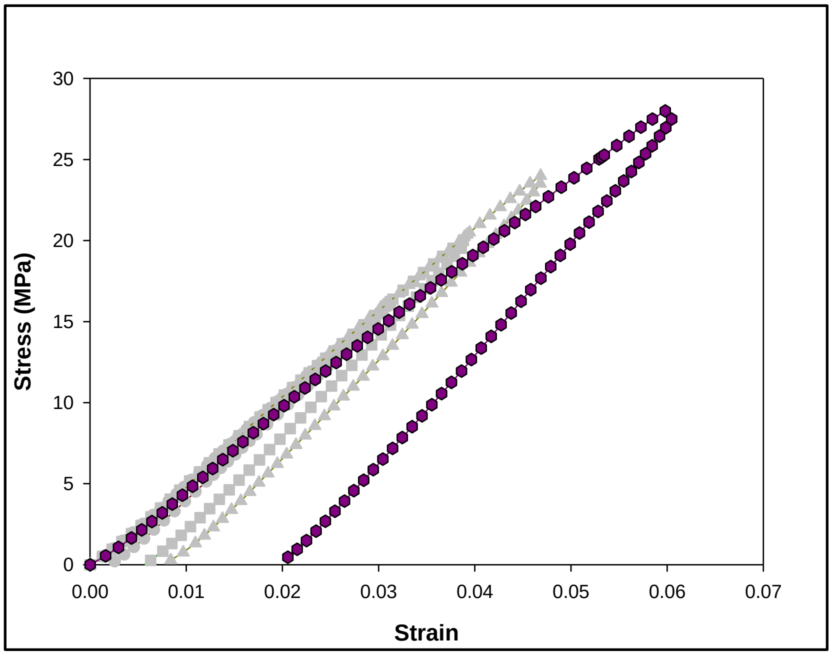

Figure A37. Hysteresis loop for SAC305 at 28MPa

Appendix B

Tables Used for the Statistical Analysis

Table B1. SAC305 shear strength two-way ANOVA analysis table

Analysis of Variance

Source	DF	Adj SS	Adj MS	F-Value	P-Value
Shear Strain rate	3	7653.5	2551.16	161.48	0.000
Surface Finish	2	276.1	138.04	8.74	0.001
Shear Strain rate*Surface Finish	6	232.7	38.78	2.45	0.037
Error	51	805.7	15.80		
Total	62	9176.6			

Table B2. Innolot shear strength two-way ANOVA analysis table

Analysis of Variance

Source	DF	Adj SS	Adj MS	F-Value	P-Value
Shear Strain rate_1	3	1442.2	480.74	20.05	0.000
Surface Finish_1	2	17841.8	8920.90	372.09	0.000
Shear Strain rate_1*Surface Finish_1	6	798.7	133.11	5.55	0.000
Error	57	1366.6	23.98		
Total	68	21621.9			

Table B3. Innolot shear strength with ENIG surface finish one-way ANOVA analysis table

Analysis of Variance

Source	DF	Adj SS	Adj MS	F-Value	P-Value
speed	3	3.951	1.317	0.05	0.987
Error	20	574.898	28.745		
Total	23	578.849			

Table B4. Shear strength comparisons among 5 solder alloys with OSP surface finish

Analysis of Variance

Source	DF	Adj SS	Adj MS	F-Value	P-Value
Alloy Type	4	2508.1	627.03	28.56	0.000
Error	24	526.9	21.96		
Total	28	3035.1			

Table B5. Tukey pairwise comparisons for 5 solder alloys with OSP surface finish

Grouping Information Using the Tukey Method and 95% Confidence

Alloy Type	N	Mean	Grouping		
Innolot	6	83.05	A		
CycloMax	6	80.67	A		
Ecolloy	6	76.794	A	B	
SAC305	6	69.03		B	
SAC-X-Plus	5	56.359			C

Means that do not share a letter are significantly different.

Table B6. Shear strength comparisons among 5 solder alloys with ImAg surface finish

Analysis of Variance

Source	DF	Adj SS	Adj MS	F-Value	P-Value
Alloy Type_2	4	2104.2	526.05	34.87	0.000
Error	21	316.8	15.09		
Total	25	2421.0			

Table B7. Tukey pairwise comparisons for 5 solder alloys with ImAg surface finish

Grouping Information Using the Tukey Method and 95% Confidence

Alloy Type_2	N	Mean	Grouping
Innolot	5	79.94	A
CycloMax	6	79.43	A
Ecolloy	5	78.18	A

SAC305	5	68.291	B
SAC-X-Plus	5	56.43	C

Means that do not share a letter are significantly different.

Table B8. Tukey pairwise comparisons for 5 solder alloys with ImAg surface finish cont.

Tukey Simultaneous Tests for Differences of Means

Difference of Levels	Difference of Means	SE of Difference	95% CI	T-Value	Adjusted P-Value
Ecolloy - CycloMax	-1.25	2.35	(-8.25, 5.75)	-0.53	0.983
Innolot - CycloMax	0.50	2.35	(-6.50, 7.50)	0.21	0.999
SAC-X-Plus - CycloMax	-23.00	2.35	(-30.00, -16.00)	-9.78	0.000
SAC305 - CycloMax	-11.14	2.35	(-18.14, -4.14)	-4.74	0.001
Innolot - Ecolloy	1.75	2.46	(-5.56, 9.07)	0.71	0.951
SAC-X-Plus - Ecolloy	-21.75	2.46	(-29.06, -14.44)	-8.85	0.000
SAC305 - Ecolloy	-9.89	2.46	(-17.20, -2.58)	-4.03	0.005
SAC-X-Plus - Innolot	-23.50	2.46	(-30.81, -16.19)	-9.57	0.000
SAC305 - Innolot	-11.64	2.46	(-18.96, -4.33)	-4.74	0.001
SAC305 - SAC-X-Plus	11.86	2.46	(4.54, 19.17)	4.83	0.001

Individual confidence level = 99.28%

Table B9. Shear strength comparisons among 5 solder alloys with ENIG surface finish

Analysis of Variance

Source	DF	Adj SS	Adj MS	F-Value	P-Value
Alloy Type_3	4	2217.4	554.36	19.34	0.000
Error	24	688.1	28.67		
Total	28	2905.5			

Table B10. Tukey pairwise comparisons for 5 solder alloys with ENIG surface finish

Tukey Pairwise Comparisons

Grouping Information Using the Tukey Method and 95% Confidence

Alloy Type_3	N	Mean	Grouping		
Ecolloy	6	66.36	A		
SAC305	5	59.294	A	B	
CycloMax	6	56.89		B	
SAC-X-Plus	6	53.30		B	
Innolot	6	40.21			C

Means that do not share a letter are significantly different.

Tukey Simultaneous Tests for Differences of Means

Difference of Levels	Difference of Means	SE of Difference	95% CI	T-Value	Adjusted P-Value
Ecolloy - CycloMax	9.47	3.09	(0.36, 18.59)	3.06	0.039
Innolot - CycloMax	-16.68	3.09	(-25.79, -7.56)	-5.39	0.000
SAC-X-Plus - CycloMax	-3.58	3.09	(-12.70, 5.53)	-1.16	0.774
SAC305 - CycloMax	2.41	3.24	(-7.15, 11.97)	0.74	0.944
Innolot - Ecolloy	-26.15	3.09	(-35.27, -17.04)	-8.46	0.000
SAC-X-Plus - Ecolloy	-13.06	3.09	(-22.17, -3.94)	-4.22	0.003
SAC305 - Ecolloy	-7.07	3.24	(-16.63, 2.49)	-2.18	0.221
SAC-X-Plus - Innolot	13.09	3.09	(3.98, 22.21)	4.24	0.002
SAC305 - Innolot	19.08	3.24	(9.52, 28.64)	5.89	0.000
SAC305 - SAC-X-Plus	5.99	3.24	(-3.57, 15.55)	1.85	0.371

Individual confidence level = 99.30%

Tukey Simultaneous 95% CIs

Interval Plot of Shear Strength at ENIG vs Alloy Type_3

Table B11. Shear strength comparisons with/without Bi

Analysis of Variance

Source	DF	Adj SS	Adj MS	F-Value	P-Value
Conditions	2	4167.4	2083.70	88.98	0.000
Error	23	538.6	23.42		
Total	25	4706.0			

Table B12. Tukey pairwise comparisons

Grouping Information Using the Tukey Method and 95% Confidence

Conditions	N	Mean	Grouping		
Bi & Ag	10	60.154	A		
Bi or Ag	10	41.17		B	
no Bi & Ag	6	28.02			C

Means that do not share a letter are significantly different.

Table B12. Tukey pairwise comparisons cont.

Tukey Simultaneous Tests for Differences of Means

Difference of Levels	Difference of Means	SE of Difference	95% CI	T-Value	Adjusted P-Value
Bi or Ag - Bi & Ag	-18.98	2.16	(-24.40, -13.57)	-8.77	0.000
no Bi & Ag - Bi & Ag	-32.13	2.50	(-38.39, -25.88)	-12.86	0.000
no Bi & Ag - Bi or Ag	-13.15	2.50	(-19.40, -6.89)	-5.26	0.000

Individual confidence level = 98.01%